Version 1.0
October 2007

DRAFT - August 2, 2007 - DRAFT

Wide Field Camera 3 Instrument Handbook for Cycle 17

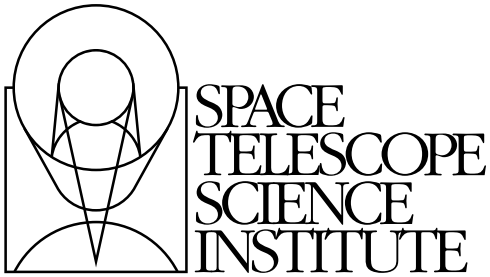

Space Telescope Science Institute
3700 San Martin Drive
Baltimore, Maryland 21218
help@stsci.edu

Operated by the Association of Universities for Research in Astronomy, Inc., for the National Aeronautics and Space Administration

User Support

For prompt answers to any question, please contact the STScI Help Desk.

- **E-mail:** help@stsci.edu
- **Phone:** (410) 338-1082
  (800) 544-8125 (U.S., toll free)

World Wide Web

Information and other resources are available on the WFC3 World Wide Web sites at STScI and GSFC:

- **URL:** http://www.stsci.edu/hst/wfc3
- **URL:** http://wfc3.gsfc.nasa.gov

WFC3 Instrument Handbook Revision History

Version	Date	Editor
1.0	October 2007	Howard E. Bond

Contributors:

Sylvia Baggett, Tom Brown, Howard Bushouse, Mauro Giavalisco, George Hartig, Bryan Hilbert, Randy Kimble, Martin Kuemmel, Harald Kuntschner, Matt Lallo, Olivia Lupie, John MacKenty, Larry Petro, Neill Reid, Massimo Robberto, Massimo Stiavelli, Jeremy Walsh.

Citation:

In publications, refer to this document as:
Bond, H. E., et al. 2007, "Wide Field Camera 3 Instrument Handbook, Version 1.0" (Baltimore: STScI)

Send comments or corrections to:
Space Telescope Science Institute
3700 San Martin Drive
Baltimore, Maryland 21218
E-mail:help@stsci.edu

Table of Contents

Acknowledgments

The WFC3 Science Integrated Product Team (2007)

Sylvia Baggett
Howard Bond
Tom Brown
Howard Bushouse
George Hartig
Bryan Hilbert
Robert Hill (GSFC)
Jessica Kim Quijano
Randy Kimble (Instrument Scientist, GSFC)
John MacKenty (Deputy Instrument Scientist)
Larry Petro
Megan Sosey
Margaret Turnbull

Past Science IPT Members

Wayne Baggett
Laura Cawley
Ed Cheng (GSFC, now Conceptual Analytics)
Ilana Dashevsky
Don Figer
Mauro Giavalisco
Shireen Gonzaga
Christopher Hanley
Ron Henry
Pat Knezek
Ray Kutina
Casey Lisse
Olivia Lupie
Peter McCullough
Neill Reid
Massimo Robberto
Michael Robinson
Massimo Stiavelli

The WFC3 Scientific Oversight Committee

Bruce Balick, University of Washington
Howard E. Bond, Space Telescope Science Institute
Daniela Calzetti, Space Telescope Science Institute
C. Marcella Carollo, Institute of Astronomy, ETH, Zurich
Michael J. Disney, Cardiff University
Michael A. Dopita, Mt Stromlo and Siding Spring Observatories
Jay Frogel, AURA
Donald N. B. Hall, University of Hawaii
Jon A. Holtzman, New Mexico State University
Gerard Luppino, University of Hawaii
Patrick J. McCarthy, Carnegie Observatories
Robert W. O'Connell, University of Virginia (Chair)
Francesco Paresce, European Southern Observatory
Abhijit Saha, National Optical Astronomy Observatory
Joseph I. Silk, Oxford University
John T. Trauger, Jet Propulsion Laboratory
Alistair R. Walker, Cerro Tololo Interamerican Observatory
Bradley C. Whitmore, Space Telescope Science Institute
Rogier A. Windhorst, Arizona State University
Erick T. Young, University of Arizona

Thanks

The Editor thanks the authors who prepared first drafts of the chapters: Larry Petro (Chapters 4 and 10), Massimo Robberto (Chapters 5 and 7), Sylvia Baggett (Chapter 6), Howard Bushouse, Martin Kümmel, Harald Kuntschner, and Jeremy Walsh (Chapter 8), Tom Brown (Chapter 9 and Appendices A, C, and D), Bryan Hilbert (Appendix A), George Hartig (Appendix B), and John MacKenty (Appendix E).

We thank the Technical Editor, Susan Rose, for her contributions to the editing and production of this *Instrument Handbook*.

List of Figures

List of Tables

CHAPTER 1:

Introduction to WFC3

In this book. . .

1.1 Overview

The Wide Field Camera 3 (WFC3) is a fourth-generation imaging instrument that is designed to be installed in the *Hubble Space Telescope* (*HST*) during Servicing Mission 4 (SM4). At this writing in the spring of 2007, SM4 is scheduled for August 2008. Cycle 17 of the *HST* observing program will begin following SM4, and is currently planned to cover the interval from the conclusion of SM4 and the ensuing orbital verification phase through June 2009 (TBD). The Space Telescope Science Institute (STScI) will accept observing proposals for WFC3 in the review process for Cycle 17.

This *WFC3 Instrument Handbook* has been prepared by the WFC3 team at STScI. It is the basic technical reference manual for WFC3 observers. The information in this *Handbook* is intended to be useful for Cycle 17 Phase I proposers, for the subsequently selected General Observers (GOs) as they prepare their Phase II specifications, and for those analyzing WFC3 data.

It should be noted that WFC3 is, at this writing, still under development. Although this *Handbook* is as accurate as possible, the information herein is still subject to possible changes before SM4, and also as a consequence of experience gained after WFC3 is operating onboard *HST*.

The WFC3 instrument will occupy *HST*'s radial scientific-instrument bay, where it will obtain on-axis direct images. During SM4 the shuttle astronauts will install WFC3 in place of the current Wide Field Planetary Camera 2 (WFPC2). WFPC2, in turn, was

installed during SM1 in December 1993, to replace the original Wide Field/Planetary Camera (WF/PC1). WFPC2, like WFC3, contains optics that correct for the spherical aberration discovered in the *HST* primary mirror following launch of the telescope in April 1990.

WFC3 uses some components of the original WF/PC1, which will thus see service once again onboard *Hubble*. WFC3 is designed to ensure that *HST* maintains its unique imaging capabilities until the end of its mission, while at the same time advancing its survey and discovery capability due to its combination of wide wavelength coverage, wide field of view, and high sensitivity. WFC3 will also provide a good degree of redundancy for the aging Advanced Camera for Surveys (ACS) and Near-Infrared Camera and Multi-Object Spectrometer (NICMOS) cameras. [Q: need to update this sentence to current ACS status.]

A key feature of WFC3 is its panchromatic wavelength coverage. By combining two optical/ultraviolet CCDs with a near-infrared HgCdTe array, WFC3 will be capable of direct, high-resolution imaging over the entire wavelength range from 200 to 1700 nm. Equipped with a comprehensive range of wide-, intermediate-, and narrow-band filters, WFC3 will have broad applicability to a variety of new astrophysical investigations.

WFC3 is a facility instrument. It is being developed, constructed, characterized, and calibrated by an Integrated Product Team (IPT) led by NASA's Goddard Space Flight Center (GSFC), and composed of staff astronomers and engineers from GSFC, STScI, Ball Aerospace & Technologies Corp., the Jet Propulsion Laboratory (JPL), and other industrial contractors.

A Scientific Oversight Committee (SOC), selected by NASA from the international astronomical community and appointed in 1998, provides scientific advice for the design and development of WFC3. The SOC's activities have been in a variety of areas, including: definition of the key scientific goals and success criteria for WFC3; participation in project reviews; recommending an optimum set of filters and grisms for the instrument and the pixel scale and field of view of the detectors; participation in the selection of flight detectors; and advice on technical trade-off decisions in the light of the scientific goals of the instrument. The SOC continues to provide oversight on all aspects of WFC3 development, with the aim of assuring that the camera will achieve its scientific goals.

1.2 Key Features of WFC3

The optical design of WFC3 features two independent channels, one sensitive at ultraviolet (UV) and optical wavelengths, approximately 200 to 1000 nm (the UVIS channel), and the other sensitive at near-infrared (near-IR) wavelengths, approximately 900 to 1700 nm (the IR channel). A channel-selection mirror will direct on-axis light from the *HST* optical telescope assembly (OTA) to the IR channel, or the mirror can be removed from the beam to allow light to enter the UVIS channel. This means that *simultaneous* observations with the UVIS and IR detectors are not

possible. However, both UVIS and IR observations can be made sequentially during the same *HST* orbit.

The extended wavelength range, combined with high sensitivity, high spatial resolution, large field of view, and a wide selection of spectral elements, make WFC3 an extremely versatile instrument. Key features of WFC3 include:

- **UVIS channel:** two 2k×4k CCDs; pixel scale 0.04 arcsec/pix; field of view 163×164 arcsec; wavelength range 200-1000 nm; S/N=10 in a 10-hour exposure (F606W filter) for a point source with *V*=28.9.
- **IR channel:** 1k×1k HgCdTe array; pixel scale 0.13 arcsec/pix; field of view 123×137 arcsec; wavelength range 900-1700 nm; S/N=10 in a 10-hour exposure (F160W) for a point source with *H*=28.0.
- 62 broad-, medium-, and narrow-band filters in the UVIS channel.
- 15 broad-, medium-, and narrow-band filters in the IR channel.
- 1 grism in the UVIS channel, and 2 grisms in the IR channel.

A "white paper," prepared by the SOC and the Science IPT, outlines the scientific areas that will benefit most from the capabilities of WFC3. These include searches for galaxies at redshifts up to $z\sim10$; studies of the physics of star formation in distant and nearby galaxies; investigations of resolved stellar populations down to faint levels in the UV, optical, and near-IR; and high-resolution imaging of objects in the solar system. Of particular interest will be programs that fully exploit the panchromatic capability of WFC3 for broad investigations of the assembly and evolution of galaxies; star birth, evolution, and death and its relation to the interstellar medium; and meteorology of the outer planets. The white paper (Stiavelli, M., & O'Connell, R.W., eds., 2000, "*Hubble Space Telescope* Wide Field Camera 3, Capabilities and Scientific Program") can be found at:

http://wfc3.gsfc.nasa.gov/white_paper.html

1.3 Current Instrument Status

At present (spring 2007), as the editing of this *Instrument Handbook* was being completed, WFC3 continues to be developed and tested.

At the time of the January 2004 decision to cancel SM4, WFC3 was reaching the end of its assembly stage. To characterize the state of the instrument at that time, NASA directed the WFC3 program to conduct a "characterization" system-level thermal-vacuum test of the instrument. The instrument proceeded into this test in the fall of 2004. This was done in spite of a significant number of known issues, which normally would have been resolved prior to a full acceptance/qualification thermal-vacuum test.

The fall 2004 testing successfully demonstrated the overall operation and performance of the instrument, and it informs the performance predictions in this

Handbook. Subsequently, with improving prospects for an SM4, WFC3 was partially disassembled to resolve both the previously known issues and additional items discovered during testing. In particular, the following problems have been addressed: significant ghost images were discovered in some of the UVIS filters and have been eliminated by replacing the affected filters; various electronics issues have been resolved; and the thermal control system has been improved. A flight UVIS detector has been selected, and a superior infrared detector (FPA 129) has been produced and is a strong candidate for flight.

At this writing, WFC3 is expected to resume thermal-vacuum testing in spring 2007.

1.4 Special Considerations for Cycle 17

TBD: put some general comments here on fact that SM4 has not occurred, WFC3 is still under development, etc.

TBD: some kind of statement that information here is best available, but there are no guarantees, etc.

TBD: OK to say that we will return to 3 gyros in Cycle 17?

1.5 Sources of Further Information

Table 1.1 provides a guide to online documents containing further information about HST, the proposal process, and data analysis.

TBD: this version of Table 1.1 is copied from the ACS Handbook & needs to be updated for WFC3.

TBD: there should also be a guide to WFC3-specific information, ISRs, etc.

Table 1.1: Useful documents

Purpose	Document or resource
General observatory information	HST Primer http://www.stsci.edu/hst/proposing/docs/proposing/documents/cp/primer.pdf
Phase I proposals	Proposing Overview http://www.stsci.edu/hst/proposing/docs/proposingOverview Call for Proposals http://www.stsci.edu/hst/hst/proposing/documents/cp/cp_cover.html
Phase II programs	Phase II Proposal Instructions http://www.stsci.edu/hst/programs/hst/proposing/docs/p2pi.html Astronomer's Proposal Tool (APT) for Phase II preparations http://apt.stsci.edu/ Two-Gyro Web site http://www.stsci.edu/hst/HST_overview/TwoGyroMode Two-Gyro Handbook http://www.stsci.edu/hst/HST_overview/TwoGyroMode/handbook/cover.html
Data analysis	ACS Data Handbook http://www.stsci.edu/hst/acs/documents/handbooks/DataHandbookv4/ACS_longdhbcover.html Dither Handbook http://www.stsci.edu/instruments/wfpc2/Wfpc2_driz/dither_handbook.html Space Telescope Analysis Newsletter http://www.stsci.edu/hst/acs/documents/isrs/hst/acs/documents/newsletters Instrument Science Reports http://www.stsci.edu/hst/acs/documents/isrs Calibration and Pipeline Information http://www.stsci.edu/hst/Post-observation

===== Sylvia's references from end of Chapter 6 =====

[** not sure if each Chapter to have references? if so, here are the ones for this Chapter]

"Operations and Data Management Plan for the WFC3," OP-01, W. Baggett et al., December 2002

"Filters for HST Wide Field Camera 3," S. Baggett et al., Proc. SPIE Vol. 6265, John C. Mather, Howard A. MacEwen, Mattheus W. de Graauw; Eds., Jul 2006.

"HST WFC3 Capabilities and Science Programs," *WFC3 Science White Paper*, SOC and Science IPT, edited by M.Stiavelli and R.W. O'Connell, 2000.

WFC3 Filter Workshop, held at Space Telescope Science Institute, July 14,1999, http://www.stsci.edu/hst/wfc3/documents/meetings/workshop/wfc3-filter_workshop

WFC3 ISR 2006-02, "FPA121 Persistence Search," B.Hilbert & M. Robberto, June 2006.

WFC3 ISR 2005-16, "Scientific Impacts of UVIS Channel Filter Ghosts," H. Bond & T. Brown, April 2005.

WFC3 ISR 2005-10, "WFC3 UVIS PSF Evaluation in Thermal-Vacuum Test #1," G.Hartig, Feb 2005.

WFC3 ISR 2004-09, "Preliminary Assessment of Image Persistence in the WFC3 UVIS CCD Detector," G. Hartig, June 2004

WFC3 ISR 2004-08, "Preliminary WFC3 UVIS PSF Evaluation," G. Hartig and S. Baggett, May 2004.

WFC3 ISR 2004-04, "Filter Ghosts in the WFC3 UVIS Channel," T. Brown, May 2004.

WFC3 ISR 2001-17, "Modeling the Impact of Ghosts in WFC3/UVIS," M. Stiavelli, June 2001.

1.6 The WFC3 Instrument Team at STScI

STScI maintains a team of Instrument Scientists, Data Analysts, Engineers, and Scientific Programmers, who support the design, development, operation, calibration, and documentation of WFC3. STScI also maintains a “Help Desk” to provide answers quickly to any WFC3- and *HST*-related questions. Please refer all questions regarding WFC3 and *HST* to the Help Desk, as follows:

- E-mail: help@stsci.edu
- Phone: (410) 338-1082

CHAPTER 2:

WFC3 Instrument Description

In this chapter . . .

2.1 Optical Design and Detectors

The optical design of WFC3 was driven by the need to provide a large field of view and high sensitivity over a broad wavelength range, excellent spatial resolution, and stable and accurate photometric performance. WFC3 features two independent imaging cameras: the UV/optical channel (UVIS) and the near-infrared channel (IR). Figure 2.1 shows a schematic diagram of the instrument's optical layout.

On-axis light coming from the *HST* optical telescope assembly (OTA) is intercepted by the flat 45° WFC3 pickoff mirror (POM) and directed into the instrument. A channel-select mechanism (CSM) inside WFC3 then diverts the light to the IR channel via a fold mirror, or the CSM mirror can be removed from the beam to allow light to enter the UVIS channel. Because of this design, only a single channel, either UVIS or IR, can be used at any one time, although it is possible to switch between them fairly quickly.

Optical elements in each channel (anamorphic aspherical correctors) correct separately for the ~1/2 wave spherical aberration of the *HST* primary mirror. Both channels also have internal flat-field illumination sources.

Two different types of detectors are used in the two channels. The UVIS channel uses two butted 4096×2051 thinned, back-illuminated Marconi (now e2v Ltd.) CCD detectors to support imaging between 200 and 1000 nm. The IR channel uses a

1024×1024 Teledyne HgCdTe detector array, with the central 1014×1014 pixels useful for imaging, and covering the near-infrared between 900 and 1700 nm.

The primary characteristics of the two channels are summarized in Table 2.1.

Table 2.1: Characteristics of the two WFC3 channels

Channel	*f*-ratio	Detector type	Spectral range (nm)	Detector pixel format	Pixel scale (arcsec)	Field of View (arcsec)
UVIS	31	CCD	200-1000	2×4096×2051	0.040×0.040	163×164
IR	11	HgCdTe	900-1700	1014×1014	0.121×0.135	123×137

Figure 2.1: Schematic optical layout of the WFC3 instrument. Yellow indicates light from the OTA, which is sent into the camera by the pick-off mirror. The Channel Select Mechanism then either allows light to pass into the UVIS channel (indicated by the blue path), or directs light into the IR channel (red path). Mechanisms and optics in both channels allow for focus and alignment, and correct for the OTA spherical aberration. Filters and grisms are contained in the UVIS SOFA and the IR FSM. The UVIS channel has a mechanical shutter, while the IR channel is shuttered electronically by the detector. Light is detected by either the UVIS CCDs or the IR focal-plane array. A separate subsystem provides flat field illumination for both channels.

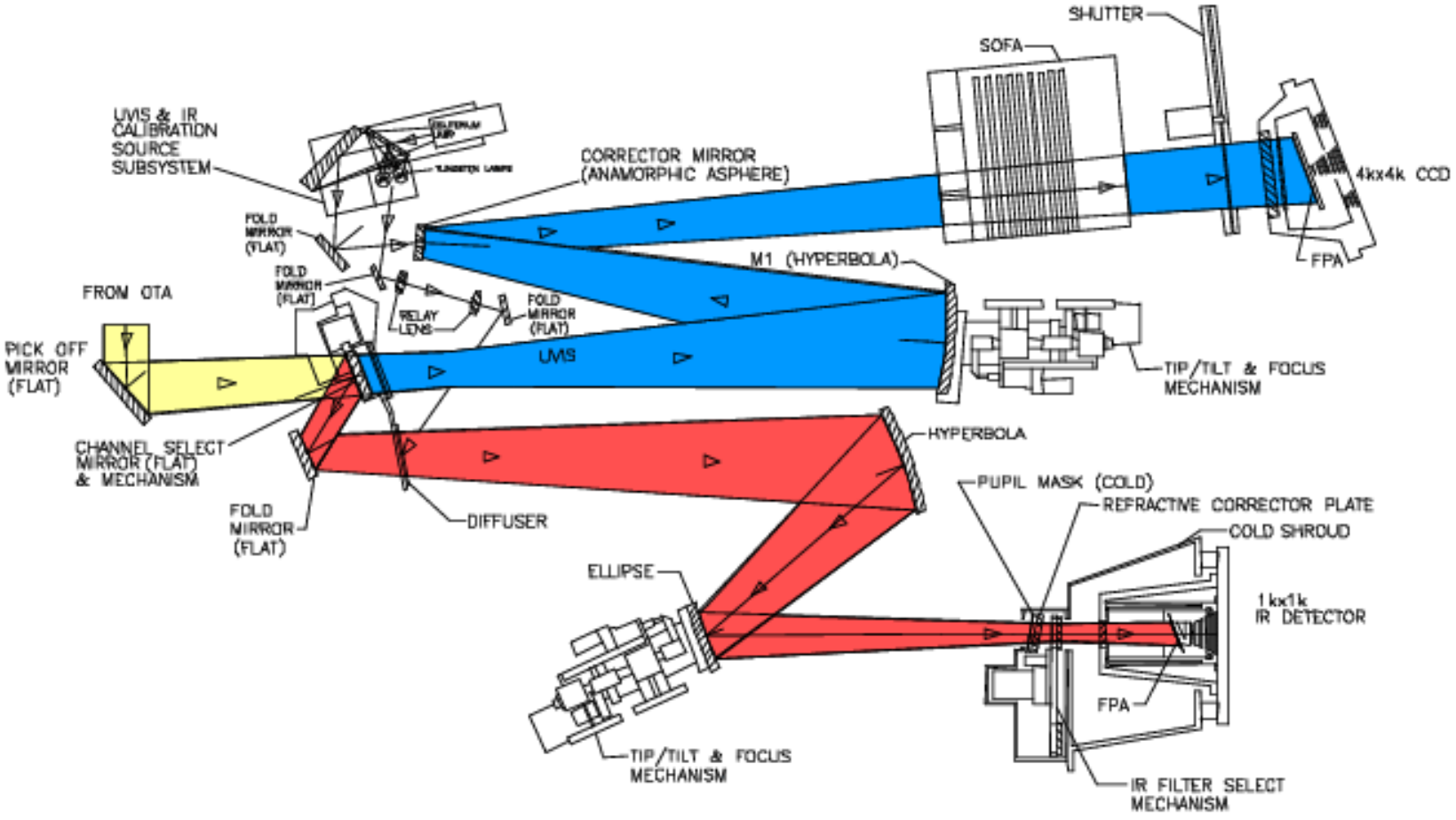

2.2 Field of View and Geometric Distortions

WFC3 replaces WFPC2, *Hubble*'s first large-area camera that included corrections for the spherical aberration of the *HST* primary mirror. The appearance of the *HST* focal plane following a fully successful SM4 is shown in Figure 2.2.

Q: Susan, Fig 2 should be the file FOV-SM4forCycle17PrimerOUTLINE.epsi

Figure 2.2: The *HST* focal-plane layout, showing the instrument complement following a successful SM4. WFC3 will be located on-axis. Outlines of its UVIS and IR channels are shown; they view nearly the same region of the sky, but not simultaneously. The diameter of the outer black circle, projected onto the sky, is about 28 arcminutes.

This is the figure caption. The title above needs to be very short.

As is the case for ACS, WFC3 images are subject to significant geometric distortions. These result primarily from the tilt of the focal plane relative to the optical axis (required for constant focus across the detectors; see Figure 2.1), which leads to a modest elongation of the field of view in both channels. In the UVIS detector, most of the distortion runs approximately parallel to the diagonal direction of the CCD, while it is parallel to the sides of the detector in the IR channel. As a result, the UVIS field projected onto the sky is shaped like a rhombus, with an acute angle between the *x* and *y* axes of the detector of approximately 86 degrees. The IR channel projected onto the sky will be rectangular, with an aspect ratio of about 0.90. For further discussion of geometric distortions in WFC3, see Chapter xxx.

2.3 Spectral Elements

2.3.1 The Selection Process

Both WFC3 channels are complemented with a broad selection of spectral elements. These elements were chosen on recommendation of the WFC3 SOC, following a lengthy process with wide scientific and community input. Initial community suggestions and advice were considered at the WFC3 Filter Selection Workshop, held at STScI on July 14, 1999. Other input came from the WFC3 Science White Paper (see section xxx), from a suite of SOC-developed test proposals representing a broad range of current astronomical investigations, and from statistics of historical filter use in previous HST imaging instruments. The filter sets were chosen to cover fully the wavelength regimes of both WFC3 channels with a range of bandwidths, while complementing the filter sets used in ACS and NICMOS.

Based upon the SOC recommendations, the WFC3 IPT (see Section 1.1) developed detailed specifications for the vendors who designed and manufactured the filters. The final flight spectral elements were fully characterized, evaluated by the IPT and SOC, approved for flight, and installed into the filter wheels.

2.3.2 Filter and Grism Summaries

On the UVIS side, the selectable optical filter assembly (SOFA) contains a stack of 12 filter wheels housing a total of 48 elements: 42 full-frame filters, 5 quad filters, and 1 UV grism. Each wheel also has an open, or empty, slot. For UVIS observations, the appropriate wheel is rotated to place the chosen filter into the light path, and the other eleven wheels are rotated to place the open slot in the light path.

The IR channel has a single filter wheel housing 17 elements: 15 filters and 2 grisms; an 18th slot contains a blank, opaque blocker. For IR observations, the requested single element is rotated into the light beam.

The filter assortments in both channels include broad-, medium-, and narrow-band filters, as well as low-dispersion grisms (one in the UVIS channel, two in the IR

channel) for slitless spectroscopy. The broad- and medium-band filters include most of the popular passbands used in extragalactic, stellar, and solar-system astronomy, as well as passbands similar to those already used in other *HST* instruments for photometric consistency and continuity. The classical *UBVRIJH*, Strömgren, and Washington systems are reproduced, along with the filters of the Sloan Digital Sky Survey (SDSS). In addition, several extremely broad-band filters have been included in both channels, for ultra-deep imaging.

There is also a total of 36 different narrow-band passbands in the UVIS channel, consisting of 16 full-field filters and 5 quad filters. (Quad filters are 2×2 mosaics occupying a single filter slot; each one provides four different bandpasses, at the cost of each one covering only about 1/6 of the field of view.) The narrow-band filters provide the capability for high-resolution emission-line imaging in many of the astrophysically important transitions, as well as the methane absorption bands seen in planets, cool stars, and brown dwarfs.

In addition to the broad-band filters, the IR channel includes six narrow-band filters, which likewise sample the most important planetary, stellar, and nebular spectral features in the near-IR.

Finally, broad-band filters with similar wavelength coverages to those of the grism dispersers are available, allowing direct images of spectroscopic targets in the same spectral regions; such images allow accurate identification of the sources as well as providing wavelength calibration.

Unlike ACS or WFPC2, no ramp filters or polarizers are included in either WFC3 channel.

Table 6.1 and Table 7.xxx provide a complete summary of the filters available for imaging with the UVIS and IR channels, respectively. Individual filter transmission curves as well as filter+WFC3+HST system throughput curves are presented in Appendix A. Figure xxx shows the overall integrated system throughputs of WFC3 compared to other instruments.

2.4 Detector Read-Out Modes and Dithering

The detectors in both channels offer readouts of subarrays, and the UVIS channel also allows on-chip binning. A variety of dithering schemes will be offered to observers by the Astronomer's Proposal Tool (APT) proposal software, including specially designed "canned" patterns as well as user-defined ones. See Chapter xxx for details.

The post-observation pipeline software will carry out calibration of data taken in all of these configurations, and will offer the option of reconstructing dithered images with a drizzling algorithm. If the dither pattern incorporates non-integer pixel offsets, it effectively improves the sampling of the point-spread function (PSF). The software will also handle mosaicked images according to a set of rules or associations, and will rectify them onto a cartesian pixel coordinate system.

CHAPTER 3:

Choosing the Optimum *HST* Instrument

In this chapter . . ..

3.1 Overview

This chapter addresses the general questions that arise when observers choose between proposing to use WFC3 or one or more of the other imaging instruments available on *HST*.

In making this decision, observers should carefully evaluate the capabilities of WFC3 and compare them to those of the other *HST* instruments, in the context of their own scientific goals. Observers should especially note that WFC3 intentionally provides some redundancy with the ACS and NICMOS instruments, in order to provide some protection against potential failures of either of those instruments. On the other hand, WFC3 also differs from those instruments (in fact, it largely complements them). Therefore, observers do need to give careful consideration to instrument capabilities in order to optimize the observations.

3.2 Choosing Between Instruments

The primary factors to consider in choosing the best instrument are areal coverage, spatial resolution, wavelength coverage, sensitivity, and availability of specific spectral

elements. Table xxx lists the primary characteristics of the imaging instruments that will be available on *HST* following a successful SM4.

For some research programs, the instrument choice may be dictated by the need for a particular spectral element. In this regard, WFC3 offers considerable capability because of its broad complement of wide-, medium-, and narrow-band filters both at UV/optical and near-IR wavelengths, as well as one UV grism and two near-IR grisms for slitless spectroscopy.

For studies at optical wavelengths, the trade-offs to consider when deciding between WFC3/UVIS and ACS/WFC include pixel size, field of view and, to some extent, throughput. WFC3 is generally preferable when angular resolution has higher priority than field of view, because of its finer pixel size. On the other hand, ACS/WFC has higher throughput than WFC3/UVIS at wavelengths longward of 400 nm (see Figure xxx) and hence it should be used if the highest possible sensitivity at such wavelengths is crucial. However, considerations of degraded charge-transfer efficiency (CTE) should also be kept in mind, since ACS will have been in the high-radiation space environment for about six years at the time when WFC3 comes on line.

At UV wavelengths, WFC3/UVIS is the only imager on *HST* to offer a large field of view combined with high throughput. However, its spectral coverage does not extend shortward of 200 nm, whereas ACS/SBC and STIS/FUV-MAMA (assuming STIS operation is restored during SM4) both reach down to 115 nm (STIS/NUV-MAMA reaches 160 nm), and also offer finer spatial sampling (see Table xxx). Thus, WFC3 will be the choice whenever both large field of view and coverage down to 200 nm are required (e.g., multi-wavelength surveys). However, if observations at extreme far-UV wavelengths are necessary, or if the highest available spatial sampling is a primary requirement, then ACS/HRC, ACS/SBC, or the STIS UV channels should be considered.

At near-IR wavelengths WFC3/IR offers a much larger field of view and, generally, higher throughput than NICMOS. It also offers greatly improved sensitivity and ease of data reduction and calibration, due to the accurate bias subtraction made possible by the presence of reference pixels. However, WFC3 sensitivity is limited to wavelengths shortward of ~1700 nm, and WFC3 has coarser pixel sizes than NIC1 and NIC2.

3.3 Comparison of WFC3 with Other *HST* Imaging Instruments

3.3.1 Wavelength Coverage

The WFC3 UVIS channel is similar in design to the Wide Field Channel (WFC) of the ACS. There are, however, a few differences. While ACS/WFC is blind at wavelengths shorter than about 370 nm (i.e., shortward of the *B* band), WFC3/UVIS has sensitivity extending down to 200 nm. The design trade-offs adopted to achieve this extended UV wavelength coverage (primarily the CCD coating and the use of

aluminum coatings for the reflective optics; see Figure 3.1) lead to a reduced sensitivity of WFC3 at longer optical wavelengths compared to that of ACS/WFC.

The ACS does have UV sensitivity in its High Resolution Channel (HRC). However, compared to ACS/HRC, WFC3/UVIS has a factor of 2 higher throughput at the *U* band (see Figure 3.2 below), and a field of view 35 times the area (but with spatial sampling that is 50% coarser). WFC3/UVIS has no sensitivity in the far-UV region below 200 nm. The far-UV is covered by the ACS Solar-Blind Channel (SBC) and, potentially, by the Space Telescope Imaging Spectrograph (STIS) FUV-MAMA, which may be restored to use during SM4.

The WFC3 IR channel also provides nearly a factor of 2 improvement in sensitivity over NICMOS. However, its wavelength coverage is shorter, ending at about 1700 nm (compared with 2500 nm for NICMOS). The WFC3/IR cutoff at 1700 nm greatly reduces the instrument's sensitivity to the thermal background. Unlike NICMOS, the WFC3 IR channel does not have a cryogenic dewar for cooling of instrument components; instead, all optical components of the IR channel are actively cooled by a thermal-control subsystem. Although much simpler than the NICMOS cryocooler, this design allows the IR detector to be cooled only to ~145 K, and thus does not provide adequate suppression of the thermal background at wavelengths longer than ~1700 nm.

3.3.2 Field of View

Figure 3.1 schematically illustrates the fields of view (FOVs), on the same scale, for all of the *HST* imaging instruments that will be available following a fully successful SM4.

Figure 3.1: Schematic diagram comparing relative sizes of the fields of view (FOVs) for all *HST* imaging instruments, following a completely successful SM4. Successive lines of text underneath each FOV give the size in pixels, the pixel scale in arcseconds, and the FOV size in arcseconds. The diagram is schematic, and does not illustrate geometric distortions nor the relative locations in the *HST* focal plane.

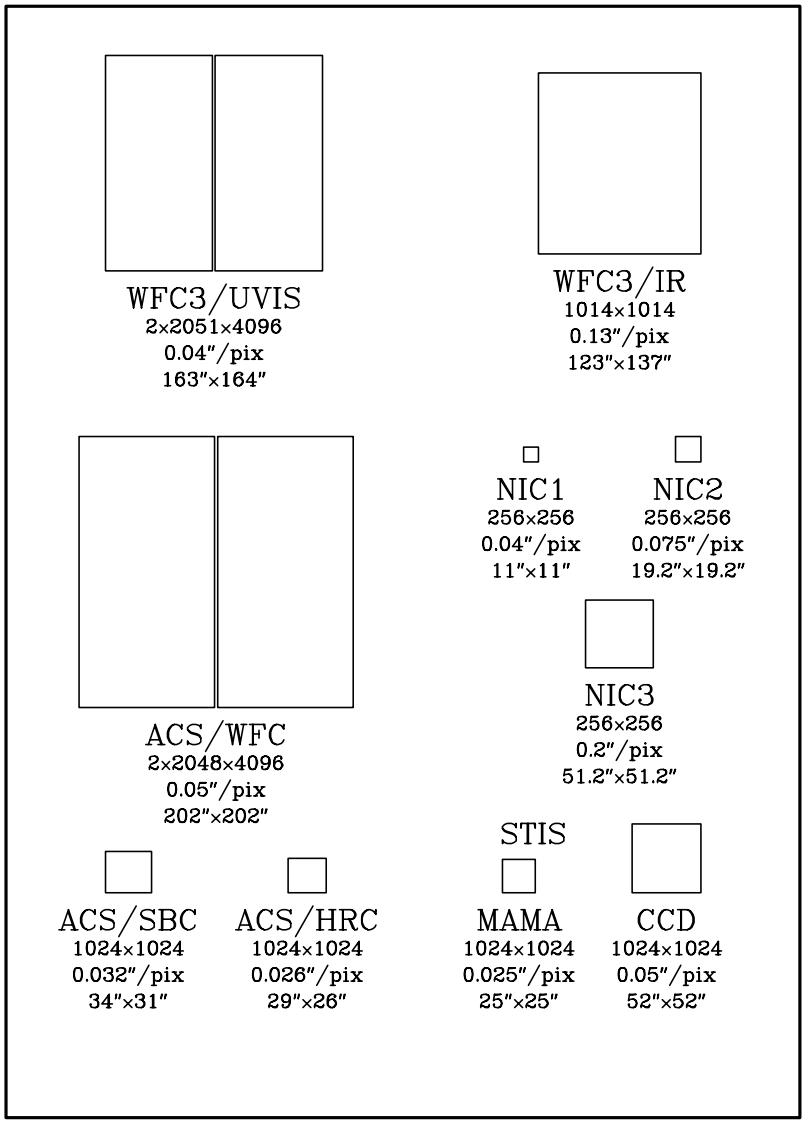

The WFC3 UVIS channel provides about 20% linearly finer pixels than ACS/WFC, obtained at the cost of covering only about 66% of the area of the latter's field of view.

The WFC3 IR channel covers about 6.4 times the area of the NICMOS NIC3 channel, with almost 2 times better spatial sampling, but it lacks the very high spatial samplings offered by the NICMOS/NIC1 and NIC2 channels.

Table 3.1 presents a comparison of the wavelength coverage, pixel scale, and FOV of WFC3 and of the other *HST* imaging instruments that will be available following a successful SM4. The table includes the imaging characteristics of STIS, which, however, has been disabled since August 2004.

Table 3.1: Comparison of wavelength coverage, pixel scales, and fields of view of *HST*'s imaging instruments after a successful SM4.

Instrument	Wavelength coverage (nm)	Pixel size (arcsec)	Field of View (arcsec)
WFC3 UVIS	**200 – 1100**	**0.04**	**163×164**
ACS WFC	370 – 1100	0.05	202×202
ACS HRC	200 – 1010	0.025	29×26
ACS SBC	115 – 170	0.03	34×31
STIS FUV-MAMA	115 – 170	0.024	25×25
STIS NUV-MAMA	160 – 310	0.024	25×25
STIS CCD	200 – 1100	0.05	52×52
WFC3 IR	**900 – 1700**	**0.13**	**123×137**
NICMOS NIC1	850 – 2500	0.043	11×11
NICMOS NIC2	850 – 2500	0.075	19×19
NICMOS NIC3	850 – 2500	0.20	51×51

3.3.3 Detector Performance

The UVIS and IR detectors are anticipated to have excellent performance in terms of read-out noise and dark current.

Table 3.3 summarizes these properties for the WFC3 flight CCD detector and the flight candidate FPA 129 IR detector, and compares them with these parameters for other *HST* imaging detectors that will be available following a successful SM4.

Chapters xxx and yyy give full details of the performance of both detectors. Chapter zzz discusses sensitivites and limiting magnitudes.

Table 3.2: Characteristics of *HST* imaging detectors available after SM4. Values for the WFC3 detectors are for the flight CCD and flight candidate IR detector FPA 129. The WFC3/IR dark current includes the instrument thermal background.

Detector	Read-out noise, e^- rms	Dark current, e^-/pix/s
WFC3/UVIS	**3.1**	**<0.00014**
ACS/WFC	5.0	0.0038
ACS/HRC	4.7	0.0044
STIS/CCD	5.4	0.004
WFC3/IR	**16**	**<0.4**
NICMOS/NIC2	26	0.3
NICMOS/NIC3	29	0.3

3.3.4 System Throughputs and Discovery Efficiencies

Figure 3.2 plots the expected system throughputs of the two WFC3 channels as functions of wavelength, compared to those of ACS, NICMOS, and WFPC2. These curves include the throughput of the OTA, all of the optical elements of the instruments themselves, and the sensitivities of the detectors. Throughputs were calculated at the central wavelength (the "pivot wavelength"; see footnote xxx to Table xxx) of each broad-band filter of each instrument. The WFC3 throughputs are based on the currently selected flight detectors, and are still subject to change at this writing based on further laboratory measurements and the final IR detector choice.

As Figure 3.2 shows, WFC3 offers a unique combination of high sensitivity and wide spectral coverage ranging from the UV to the near-IR. WFC3 extends and complements, over a large field of view, the optical performance of ACS/WFC at wavelengths shorter than ~400 nm and longer than 1000 nm. The good degree of functional redundancy with ACS and NICMOS will help ensure that the unique scientific capabilities of *HST* will remain available until the end of its mission.

Another quantity that is useful when comparing different instruments, especially in the context of wide-angle surveys, is the "discovery efficiency," defined as system throughput times area of the FOV as projected onto the sky. In Figure 3.3 we plot the discovery efficiencies of the *HST* imaging instruments, again vs. wavelength. Note that the *y*-axis is now logarithmic. This figure dramatically illustrates the enormous gains that WFC3 will offer, compared to previous *HST* instruments, both in the optical/UV below 400 nm, and in the near-IR.

Figure 3.2: System throughputs of imaging instruments on *HST* as functions of wavelength. The plotted quantities are end-to-end throughputs, including filter transmissions, calculated at the pivot wavelength of each broad-band filter of each camera. Throughputs for WFC3 are estimated based on the best information currently available.

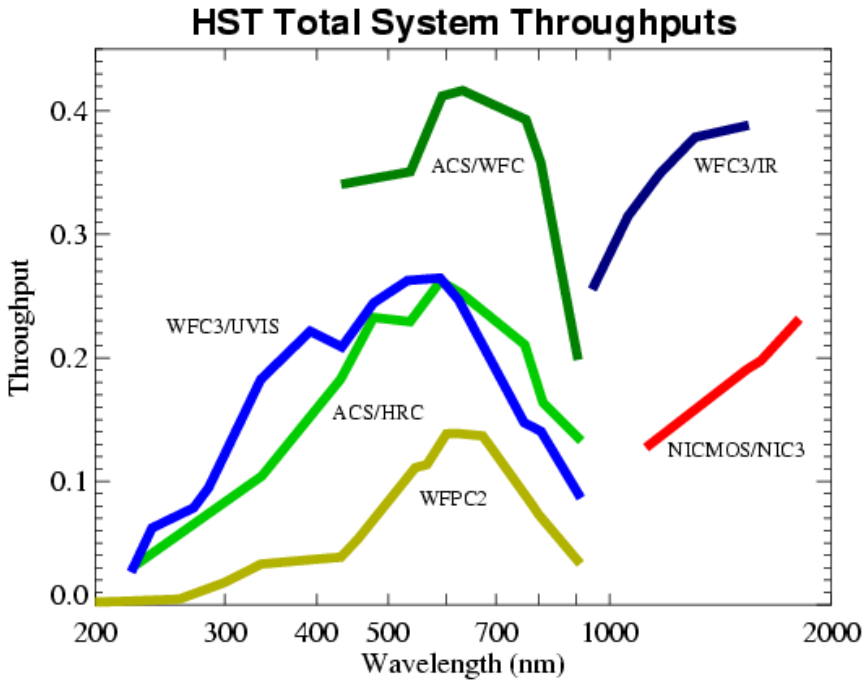

Figure 3.3: Discovery efficiencies of *HST* imaging instruments, including those expected for WFC3. Discovery efficiency is defined as the system throughput (plotted in Figure 3.2) multiplied by the area of the field of view. Note that the *y*-axis is now logarithmic.

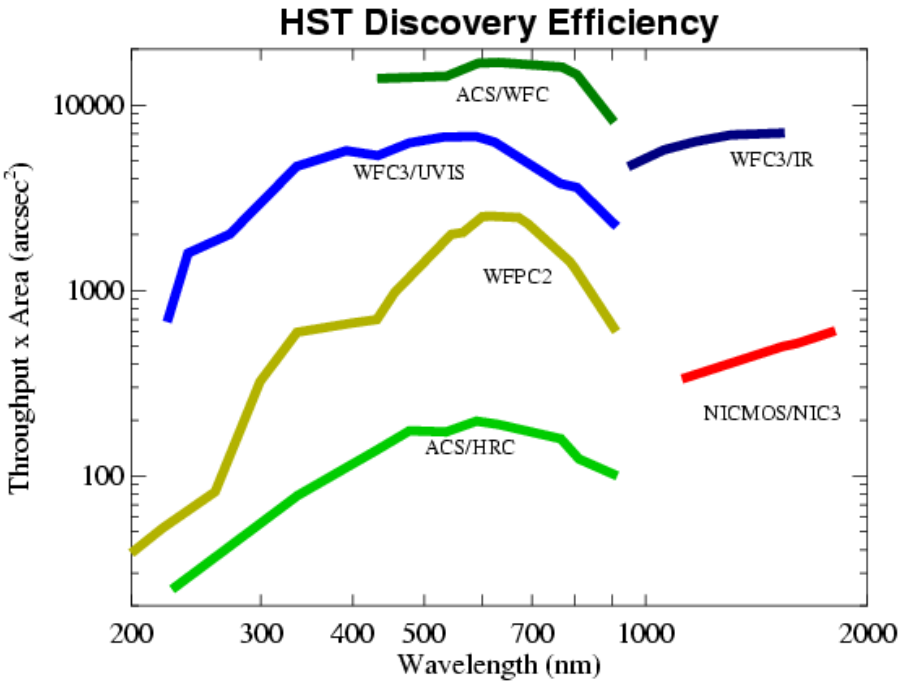

3.4 Designing an ACS Observing Proposal

TBD: This section, copied from the ACS Handbook, needs to be updated for WFC3, and probably moved to Chapter 4.

In this section, we describe the sequence of steps you will need to take when designing your ACS observing proposal. The process is an iterative one, as trade-offs are made between signal-to-noise ratio and the limitations of the instrument itself. The basic sequence of steps in defining an ACS observation are:

- Identify science requirements and select the basic ACS configuration to support those requirements.
- Estimate exposure time to achieve the required signal-to-noise ratio, determine GAIN selection, CR-SPLIT, dithering and mosaic strategy and check feasibility, including saturation and bright-object limits.
- Identify any additional target acquisition (coronagraph), and calibration exposures needed.
- Calculate the total number of orbits required, taking into account the overheads.

Figure 3.4: HST Field of View Following SM3B

Figure 3.5: Defining an ACS Observation

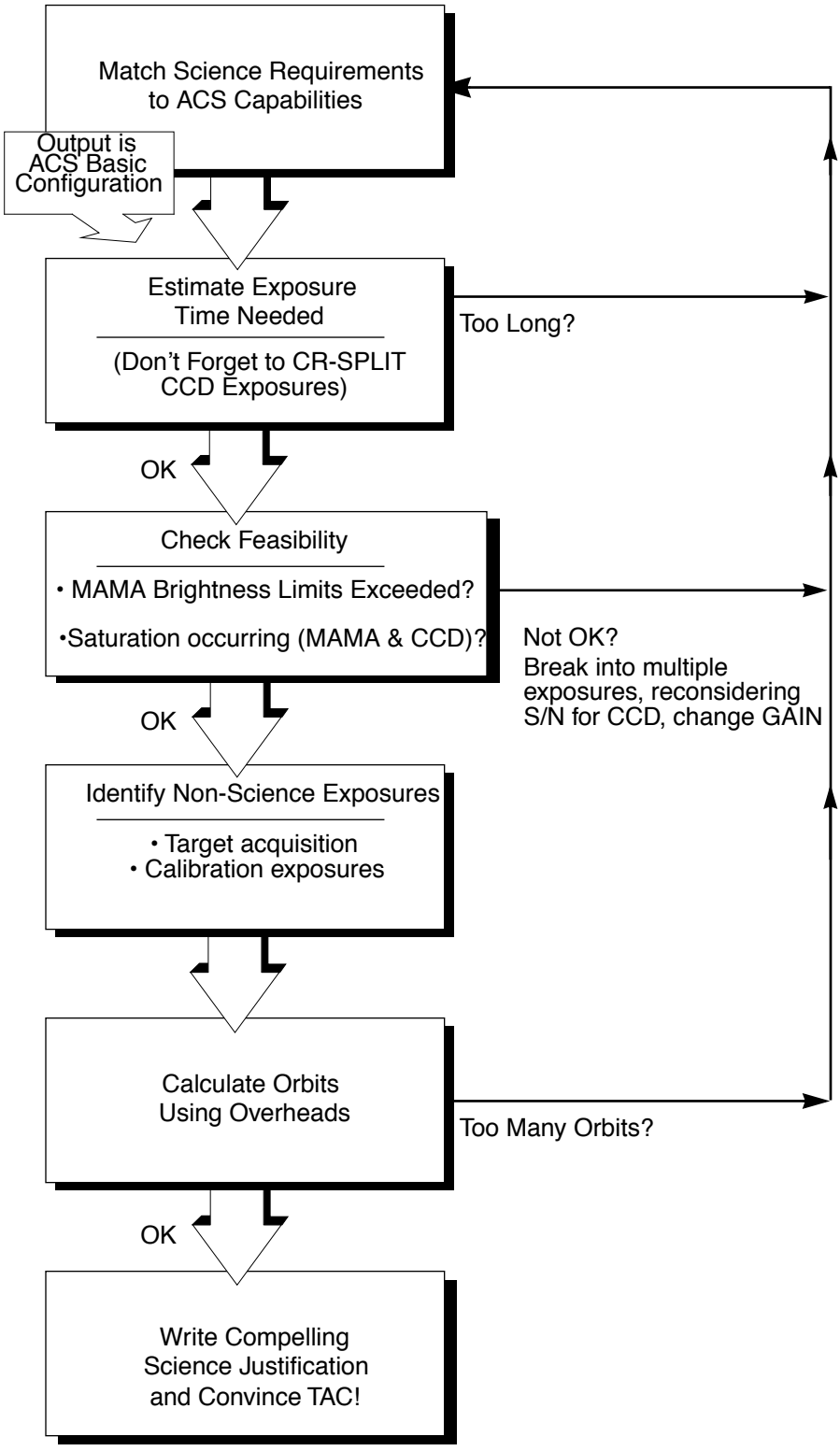

3.4.1 Identify Science Requirements and Define ACS Configuration

First and foremost, of course, you must identify the science you wish to achieve with ACS. Basic decisions you will need to make are:

- Filter selection
- Nature of target

As you choose your science requirements and work to match them to the instrument's capabilities, keep in mind that those capabilities differ greatly depending on whether you are observing in the optical or near-UV with the CCD, or in the far-UV using the MAMA detector. Tradeoffs are described in Table 3.3.

Table 3.3: Science Decision Guide

Decision	Affects	Tradeoffs
Field of view	Camera Filter selection	WFC: 202 x 202 arcseconds HRC: 29 x 26 arcseconds SBC: 35 x 31 arcseconds
Spectral response	Camera Filter selection	WFC: 3700-11,000Å HRC: 2000-11,000Å SBC: 1150-1700Å
Spatial Resolution	Camera	WFC: ~50 milliarcsecond pixels HRC: ~ 27 milliarcsecond pixels SBC: ~32 milliarcsecond pixels
Filter Selection	Camera	WFC: broad, medium & narrow band, ramps HRC: Visible, UV, ramp middle sections
Spectroscopy	Camera Spatial resolution Field of View Wavelength range	Grism (G800L): WFC and HRC Prism (PR200L): HRC Prism (PR110L, PR130L): SBC
Polarimetry	Filters	UV polarizers combine with Wheel 2 filters VIS polarizers combine with Wheel 1 filters
Coronagraphy	Filter selection	Coronagraphic imaging available with HRC only

Imaging

For imaging observations, the base configuration is detector (Configuration), operating mode (`MODE=ACCUM`), and filter. Chapter 4 presents detailed information about each of ACS's imaging modes.

Special Uses

We refer you to Chapter 5 if you are interested in any of the following special uses of ACS: slitless spectroscopy, polarimetry and coronagraphy.

3.4.2 Determine Exposure Time and Check Feasibility

Once you have selected your basic ACS configuration, the next steps are to:

- Estimate the exposure time needed to achieve your required signal-to-noise ratio, given your source brightness. (You can use the ACS Exposure-Time Calculator for this, see also Chapter 6 and the plots in Chapter 10).
- For observations using the CCD detectors, assure that for pixels of interest, you do not exceed the per pixel saturation count limit of the CCD full well or the 16 bit word size at the `GAIN` setting you choose.
- For observations using the MAMA detector, assure that your observations do not exceed brightness (count-rate) limits.
- For observations using the MAMA detector, assure that for pixels of interest, your observations do not exceed the limit of 65,535 accumulated counts per pixel per exposure imposed by the ACS 16 bit buffer.

To determine your exposure-time requirements consult Chapter 6 where an explanation of how to calculate a signal-to-noise ratio and a description of the sky backgrounds are provided. To assess whether you are close to the brightness, signal-to-noise, and dynamic-range limitations of the detectors, refer to Chapter 7. For a consideration of observation strategies and calibration exposures, consult Chapter 8.

If you find that the exposure time needed to meet your signal-to-noise requirements is too great, or that you are constrained by the detector's brightness or dynamic-range limitations, you will need to adjust your base ACS configuration. Table 3.4 summarizes the options available to you and steps you may wish to take as you iterate to select an ACS configuration which is both suited to your science and is technically feasible.

Table 3.4: Science Feasibility Guide

Action	Outcome	Recourse
Estimate exposure time	If too long -> re-evaluate instrument configuration.	Consider use of an alternative filter.
Check full-well limit for CCD observations	If full well exceeded and you wish to avoid saturation-> reduce time per exposure.	Divide total exposure time into multiple, short exposures.[1] Consider use of different Gain.
Check bright-object limits for MAMA observations	If source is too bright -> re-evaluate instrument configuration.	Consider the use of an alternative filter or change detectors and wavelength regime.
Check 65,535 counts-per-pixel limit for MAMA observations	If limit exceeded -> reduce time per exposure.	Divide total exposure time into multiple, short exposures

1. Splitting CCD exposures affects the exposure time needed to achieve a given signal-to-noise ratio because of the read noise.

CHAPTER 4:

Designing a Phase I WFC3 Proposal

In this chapter . . .

4.1 Phase I and Phase II Proposals

In this Chapter we give an overview of the steps that are taken in preparing an HST observing proposal that involves WFC3 observations. "Phase I" refers to the initial proposal that is reviewed by the Telescope Allocation Committee (TAC). The Phase I proposal presents the scientific justification for the project, lists the targets to be observed and the instrument(s) to be used, and includes a request for a specific number of spacecraft orbits.

Only those proposals accepted by the TAC and approved by the STScI Director proceed to "Phase II," in which full details of the observations are specified.

This Chapter focuses on the steps needed to complete the Phase I proposal.

Q: Larry, a general comment is that this Chapter probably needs to more clearly distinguish between Phase I and Phase II items. There may be an argument that Phase II items should be de-emphasized, or dropped. It kind of depends on what the philosophy of this chapter is. We should check what the other handbooks do with this issue...

4.2 Preparing a Phase I Proposal

An HST program is a set of exposures specified so as to achieve one or more scientific objectives. We can break down the development of a WFC3 observing program, imaging and/or spectroscopic, into a five-step process. Often there is not a unique way in which to achieve the scientific objectives, and you must assess their trade-offs and feasibilities. Furthermore, you will wish to use HST and WFC3 efficiently, in order to obtain as much science within your orbit allocation as possible. Therefore, you may need to iterate these steps in order to achieve a final feasible and optimal program.

In this chapter we introduce issues that you may need to consider in designing your observations. Later chapters in this *Handbook* will present detailed information for your use. You will also find the Astronomer's Proposal Tool, the Phase II Proposal Instructions, and the WFC3 Exposure Time Calculator to be useful in designing your program. These five steps, and the considerations they entail, are described in the following subsections.

4.2.1 Which WFC3 Channel(s) and Filter(s)?

First, from your science requirements, determine the desired wavelength(s) of observation. Those requirements may include considerations of the spectral energy distribution (SED) of the target, or the required angular resolution, which also varies as a function of wavelength. Typically, if the wavelength of observation is less than 1000 nm, then the WFC3 UVIS channel will be used; or if the wavelength is greater than 1000 nm, then the WFC3 IR channel will be used.

The angular resolution, field of view (FOV), and sensitivity of the two channels differ appreciably, and may also influence your selection of the WFC3 channel(s) to use (see Chapter 2 for an overview of the UVIS and IR channels). Features of interest in the target's SED can be matched to the spectral resolution of the observation by selecting an appropriate filter (see Chapter 6 for the UVIS channel, Chapter 7 for the IR channel, and Appendix A1 for detailed filter passbands), or grism (see Chapter 8).

To match continuum features, wide-, medium-, and/or narrow-band filters may be selected, presenting the possibility of a trade-off between detector signal and spectral resolution. Note that the UVIS narrow-band quad filters limit the FOV to one quadrant of the full field.

4.2.2 What Exposure Times?

Second, you should determine the exposure time and exposure sequences needed to achieve the required signal-to-noise (S/N) with the chosen filter(s) or grism(s). A full discussion of calculating the exposure time is presented in Chapter 9. The S/N depends upon the target's incident flux and the noise from the background and detector

sources. These sources include zodiacal light, detector dark current, and stray light from both Earth and bright targets in the FOV.

Having determined the basic exposure time necessary to achieve the required S/N, you will in most cases find it necessary to obtain that total exposure time through a sequence of shorter exposures. For instance, if the exposure time is greater than the maximum orbital target visibility, it will be necessary to obtain a sequence of exposures. UVIS exposures exceeding 3,600 seconds require more than one exposure as will IR exposures greater than 2,800 seconds (see Chapter 5 for a fuller discussion).

Q: Where do the 3600 and 2800 limits come from? They aren't in Chapter 5 or elsewhere, as far as I know.

Dithering and Mosaicking

A sequence of exposures obtained in a dither pattern of HST pointings will often be used to reduce the noise from flat-field calibration error. Including sub-pixel displacements in the dither pattern will allow better sampling of the point-spread function (PSF). You may design and specify a dither pattern, or use one of the pre-defined patterns already designed to sub-sample the PSF, to cover the UVIS inter-chip gap, or to mosaic a large field. The pre-defined sequences are presented in the Phase II Proposal Instructions, and information on designing your own patterns is presented in Appendix C of this *Handbook*.

Bright Targets

For bright targets, a sequence of shorter exposures may be needed to avoid entering the non-linear or saturation regimes of the detectors (see Chapters 5, 6, and 7).

Saturated images of bright targets may leave a persistent image of that target in subsequent images, which could degrade the quality of the image at the same position of a faint target, as described in Appendix D.

UVIS Exposures

For UVIS observations, it will almost always also be desirable to use a sequence of exposures, in order to remove cosmic-ray impacts. For observations with the UVIS channel of faint targets, the effects of charge transfer efficiency (CTE) during readout of the detector must be considered (see Chapters 5 and 6). Charge injection for such images will mitigate the non ideal CTE.

Q: I don't think charge injection is mentioned in Chapter 6?

IR Exposures

For observations with the IR channel you must choose a readout method from the 16 available kinds of sample sequences. These include RAPID, up-the-ramp (SPARS), and Fowler (MPI) sequences (see Chapter 7). The exposure time is dictated by the sequence chosen. The ability to remove cosmic-ray impacts will depend upon the sequence chosen.

4.2.3 What Aperture or Subarray?

Next, from considerations of the target's angular size and structure, and of data volume, you should determine the WFC3 aperture or subarray you will use. The available UVIS apertures and subarrays are presented in Chapter 6, and those for the IR channel in Chapter 7.

In some cases, correct placement of an extended target within an aperture may require you to specify a special HST pointing and possibly the orientation of the FOV (which is determined by the spacecraft roll angle). Additional considerations may include detector imperfections such as the UVIS inter-chip gap (Chapter 5), diffraction spikes (Chapters 6 & 7), filter ghost images (see Chapters 6 & 7), detector saturation (i.e., for bleeding in a UVIS image along a detector column; Chapter 5), detector charge transfer (Chapter 5), distortion of the image (Appendix B), or dispersion direction of dispersion of the grism (see Chapter 8). However, most of these only need to be considered at the Phase II stage, unless they affect the number of orbits needed for the proposal.

Note that selection of a WFC3 aperture without specifying further constraints implicitly specifies: (1) the full image will be read out, (2) the target coordinates will be placed at a default location on the detector (see Chapters 6 & 7), and (3) the image will be arbitrarily rotated with respect to the detector, depending on the date the exposure is executed. These defaults may be over-ridden, however.

You can reduce the size of the image read out and thus the volume of data obtained by selecting a subarray. For the UVIS detector, on-chip binning of the pixels will also reduce the data volume, but at the expense of angular resolution (see Chapters 5 & 6). Reducing the data volume will reduce the overhead to read out and transfer images, which may be desirable in order to allow more images of the target of interest to be obtained during an HST orbit. The location of the target can be specified with the POS TARG special requirement and the rotation of the image can be specified with the ORIENT special requirement (see Chapters 6 &7).

4.2.4 What Overheads?

Fourth, determine the overhead times required in addition to the exposure time in order to operate WFC3 and HST (see Chapter 10). This total time is expressed as the number of HST orbits required to obtain the observations, which is useful due to the activities that are associated with the occultation of a target during each HST orbit.

The overhead activities include guide-star acquisition or re-acquisition at the beginning of each orbit, filter changes, changing between the UVIS and IR channels, readout of a detector to the WFC3 buffer, and transfer of images from the WFC3 buffer to the HST science data store. Note that overheads are especially severe for sequences of short exposures, but these can sometimes be mitigated by using small subarrays.

4.2.5 Any Special Observations?

You may find that some non-standard observations are necessary. These capabilities include non-standard subarrays, UVIS bias images, and detector gain.

Q: Do we actually offer bias images, non-default gain, etc??

Your program may require calibration of WFC3 to greater accuracy than the standard calibrations (Appendix A5) provide. If so, you may need to propose additional observations to better calibrate your science program. These additional observations must be justified in your proposal submission. Unsupported modes of operating WFC3 should be discussed with a contact scientist, or program coordinator.

4.2.6 What is the Total Orbit Request?

Q: add some summary text here. Also, maybe a table or numerical listing that briefly summarizes all of the steps detailed above.

CHAPTER 5:

WFC3 Detector Characteristics and Performance

In this chapter . . .

5.1 Overview of this Chapter

This chapter describes the detectors used in the UVIS and IR channels of WFC3. All observers should have a basic understanding of how the detectors operate, and of their characteristics and limitations. For some observations, for example at very faint levels or for exposures using non-default parameters, a fuller understanding of the detectors may be needed. This chapter provides both basic and in-depth information on the detectors used in both WFC3 channels. Sections 5.2-5.4 discuss the CCD detectors used in the UVIS channel, and sections 5.5-5.8 discuss the infrared detector used in the IR channel.

Table 5.1 summarizes the basic parameters of the CCD detectors used in the UVIS channel and of the IR detector used in the IR channel. For the CCDs the information is an average for the two chips; the sections below give more details for each chip.

Table 5.1: Overview of WFC3 detector performance. NOTE: the table entries are place holders from the ACS; need to insert WFC3 parameters!!!

Characteristic	UVIS Channel CCDs	IR Channel Detector
Architecture	Thinned, backside illuminated anti-reflection coated multi-phase pinned	Thinned, backside illuminated anti-reflection coated multi-phase pinned
Wavelength range	~3500 Å to 11,000 Å	~1700 Å to 11,000 Å
Pixel Format	2 butted 2048 × 4096	1024 × 1024
Field of View	202" × 202"	29" × 26"
Pixel Size	15 μm × 15 μm	21 μm × 21 μm
Pixel Plate Scale	~0.05”/pixel	~0.028 × 0.025"/pixel
Quantum Efficiency	~77% @ 4000 Å ~83% @ 6000 Å ~67% @ 8000 Å	~33% @ 2500 Å ~69% @ 6000 Å ~53% @ 8000 Å
Dark Count (as of July’05)	~0.0038 e^-/second/pixel	0.0044 e^-/second/pixel
Read Noise	5.0 e^-	4.7 e^-
Full Well	~84,700 e^-	~155,000 e^-
Gain (max. 65, 535 DN)	1,2,4 and 8 e^-/DN (Max 65,535 DN)	1,2,4 and 8 e^-/DN (Max 65,535 DN)
Operating Temperature*	–77°C	–81°C
Limiting mag, 1-hour exposure, S/N=TBD	V=TBD	H=TBD

Q: NOTE that Table 5.1 is currently just copied from the ACS Handbook; need to insert the parameters for the WFC3 detectors!

5.2 The WFC3 UVIS Channel CCD Detectors

5.2.1 Basics of CCD Operation

A charge-coupled device (CCD) is a silicon-based detector containing a two-dimensional array of summing wells, called pixels (short for picture elements). Each pixel accumulates electric charge in proportion to the number of photons striking that location on the detector. Physically, the summing wells are created by electric fields established at the depletion (charge-free) regions of the Is-SiO_2

metal-oxide-semiconductor (MOS) capacitors. In a typical three-phase CCD, the size of the depletion region is controlled by the voltage of three gates. The gates are arranged in parallel, with every third gate connected together.

At the end of an exposure, by changing the voltage of the gates with an appropriate clocking pattern, all packets of charge are sequentially transferred to the next pixel, until they reach the readout circuitry at the detector's edge. It is important to distinguish between parallel and serial charge transfers: the transfer of charges between pixels occurs in parallel, row by row, whereas the extraction of the “zero” row at the edge occurs along an external serial register, where each packet is serially transferred to an output amplifier at the detector corner.

5.2.2 The WFC3 CCDs

The WFC3 UVIS channel uses two CCD detectors fabricated by e2v Ltd. (formerly Marconi Applied Technologies Ltd.), model CCD43-62. Both CCDs are 2051×4096 devices with 15×15 micron square pixels. There are 2051 rows by 4096 columns, where the row/columns definition follows the convention of having the parallel direction first and the serial direction second. Having the serial register along the long (4096 pixel) edge reduces the number of transfers needed on the photosensitive pixels, which are more sensitive to radiation damage events.

The WFC3 CCDs are three-phase devices, thinned and back-illuminated (“backthined”) to improve the sensitivity to UV light. “Back-illumination” means that the image is focused on the back side of the chip, without having to pass through the opaque gate structure implanted on the front side. “Thinning” refers to the removal of the thick substrate on which the chip was originally built, which is done because only those electrons generated in the vicinity of the gate structure can be collected efficiently.

The WFC3 CCDs also have buried channels and are operated in multi-pinned phase (MPP) mode. [Q: can you explain more clearly what a buried channel is?] Within the buried channel there is also an extra-doped mini-channel to store and transfer small charge packets (~5-10 e^-) to improve the charge-transfer efficiency (CTE) at low signal levels. The buried channels also have the capability of injecting charges to fill in the traps and improve the CTE. These features will all be discussed in detail in later sections.

The two WFC3 CCDs are butted together along their long dimension to create a 2×1 mosaic. Figure 5.1 shows a magnified view of the CCDs. The butted configuration is equivalent to a 4102×4096 array, but with a 200-micron (~13-pixel) gap beteween the two chips. The CCDs are packaged inside a cold enclosure, which is nearly identical to the one used for ACS, itself a scaled-up version of the STIS design. The package includes a second cooled window to reduce the radiative heat load. To increase the useful life of the CCDs in orbit, the assembly is enclosed in a one cm [check] molybdenum radiation shield with low secondary emission. It [Q: what does "it" refer to?] also provides a highly conductive thermal path to remove heat from the TEC. The nominal operating temperature of the WFC3 CCDs is -83° C. [Q: "TEC" is not explained, and it doesn’t seem to be explained how the CCDs are cooled]

The WFC3 CCDs are quite similar to those used in the ACS Wide Field Channel (WFC). They have the same pixel size, nearly the same format (2051×4096 in WFC3, compared to 2048×4096 in ACS), the same orientation of the serial and parallel registers, similar technology (buried-channel, MPP operation, minichannel), and nearly identical mechanical interfaces. The main differences of the WFC3 chips compared to those in ACS/WFC are:

- UV optimization of the WFC3 detector response.
- significantly lower readout noise for the WFC3 chips (~3.5 e^- compared to ~7 e^-).
- 2051 rows instead of 2048.
- output amplifiers (2 instead of 4 on each CCD).
- charge-injection capability.
- 200 micron (~13 pixels) gap instead of 750 micron (50 pixels).

An overview of the WFC3 CCD performance was given above in Table 5.1. Table 5.2 presents some detailed performance characteristics for the individual chips.

Table 5.2 WFC3 CCD performance

	CD43-178	CCD43-018
READ NOISE	3.2 e-RMS	3.2 e- RMS
DARK RATE (-83 C)	0.25 e-/pix/hr	0.4 e-/pix/hr
FULL WELL	86,000 e-	92,500 e-
Bad Pixel Fraction	0.25 %	0.40 %

Figure 5.1: Detector package similar to the two WFC3 CCD detectors. The size of the 4kx4k array is approximately 6x6 cm, and it consists of two butted 2051x4096 CCDs with a small gap between them.

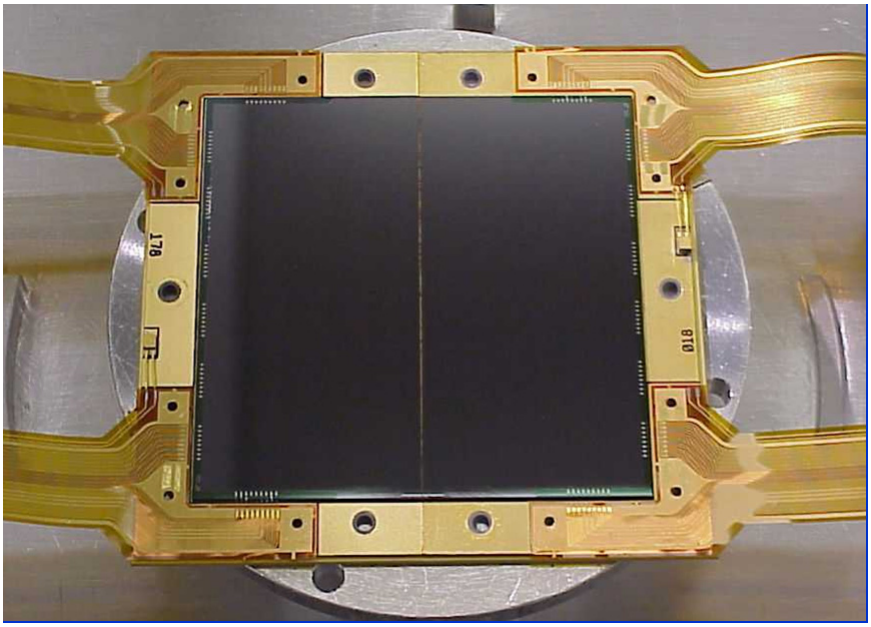

5.3 WFC3 CCD Readout Formats

5.3.1 Full-frame Readout

[Q: this section is so unclear to me that I can't edit it very much without discussing it in person with experts--HEB] Whereas each CCD detector contains 2051x4096 pixels, the raw images returned by the WFC3 electronics contain a larger number of pixels. This is due to the detector overscan, a term which refers to portions of the detector which are not exposed to light. [Q: aren't they "virtual" pixels? All of the physical pixels are exposed to light, aren't they?] Overscan regions are useful for characterizing detector performance and efficiency.

Serial overscan corresponds to a fixed number of unexposed pixels at each end of each serial shift register. Viceversa, parallel overscan is generated by additional parallel shifting before or after all of the exposed rows of the detector have been read out. Both serial and parallel overscan can be implemented either as physical overscan or virtual overscan. The physical overscan is a characteristic of the detector hardware, whereas virtual overscan is a software function, and the number of rows and columns of virtual overscan generated with an image is controllable via the readout timing pattern.

The CCD devices of WFC3 have each row divided into two regions which, although they belong to the same physical chip, are associated with different

amplifiers, either A,B or C,D for the two chips. The association between CCD name, amplifiers and fits file extension in the WFC3 data is presented in Table 5.3.

Table 5.2: WFC3 CCD Conventions

CCD name	Amplifiers	CCD extension
CCD018	C, D	[1]
CCD178	A, B	[4]

Physical overscan pixels are located along the edges of the detector in the serial direction only. There are 25 overscan columns along each edge, or 50 columns total. In addition, there are two regions of virtual overscan. In standard four-amplifier readout mode, 60 columns (30 in each half) of serial overscan in the center of each row between the exposed areas corresponding to the two halves, and 38 rows (19 on each chip) of parallel overscan abutting the inter-detector gap. See Figure 4-2 for an illustration of the location of the overscan regions. The serial physical overscan pixels at the edges are known as “serial prescan” or “leading edge” overscan pixels; the serial virtual overscan pixels in the center are known as “trailing edge” overscan pixels. The trailing edge is considered more useful than the leading edge for bias subtraction. The final images derived by the WFC3 electronics therefore consists of a 4140x4026, i.e. (4051+19)x2 on the parallel side and (2048+25+30)x2 on the serial side.

If two-amplifier readout is used, the final image maintains the same number of rows and columns as the four-amplifier image, but all 60 serial virtual overscan pixels are located at the end of each row; see Figure 5.3 for an illustration of a full-frame readout using amps A and C.

5.3.2 Subarrays

The default mode is to read out all pixels of both CCDs. However, it is possible to define rectangular subarrays. Only data from the area within the subarray is stored in buffer memory, and the rest of the image is discarded. [Q: we haven’t said anything yet about buffer memory, where the images are stored, how they get to the ground, etc.] The subarray size, in one or both detector axes, is specified by the observer. [Q: give more details about available sizes of subarrays, how to request them, etc. What’s the advantage? Faster readout? Smaller storage?]

UVIS subarray images contain no virtual overscan data, and serial physical overscan is present only if it is part of the defined subarray area.

5.3.3 On-Chip Binning

The UVIS CCDs also provide an on-chip binning capability, in which several adjacent pixels may be read out as a single pixel. The available choices are 2x2 and 3x3 on-chip binning. If on-chip binning is used (again assuming four-amplifier

readout), the overscan geometry is complicated by the need to truncate "odd" pixels, and each half of a row must be considered separately. With 2x2 binning, the first and last exposed pixels in each half of each row is combined with the adjacent overscan pixels. The last of the serial virtual overscan pixels in each half is not be read out. There are 1051 binned pixels in each half: 12 physical overscan pixels, 1023 exposed pixels, two pixels consisting of combined overscan and exposed pixels, and 14 virtual overscan pixels. In the parallel direction, the physical row on each chip nearest the inter-detector gap will be combined with the adjacent overscan row. That leaves 1035 binned rows on each chip: 1025 exposed rows, one row consisting of combined overscan and exposed pixels, and 9 virtual overscan rows. The binned array size is 2070x2102.

With 3x3 binning, there are 701 binned pixels in each half of each row: 8 physical overscan pixels, one pixel combining the last physical overscan pixel with the first two exposed pixels, 682 exposed pixels, and 10 virtual overscan pixels (which should be adequate for bias subtraction). In the parallel direction, the two physical rows on each chip nearest the inter-detector gap will be combined with the adjacent virtual overscan row. That leaves 690 binned rows on each chip: 683 exposed rows, one row consisting of combined overscan and exposed pixels, and six virtual overscan rows. The binned array size is 1380x1402.

Two-amplifier readouts with on-chip binning proceed in a similar manner. With 2x2 binning, the first exposed pixel in each row will be combined with the last serial physical overscan pixel at the start of the row, and the last exposed pixel in each row will be combined with the first serial physical overscan pixel at the end of the row. Thus, each row will contain 12 binned serial physical overscan pixels, a single binned pixel from the addition of the last serial physical overscan pixel and the first exposed pixel, 2047 binned exposed pixels, a single binned pixel from the addition of the last exposed pixel and the first serial physical overscan pixel at the end of the row, 12 binned serial physical overscan pixels, and 29 binned serial virtual overscan pixels. In the parallel direction, the last exposed row (nearest the inter-chip gap) will be combined with the first parallel virtual overscan row, leaving 1035 total rows from each chip. The final image size is 2070x2102.

With 3x3 binning, each binned row consists of 8 binned serial physical overscan pixels, one pixel from the addition of the last serial physical overscan pixel and the first two exposed pixels, 1364 binned exposed pixels, 1 binned pixel from the addition of the last two exposed pixels and the first serial physical overscan pixel, 8 binned serial physical overscan pixels, and 20 binned serial virtual overscan pixels. The parallel direction is treated identically to the four-amplifier readout with 3x3 binning, resulting, again, in a final image size of 1380x1402 pixels.

Figure 5.2: Location of the serial and parallel overscan regions.

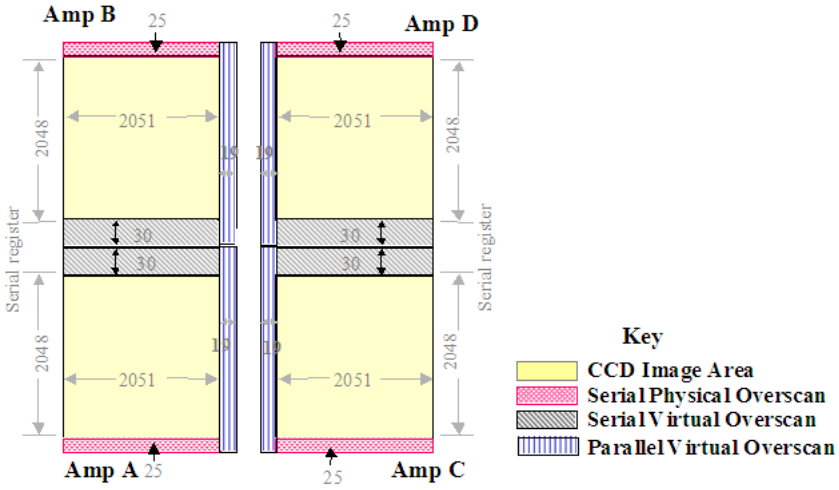

Figure 5.3: Location of the serial and parallel overscan regions in the raw, full-frame images

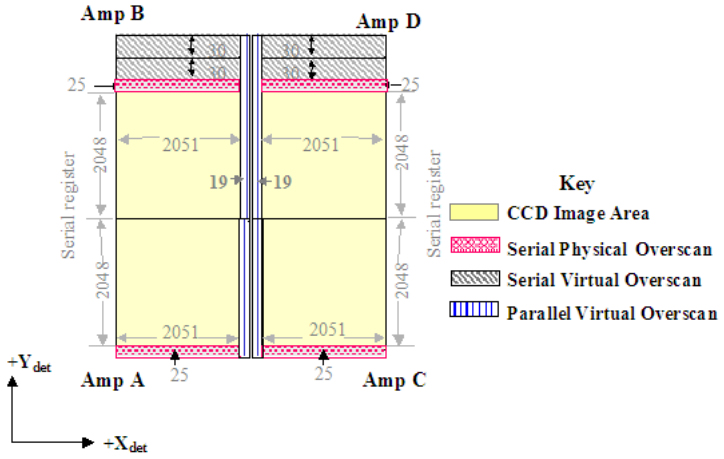

5.4 WFC3 CCD Characteristics and Performance

5.4.1 Quantum Efficiency [I INCLUDED SECTION 5.3.4 OF SYLVIA ON QUANTUM YIELD]

The quantum efficiencies (QEs) of the two WFC3 CCDs are plotted against wavelength in Figure 5.4. Here the QE is defined as electrons yielded per incident photon [Q: is this a correct statement?], and the plotted values were measured at the Goddard DCL [Q: explain DCL]. The plots demonstrate the high sensitivity of the CCS in the UV down to 2000 A. On the other hand, the peak QE at ~6000 is less than 70%, whereas the ACS/WFC detectors reach ~85% [Q: check] at their peaks.

The WFC3 CCD detectors are tilted by ~20 degrees with respect to the normal. The nominal change in thickness is ~6%, but the QE variations, as measured at the DCL, turn out to be negligible.

5.4.2 Multiple-Electron Events at Short Wavelengths

In silicon, photons of energy higher than 3.1 eV (i.e., wavelength shorter than ~4000 A) can produce multiple electron-hole pairs when the energetic conduction-band electron collides with other valence-band electrons. At higher energies (energy above 3.65 eV, or wavelength below ~3400 A) the incident photons can directly extract more than one electron from the valence band. This effect (called "quantum yield") of a single photon producing more than one electron must be taken into account properly when estimating the noise level for short-wavelength observations.

Since the generation of multiple electrons is a random phenomenon, an extra noise term must be added to account for an observed variance larger than that associated with the normal Poisson distribution of incoming photons. The QE curves presented in Figure 5.4 include the quantum-yield gain, which at 2000 A is about 1.7 e^-/photon. The algorithms in the WFC3 Exposure Time Calculator take the quantum-yield effect into account and apply the proper reduction to the estimated S/N ratio.

Figure 5.4: Quantum efficiency of the WFC3 CCDs . The two lines on each plot show the result obtained with the two different amplifiers.

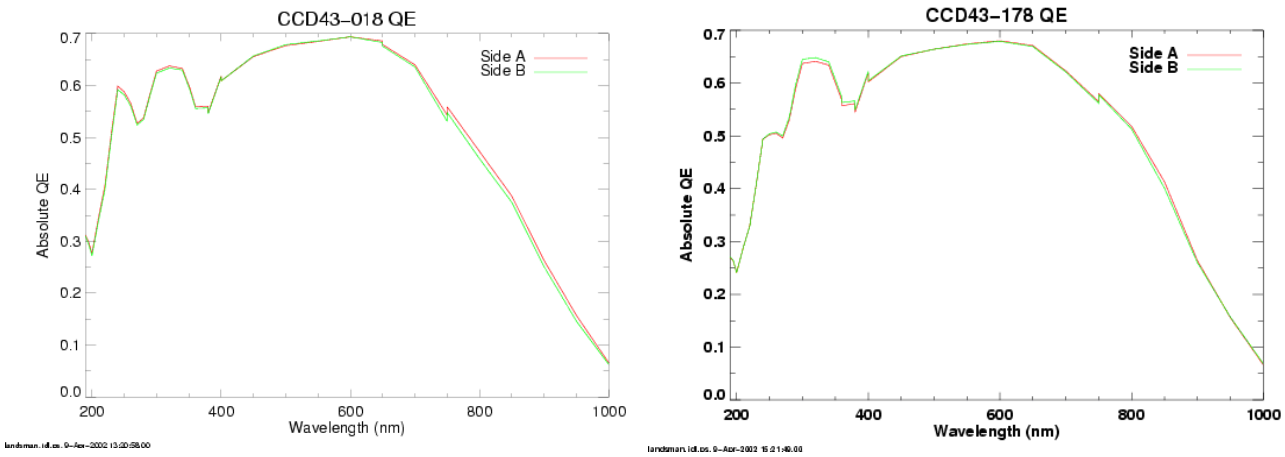

5.4.3 Flat Fields

The flat fields needed in the reduction of WFC3 images will combine information from two sources. Before lanuch, ground-based flats have been obtained for all filters at a S/N of TBD [Input from Sylvia/Howard] per pixel. To refine the low-frequency domain of the ground flats, in-flight observations of a rich stellar field with large-scale dithers will be used. The resulting library of flat-field images will support photometry to ~1% accuracy over the full WFC3 CCD field of view. Figure 5.5 shows examples of corrected [Q: what does "corrected" mean here?] WFC3 ground-based flats for several broad-band filters.

Figure 5.5: WFC3 flat field. [TO BE PROVIDED BY SYLVIA, possibly at 2 wavelengths]

5.4.4 Long-Wavelength Fringing

Like most back-thinned CCDs, the WFC3 CCDs exhibit fringing at wavelengths longward of ~7500 Å (see Figure 5.6). The peak-to-peak variation in the brightness of the flat-field image is of order 50% of the mean intensity (see Figure 5.7).

Fringing results from the interference of light being reflected back and forth between the front and back surfaces of the CCD. The amplitude of the fringes is a strong function of the detector thickness, wavelength, and spectral resolution. For broad-band illumination, the fringe pattern will depend on the spectrum of the incident light and on the bandwidth of the filter. The fringe pattern has been shown to be very

stable, as long as the wavelength of light on a particular part of the CCD stays constant. Fringing can therefore be corrected if an appropriate flat field is available.

The fringe pattern can also be modeled, either by interpolating between or combining monochromatic patterns previously obtained in the laboratory, or from theoretical calculations, using for any given illumination the equation that relates the phase difference of monochromatic light \delta to the substrate thickness \Delta x (Janesick, op. cit., p.205)

$$
\Delta x = {\delta\lambda \cos(\theta) \over 4\pi n_{Si} }
$$

where \delta is the phase difference, \lambda is the wavelength, \theta is the angle from normal in the silicon, and \n_{Si} is the index of refraction. Note that the index of refraction also changes with wavelength.

For a detailed explanation of how to model the WFC3 fringe pattern, see Malumuth et al., Proceedings of SPIE - Volume 4854 -

[Future EUV/UV and Visible Space Astrophysics Missions and Instrumentation, J. Chris Blades, Oswald H. W. Siegmund, Editors, February 2003, pp. 567-576]

Figure 5.5: Fringe pattern of CCD43-018 with flat field illumination monochromatic at 976nm.

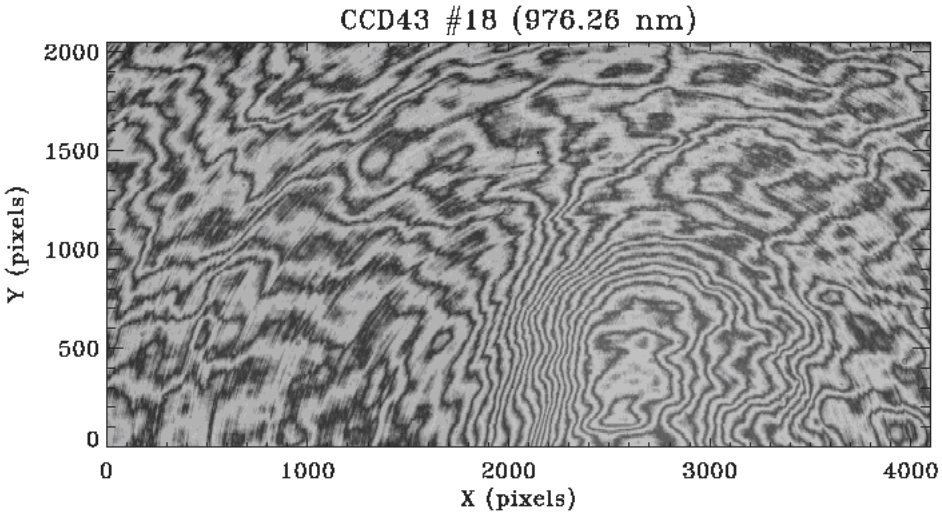

Figure 5.6: A normalized line plot of row=999 from the image shown if Figure 5.6.

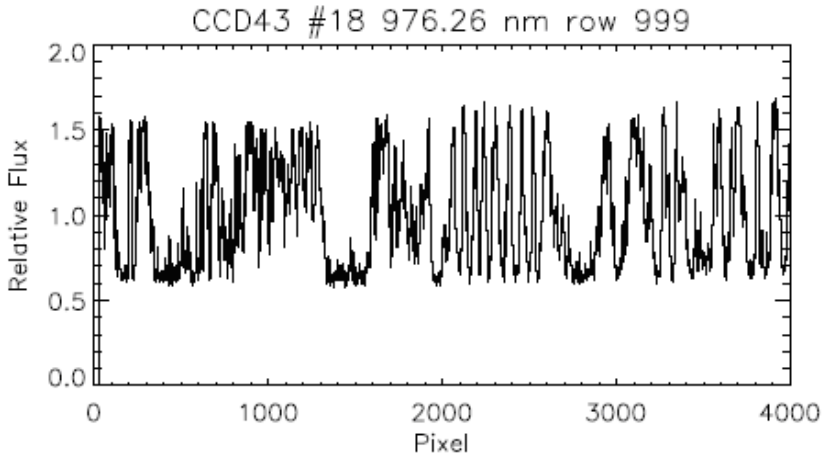

5.4.5 Linearity and Saturation

In general, the response of CCDs is intrinsically linear, with significant departures encountered only in the vicinity of full well. The departure from linearity of WFC3 CCDs remains well below 1% until ~90,000 electrons are accumulated on each pixel. Different pixels have different saturation levels, and the range for each detector and output amplifier is reported in Table 5.3.

When CCDs become over-exposed, blooming occurs: if a pixel becomes full, the photo-generated excess charge spills into adjacent pixels along the column. Extreme overexposure is not believed to cause any long-term damage to the CCDs, so there are no bright-object limits for the WFC3 CCDs.

Table 5.3: Saturation levels of the WFC3 CCDs

	CCD178	CCD018
Channel A	83,300 - 89,700	92,000 - 93,000
Channel B	82,300 - 87,000	92,000 - 93,000

5.4.6 Gain

Electrons which accumulate in the CCD wells are read out and converted to data numbers (DNs), often called Analog-to-Digital Units (ADUs), by the analog-to-digital converter (ADC). The ADC output is a 16-bit number, producing a maximum of 65,535 ADU for each pixel. A straightforward scheme in which one ADU corresponded to one electron would make it impossible to measure signals larger than 65,535 electrons. Hence the conversion gain parameter provides a way of adjusting the scale so that multiple counts correspond to a single ADU, allowing larger numbers of

electrons to be measured. The conversion gain is defined as the number of electrons per ADU.

Although it is possible to operate the WFC3 CCDs at gains of 1, 1.5, 2, and 4 electrons/ADU, only a gain of 1.5 e/ADU will be supported. This gain permits sampling of the entire dynamic range of the detectors, with negligible impact on the readout noise.

The gains for the integrated WFC3 instrument were measured during the 2004 thermal vacuum campaign (WFC3 ISR 2005-08). The results are summarized in Table 5.3.

Table 5.4: WFC3 CCD standard conversion gain

		Gain=1.5	
Chip	**Amp**	**Gain**	**Stdev**
CCD43-178	A	1.53	0.01
CCD43-178	B	1.52	0.01
CCD43-018	C	1.56	0.01
CCD43-018	D	1.55	0.01

5.4.7 Readout Noise

The readout noise level in the active areas and overscan regions for all of the amplifiers at the default gain setting was measured during the 2004 thermal vacuum campaign with a varity of methods (WFC3-ISR 2005-13). Table 5.5, show the results obtained at the default gain setting of 1.5 e/ADU.

Table 5.5: Readout noise of WFC3 CCDs at gain =1.5 e/ADU

	CCD43-178				**CCE43-018**			
	Image area		**Overscan**		**Image area**		**Overscan**	
	AmpA	**AmpB**	**AmpA**	**AmpB**	**AmpC**	**AmpD**	**AmpC**	**AmpD**
Mean	3.12	3.23	2.99	3.05	3.11	3.24	2.95	3.07
Stdev	0.03	0.04	0.01	0.01	0.03	0.02	0.02	0.01

The readout noise values measured at the other gain values are presented in Table 5.6. [Q: do we really need to list the RN at non-default gains?] The readout noise measured with GAIN=1 is on average comparable to that measuread with GAIN=1.5, and in general the noise increase associated to the higher conversion gain values is equivalent to that produced by adding in quadrature a noise equal to the gain itself, i.e. to the number of electrons in least significant digit. Thus, in terms of readnoise, the

advantage of using GAIN=1 instead of GAIN=1.5 is minimal, whereas by adopting GAIN=1.5, the entire dynamic range of the CCD can be sampled before ADC saturation occurs. This has many obvious advantages, e.g. it allows to use all unsaturated sources for cross-image registration and to perform photometry several magnitudes beyond saturation, at least for point sources in non crowded fields.

A preliminary analysis of the statistical behavior of the Analog to Digital Converters in WFC3 shows some tendency of the least significant bits to be slightly biased at the readout speed adopted by the WFC3 electronics (see WFC3-ISR 2005-27). This effect should not degrade the photometric and noise characteristics of the WFC3/CCD images.

Table 5.6: Readout noise of WFC3 CCDs at non-nominal gain

A	B	C	D	
RON (G=1)	3.09	3.05	2.97	3.18
RON (G=2)	3.55	3.56	3.69	3.78
RON (G=4)	5.14	5.31	5.50	5.59

5.4.8 Dark Current

[Q: isn't this section going into too much detail for typical users?] The WFC3 CCDs, like most large-area scientific CCDs, operates with buried channels. Earlier generations of CCDs worked with surface channels, i.e., storing and transferring charges along the surface of the semiconductor. In these earlier devices the Si-SiO_2 interface between the detector material Si (p-doped conductor) and the surface layer of SiO_2 (isolator) created significant charge traps, which limited both the charge-transfer efficiency and the dark current. In buried-channel devices a shallow (~0.5 micron thick) n-type Si layer is implanted just below the surface between the p-doped Silicon and the SiO_2 surface, to store and transfer the collected signal charge away from the traps at the interface.

Dark current in WFC3 detectors is further reduced using MPP technology. The dark current generated at the Si-SiO_2 interface ultimately depends on two factors: the density of interface states and the density of free carriers (holes and electrons) that populate the interface. Electrons can thermally "hop" from the valence band to an interface state (sometimes referred to as "a mid-band state") and from there to the conduction band, producing a dark e-h pair. Free carriers also fill interface states and, if these states were completely populated, can suppress hopping and conduction, reducing the surface dark current at levels comparable to the bulk dark. Unfortunately, normal CCD operations deplete the interface of free carriers, maximizing dark current generation.

In MPP technology, the Si-SiO_2 interface is populated with holes that suppress the hopping conduction process. MPP mode is applied to the CCD by significantly biasing

the array clocks negatively to invert (push electrons away from) the n-buried channel and "pin" the surface potential beneath each phase to substrate potential (hence the name multi-pinned phase). Biasing the array clocks in this manner causes holes from the p+ channel stops to migrate and populate the Si-SiO_2 interface, eliminating surface dark-current generation. Note that it is not possible to invert conventional CCDs in this way, as the sensor's full-well capacity would be annihilated since the potential wells within a pixel all assume the same level. To circumvent this difficulty in MPP CCD technology an additional implant is included below one of the phases, allowing charge to accumulate in collecting sites when biased into inversion.

Besides eliminating surface dark current, MPP CCD technology offers additional advantages. For example, the charge-transfer efficiency of a CCD generally degrades with decreasing operating temperature. Therefore, MPP technology assists in the charge-transfer process since it permits the use of higher operating temperatures.

The MPP CCD also eliminates residual image, a serious problem that has plagued low-signal-level CCD users for many years. Residual image, also known as quantum-efficiency hysteresis, results when the sensor is either overexposed or first powered up. Under these circumstances, electrons are found trapped at the Si-SiO_2 interface that slowly de-trap into the pixel's potential well. Residual charge may take hours or even days before its level falls below the read-noise floor. Inverting the CCD causes holes to immediately recombine with the trapped residual electrons, eliminating remnant image effects during integration as well as readout.

The WFC CCDs are operated in MPP mode only during integration, so the total dark current figure for WFC includes a small component of surface dark current accumulated during the readout time. [THIS IS TRUE FOR ACS, NEED TO CHECK!].

During pre-flight tests, the dark current was measured both in ideal cryogenic environment at the Detector Characterization Laboratory (DCL) of the NASA - Goddard Space Flight Center and during thermal vacuum campaign. The dark current values are reported in Table. 5.7, in units of e/pix/hr, were obtained during the 2004 thermal vacuum (see WFC3 ISR- 2005-13).

Like all CCDs operated in a low-earth-orbit radiation environment, the WFC3 CCDs will be subject to radiation damage by energetic particles trapped in the radiation belts. Ionization damage and displacement damage are two types of damage caused by protons in silicon. The MPP mode is very effective in mitigating the damage due to ionization such as the generation of surface dark current due to the creation of new trapping states in the Si-SiO2 interface. Although protons lose only a minor fraction of their total energy via nonionizing energy loss, the lattice displacement damage can cause significant performance degradation in CCDs by decreasing the charge transfer efficiency (CTE), increasing the average dark current, and introducing pixels with very high dark current (hot pixels). Displacement damage to the silicon lattice occurs mostly due to the interaction between low energy protons and silicon atoms. The generation of phosphorous-vacancy centers introduces an extra level of energy between the conduction band and the valence band of the silicon. As described above, new energy levels in the silicon bandgap increase the dark current as they allow

thermally generated charges to reach the conduction band. As a consequence, the dark current of CCDs operated in a radiative environment is predicted to increase with time.

Table 5.7:

	CCD43-178		CCE43-018	
	AmpA	**AmpB**	**AmpC**	**AmpD**
Dark	0.16	0.32	0.34	0.41
Sigma	0.09	0.10	0.10	0.11

5.4.9 Bad Pixels

Pre-flight tests of the WFC3 CCDs allowed classifying a number of pixels as either hot, dead, or QE outliers. The definitions of the relative thresholds are somewhat arbitrary, but the following are adopted: (1) hot pixels, identified using 1 hr long dark-current frames, are those that depart from the average dark current by more than 100 times the standard deviation of the main population; (2) dead pixels, measured with flat-field illumination of ~50% full well, are those that remain below 1000 electrons (the large majority being close to 0 electrons); and (3) outliers, also identified with flat-field illumination, are those that depart from the average by than 50 times the standard deviation of the main population.

Tables 5.8 and 5.9 summarize the results, providing both the total number of pixels and their fraction. With 0.25% and 0.40% flagged as bad, the cosmetic quality of the WFC3 CCD is excellent. Bad pixels are constantly monitored and the masks to be applied for their subtraction regularly updated in the standard data reduction pipeline.

Table 5.8: Summary of the bad pixels for CCD43-178

Bad Pixel Type	Channel A	Channel B	Array Total	% of Array
Hot Pixels	458	718	1,176	0.03
Dead Pixels	1,110	16	1,126	0.03
QE Outliers	5,337	4,088	9,425	0.22
Total Nonfunctional*	5,794	4,806	10,600	0.25

*Note that the total may differ from the sum of the different types of of pixels because some of the pixels are a combination of types (e.g., dead and QE outlier, etc.).

Table 5.9:

Bad Pixel Type	Channel A	Channel B	Array Total	% of Array
Hot Pixels	5,444	5,307	10,751	0.26
Dead Pixels0	0	0	0	
QE Outliers	2,716	3,443	6,159	0.15
Total Nonfunctional*	8,154	8,748	16,902	0.40

*Note that the total may differ from the sum of the different types of of pixels because some of the pixels are a combination of types (e.g., dead and QE outlier, etc.).

5.4.10 Cosmic Rays

Pending on-orbit measures, we can use ACS data to get important clues on the effect of cosmic rays on the WFC3 CCDs. The fraction of ACS pixels affected by cosmic rays varies from 1.5% to 3% during a 1000-second exposure for both cameras, similar to what was seen on WFPC2 and STIS. This number provides the basis for assessing the risk that the target(s) in any set of exposures will be compromised. The affected fraction is the same for the ACS WFC and HRC, despite their factor of two difference in pixel areas because the census of affected pixels is dominated by charge diffusion, not direct impacts.

Observers seeking rare or serendipitous objects, as well as transients, may require that every single WFC3 pixel in at least one exposure among a set of exposures is free from cosmic-ray impacts. For the cosmic-ray fractions of 1.5% to 3% in 1000 seconds, a single ~2400 second orbit must be broken into 4 exposures (4 CR-SPLITs of 500 to 600 seconds each) to reduce the number of uncleanable pixels to 1 or less. (We recommend that users dither these exposures to remove hot pixels as well.)

The flux deposited on the CCD from an individual cosmic ray does not depend on the energy of the cosmic ray but rather the length it travels in the silicon substrate. The electron deposition due to individual cosmic rays has a well defined cut-off with negligible events of less than 500 e- and a median of ~1000 e- (see Figure 5.7).

Figure 5.7: Electron deposition by cosmic rays on ACS/WFC

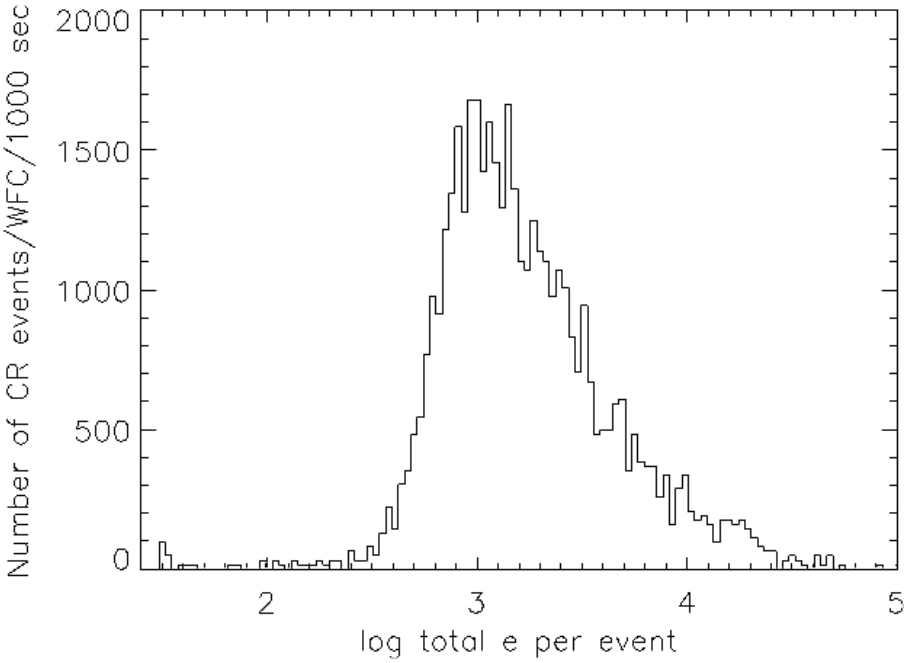

The distribution of the number of pixels affected by a single cosmic ray is strongly peaked at 4 to 5 pixels. Although a few events are seen which encompass only one pixel, examination of these events indicate that at least some, and maybe all of these sources are actually transient hot pixels or unstable pixels which can appear hot in one exposure (with no charge diffusion) and normal in the next. There is a long tail in the direction towards increasing numbers of compromised pixels.

Distributions of sizes and anisotropies can be useful for distinguishing cosmic rays from astrophysical sources in a single image. The size distribution for both chips peaks near 0.4 pixels as a standard deviation (or 0.9 pixels as a FWHM). This is much narrower than for a PSF and is thus a useful discriminant between unresolved sources and cosmic rays.

5.4.11 Charge-Transfer Efficiency

Charge-transfer efficiency (CTE) is a measure of how effective the CCD is at moving charge from one pixel location to the next when reading out the chip. A perfect CCD would be able to transfer 100% of the charge as the charge is shunted across the chip and then out through the serial register. In practice, small traps in the silicon lattice compromise this process by holding on to electrons, releasing them at a later time. (Depending on the trap type, the release time ranges from a few microseconds to several seconds.) For large charge packets (several thousand electrons), losing a few electrons along the way is not a serious problem, but for smaller (~100 e- or less) signals, it can have a substantial effect.

CTE is typically measured as a pixel transfer efficiency, and would be unity for a perfect CCD. The CTE numbers for the WFC3 CCDs were measured at DCL using

Fe^55 and showed that charge loss is of the order of 3-5x10^-7 e/transfer, which represents an excellent value for pre-flight devices.

5.4.12 CCD Shutter Effects

The WFC3 camera has a very high-speed shutter; even the shortest exposure times are not significantly affected by the finite traversal time of the shutter blades. Pre-flight testing reported in WFC3-2004-14 has verified that shutter exposure times deviate by less than 1.5%, with 1.5 ms typical variations in a set of 0.5 sec exposures. Shading corrections are therefore not necessary to support better than 1% photometry.

The integration time is specifiable from a minimum of 500 msec to a maximum of 3600 seconds, in steps of 100 msec. The value of 600 msec, however, is not allowed, as it could not be supported with a uniform illumination of the detector. [Q: what about 500 msec??]

5.5 The WFC3 IR Channel Detector

5.5.1 Overview

The infrared channel of WFC3 employs a low-noise, high-QE, 1024×1024 pixel HgCdTe array manufactured by Teledyne Imaging Sensors (formerly Rockwell Science Center). Active cooling by a six-stage thermoelectric cooler keeps the detector at a nominal operating temperature of 145 K. Although the IR detector is sensitive between 0.4 and 1.7 micron, the detector coating is optimized for wavelengths longward of ~1 micron, where the QE reaches its peak. The IR channel filter set is also limited to the wavelength range above 1.0 micron, making the IR channel complementary to the UVIS channel.

Compared to CCD detectors, IR detectors like the one used in the IR channel show higher read noise and dark current. Unlike CCDs, however, IR detectors allow the accumulated signal to be read out multiple times, non-destructively and without affecting other pixels. The capability to sample the signal multiple times during the integration significantly reduces the effective read-out noise. IR detectors are also immune to the charge bleeding exhibited by CCDs at high signal levels; however, saturation may still be a problem because pixels subject to the highest signal levels show higher dark current rates (“image persistence”) in subsequent exposures [Q: is this wording correct as edited by me?-HEB].

The capability of multiple readouts and the absence of bleeding makes IR detectors capable of very high dynamic-range observations. Non-destructive readout also allows recovering pixels affected by cosmic rays (CRs), since CR hits may be isolated between adjacent reads. Unlike CCDs, IR detectors do not show long-term on-orbit CTE degradation, since they do not employ the charge-transfer mechanism used in CCDs. IR detectors, however, are intrinsically non-linear. At low and intermediate

count levels, however, the departure from linearity is quite modest and can be well calibrated by a quadratic fit, whose parameters can be determined for each pixel.

5.5.2 IR Detector Basics

In this subsection we briefly describe the operational principles of the WFC3 IR detector. Figure 5.8 (adapted from McLean 1997) shows the basic physical structure of the photovoltaic HgCdTe detector used in WFC3.

Figure 5.8: Cross-section of a WFC3-IR detector (not to scale).

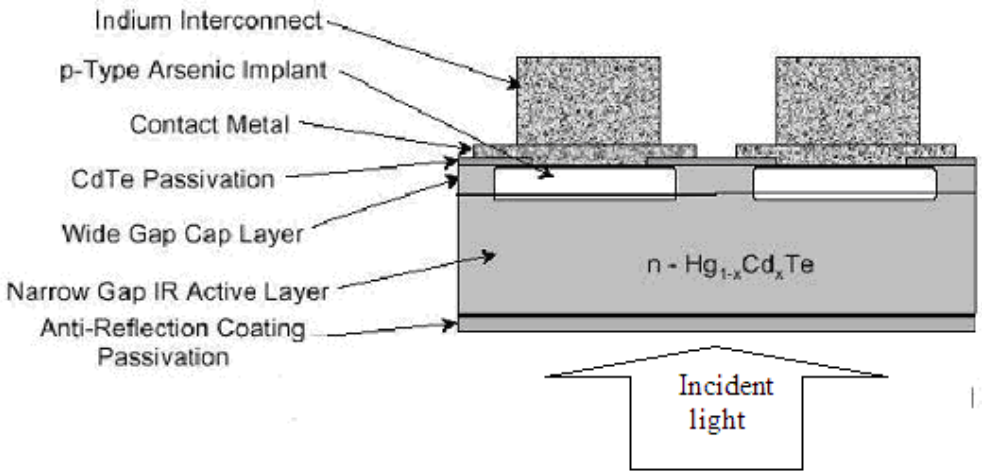

Infrared detectors used in astronomy today are basically two-dimensional arrays of p-n junctions working as photodetectors (photodiodes). In a p-n junction, negative charges migrate from the n-type doped material to saturate the unmatched covalent bonds of the adjacent p-type material. The displaced carriers establish an electric field across the junction, setting up an intermediate region depleted of free carriers. The depletion region is therefore both charged and highly resistive. The strength of the electric field and the size of the depletion region may be increased by applying an external electric field ("negative bias"). This biasing corresponds to the initial RESET applied at the beginning of the integration. When an incident IR photon is absorbed by the photosensitive material, it creates a free electron-hole pair. The two photo-generated charges drift in the material and would eventually recombine. However, if the mobility of the charge carrier (a hole in an n-type material) is high enough, it will reach the depletion region before recombining and be swept to the other side of the junction by the electric field. There, in the p-type region, it will recombine with one of the electrons of the ionized holes, causing a reduction of the voltage across the junction. This change of voltage can be measured and, being proportional to the number of photo-generated charges, provides a direct measure of the photons captured on each pixel.

In the case of the WFC3 IR detector, the photosensitive material is made of HgCdTe grown with a molecular beam epitaxial (MBE) process on a ZnCdTe substrate. The fraction (stoichiometric ratio) of Hg vs. Cd controls the cutoff wavelength of the material, whereas the doping material (As for the p-type, In for the n-type) creates the p-n junction. The MBE growth process is different from that used in the NICMOS detectors on HST, in which the HgCdTe was grown on sapphire in a liquid phase (PACE process). MBE growth on a ZnCdTe substrate is expected to provide a better lattice match to HgCdTe than sapphire, creating fewer defects and charge traps at the interface between the two materials. The MBE growth process is followed by the processing phase, in which the implants and contacts of each pixel are realized.

As usual with IR arrays, the readout circuitry is made on a separated C-MOS chip (multiplexer or MUX), which is eventually hybridized to the detector with an indium contact for each pixel (see Figure 5.9). After the two chips have been hybridized, the ZnCdTe substrate is removed to reduce the susceptibility of the device to cosmic-ray events and to increase the sensitivity at short wavelengths. The final chip can therefore be regarded as C-MOS device connected through indium columns to a thin layer (a few microns thick) of HgCdTe photosensitive material.

Figure 5.9: Basic "hybrid" structure of infrared array detectors (not to scale)

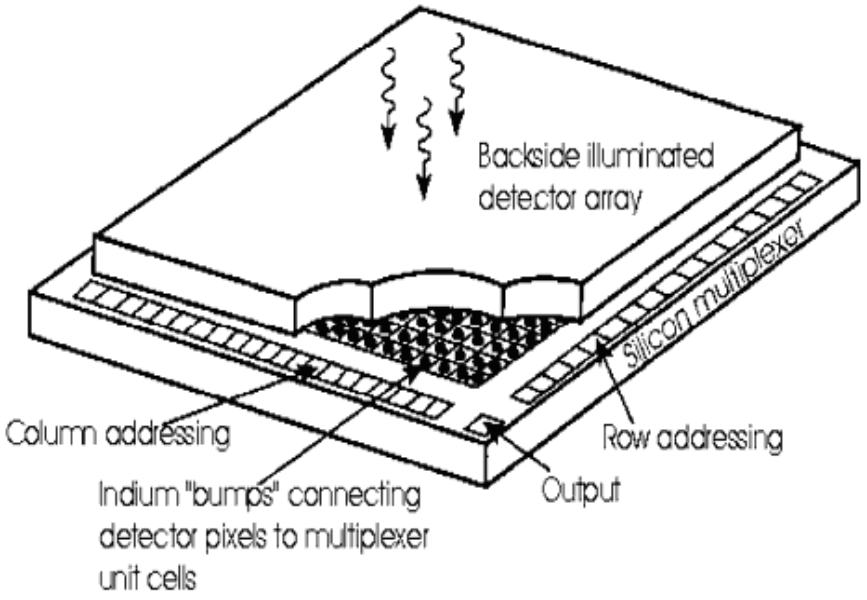

In the MUX, each pixel has its own dedicated readout circuitry (unit cell). In particular, the voltage change across the p-n junction is monitored by a field-effect transistor (FET) configured as a source-follower amplifier, which has gain of 1 and effectively decouples the detection process from the noisy readout circuitry. Two other FETs connect the pixel to the reset voltage and the output line. Figure 5.10 shows the equivalent circuit diagram for the WFC3 detector unit cell. Each WFC3 IR unit cell contains three transistors. For comparison, the NICMOS detectors have four

transistors, whereas the latest generation of Hawaii-2RG detectors for JWST has seven transistors per unit cell. A higher number of transistors increases the versatility of the device. For example, on the NICMOS detectors it is possible to reset each individual cell, whereas on WFC3 detectors the reset is sent simultaneously to all cells on the same row. Note that since there are no potential barriers between pixels, pixels do not spill charges into nearby pixels when they reach a certain level (“blooming full well”) of accumulated charges, as in typical multiphase CCDs. Therefore, IR detectors do not show "bleeding" along columns. Moreover, due to individual readout, bad pixels do not block the rest of the column as they do in a CCD.

Figure 5.10: Equivalent circuit diagram of the WFC3 IR unit cell.

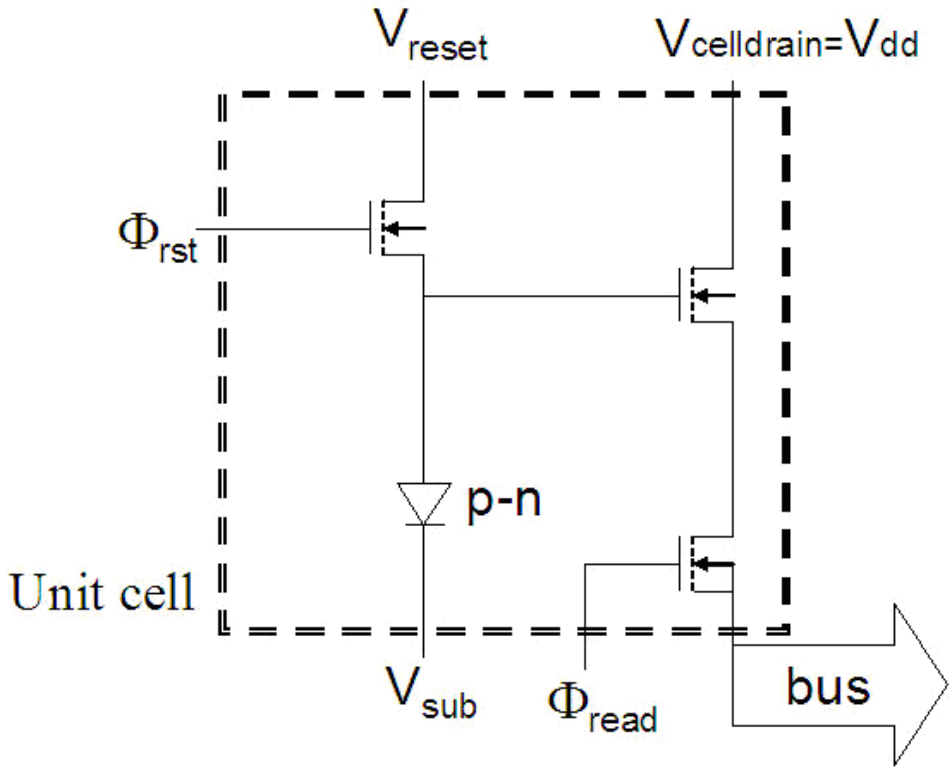

5.6 WFC3 IR Readout Formats and Reference Pixels

The WFC3 IR detector contains 1024×1024 square pixels of 18×18 micron physical size. The detector is divided into four quadrants of 512×512 pixels, each of which is read out independently from its outer corner, as illustrated in Figure 5.11.

Figure 5.11: Schematic layout of the WFC3 IR detector. The long (red) and short (blue) arrows indicate the direction of the fast and short readout, respectively.

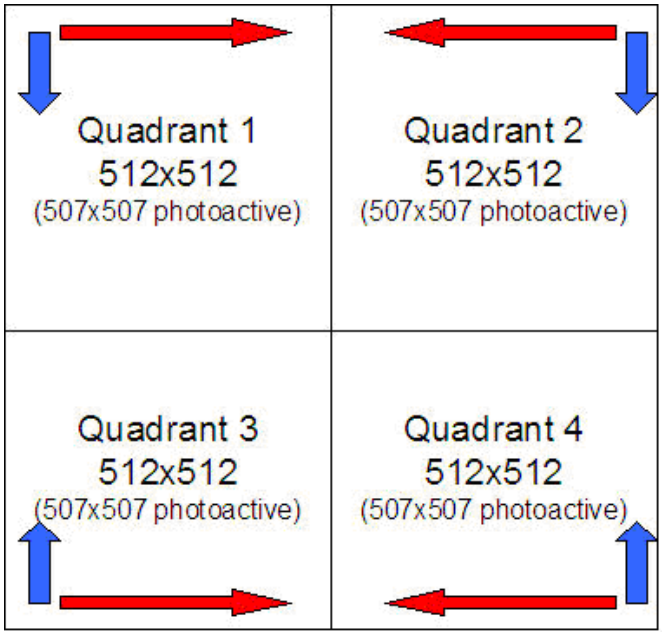

A major effort has been made to eliminate both the amplifier glow and bias jumps that have affected the NICMOS detectors.

To eliminate entirely the amplifier glow, WFC3 uses external amplifiers located in the immediate vicinity of the detector, rather than those directly on the multiplexer (which are also present).

In regard to bias jumps, the WFC3 IR class of detectors has been the first to use reference pixels, configured as follows. Of the 1024×1024 pixels, only the inner 1014×1014 pixels are light-sensitive (see Figure 5.12). The five outer rows and columns of pixels all around the array use fixed capacitances to provide constant-voltage reference values. There are actually two flavors of reference pixels: (1) the pixels on the outermost columns/rows are connected to capacitors located out of the unit-cells. Their values follow a 4x periodic pattern, providing 4 sequentially increasing voltage levels all within the range of the detector output signal; (2) the 4 inner rows/columns are instead connected to capacitors created within their cells. These on-board capacitors are identical by design and all provide nearly the same reference signal. The present version of the WFC3 IR data-reduction pipeline uses only the on-board reference pixels, as they provide a more robust statistical estimate of the variable detector pedestal.

The reference pixels track the low-frequency drift of the readout electronics and efficiently remove the “pedestal” variations that affected, for example, NICMOS. Pre-launch tests have also shown that the reference pixel signal is sensitive to the detector temperature and may therefore be used to assess the expected level of dark current during the integration.

Figure 5.12: Schematic layout of the active pixels (dark blue) and of the reference pixels at one of the corners of the WFC3 IR detector. The color coding represents different values of the reference pixel capacitances.

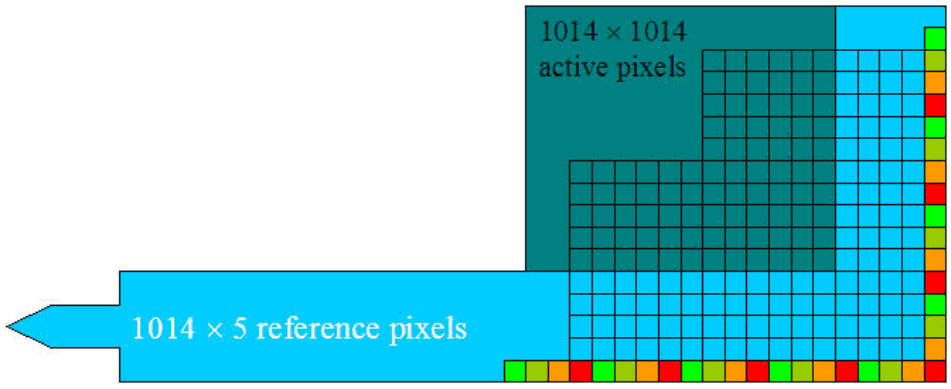

5.7 WFC3 IR Detector Characteristics and Performance

An overview of the IR detector characteristics was given in Table 5.1 above. Further details are given below in Table 5.9. These values are based on the current (January 2007) flight detector (FPA 129) and will be revised when the final detector is selected for flight.

Table 5.10: Flight Array Characteristics. Please see the following sections, which provide more information for each of the quantities listed.

Characteristics	Performance
Dark Current (e- /second)[1]	0.015e/s/pix (mode) 0.054e/s/pix (median)
Read Noise (e-)[2]	16.5 (16 read)
Bad Pixels (including particles)	213 (0.33%)
Conversion Gain (e- / ADU)	2.5 (default value)
Well Depth (ADU)	96,000
Saturation (ADU)[3] (95% Linearity)	76,500
50% QE Cutoff Wavelength (microns)	1.72

1. These numbers are the typical signal level in a "dark" exposure, and can be used for sensitivity calculations. They contain contributions from linear dark current, amplifier glow, and possibly low-level cosmic ray persistence.

2. The quoted readout noise is the RMS uncertainty in the signal of a differenced pair of readouts (measured as the mode of the pixel distribution).
3. Saturation is defined as a 5% deviation from an (idealized) linear response curve.

The currently selected candidate flight detector (FPA 129) has a read-out noise of about 16 electrons RMS per pixel after 16 uniformly spaced reads [to be confirmed with real WFC3 TV data]. The sum of detector dark current and thermal background contributions is predicted to be lower than the requirement of 0.4 electrons per pixel per second.

5.7.1 Quantum Efficiency

The quantum efficiency of the flight detector, as measured at the Goddard Detector Characterization Lab (DCL), is presented in Figure 5.13

Figure 5.13: quantum efficiency curve of FPA129. The red line indicates the range of wavelengths covered by the filters available on the WFC3 IR channel.

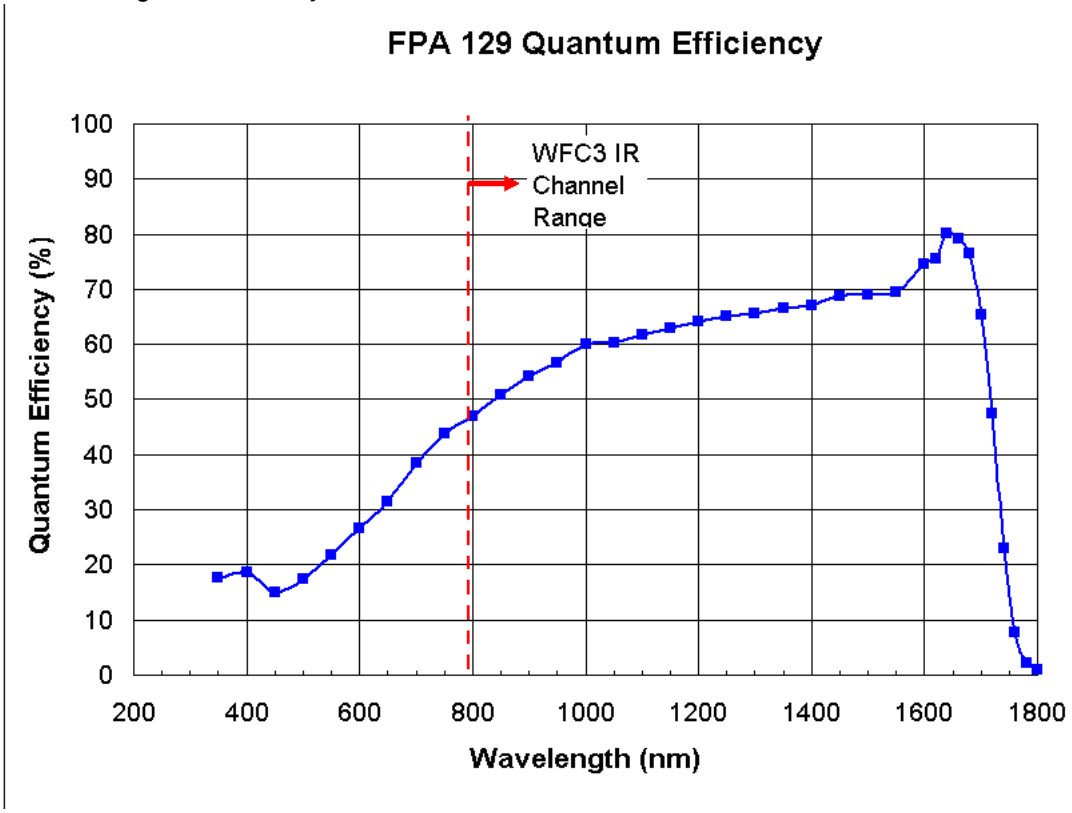

5.7.2 Dark Current

To avoid the complexity and limited lifetime of a stored-cryogen system, while at the same time provide the low operating temperatures required for dark-current and

thermal-background reduction, the WFC3 IR detector is refrigerated with a six-stage thermoelectric cooler to a nominal operating temperature of 145 K. This is an unusually high temperature for near-IR detectors, and has required tailoring the composition of the HgCdTe material for a long-wavelength cutoff at ~1.7 micron. The higher band-gap associated with the short cutoff wavelength effectively limits both the intrinsic detector dark current and its sensitivity to the internal thermal background.

WFC3 IR exposures taken with a blank filter in place provide a measure of the detector dark current. For FPA 129 the mean dark current is 0.015 e/s/pix and the median dark current is 0.054 e/s/pix. The difference between these two values is due to the asymmetry of the dark-current distribution among the pixels, which is characterized by a long tail of "hot pixels" randomly located across the detector. The cumulative dark-current distribution, i.e., the fraction of pixels with a dark current higher than a certain level, is shown in Figure 5.14.

Early ground-based tests have shown for FPA 64 (an earlier flight candidate detector) a dark-current level significantly dependent on the power dissipated by the array's thermoelectric cooler. A major effort has been made to operate the cooler in the most stable conditions. Tests made on similar detectors indicate that the dark-current variations can be largely calibrated and subtracted out using reference pixels.

Figure 5.14: Histogram of the dark current level of FPA 129.

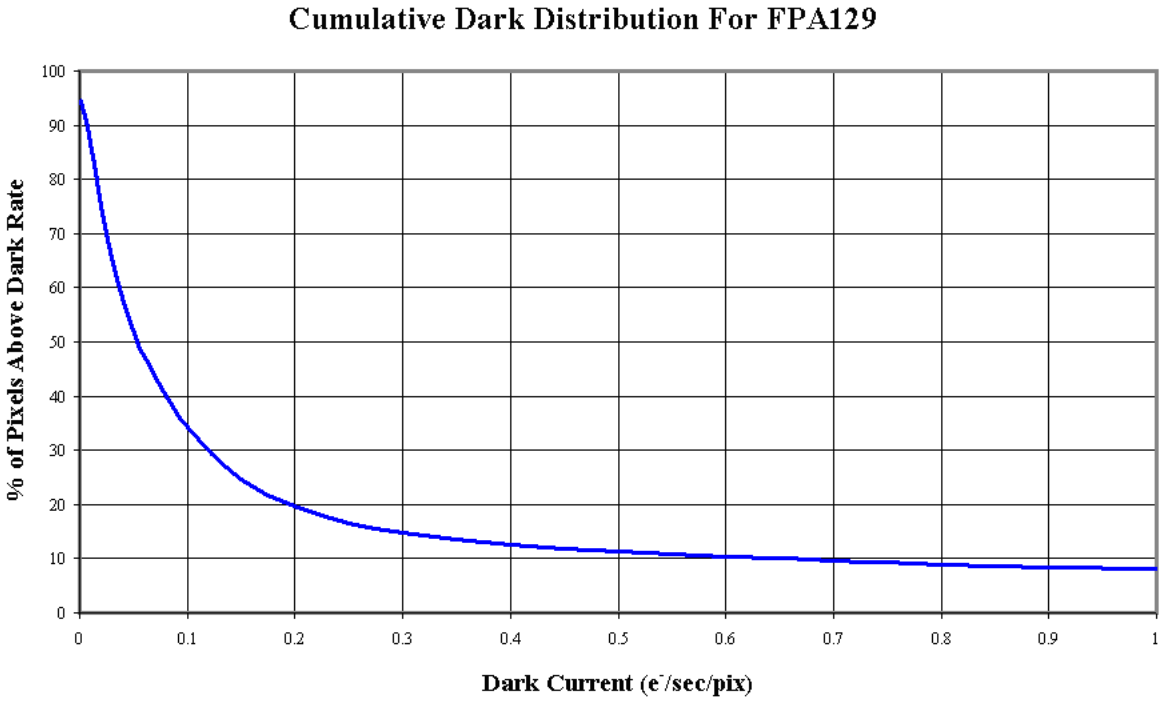

5.7.3 Read Noise

Each detector has four independent readout amplifiers, each of which reads a 512x512 quadrant. The four amplifiers generate very similar amounts of read noise.

This is illustrated in Figure 5.15, which compares the pixel read noise distributions for the four quadrants of the detector.

Figure 5.15: Histogram of the readout noise characteristics of the WFC3-IR detector. TO BE DONE AFTER TV

The data presented in Figure 5.15 represent the distribution of electronics-induced RMS uncertainties, as measured from a series of difference images of short uniformly spaced ramps. The distributions for all quadrants are relatively narrow, with a FWHM of about 16 electrons, indicating that there are only few anomalously noisy pixels. The read noise is independent of temperature.

For some scientific programs, such as ultra-low background observations, read noise becomes a non-negligible component of the noise floor. The contribution to the read noise in WFC3 IR data due to digitization errors associated with the conversion from electrons to data numbers (DN) is negligible.

5.7.4 Flat Fields

Uniformly illuminated frames, the so-called "flat fields", taken with the WFC3-IR array show response variations on both large and small scales. In Figure 5.16 we show the flat-field pattern and corresponding histograms at four wavelengths: 1, 1.3, 1.6, and 1.72 microns. This last measure, at the detector cutoff wavelength, shows significant non-uniformity due to variations in the stoichiometric composition of the HgCdTe photoactive material.

Figure 5.16: Flat-field exposures at 1, 1.3, 1.6, and 1.72 microns.

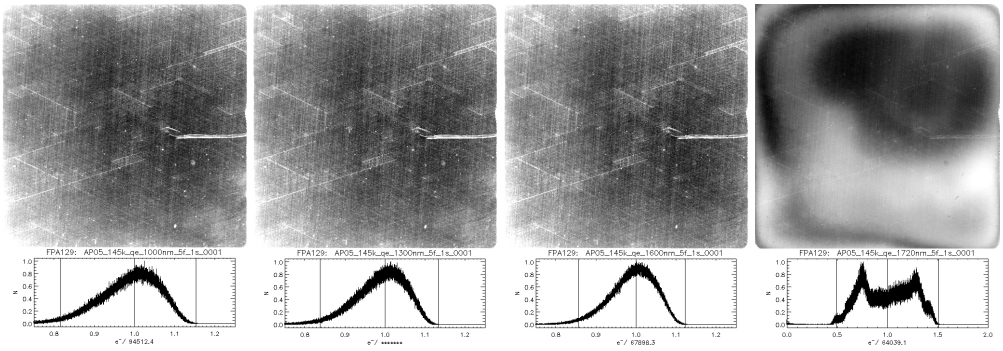

The high-frequency flat-field pattern contains a number of defects that are related to blemishes on the detector surface (Figure 5.17). Being on the focal plane, they show a very sharp profile. Defects on the optical path, especially particulates on the cold enclosure window and filters, are out of focus and show a more diffuse, nearly circular pattern. Flat-field procedures remove their effect to better than 1% [to be confirmed by TV data].

Figure 5.17: Detector blemishes seen on the readout image (left) and on a direct photograph of the device (right).

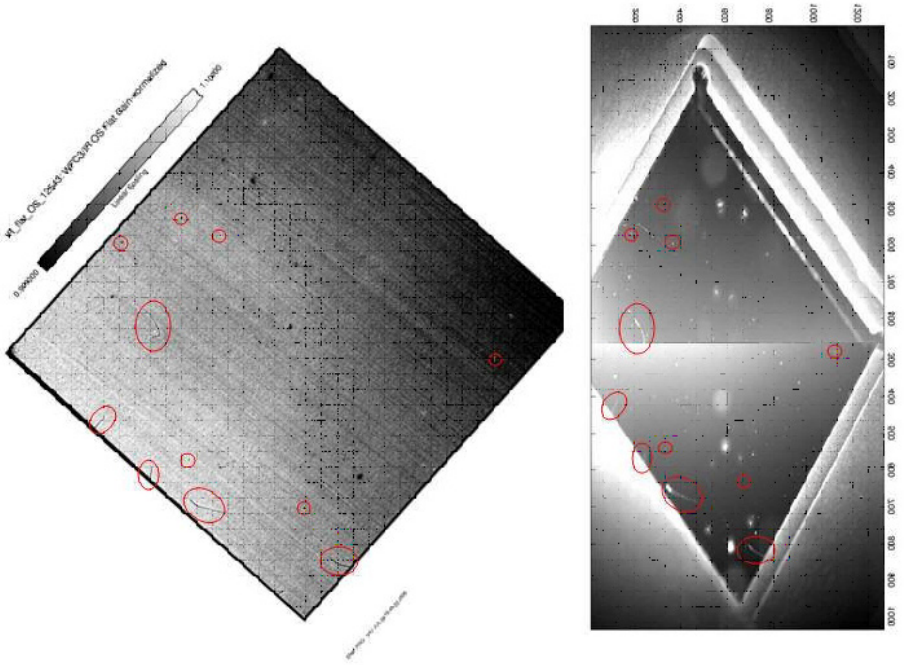

Flat-field frames are normally generated using the internal calibration system from a pair of "lamp-off" and "lamp-on" exposures. Differencing these two exposures then leaves the true flat-field response. The count rate in such an image is a direct (albeit relative) measure of the QE uniformity modulated by the field dependency of the throughput of the optical system.

5.7.5 Linearity and Saturation

The WFC3 IR calibration program shows that the detector response is in fact (slightly) non-linear over the full dynamic range. Figure 5.18 illustrates this behavior.

Figure 5.18: Average count rate as a function of total accumulated counts for FPA64.

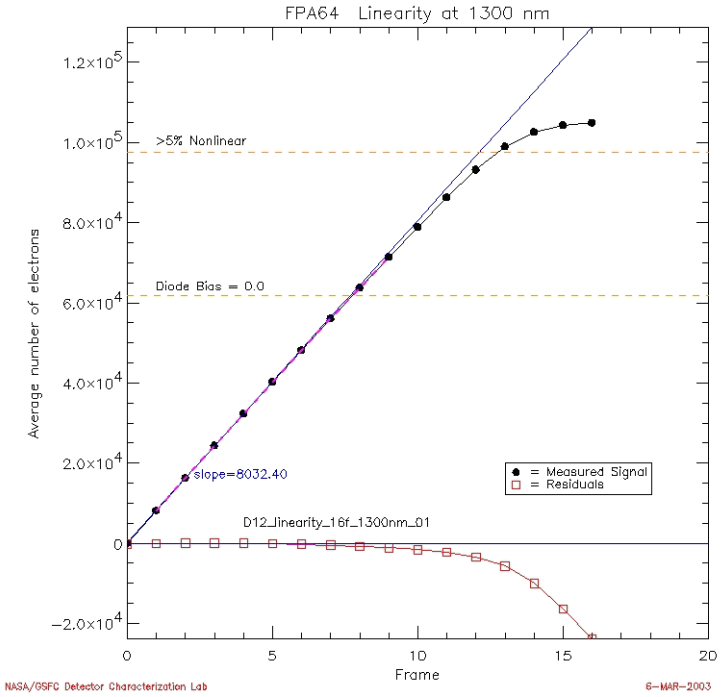

The linearity correction implemented in the WFC3 IR calibration pipeline corrects over the entire dynamic range between zero and the flux level at which the response function deviates by more than 5% from the linear approximation. Pixels that reach this threshold during an exposure are flagged as saturated, and are not corrected during the pipeline processing.

5.7.6 Detector Cosmetics

Each WFC3 IR detector has a number of pixels that show an anomalous responsivity. Such "bad pixels" come in various flavors. So-called "hot" pixels have a higher than average dark current, and thus show excessive charge compared to the surrounding pixels. On the other hand, "cold pixels" are less sensitive to incident photons than the typical pixel. The anomalously low responsivity of a "cold" pixel could be due to a lower intrinsic QE of the pixel, or to surface defects. Some pixels do not respond at all ("dead pixels") to incoming light. Quantitative statistics of the hot/cold pixels in the three [Q: three??] WFC3 IR cameras are given in Table 5.52. It is important to note that the impact of bad pixels on the quality of WFC3 IR images can be minimized by dithering the observations

Table 5.11: Bad Pixels in WFC3-IR

Pixel Characteristics	FPA 129 (%)
Cold1[1]	xx
Hot[2]	xx

1. A cold pixel is defined as having a response 5 sigma lower than the median value of all pixels.
2. A hot pixel is defined as having more than three times the median dark current of the array.

CHAPTER 6:

UVIS Imaging with WFC3

In this chapter . . .

6.1 WFC3 Imaging: Overview of Chapters 6 and 7

Q: the draft of this chapter as prepared by Sylvia has been extensively edited. Some of the material in the draft was already covered in other chapters and was thus removed, and other material originally in the draft of this chapter has been moved to the other chapters, especially chapters 2 and 5. Moreover, material in this chapter relating to the IR channel has mostly been moved to chapter 7. The organization of chapters 6 and 7 has been made as similar as possible. So, review of this chapter should be done in conjunction with an examination of chapters 2, 5, and 7. - HEB

As described in Chapter 2, the optical design of WFC3 features two independent channels, each with its own separate optics, filters and grisms, and detectors. The **UVIS channel** is sensitive to UV and optical wavelengths (200-1000 nm), and the **IR channel** is sensitive to near-infrared wavelengths (900-1700 nm).

Only a single channel, either UVIS or IR, can be used at any one time. Thus they cannot be used in parallel, but only sequentially.

This chapter describes the capabilities of the UVIS channel. The following chapter, Chapter 7, describes the IR channel. Detailed characteristics of the detectors used in both channels are given in Chapter 5.

6.2 UVIS Channel Characteristics

In concept and functionality, as well as in many design details, the WFC3 UVIS channel is patterned after the ACS WFC channel. The UVIS channel contains an optical train providing focus and alignment adjustments as well as a correction for the OTA spherical aberration, a filter-selection mechanism, a shutter mechanism, and a CCD detector assembly (which uses the same camera-head design as ACS/WFC). These are supported by a thermal-control subsystem and also by control and data-handling electronics subsystems.

The UVIS channel was designed for highest performance in the 200-400 nm wavelength range. This optimization for the ultraviolet includes an optical design employing aluminized mirrors with magnesium fluoride coatings, and CCDs whose sensitivity extends down to 200 nm. In spite of the UV optimization, the UVIS channel remains sensitive well out into the visible, red, and near-IR part of the spectrum. Fig. xx provides a comparison of the WFC3 UVIS and ACS system throughputs.

The detectors in the WFC3 UVIS channel are two 4096×2051 pixel CCDs, butted together to yield a 4096×4102 array with a ~50 pixel (2 arcsecond) gap. The gap can, of course, be filled in by using appropriate dithering strategies. The CCDs are thinned, back-illuminated Marconi Corporation (now e2v technologies Ltd.) devices wtih UV-optimized anti-reflection coatings and 15 micron pixels. The plate scale is approximately 0.04 arcseconds per pixel, which provides a good compromise between adequately sampling of the PSF and a wide FOV. Geometric distortions induced by the WFC3 optics cause the nominally square detector to map onto the sky as a skewed rhombus, 163x×162 arcsec in size.

Uniform response within each pixel and excellent charge-transfer efficiency (CTE) are key to achieving accurate photometric performance. The anticipated CTE performance of the UVIS detectors over WFC3's lifetime is expected to be better than previous HST instruments due to several factors. First, shielding (similar to ACS/WFC and WFPC2) has been used to protect the CCDs from the high-radiation space environment, thereby slowing the production of charge traps. The WFC3 CCDs have also been designed with a mini-channel (improved over ACS/WFC), which will reduce the number of traps seen by small charge packets during read-out transfers. In addition, the WFC3 CCDs have the option of charge injection, which, by filling traps, can mitigate the effects of CTE losses without an excessive increase in noise level.

6.3 UVIS Field Geometry

6.3.1 Field of View and Pixel Size

As described above, the UVIS channel uses two 4096×2051 CCDs, butted together to yield a 4096×4102 array with a ~50 pixel (2 arcsecond) gap. The field of view is 163×162 arcsec. The average values of the x and y pixel scales across the FOV are 0.0397 and 0.0395 arcsec/pixel.

Q: I've seen different numbers for the FOV, and also I'm confused whether the gap is parallel to the x axis or the y axis. Can you clarify? I suggest the FOV value should INCLUDE the gap.

6.3.2 Geometric Distortion

Distortions due to the WFC3 optics cause a the nominally square FOV of the UVIS detector to map onto the sky as a skewed rhombus. Instrument requirements called for the FOV distortions to fall below 5% for the UVIS channel. It easily satisfies this specification, since the FOV measures 162×163 arcsec, or a ~2% distortion.

The distortion will affect both the photometric accuracy and the astrometric precision; nominal calibrations for these effects will be provided. For further discussion of WFC3 geometric distortion, see Appendix B

6.3.3 Coordinate Systems

Q: we need to add a discussion of the x,y system, POS TARG coords, etc. Needs to include some figures showing the POS TARG system. Similar to the corresponding section in Chapter 7 for the IR channel.

6.3.4 Subarrays and On-chip Binning

Q: need a discussion and tables similar to corresponding subsection of Chapter 7.

Q: note that Chapter 10, section 10.3, says that arbitrary subarrays can also be specified by users. Correct? Give details, if so.

6.3.5 Apertures

Q: Need discussion similar to corresponding subsection of Chapter 7.

Q: We need to clarify the terminology. The pre-defined subarrays, Larry Petro tells me, are implemented as Apertures. But the user-defined subarrays are defined by Optional Parameters. All of this needs to be explained.

6.4 UVIS Spectral Elements

6.4.1 Filter and Grism Summary

An overview of the UVIS spectral elements, and of the process by which they were selected, was given in Section 2.3. This section gives further details of the UVIS filters and grism. Table 6.1 contains a complete listing of the spectral elements in the UVIS channel.

The UVIS filters have been chosen to cover a wide variety of scientific applications, ranging from color selection of distant galaxies to accurate photometry of stellar sources and narrow-band imaging of nebular gas. The set includes several very broad-band filters for extremely deep imaging, filters that match the most commonly used filters on WFPC2 (to provide continuity with previous observations), the SDSS filters, and filters that are optimized to provide maximum sensitivity to various stellar parameters (e.g., the Stromgren and Washington systems, and the F300X filter for high sensitivity to the stellar Balmer jump). There is a variety of narrow-band filters, which will allow investigations of a range of physical conditions in the instellar medium, nebulae, and solar system. A few of the narrow-band filters are also provided with slightly redshifted wavelengths, for use in extragalactic applications. Finally, there is a UV grism which provides slitless spectra covering 200-400 nm.

Note that, in contrast to ACS, WFC3 does not have any polarizers or ramp filters.

Table 6.1: WFC3 UVIS filters and grism characteristics, based on filter and grism throughput (for full filter+WFC3+HST system characteristics, see [**reference to table in Chap9 needed here]). [** insert Table 4 from minihandbook here].

Name	Description	Pivot λ (Å)	Width (Å)	Peak Tranmsission

Most of the UVIS filters, as well as the UVIS grism, are full-sized elements that

number of bandpasses, there are five “quad” filters, identified with "FQ" in the filter name, where each bandpass covers ~1/4 of the WFC3 UVIS FOV. The quad filters are discussed in more detail below.

The UVIS channel is designed to be used with a single filter or grism in the light path; although possible in principle, unfiltered imaging, or imaging through two filters, would lead to significantly degraded image quality and is not supported or recommended. For “clear” imaging, the UVIS channel contains an F200LP filter which covers the entire 200 to 1000 nm bandpass of the CCD detectors. (Q: wouldn’t the image quality be degraded somewhat in this filter?)

While the red blocking in the WFC3 UV filters is generally very good, resulting in negligible red leaks for hot objects (typically <<1% for targets with effective temperature Teff>10000 K), the red leak can become significant in some filters for cooler targets (e.g., ~10% in F225W for star with Teff = 5000 K). More details are available in “Filter Red Leaks” on page 67; Table 6.2 in that section tabulates red leak values as a function of effective temperature.

UV Filters

As mentioned earlier, the WFC3 UVIS optics and CCDs have been optimized for UV imaging. As such, the UV filters play a key role and considerable effort has been made to procure filters with the best possible characteristics, including maximum throughput, minimum blocking, and minimal ghosts. (Q: what does minimum blocking mean?)

The UV filters include the shortest-wavelength F218W, intended for studies of the ISM absorption feature; the wide F225W and F275W for broad-band UV imaging; the Stromgren u (F336W) and Washington C (F390W) for stellar astrophysics; the extremely wide F300X for very deep imaging; and narrow bands such as the F280N (Mg II) and the quad filters FQ232N and FQ243N (C II] and [Ne IV]).

There is also an ultra-wide F200LP filter; it is simply a fused-silica element with a UV-optimized anti-reflection coating which covers the UVIS channel’s entire spectral range (200-1000 nm). The F200LP filter is analagous to the clear filter on STIS.

WFC3’s maximum sensitivity to hot sources can be obtained by combining F200LP and F350LP images, as shown in Figure 6.1; for redder targets, some additional calibration may be necessary to account for differences in the transmission of the two filters longward of ~450 nm [**add pointer here to F200LP and F2350LP system throughputs in appendix].

Q: in Fig 6.1 it’s hard to tell the lines apart...was the figure originally in color?? Also, I need a more detailed description of what is plotted in the figure.

Figure 6.1: Sensitivity of F200LP-F350LP compared to other UV filters. [**add uvbandpasses.ps here]

Wide-band Filters

The most commonly used wide WFPC2 and ACS filters are also included in the WFC3 filter set. In addition to a wide V-band filter (F606W), there is the Johnson-Cousins *BVI* set (F438W, F555W, F814W).

The Sloan Digital Sky Survey (SDSS) *griz* filter set (F475W, F625W, F775W, F850LP) is designed to provide high throughput for the wavelengths of interest and excellent rejection of out-of-band wavelengths. These filters will provide wide, non-overlapping filter bands that cover the entire range of CCD sensitivity from blue to near-IR wavelengths.

Medium-band Filters

The medium-band filters include the Stromgren set (u, v, b, and y), as well as some continuum bands needed for use with narrow-band imaging (F390M, FQ422M). The four 11% passband filters were added to the WFC3 UVIS set in order to cover the ~600-900 nm wavelength region with equal-energy filters. The "11%" refers to the filter bandwidths, which are ~11% of the central wavelength.

Narrow-band Filters

The WFC3 UVIS channel contains 36 different narrow-band filters, covering a variety of species and most of the astrophysically interesting transitions, including Hα Hβ, Hγ, He II, C II], [N II], [O I], [O II], [O III}, [S II], Ca II, [Ne IV], and [Ne V]. The methane absorption bands seen in planets, cool stars, and brown dwarfs are also covered.

Quad Filters

The WFC3 UVIS channel contains five quad filters: each is a 2×2 mosaic of filter elements occupying a single filter slot, with each quadrant providing a different bandpass (typically narrow-band, although there are also several bandpasses intended for continuum measurements).

A quadrant nominally covers only 1/4 of the WFC3 total FOV or about 80"×80", although edge effects will result in an unvignetted field somewhat smaller than the 1/4 FOV. The five quad filters on WFC3 significantly increase the number of available narrow-band filters. The WFC3 quad filters are identifed by the prefix "FQ" in the filter name in Table 6.1.

Grism

The UVIS channel has a UV grism (G280), a spare from WF/PC-1. It provides slitless spectra with a dispersion of about 1.4 nm/pix, or a 2-pixel resolving power of about R=125, over the 200-400 nm wavelength range. Typically, a grism observation will be accompanied by a direct image, for source identification and wavelength calibration; an ideal filter for the identification image would be the F200LP discussed above. Chapter 8 discusses WFC3 slitless spectroscopy in detail.

6.4.2 Filter Red Leaks

The design and manufacture of the UV filters was based on a careful balance of the in- and out-of-band transmissions: in general, higher in-band transmission results in poorer suppression of out-of-band transmission, and vice-versa. The WFC3 filters represent an attempt to achieve an optimum result, maximizing the in-band transmission while keeping the out-of-band transmission as low as possible in order to minimize red leaks.

table 6.2 below summarizes the red-leak levels for the WFC3 UV filters. The table lists the fraction of flux longward of 400 nm as a function of stellar effective temperature. As can be seen from the table, red leaks should not be an issue for observations of any target taken with F275W or F336W. The other UV filters will have some red leak, whose importance depends on stellar temperature. The red leaks in F218W and F225W, for example, will exceed ~1% for objects cooler than ~6000 K, while in F300X the red leak reaches ~1% for objects as hot as 10,000 K. The most extreme red leaks will arise from F218W and F225W observations of objects with $T_{\rm eff}$ of ~5000 K or cooler, necessitating appropriate corrections.

Q: What is the exact definition of the entries in Table 6.2? Is it (red-leak signal)/(main-band signal + red-leak signal)?

Table 6.2: Fraction of flux longward of 400 nm as a function of effective temperature [** insert uvis.redleak.tab here; may want to include f200lp]

Teff	F218W	F225W	F275W	F300X	F336W

6.4.3 Ghosts

The WFC3 UVIS channel exhibits three different types of optical ghosts: those due to reflections between the CCD front surface and the two detector package windows,

those due to reflections between the window surfaces, and those due to reflections between the surfaces of the particular filter in use.

Window Ghosts

When a point source is positioned at the lower right of the FOV, reflections between the CCD and windows appear along the diagonal from the center of the FOV towards the upper left; these ghosts gradually move outside the FOV as the target source moves out of the lower right corner of the FOV. Smaller ghosts appear closer to the target source: they are due to reflections between the window surfaces (see "PSF Characteristics" on page 71 for an image showing these ghosts).

Measurements during ground testing have shown that window ghosts typically satisfy the requirement that each ghost contain no more than 0.2% of the total light.

Q: however, the footnote to the table below states that the requirement was 2% of the total light.

Filter Ghosts

Filter ghosts, however, can occasionally fail to satisfy the specification. During initial instrument-level ground tests, while most of the WFC3 UVIS filters performed consistently with or exceeding expectations, a few of the filters were found to have filter ghosts. The highest-priority filters affected by ghosts were remanufactured and reinstalled into the SOFA. The levels of filter ghosts in the majority of the final flight filter set are now <0.1%, well within the specified requirements. However, a subset of the final flight filters still have ghosts exceeding that level.

These out-of-spec filters are listed in table 6.3. They have been retained in the flight instrument either because they were of lower scientific priority, or because the ghost level was deemed acceptable in light of the otherwise excellent performance characterstics of the filters (e.g., in- and out-of-band transmission, sharpness of bandpass edges). While some scientific programs (e.g., stellar photometry) may be unaffected by filter ghosts, others (e.g., observations of extended targets or of faint objects adjacent to bright ones) could be adversely affected. In such cases, extra planning and/or data-analysis efforts may be needed, e.g., combining images taken at different dither positions and/or roll angles, or by applying a deconvolution algorithm.

Table 6.3: Filters which do not meet the filter ghost requirement[1]; these values will be verified during future ground testing of the integrated instrument.

filter	description	ghost level (in percent)	filter	description	ghost level (in percent)
F200LP	Clear, grism reference	0.35	F218W	ISM feature	3.3
F225W	UV wide	0.3	FQ232N	CII] 2326	5.0

1. The ghost requirement calls for <2% of the total flux to reside in the ghost.

filter	description	ghost level (in percent)	filter	description	ghost level (in percent)
FQ243N	[Ne IV] 2425	5.0	F280N	Mg II 2795/2802	
F300X	Extremely wide UV	0.2	F656N	Hα 6562	0.5
F658N	[N II] 6583	0.4	F665N	z(Hα + [N II])	0.4
F673N	[S II] 6717/6731	0.3	F680N	z(Hα + [NII])	0.3

Figure 6.2: System throughputs of the imaging instruments on HST as functions of wavelength. The plotted quantities represent end-to-end throughputs, including filter transmission, calculated at the pivot wavelength of each broad-band filter of each camera. [**insert Fig4 from mini-handbook here]

6.5 UVIS Optical Performance

Q: Sylvia, check the following paragraph which I wrote.

At this writing, we do not have any direct observations of the sky using WFC3 installed in HST. However, extensive laboratory measurements have been made during ground testing of WFC3, and these indicate that excellent optical performance will be achieved. Many of these measurements have been made with a device called an "optical stimulus," or CASTLE, which inputs calibrated artificial images into WFC3 that closely simulate light from the HST OTA. ("CASTLE" is an abbreviation for "Calibrated Stimulus from Leftover Equipment.")

The following subsections summarize the expected flight optical performance for the UVIS channel.

6.5.1 Encircled Energy

In the UVIS channel, ground-based point-source measurements of artificial sources from the CASTLE have been taken at 16 positions across the FOV and at four different wavelengths. These show excellent imaging performance over the entire FOV that satisfies the required specifications.

Average results for the encircled energy (EE) are listed in the first four rows of Table 6.9. Note that due to test-schedule constraints, the data were obtained with the flight detector slightly out of alignment; modelling indicates that the effect should be insignificant over most of the field, as long as a stable, appropriate focus is maintained. The expectation is that once the UVIS detector is optimally aligned, the EE performance at the field edges should be even better than that shown in Table 6.9.

Q: Insert Table 6.9 here.

Results obtained from ground data taken with the CASTLE do require corrections in order to estimate the on-orbit performance, e.g., by taking into account the differences in the central obscuration ratios and the spider widths. Extrapolation of the EE results from ground-based to on-orbit (accounting as well for the mid-frequency wavefront errors of the HST OTA) shows that the goal requirement at 633 nm will likely be met on-orbit, but the core requirement at 250 nm will not be met. However, the 250 nm specification as written is considered to be overly stringent, given the known OTA performance: the EE in the core and near wings is significantly reduced by the OTA mirror surface errors. As such, the shortfall is viewed not as a lack of optical performance of the WFC3 UVIS channel but as due to the HST OTA.

The WFC3 UVIS measured EE curves are shown in Figure 6.4 along with the optical stimulus (CASTLE) HST OTA models, at four wavelengths (250, 350, 633, and 810 nm). The left frames present the EE results while the right frames show the azimuthally averaged PSF; requirements (at 250 and 633 nm) are shown as diamonds.

Tabulated values of the EE for diameters of 0.15, 0.2, 0.25, and 0.35 arcseconds as well as PSF peak fraction for all measured PSFs (16 field points × four wavelengths),

are available from WFC3 ISR 2005-10 (available at http://www.stsci.edu/hst/wfc3/documents/ISRs/WFC3-2005-10.pdf]

6.5.2 Pixel Response Function

Charge diffusion, or the migration of charge into adjacent pixels, can degrade the sharpness of a CCD PSF. The effect is usually described in terms of the pixel response function (PRF), which gives the distribution of flux from within the pixel into adjacent pixels. Initial modeling, including only an independent assessment of the low-order wavefront error, the pupil mask, and a reasonable estimate of the detector MTF, yield good agreement with the EE curves at 350 and 633 nm. The best empirical fit to the pixel response convolution kernel is shown in Figure 6.3. The specification requires that 90% of the energy from a small spot reside within the central pixel, which these results indicate will not be met.

Q: I'm a little puzzled whether the "pixel response function" is the same thing as the PSF? Can the wording be clarified a bit?

Figure 6.3: CCD PIxel Response functions at 250 nm (top) and 810 nm (bottom).

$$\begin{bmatrix} 0.027 & 0.111 & 0.027 \\ 0.111 & 0.432 & 0.111 \\ 0.027 & 0111 & 0.027 \end{bmatrix}$$

$$\begin{bmatrix} 0.002 & 0.037 & 0.002 \\ 0.037 & 0.844 & 0.037 \\ 0.002 & 0.037 & 0.002 \end{bmatrix}$$

6.5.3 PSF Characteristics

To allow for a more extensive assessment of the UVIS PSF, unsaturated data (highlighting the bright PSF core) were combined with highly saturated data (emphasizing the faint PSF wings), producing the high-dynamic-range composite images shown in Figure 6.6. As noted in the figure caption, the streaks to the right of the 250 and 350 nm images are artifacts due to the optical stimulus; there is also a slightly warm column near the left edge of the 250 nm image and a blocked column just to the left of the 350 nm PSF.

Different types of ghosts are visible in the images. As expected from the UVIS channel design, there are low-level ghosts due to reflections between the four surfaces of the two AR-coated detector windows: these are the sets of relatively large diameter,

ring-shaped ghosts seen in all but the 250 nm images. Ghosts due to reflections from the CCD to the windows, as discussed above in Section 6.3.3, fall further from the PSF, along the diagonal from lower right to upper left of the FOV, and are not visible in these frames which image only a subsection of the WFC3 FOV. Typically, window-related ghosts easily satisfy the ghost requirement (the flux in a ghost must be <0.2% of the total light in the PSF).

Also evident are filter ghosts, due to reflections between the surfaces of a given filter. In single-substrate or air-gap filters (the latter consisting of two substrates joined via thin spacers), filter ghosts appear as small extended shapes, closer to the PSF centers than the window ghosts, e.g., the ring-shaped features in the 250 and 350 nm images (F275W and F336W filters, respectively). In multi-substrate filters (a stack of two or more substrates bonded or laminated together with a layer of optical adhesive) filter ghosts appear as faint, point-like features, such as the ghost in the 633 nm (F625W) image. Note: the F275W filter, used for the 250 nm image in Figure 6.6, has since been replaced with an improved filter, reducing the filter ghost level from 0.7% to <0.1%. The filter ghosts in the other images easily satisfy the requirement (<0.05% in 350 nm image and <0.1% in the 633 nm image). A small number of filters exhibit filter ghost levels which exceed the requirement somewhat; these are discussed in detail in Section 6.3.3 and are tabulated in table 6.3.

Finally, a ring of very faint spots centered on the point-source images appear in the image in Figure 6.6; their origin is unknown. The spots may be some sort of diffraction effect, as the radius is proportional to the wavelength; since the position angle does not vary with position in the WFC3 FOV (as, e.g., the spider diffraction spikes do), the source of the spots resides probably not in the optical stimulus but somewhere further down the light path, perhaps within the WFC3 instrument. Two slightly brighter spots may be related to the ring spots: they appear at the same distance from the PSF as the ring spots, just off the lower left and upper right spider features.

6.6 UVIS Exposure and Readout

6.6.1 Exposure Time

Q: Need to mention minimum & maximum exposure time, exposure-time quantization (if any), CR-splitting (defaults to 2 for ALL exposures), etc.

6.6.2 ACCUM Mode

Q: need to add discussion of ACCUM mode similar to corresponding IR section in Chapter 7.

6.7 UVIS Sensitivity

6.7.1 Limiting Magnitudes

Table 6.7 presents the predicted limiting-magnitude performance of WFC3 and compares it with that of the ACS camera. The calculations are based on a 3×3 pixel extraction box on a point source. The limiting ABMAG at a S/N of 10 was calculated for a 1-hour and a 10-hour exposure. The WFC3 filters used are listed in column 2; for ACS, the most comparable wide-band filter was used and its name is given in column 4. The ACS/HRC camera was assumed for the NUV and U-band comparison, and ACS/WFC was assumed for B, V, and I.

Table 6.4: Anticipated limiting-magnitude performance of WFC3 compared with that of ACS. The table provides limiting ABMAGs at a S/N of 10 for the indicated WFC3 filters and for ACS with its most similar filters. WFC3 UVIS comparisons are with the ACS HRC channel (NUV and U) and the ACS WFC channel (B,V,I).

Band	WFC3 Filter	ACS Filter	WFC3 limiiting mag in 1 hr.	ACS limiting mag in 1 hr.	WFC3 limiting mag in 10 hr.	ACS limiting mag in 10 hr.
NUV	F225W	F220W	26.2	25.0	27.7	26.4
U	F300X	F330W	27.0	26.0	28.5	27.4
B	F438W	F435W	26.9	27.4	28.3	28.7
V	F606W	F606W	27.5	27.7	28.9	29.0
I	F814W	F814W	26.6	27.1	28.0	28.4

Chapter 9 gives further details on estimation of exposure times. More accurate estimates will require use of the WFC3 Exposure Time Calculator (ETC), available online at http://TBD.

6.8 Other Considerations for UVIS Imaging

6.8.1 Gain and Full-well Saturation

The default gain setting for WFC3 CCD observations is 1.5 electrons/DN. This provides reasonable sampling of the readout noise while still achieving sufficient use of the full-well counts.

Note that saturation in in the UVIS channel occurs at ~75,000 e^- (corresponding to ~50,000 DN at the default gain).

Q: what happens at saturation? Do the DN values top out around 50,000, or keep going up, or go to zero, or what?

6.8.2 Cosmic Rays and Hot Pixels

The cosmic-ray fluxes for WFC3 UVIS are expected to be comparable to the levels seen in ACS, STIS CCD, and WFPC2. As with these previous HST instruments, typical WFC3 imaging observations will need to be split or dithered to obtain adequate cosmic-ray rejection.

The hot-pixel behavior in the UVIS channel is expected to be similar to that seen in previous HST instruments; small dithers between separate exposures will useful in identifying and removing residual hot pixels

Q: can we be more specific about hot pixels, such as the expected number?

6.8.3 Charge-Transfer Efficiency

The WFC3 UVIS CCDs are large-format devices, similar in size to those in the ACS WFC, and thus require significantly more charge-shifting during readout compared to the smaller STIS and WFPC2 CCDs. As a result, effects due to decreasing charge transfer efficiencies will be encountered earlier than for the smaller-format detectors. Section xx details current expectations for WFC3. Note that the WFC3 CCDs do have charge-injection capability, which will provide some mitigation of charge transfer inefficiencies once they arise

6.8.4 Image Persistence

No significant image-persistence effects following overexposure have been observed in preliminary instrument-level ground test data using the UVIS CCDs, as expected for back-illuminated devices.

6.8.5 Quantum Yield

Like the ACS HRC and STIS CCDs (and unlike WFPC2), the WFC3 UVIS CCDs are directly sensitive to UV photons. There is a critical wavelength, 339.68 nm, above which photons cannot produce more than one electron/hole pair in silicon (the corresponding energy is 3.65 eV). For wavelengths shorter than this critical wavelength, there is a finite probability that a single photon will produce two electrons on the detector.

This "quantum-yield" effect must be taken into account when estimating the detector QE and noise level of a UV observation, since multiple photons cause a distortion in the Poisson distributions of electrons. The correction is about 1.7 e^-/photon at 200 nm. The S/N algorithms incorporated in the WFC3 Exposure Time Calculator include the quantum-yield effect. See also Section 9.x.

6.9 UVIS Observing Strategies

Q: Need a discussion here similar to the corresponding IR Section. It would include dither strategies.

Q: Nothing is said anywhere in the Handbook about parallel observations involving WFC3. Is this beyond the scope of the Handbook??

CHAPTER 7:

IR Imaging with WFC3

In this chapter . . .

7.1 WFC3 IR Imaging

This chapter describes the capabilities of the IR channel, which is sensitive to near-infrared wavelengths (900-1700 nm). The preceding chapter, Chapter 6, describes the UVIS channel. Detailed characteristics of the detectors used in both channels are given in Chapter 5.

7.2 IR Channel Characteristics

Q: the draft of this chapter as prepared by Massimo has been extensively edited. Some of the material in the draft was already covered in other chapters and was thus removed, and other material originally in the draft of this chapter has been moved to the other chapters, especially chapters 2 and 5. Some material originally in other chapters has been moved into this one. The organization of chapters 6 and 7 has been made as similar as possible. So, review of this chapter should be done in conjunction with an examination of chapters 2, 5, and 6. - HEB

The WFC3 IR channel has been optimized for observing over the wavelength range 900-1700 nm. All the IR reflective optics (except for the WFC3 pick-off mirror, which intercepts on-axis light from the HST OTA and is shared with the UVIS channel) are coated with a silver layer for maximum IR throughput.

A schematic diagram showing both channels of WFC3 is given in Figure xx. Components of the IR channel include: the Channel Select Mechanism (CSM), which directs on-axis light from the HST OTA to the IR channel; a flat folding mirror; a two-mirror mechanism for providing focus and alignment adjustments; the Refractive Corrector Plate (RCP), which applies the spherical-aberration correction; the IR filter wheel (FSM or Filter Selection Mechanism); and finally the HgCdTe IR detector package sealed inside a vacuum enclosure. The IR optical chain is supported by a thermal control subsystem and by control and data-handling electronics subsystems. There is no mechanical shutter in the IR channel; instead, the detector provides electronic shuttering. Bright-object protection and dark-current measures can be obtained by using the blank, opaque blocker in the filter wheel.

The WFC3 IR detector is a Rockwell (now Teledyne) HgCdTe 1024×1024 array, wiith 18 micron pixels, bonded to a silicon multiplexer. It is a direct descendant of the NICMOS 256×256 and Hawaii 1024×1024 arrays. The inner 1014×1014 pixels are active, light-sensitive pixels for scientific imaging. The bordering 5 pixels around the edge of the detector are non-light-sensitive reference pixels, used in subtracting the electronic bias level.

The detector is cooled to its operating temperature of 145 K by a six-stage thermoelectric cooler. The long-wavelength cutoff at 1700 nm was chosen to limit the effective dark current (which is the sum of the intrinsic detector dark current and the instrument's internal thermal background). A longer cutoff wavelength would have significantly increased the effective dark current due to sensitivity to the thermal background from HST and the optical bench.

The pixel size for the IR detector as projected onto the sky was chosen to provide an optimal balance between FOV size, PSF sampling, and instrument packaging requirements. Simulations showed that dithering and image-reconstruction techniques would be able to reconstruct a good-quality PSF as long as the IR pixel size was below 0.15 arcsec. The final choice was a nominal pixel scale of 0.13 arcsec/pixel. The focal plane is tilted by ~22 degrees with respect to the beam, resulting in a rectangular FOV with an aspect ratio of ~0.90.

7.3 IR Field Geometry

7.3.1 Field of View and Pixel Size

The entire field of the IR detector is exposed to incoming light. There are no gaps in the field (such as the gap between the two CCDs in the UVIS channel), or mechanical occultations (such as the coronagraphic spots on NICMOS-2).

As noted above, the nominal pixel scale is 0.13 arcsec/pixel. However, since the focal plane is tilted with respect to the incoming beam, the field of view (FOV) as projected onto the sky is rectangular, with an aspect ratio of ~0.90. The pixels projected onto the sky are thus also rectangular, covering approximately 0.121×0.135 arcsec, with the shape varying slightly across the field. The FOV is 123×137 arcsec, or 4.68 square arcminutes.

7.3.2 Geometric Distortion

In addition to the rectangular field shape described above, the optical design of the IR channel also produces appreciable geometric distortion along the diagonal of the FOV, with the greatest distortion along the Amp A-Amp C line.

This distortion will have significant ramifications concerning appropriate techniques for flat-fielding, photometric calibration, and astrometry, especially when complicated by resampling in order to combine dithered image sets. Plans are in place to update the multidrizzle software with the necessary corrections for WFC3 data. An introduction to multidrizzle is available online at:

http://www.stsci.edu/hst/acs/analysis/multidrizzle.

Figure X shows a projection of the IR detector onto the sky. The X-Y axis in units of arcsec are arbitrary in this illustration.

Q: What's Figure X?

Geometric distortions in both channels are discussed in more detail in Appendix B.

7.3.3 Coordinate Systems

Like the CCD, the IR channel requires multiple coordinate reference frames, each relevant for a specific goal. The coordinate systems used for the IR channel are:

1. The detector-based system
2. The image-based system
3. The POS TARG system
4. The HST-based system

The detector-based (Xdet, Ydet) system (see Figure 7.1) specifies positions on the detector in pixel units. This system is orthogonal on the detector but not on the sky, due to field distortion. It is relevant to the commanding of the detector and it is used, for example, to specify positions of the apertures on the detector. The origin of the detector (Xdet, Ydet) coordinate system is at amplifier A, with the fast horizontal shift register along the Ydet axis. Thus, each set of pixels with the same Xdet coordinate represents a "row," and each set of pixels with the same Ydet coordinate represents a "column."

The image-based (AXIS1, AXIS2) system, also called the AXIS system, is used when an image is displayed on a computer screen. Here the X axis increases to the right and the Y axis to the top of the screen. It is expressed in pixel units. This system is used primarily by the generic conversion pipeline software, which creates science fits files from the data telemetry coming from the telescope. Figure 7.2 shows the orientation, with AXIS1 increasing to the right and AXIS2 increasing up with respect to the location of the Amplifiers and the V2,V3 on-sky reference frame.

The POS TARG (X-POS, Y-POS) system is orthogonal on the sky, in units of arcseconds. It is used to define telescope offset pointings in arcseconds, e.g., for dithering purposes or for placing an object in a desired non-central location in the FOV. In the case of the IR channel, the POS TARG reference frame is designed to be colinear with the AXIS reference frame and with its center corresponding to each IR aperture. The transformation between the undistorted POS TARG (arcsec) frame and AXIS frame (pixels) contains the non-linear distortion coefficients.

The HST-based (V2, V3) system refers to on-sky celestial coordinates and is related to the main HST focal plane (U2, U3) by a simple translation and rotation. It is used as the slewing reference frame. Figure 7.2 displays a compass with the POS TARG and HST-based on-sky reference frames. Note that the edges of IR detector are rotated by about 45 degrees with respect to the V2, V3 axes.

Q: There is a TBD in the figure.

Figure 7.1: Representation of the Detector-based coordinate system.

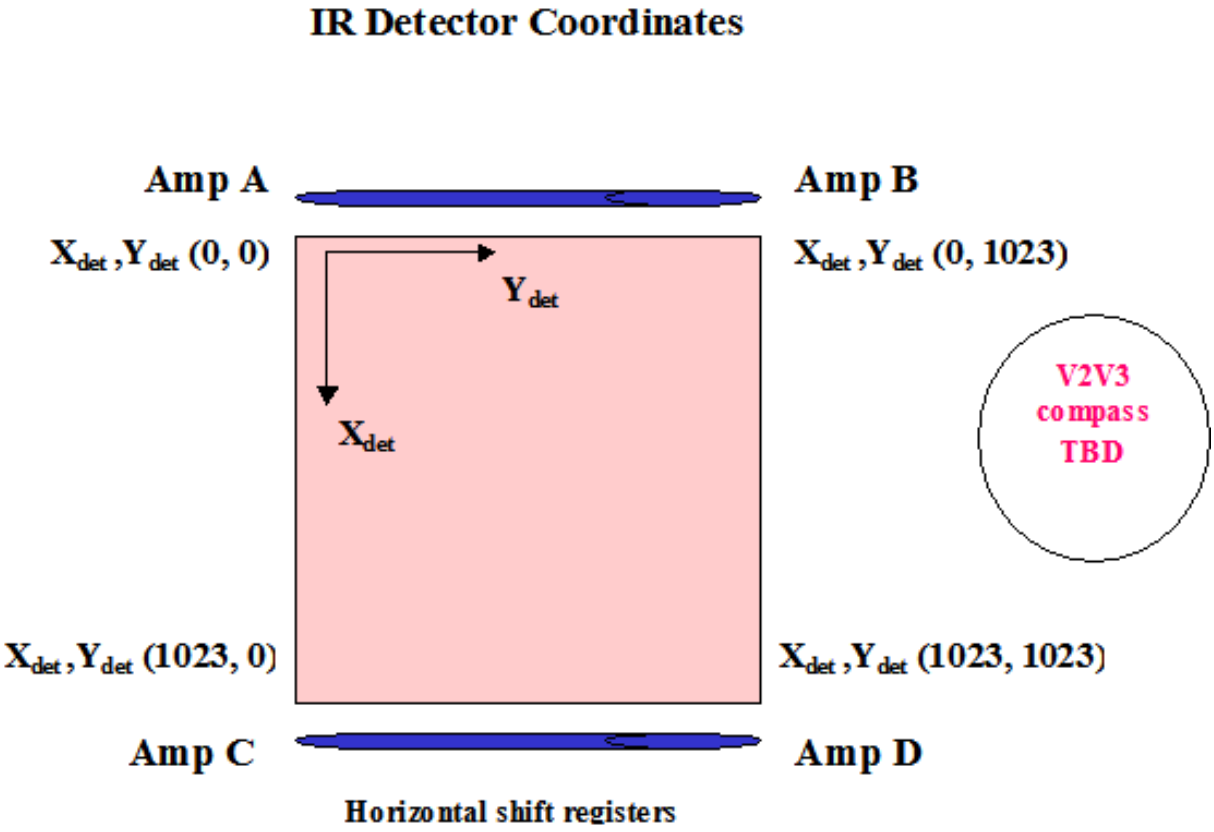

Figure 7.2: Representation of the Image based (Axis1-Axis2), Pos-Targ and HST based coordinate systems. The geometric distortion is not shown in this image. This distortion results in a projection of the IR onto the sky with non-orthogonal axes.

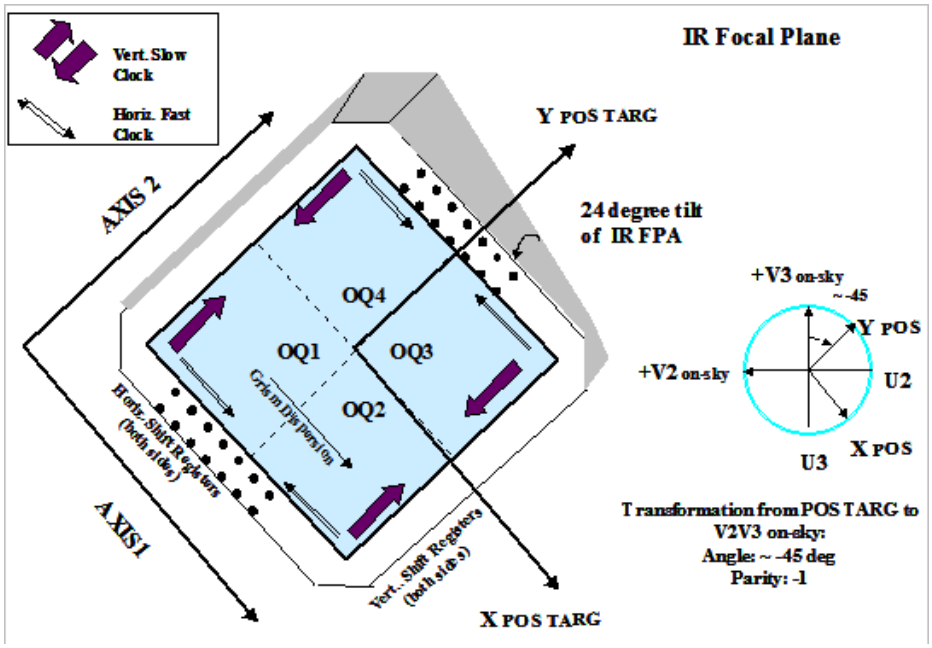

7.3.4 Subarrays

Of the 1024×1024 pixels of the WFC3 IR detector, only the inner 1014×1014 pixels are light-sensitive. The 5 rows and columns of pixels around the edge of the array use fixed capacitances to provide constant-voltage reference values.

In addition to obtaining standard full-field 1014×1014 images, users can read smaller portions of the field, called subarrays. Subarrays are useful to achieve reduced data volume, and/or to allow shorter exposure times. Shorter exposure times are especially important for the IR channel, because there is no physical shutter and the minimum integration time is limited by the time to read out the detector (2.9 seconds for full-frame readout). Very bright sources--including some of the primary "faint" IR photometric standards--may easily exceed the detector full-well of ~100,000 electrons in only a fraction of a second. Since the readout time is nearly proportional to the number of pixels read, subarrays can be used to reduce the effective integration time and make such observations feasible. This has been implemented in the IR cannel with the RAPID readout mode, which in subarray mode runs at a speed nearly proportional to the inverse square of the subarray size.

All of the IR subarrays are geometrically located at the center of the detector FOV. Four subarray sizes are supported, with pixel dimensions of 512×512, 256×256, 128×128, and 64×64. Note that the sizes of the subarrays refer to the actual active pixels, i.e., they do not include the reference pixels. The reference pixels, however, are still included in the output images, resulting in final images of 522×522, 266×266, 138×138, and 74×74 pixels. **Q: The next sentence is still not very clear; are you simply saying that the same reference pixels from around the edge of the full detector are added to the edge of the subarray image?** For subarray images, the reference pixels come from the same rows and columns of the subarray, with the 5×5 pixel region at each corner filled with the reference pixels at the corresponding corner of the detector.

7.3.5 Apertures

For Phase 2 proposal preparation, observers must specify where they want to position their targets on the focal plane. For this purpose, there are a number of predefined positions, called apertures, that are precisely defined and whose locations are carefully monitored and maintained by STScI. Apertures are defined relative to both the full array and subarrays. Historically, HST instruments have used apertures centered either at the geometric centers of the array (or subarray) or at optimum positions, defined on the basis of best image quality and detector cosmetics.

In the case of the IR channel, since all subarrays are centered on the geometric center of the detector, the geometric centers of the various subarrays are all coincident with the geometric center of the detector. These fixed apertures all have names ending in "-FIX." The optimum centers may eventually be shifted slightly, depending on the image quality and cosmetics of the flight instrument and detector. At the moment, all of the optimum apertures are set to be coincident with the fixed geometric centers.

The available set of IR apertures is given in Table 7.1

Q: why is it IIRS?? what does that stand for?

Q: Larry Petro tells me that the aperture names are wrong here. He says they should be names similar to IRSUB64, not IIRS64.

Table 7.1: WFC3 IR Apertures

Aperture Name	Description
IR	Optimum center of HgCdTe detector
IR-FIX	Geometric center of HgCdTe detector
IIRS64	Optimum center of 64x64 subarray
IIRS64-FIX	Geometric center of 64x64 subarray
IIRS128	Optimum center of 128x128 subarray
IIRS128-FIX	Geometric center of 128x128 subarray
IIRS256	Optimum center of 256x256 subarray
IIRS256-FIX	Geometric center of 256x256 subarray
IIRS512	Optimum center of 512x512 subarray
IIRS512-FIX	Geometric center of 512x512 subarray
G102-REF	G102 reference aperture for undispersed exposures
G141-REF	G141 reference aperture for undispersed exposures

7.4 IR Spectral Elements

7.4.1 Filter and Grism Summary

The IR channel is equipped with a single filter wheel with 18 slots, containing 15 passband filters, two grisms, and an opaque mask for dark-current measures. The filter complement samples the spectral region between 900 and 1700 nm. All of the IR filter elements are full-sized and cover the entire FOV of the IR detector. Since all of the elements are in a single wheel, only one element can be used at a given time.

This wavelength range is covered by a series of broad- and medium-band filters, with little wavelength overlap. Additional medium-band filters are centered on molecular bands and nearby continua, and several narrow-band filters are available for probing interstellar and nebular recombination lines.

The filter set is designed to include the most popular passbands used in extragalactic, stellar, and solar-system astronomy, as well as passbands similar to those already used in previous HST instruments.

Table 7.2 lists the IR channel's filters, with a general description and fundamental parameters of each. Figures 7.3 and 7.4 show the effective throughput curves, including the filter transmission convolved with the OTA, WFC3 optics and detector response (currently FPA129).

Appendix A provides further details and the individual filter throughput curves.

Table 7.2: WFC3 IR Channel Filters and Grisms

Name[1]	Description	Pivot[2] λ (nm)	Width[3] (nm)	Peak Transmission
	IR Wide-Band (W) Filters			
F105W	Wide *Y*	1048.95	292.30	0.98
F110W	Wide *YJ*	1141.40	503.40	0.99
F125W	Wide *J*	1245.90	301.50	0.98
F140W	Wide *JH* gap; red grism reference	1392.10	399.00	0.99
F160W	Blue-shifted *H*	1540.52	287.88	0.98
	IR Medium-Band (M) Filters			
F098M	Blue grism reference	982.93	169.48	0.97
F127M	H_2O/CH_4 continuum	1273.64	68.79	0.98
F139M	H_2O/CH_4 line	1383.80	64.58	0.98
F153M	H_2O and NH_3	1533.31	68.78	0.98
	IR Narrow-Band (N) Filters			
F126N	[Fe II]	1258.26	11.83	0.90
F128N	Paschen beta	1283.30	13.54	0.94
F130N	Paschen beta continuum	1300.62	13.28	0.96
F132N	Paschen beta (redshifted)	1319.04	13.07	0.91
F164N	[Fe II]	1645.13	17.48	0.93
F167N	[Fe II] continuum	1667.26	17.16	0.93
	IR Grisms (G)			
G102	"Blue" high-resolution grism	(1025)	250	
G141	"Red" low-resolution grism	(1410)	600	

1. See footnote 1 of Table 4 for naming conventions.
2. "Pivot wavelength" is defined as in Table 4.
3. Full width at 50% of peak transmission.

Broad-band Filters

The IR channel's versions of the ground-based J and H filters are F125W and F160W, respectively. The F125W filter has a width somewhat wider than that of a typical J passband used in ground-based cameras. The F160W filter's bandpass has been blue-shifted relative to ground-based H in order to give a better fit to the QE curve of the IR detector. Specifically, the H bandpass has been narrowed to approximately 1400-1700 nm, in order to limit thermal background and to have the

filter define the bandpass on the red side rather than the detector sensitivity cutoff. By contrast, NICMOS H filter (F160W) covers about 1400-1800 nm. This narrowing for WFC3 minimizes photometric errors due to spatial variations in the detector's QE cutoff.

The wide F140W filter covers the gap between the J and H bands that is inaccessible from the ground. F105W has a central wavelength similar to ground-based Y, but is considerably wider. The IR channel also includes a very wide filter, F110W, spanning the ground-based Y and J bands. This filter can be used for deep imaging, with a bandpass fairly similar to that of the corresponding broad-band filter in NICMOS (also called F110W).

Narrow-band Filters

The IR channel includes six narrow-band filters which sample some of the most astrophysically important planetary, stellar, and nebular spectral features in the near-IR (e.g., [Fe II] and Paschen-beta).

Grisms

The IR channel has two grisms which provide slitless spectra. The "blue" G102 grism provides a dispersion of 2.5 nm/pix (or a two-pixel resolving power of ~200) over the 900-1150 nm wavelength range. The "red" G141 grism has a dispersion of 4.7 nm/pix (resolving power of ~140) over the 1080-1700 nm range. In most cases, a grism observation will be accompanied by a direct image, for source identification and wavelength calibration. Recommended filters for this purpose are F098M for the G102 grism, and F140W for G141.

See Chapter 8 for a detailed discussion of slitless spectroscopy with WFC3.

7.4.2 Filter Blue Leaks

All of the IR filters have been constructed using IR-transmitting colored glass with thin-film coatings to achieve the desired bandpasses. As for the UV filter designs, better in-band transmission generally means somewhat less supression of out-of-band transmission. While the final IR filters have excellent in-band transmission (>90%), a few also have a small, narrow peak of transmission between 750-800 nm. With the original IR detector, FPA64, this was not an issue as the device had a CdZnTe substrate that provides a strong blue cutoff (QE ~0% at 800 nm and QE ~40% at 1000 nm). Since the flight filters were manufactured, however, new detectors have been developed which have 50-80% and 60-85% QE at 800 nm and 1000 nm, respectively. Some of the IR filters may therefore have a small amount of blue leak. None of them have significant red leaks.

Methods of reducing the blue leak before launch (e.g., applying detector window coating to provide additional blocking in the problem area while still maintaining excellent inband transmission) are still being investigated [Q: Massimo added a note saying "check if this is still true"] but if ultimately proven unfeasible, table 6.8 provides an estimate of what the blue-leak effect may be. Tabulated is the fraction of flux expected shortward of 900 nm as a function of target spectral type (a flat spectrum

is listed as well); the throughput calculation includes transmission of the filter, the throughputs of the HST OTA and the IR optics, and the QE of the FPA129 detector (which is ~50% and 60% at 800 and 1000 nm, respectively. The filters that have significant in-band transmission below 900 nm (F098M, F105W, and F110W) are not included.

As can be seen from the table, blue leaks in all the wide-band and some of the narrow- and medium-band filters are minimal; however, several filters, notably F126N, F128N, and F153M, will have some blue leak. In this example, which assumes an FPA129-like QE, the blue leak is ~1% for stellar targets hotter than spectral type G5. Plans are being made to quantify and calibrate the effect as thoroughly as possible before launch. In programs that may suffer adverse effects due to the blue leaks, it might prove useful to obtain UVIS images in the F763M filter, which covers the problematic wavelength region (750-800 nm).

Table 7.3: Fraction of flux shortward of 900 nm as a function of stellar type, assuming a detector with improved QE over current flight FPA64; these numbers will be revised after the final IR detector is chosen. [** insert ir.blue leak.tab here]

Filter	Flat	O5	B5	A5	F5	G5	K5	M5	L2

7.4.3 Ghosts

No significant ghosting is present in the IR channel.

Figure 7.3: Integrated system throughput of the WFC3 IR wide band filters. The throughput calculations include the HST OTA, WFC3 IR-channel internal throughput, filter transmittance, and the QE of the FPA129 flight candidate IR detector.

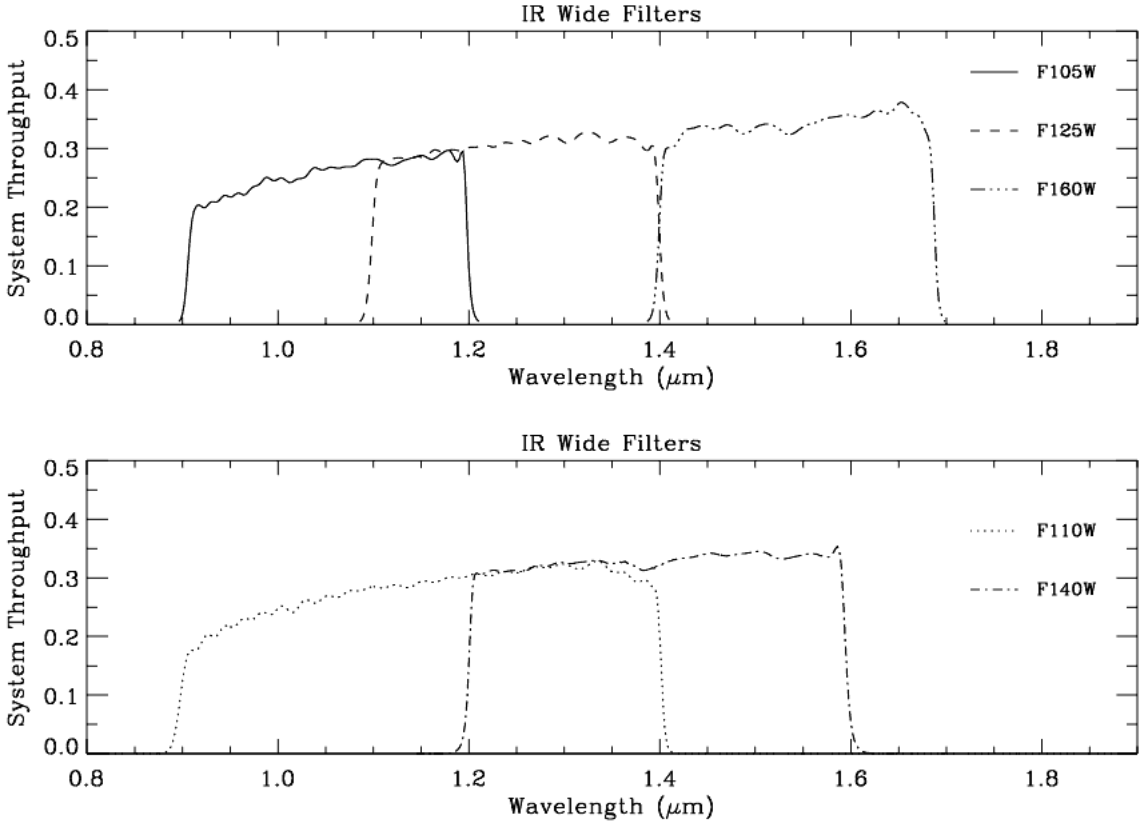

Figure 7.4: Integrated system throughput of the WFC3 IR medium (top panel) and narrow-band (bottom panel) filters. The throughput calculations include the HST OTA, WFC3 IR-channel internal throughput, filter transmittance, and the QE of the FPA129 flight candidate IR detector.

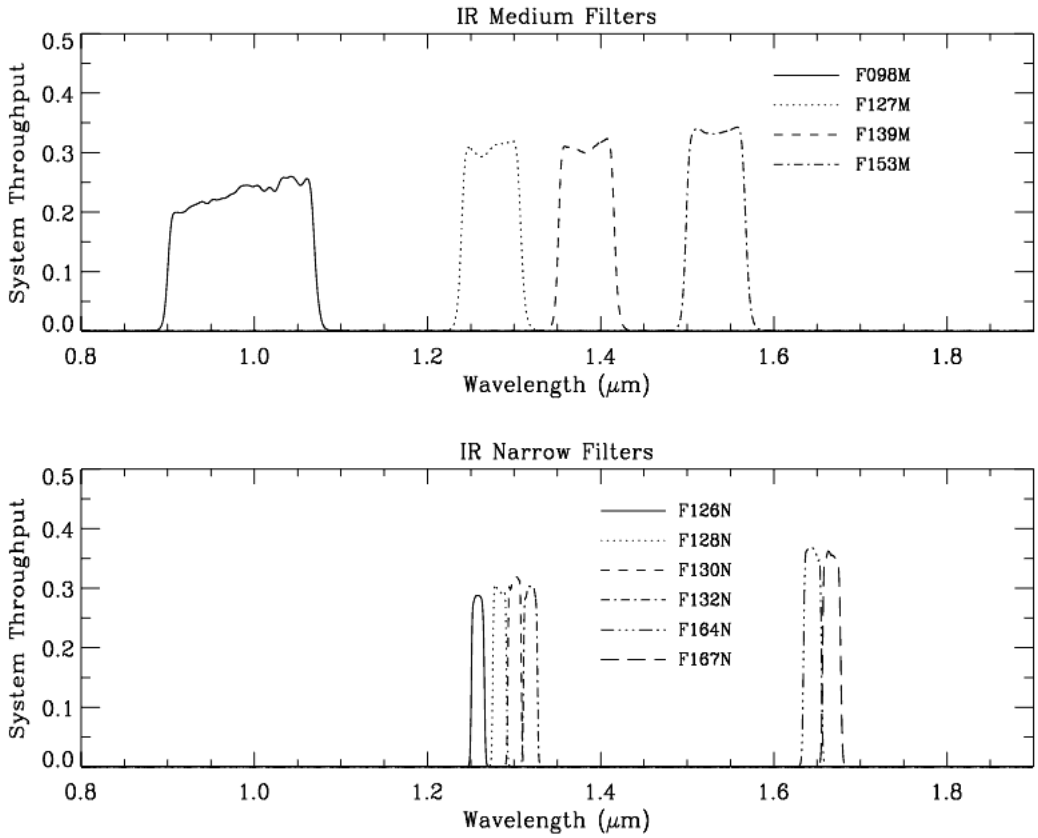

7.5 IR Optical Performance

Q: For this section, I have input from both Massimo and from Sylvia. These need to be combined in the final edit, but for now portions of both versions are present. Also, Sylvia's part includes some material for the UVIS channel mixed in with the IR channel, so this part will have to be moved back to Chapter 6.

Another problem is that Massimo goes into much more detail for the IR channel than Sylvia did for UVIS, e.g., with lots of material about Strehl ratios, sharpness, etc. Should we add such material to the UVIS channel, delete some of it from the IR chapter, or just leave it as it is?- HEB

As noted in Section 6.x, we do not have at this writing any direct observations of the sky using WFC3 installed in HST. However, extensive measurements have been made during ground testing of WFC3, and these indicate excellent optical performance.

The following subsections summarize the expected flight optical performance for the IR channel.

The performance of an imaging system can be characterized by a number of metrics, including the full width at half maximum (FWHM), the Strehl ratio, the encircled energy, the ensquared energy, and various characterizations of sharpness.

The **FWHM** encapsulates in a single value the width of the PSF peak, but it carries no information on the shape of the PSF itself and can therefore be misleading. The original uncorrected PSF of the HST is a classical example in this respect, with an excellent FWHM despite a dramatic amount of spherical aberration.

The **Strehl ratio** measures the normalized peak intensity of the PSF compared to that of an ideal, diffraction-limited PSF. The main advantage of the Strehl ratio is that it has been shown to be proportional to the rms wavefront error via the Marechal approximation, and can therefore be easily estimated theoretically. Measures of the Strehl ratio, on the other hand, are often difficult due to the presence of noise and the determination of the PSF peak in critically sampled data.

The **encircled energy** provides the fraction of light from a point source falling within a given circular aperture. Like the FWHM, it is useful for comparison of well-behaved PSFs, but can be misleading if the PSF is affected by significant problems. Since modern detectors have nominally square pixels, it is often more convenient to evaluate the energy falling within a certain number of pixels (**"ensquared energy"**) instead of the encircled energy, which requires interpolation to account for the fractional pixels intercepted by a circular aperture.

The **sharpness** metrics are a class of functions that reach their maximum value for perfect images (Muller & Buffington 1974, JOSA 64, 1200). The S1 sharpness metric is the normalized sum of the squared image intensity. The sharpness is the reciprocal of the number of pixels contributing background noise (equivalent noise area), and it is therefore a key ingredient for estimating the instrument sensitivity (Mighell 2003, in ASP Conf. Ser., Vol. 295, Astronomical Data Analysis Software and Systems XII, p. 395). It is also simply related to the intensity variance of the image, and therefore to the Strehl ratio and the rms wavefront error.

In this section we will illustrate the various metrics for WFC3-IR, estimated from a theoretical model that includes residual aberration, the mid-frequency wave-front error of the OTA, the effect of the detector inter-pixel cross-talk, charge diffusion blur, and first-order geometric distortion. The model reproduces with high accuracy the PSF observed during the thermal vacuum tests of WFC3.

7.5.1 Theoretical PSF

The theoretical PSF of the IR channel at 1000 nm, assuming the source to be centered at the center of a pixel, is shown in Figure 7.5. The corresponding values for the inner 7×7 pixels, normalized to give a total flux equal to 1, are given in Table 7.4.

Figure 7.5: FIGURE 7.5: model of the WFC3-IR PSF at 1000 nm.

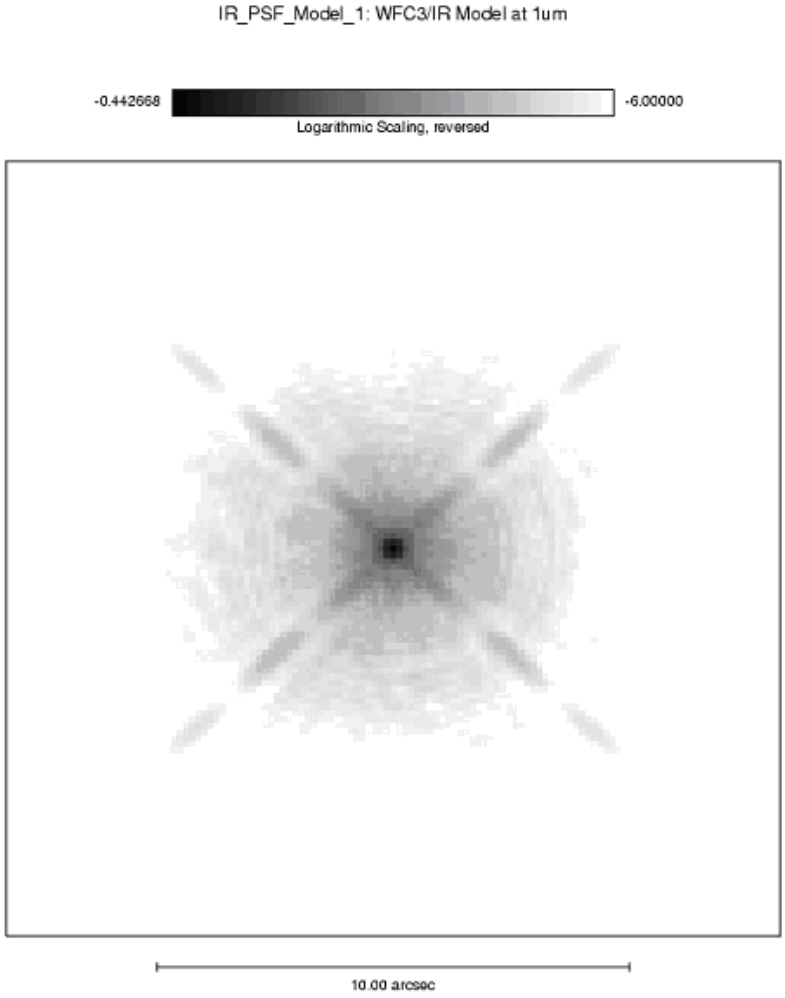

Table 7.4: model PSF of WFC3-IR at 1 micron.

0.001	0.001	0.002	0.001	0.001	0.002	0.001
0.002	0.002	0.004	0.006	0.003	0.002	0.002
0.002	0.004	0.033	0.071	0.033	0.004	0.002
0.002	0.008	0.075	0.361	0.075	0.008	0.002
0.002	0.005	0.037	0.075	0.035	0.004	0.002
0.002	0.002	0.004	0.007	0.004	0.002	0.002
0.001	0.002	0.002	0.002	0.002	0.002	0.001

7.5.2 Encircled Energy

The encircled energy profiles at representative wavelengths are shown in Figure 7.6. The corresponding numerical values are presented in Table 7.5. The ensquared energy, which provides the flux per pixel, is presented in Table 7.6.

Figure 7.6: Encircled Energy for the WFC-IR channel

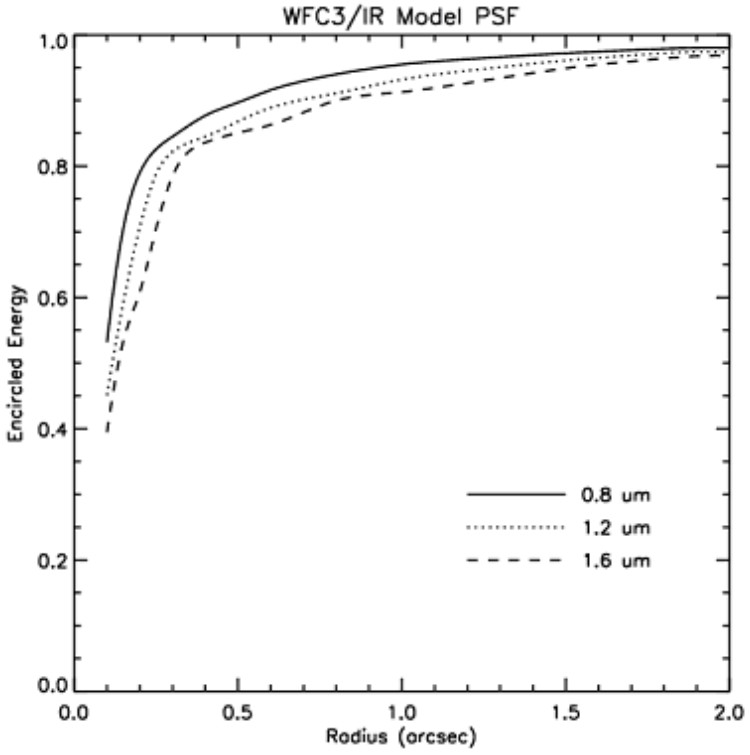

Table 7.5: WFC3/IR PSF Encircled Energy Fraction vs. Aperture Radius (arcsec)

wl(micron)	0.7	0.8	0.9	1.0	1.1	1.2	1.3	1.4	1.5	1.6	1.7
0.10	0.557	0.532	0.508	0.486	0.468	0.451	0.436	0.422	0.410	0.395	0.379
0.15	0.727	0.706	0.677	0.648	0.619	0.593	0.572	0.555	0.545	0.534	0.524
0.20	0.799	0.790	0.775	0.757	0.734	0.707	0.679	0.651	0.630	0.608	0.591
0.25	0.830	0.826	0.819	0.811	0.801	0.788	0.772	0.751	0.731	0.705	0.678
0.30	0.851	0.845	0.838	0.833	0.828	0.822	0.815	0.806	0.800	0.785	0.766
0.40	0.881	0.877	0.869	0.859	0.851	0.845	0.841	0.838	0.840	0.836	0.832
0.50	0.903	0.897	0.890	0.885	0.877	0.868	0.858	0.852	0.854	0.851	0.848
0.60	0.921	0.916	0.906	0.899	0.894	0.889	0.883	0.874	0.870	0.863	0.859
0.80	0.943	0.940	0.933	0.926	0.919	0.911	0.905	0.901	0.904	0.900	0.896
1.00	0.956	0.955	0.949	0.944	0.937	0.932	0.927	0.920	0.918	0.913	0.910
1.50	0.972	0.972	0.970	0.967	0.965	0.961	0.956	0.952	0.953	0.949	0.944
2.00	0.979	0.980	0.979	0.977	0.975	0.973	0.971	0.968	0.972	0.968	0.964

Table 7.6: Table 7.6: WFC3/IR PSF Encircled Energy Fraction vs. Aperture Size (pixels)

wl(micron)	0.7	0.8	0.91.0	1.1	1.2	1.3	1.4	1.5	1.6	1.7	
1	0.410	0.392	0.374	0.358	0.342	0.327	0.312	0.297	0.284	0.269	0.254
2	0.719	0.697	0.670	0.641	0.613	0.588	0.567	0.550	0.539	0.527	0.516
3	0.814	0.809	0.799	0.786	0.771	0.751	0.728	0.702	0.680	0.654	0.631
5	0.874	0.869	0.858	0.850	0.844	0.840	0.835	0.830	0.830	0.825	0.820
7	0.909	0.903	0.895	0.889	0.882	0.872	0.862	0.855	0.857	0.854	0.852
9	0.932	0.928	0.919	0.911	0.905	0.899	0.894	0.888	0.886	0.876	0.868
11	0.947	0.944	0.937	0.930	0.923	0.915	0.911	0.906	0.906	0.902	0.897
13	0.956	0.955	0.950	0.943	0.938	0.932	0.925	0.918	0.920	0.916	0.911
15	0.962	0.963	0.958	0.954	0.948	0.943	0.938	0.932	0.932	0.926	0.922
17	0.966	0.967	0.965	0.961	0.957	0.952	0.947	0.943	0.943	0.939	0.933
19	0.969	0.970	0.969	0.967	0.963	0.959	0.955	0.950	0.952	0.948	0.943
21	0.972	0.973	0.972	0.970	0.968	0.965	0.961	0.958	0.959	0.954	0.951
23	0.975	0.975	0.974	0.972	0.971	0.969	0.966	0.963	0.965	0.961	0.957
25	0.978	0.978	0.976	0.975	0.973	0.972	0.970	0.967	0.969	0.966	0.963
51	0.993	0.994	0.992	0.991	0.990	0.989	0.987	0.986	0.989	0.988	0.987
101	0.998	0.999	0.998	0.998	0.997	0.997	0.996	0.996	0.998	0.998	0.997

========== material below is from Sylvia ==========

Q: Massimo comments: who cares about our requirements?

In the IR channel, point source measurements at 16 field positions and two wavelengths during TV testing show that the imaging performance generally meets the specifications *using the optical stimulus (CASTLE)*; the measured EEs for the IR channel are listed in the last four rows of table 7.7. However, it is likely that the on-orbit image quality may be somewhat worse than that seen on the ground: corrections required to account for differences between the HST OTA versus the CASTLE indicate that the 1600 nm core EE may fall just below the requirement; the 1000 nm core on-orbit EE should still meet the requirement. A sample IR image along with its EE curve and azimuthally-averaged PSF profile is shown in Figure 7.8. The image was taken with the F105W filter near the center of the IR FOV; the measured EEs of 0.56 and 0.73 (within 0.25" and 0.35" diameter apertures, respectively) meet the requirements.

Table 7.7: Encircled energy measurements for the WFC3 UVIS and IR channels, based on ground test TV data. Requirements listed apply to on-orbit data; measured values will require corrections for difference between ground stimulus and the HST OTA (see text for discussion).

Channel	Measured encircled energy		On-orbit EE requirement
	Center of field	Edge of field (avg of four corners)	
UVIS at 250 nm in 0.20 " diam	82.2%	79.4%	>75%
UVIS at 350 nm in 0.20 " diam	80.8%	78.2%	--
UVIS at 633 nm in 0.25 " diam	80.3%	78.6%	>75%
UVIS at 810 nm in 0.25 " diam	74.5%	73.5%	--
IR at 1000 nm in 0.25 " diam	52-56%	--	>56%
IR at 1000 nm in 0.37 " diam	73-77%	--	>72%
IR at 1600 nm in 0.25 " diam	40-44%	--	>48%
IR at 1600 nm in 0.37 " diam	77-91%	--	>75%

7.5.3 IR Encircled Energy

Figure 7.7: Measured encircled energies (left plots) and azimuthally-averaged PSFs (right plots) are shown as solid lines; the optical stimulus and OTA models are shown as dotted and dashed, respectively. Wavelengths covered were 250, 350, 633, and 810 nm (in that order, from top down); point sources were placed in a quadrant center (different quadrant for each wavelength). Diamonds mark the requirements at 250 and 633 nm. (**insert EE plots & azimuthally-avg'd PSFs figures here, in 2-across, 4-down format; individual figures are in psfmods_compare_2212.EE.ps).

Figure 7.8: IR image near field center (left) and encircled energy curve along with azimuthally-average PSF profile (right). [** need to insert ir.image.ps (left) and ir.EE.ps (right)]

An example of the IR PSF is shown in Figure 7.8, along with its encircled energy curve and the azimuthally-averaged PSF. More detailed studies of the IR PSF will be performed during the TV testing planned for 2007.

Figure 7.9: HIgh dynamic range composite WFC3 UVIS PSFs at four wavelengths (250, 350, 633, and 810 nm, first two in the upper row, last two in the bottom row); image stretch is logarithmic (1 to 10^6 e^-). Streaks to the right of the PSF in the 250 and 250 nm images are due to the optical stimulus; there is a slightly warm column at the left edge of the 250 nm images and a blocked column just to the left of the PSF in the 350 nm image. [**insert individual images to form 2x2 mosaic: psf_combine_250_uvn13.image.ps, psf_combine_350_uvn14_e6.image.ps, psf_combine_633_uvn15.image.ps, and psf_combine_810_uvn16.image.ps)

==== end Sylvia ====

7.5.4 PSF Characteristics

FWHM

The FWHM of IR images are generally close to 1 pixel, but increases gradually with wavelength.

Table 7.x presents gives the FWHM as a function of wavelengths.

Q: There should be more explanation of this subsection. Are these all purely theoretical values, or are they measurements? It might be more useful if the table used specific filters, rather than wavelengths. [Massimo says this section comes from George Hartig.]

WFC3/IR PSF FWHM (pixels) vs. wavelength

wl(um):	0.7	0.8	0.9	1.0	1.1	1.2	1.3	1.4	1.5	1.6	1.7
WFHM (pix):	0.997	0.997	0.999	1.009	1.026	1.049	1.079	1.115	1.154 1.199	1.199	1.248

Strehl Ratio

The Strehl ratio, defined as the ratio of the observed-to-perfect peak fluxes of the stellar PSF, is unity when the images are perfectly diffraction-limited. This definition does not take pixelation into account, however. In practice, it is more convenient to compare the energy measured ("ensquared") in the central pixel with that predicted by a model that neglects all aberrations, telescope jitter, and detector effects (other than pixelation). The results for WFC3-IR at various wavelengths are shown in Table 7.7.

In principle, the Strehl ratio should always increase with wavelength, since the optical performance approaches diffraction-limited conditions at longer wavelengths. This is observed in the third row of Table 7.7 at \λ> 1000 nm. The Strehl ratio at shorter wavelengths should flatten out, since there is not much gain once the Airy disk is fully included in the central pixels. In practice, however, the Strehl ratio for WFC3-IR appears to increase below 1000 nm. This is due to a detector effect, the capacitive coupling of adjacent pixels (see Section. 6.X), which causes a general loss of ~15% charge from one pixel to the four adjacent ones. At the shortest wavelengths the first Airy ring approaches the central pixel and refills it with charges, mitigating the loss. This causes a relative increase of the encircled energy.

Table 7.8: Table 7.7Ensquared energy in the central pixel in the ideal and observed cases, and resulting Strehl ratio.

wl(micron)	0.7	0.8	0.9	1	1.1	1.2	1.3	1.4	1.5	1.6	1.7
EE(1pix) ideal	0.57	0.56	0.55	0.54	0.51	0.48	0.45	0.42	0.39	0.36	0.3
EE(1pix) observed	0.41	0.39	0.37	0.36	0.34	0.33	0.31	0.3	0.28	0.27	0.2
Strehl	0.72	0.70	0.63	0.67	0.67	0.68	0.69	0.71	0.72	0.74	0.7

Sharpness

Q: I wonder if the Sharpness subsection can be omitted? I think it's too specialized for a general handbook (but I am not at all an expert in IR imagin!) - HEB. If we retain it, I think the present version is not very clear and needs much improvement. Massimo replies it is the best way to predict the SNR, for both CCD's and IR. Current version includes one round of improvements by Massimo.

Faint sources are generally those observed in read-noise, dark-current, or sky-noise-limited conditions. In such cases, the SNR can be estimated from the expected number of detected photons S from the source, the average effective background count rate B in each pixel, the PSF, and the weights used to average the signal in the pixels affected by the source. It is easy to show (Mighell 2003) that the SNR for optimal weights (which are proportional to the point spread function) is given by:

$$SNR = \frac{S}{\sqrt{B}} \cdot \left(\sum_{i,j} (PSF)_{i,j}^{2}\right)^{1/2} = \frac{S}{\sqrt{B}} \cdot (sharpness)^{-1/2} \qquad (6.5)$$

where sharpness is effectively the reciprocal of the number of pixels contributing background noise. [Q: Massimo added some math to this sentence, which (a) I can't really read clearly, and (b) don't know how to typeset in FrameMaker. Can we avoid math in this sentence?] For WFC3 IR, the summation is tabulated for two representative cases, PSF centered at the center and at the corner of a pixel, in Table 7.8.

Table 7.9: WFC3/IR PSF Sharpness

wl(um):	0.7	0.8	0.9	1.0	1.1	1.2	1.3	1.4	1.5	1.6	1.7
Ctr'd	0.194	0.180	0.167	0.155	0.143	0.132	0.122	0.112	0.104	0.095	0.088
Cornr	0.131	0.124	0.115	0.107	0.099	0.092	0.086	0.081	0.079	0.075	0.072

Temporal Dependence of the PSF: HST Breathing

The WFC3-IR PSF will suffer from small temporal variations induced by the HST breathing. The HST focus position is known to oscillate with a period of one HST orbit. The focus changes are attributed to the contraction/expansion of the OTA due to thermal variations during an orbital period. These short-term focus variations are usually referred to as "OTA breathing," "HST breathing," "focus breathing," or simply "breathing." Breathing affects all data obtained with all instruments onboard HST.

Thermally induced HST focus variations also depend on the thermal history of the telescope. For example, after a telescope slew, the telescope temperature variation exhibits the regular orbital component plus a component associated with the change in telescope attitude. The focus changes due to telescope attitude are complicated functions of Sun angle and telescope roll. More information and models can be found on the "HST Thermal Focus Modeling" at:

http://www.stsci.edu/hst/observatory/focus/thermal.html.

Breathing is expected to produce variations of the WFC3-IR FWHM by ~0.3% at 0.7 micron, and less than 0.1% longer than 1.1 micron, on typical timescales of one orbit.

Intra-pixel Response

The response of a pixel of an IR detector to light from an unresolved source varies with the positioning of the source within the pixel due to low sensitivity at the pixel's edges and dead zones between pixels. For NICMOS, the intra-pixel sensitivity was found to be an important effect as it varies by as much as 30%. This effect has an impact on point sources which depends on the sampling, and therefore, for a given pixel scale, on the wavelength of the diffraction-limited images. Well-dithered exposures will average out this effect, but photometric accuracy for stellar sources with few dither positions can be limited by uncertainties related to intra-pixel response.

For WFC3-IR, the intrapixel response is expected to be significantly better (more uniform) than NICMOS, likely due to the much higher detector temperature which increases the electron mobility. Intra-pixel response has been measured in early phases of WFC3 development on detectors with the substrate on. Measures will be performed at DCL to estimate this effect on more recent substrate removed devices.

Inter-pixel Capacitance

The smaller pixels increase the relevance of capacitive coupling between nearby pixels. This affect not only the gain measures (See Chapter on IR detectors) but also the PSF (see Section 7.3.3).

Q: Massimo wrote that something is missing from the above, but didn't say what.

7.6 IR Exposure and Readout

The general operating modes of IR detectors have been described in Chapter 5.X. In this section we will detail the readout modes implemented in WFC3. Note that changes are still possible since the optimal data-acquisition strategy may depend upon the actual performance of the flight detector.

7.6.1 Exposure Time

Q: check the following paragraph, which I wrote, and re-wrote following Massimo's corrections. I suggest retaining section 7.6.1, to parallel the same section in Chapter 6, and also because Exposure Time is something one enters into APT. - HEB

Q: Actually, I might be wrong...does one enter Exposure Time in APT for IR exposures??

Unlike the UVIS channel, the IR channel does not have a mechanical shutter. Integration times are thus determined purely electronically, by resetting the charge on the detector to zero, and then accumulating signal until the exposure is completed. A second difference from the UVIS channel is that the IR detector can be read out non-destructively as the exposure accumulates, as opposed to the single destructive readout at the end of a CCD exposure.

There is a set of pre-defined accumulation and readout sequences available to IR observers, which are used to set the exposure time as described in the next subsection.

7.6.2 MULTIACCUM Mode

In IR observing it is desirable to sample the signal multiple times as an exposure accumulates, and the MULTIACCUM mode accomplishes this. MULTIACCUM is the only observing mode available for the IR channel.

Multiple readouts offer two major advantages. First, the multiple reads provide a way to record a signal in a pixel before it saturates, thus effectively increasing the dynamic range of the final image. Second, the multiple reads can be analyzed to isolate and remove cosmic-ray events.

The disadvantage of multiple readouts is that they are data-intensive. The HgCdTe detector array is 1024×1024 pixels, which is only about 1/16 of the 4096×4102 pixel size of UVIS images. However, since typically 16 IR readouts are used, the data volume of a single final IR image is generally the same as that of a single UVIS frame. A maximum of 32 IR readouts can be stored in the instrument buffer, after which the content of the buffer must be dumped to the HST Solid State Recorder (SSR). A buffer dump of 16 reads takes about 5.8 minutes.

MULTIACCUM readout consists of the following sequence of events:

1. Array reset: After a fast calibration of the Analog to Digital Converters, all pixels are set to a zero signal (i.e., to the detector bias level), with two rapid reset cycles of the entire chip. Q: is the wording here correct?
2. Array read: The charge in each pixel is measured and stored in the on-board computer's memory. This is done as soon as practical after the second array reset. In effect, given the short delay and the time needed to read the array, a very short-exposure image is stored in memory.
3. Multiple integration-read cycles: The detector integrates for a certain amount of time and then the charge in each pixel is read out. This step can be repeated up to a total of 15 times during the exposure. All frames are individually stored in the on-board computer memory. The readout timing is the same of the very first read, so the very short initial image is effectively subtracted out. Q: I don't quite understand the last sentence...Massimo wrote some more words, but they are still unclear.
4. Return to idle mode: the detector returns in idle mode, where it is continuously flushed in order to prevent the build-up of charge.

All sequences start with the same "reset, read, read" sequence, where the two reads are done as quickly as possible. This is in practice a "double reset read", and was originally implemented because early on the development of the WFC3-IR detectors it was found that the very first read after the reset shows a shading pattern that does not reproduces in the following reads. This anomaly is not present in the flight detector. [need to CHECK on the actual part]

The difference between two reads ("double correlated sampling") is required for capturing the kTC noise, which is the uncertainty on the charge effectively loaded on a capacitance C at a temperature T. The kTC noise is left in the detector by the reset and by definition remains constant throughout the exposure. Subtracting the first reset read from all subsequent reads is the standard way of removing the kTC noise. It is the so-called correlated double sampling (CDS).

Q: preceding 2 paragraphs still a little awkward

7.6.3 MULTIACCUM Timing Sequences

There are 15 pre-defined timing sequences, optimized to cover a wide range of observing situations, available for the IR channel.

As noted in step 3 of the observing sequence described in Section 7.7.1, the maximum number of reads during an exposure is 15, which are collected as the signal ramps up. It is possible to select less than 15 reads, thus cutting short the ramp. However, the timing of the individual reads within any of the 15 sequences cannot be adjusted by the user. This approach has been adopted because of the experience with NICMOS, which indicates that optimal calibration of IR detectors requires a dedicated set of reference files (e.g., dark frames) for each timing pattern.

Q: could you give one or more examples of how the observer would select an exposure time, by adjusting NSAMP?

In summary, a WFC3 IR exposure is fully specified by choosing:

- one of the 15 pre-defined timing sequences, and
- the total number of samples (NSAMP, which must be no more than 15), which effectively determines the total exposure time

The 15 pre-defined timing sequences for the IR channel are the following:

- One **RAPID** sequence: the detector is sampled at the shortest possible time interval.
- Five linear (**SPARS**) sequences: the detector is sampled with uniform time intervals between reads, a so-called "linear sample up the ramp." ("SPARS" is a contraction of the word "sparse.")
- Five log-linear (**STEP**) sequences: the detector is initially sampled with reads spaced logarithmically in time. After a specified time, the sampling then becomes uniform until the last sample;
- Four pseudo-Fowler (**MIF**) sequences, in which the signal is mostly sampled at the beginning and at the end of the ramp (see Fowler & Gatley, 1990, ApJ, 353, L33). Six readouts each are made at the beginning and end of the ramp, with the remaining three uniformly spaced in between. ("MIF" stands for "Multiple Initial and Final.")

All 15 of these sequences refer to readouts of the full 1024×1024 detector array. See Section xx below for the timing sequences available when reading out subsrrays of the full field.

Details of the sequences are in the following paragraphs. The timings of the individual reads are given in Table 7.9

Q: Please explain briefly exactly what the numbers are in Table 7.9. Are the "Sample Times" the TOTAL accumulated exposure time at each step? If so, it doesn't seem to me that "Sample Times" is quite the right wording; it should be something like "Total accumulated exposure" or maybe something shorter. Many of the sequences go up to absurd total times, so I assume that in these cases the NSAMP would always be set to a small number, but there should be some wording to make all of this clearer.

RAPID Sequence

The RAPID sequence provides linear sampling at the fastest possible speed. For the full array, this means one frame every 2.9 seconds, and the entire set of 16 reads completed in less than 44 seconds. The RAPID mode is mainly intended for the

brightest targets. Due to the overheads imposed by buffer dumps (see Chapters xx and 10), observations in this mode done continuously would have low observing efficiency.

SPARS Sequences

The SPARS sequences use evenly spaced time intervals. The five available SPARS sequences are designated SPARS10, SPARS25, SPARS50, SPARS100 and SPARS200, corresponding to sampling intervals of approximately 10, 25, 50, 100, and 200 seconds, respectively.

The SPARS modes can be regarded as the most basic readout modes, and they are applicable to a wide range of target fluxes. They provide flexibility in integration time and are well suited to fill an orbital visibility period with several exposures.

STEP Sequences

The five available logarithmic/linear sequences are STEP25, STEP50, STEP100, STEP200, and STEP400. They begin with logarithmic spacing up to the given number of seconds (e.g., 50 seconds for STEP50), and then continue with linear spacing for the remainder of the sequence.

The STEP mode is intended to provide a more uniform sampling across a wide range of stellar magnitudes, which is especially important for imaging fields containing both faint and bright targets. The faint targets require a long, linearly sampled integration, while the bright targets need to be sampled several times early in the exposure, before they saturate. Thus, the dynamic range of the final image is increased.

Fowler (MIF) Sequences

The four pseudo-Fowler sampling sequences perform six rapid reads at both the beginning and end of each exposure, plus three reads uniformly spaced through the middle of the exposure. The MIF sequences are MIF600, MIF900, MIF1200, and MIF1500. The numbers refer to the delays (in seconds) beteween the first and second groups of reads.

The MIF sequences allow the user to form an average of the initial and final reads (Fowler sampling), forming an image from the difference of these two images. The middle readouts allow for recovery of sources that would saturate at the end of the exposure, and for cosmic-ray removal. Note that these sequences are not useful unless all 16 reads are executed. In theory, Fowler sampling allows reduction of the readout noise by 1/SQRT(n) where n is the number of reads. In practice, the maximum improvement in effective read noise over a single initial and final read may be limited by other source of noise (e.g., 1/f noise)

Q: Fig 7.10 needs some explanatory text to go with it. Also, we need a little more text explaining that NSAMP can be less than 15, and how to decide when to do that.

Q: Larry and I think that Fig 7.10 describes an NSAMP=4 observation, not 5. Are we right???

Figure 7.10: Example of STEP sequence stopped at read nr. 5 (NSAMP=5) (taken from NICMOS handbook).

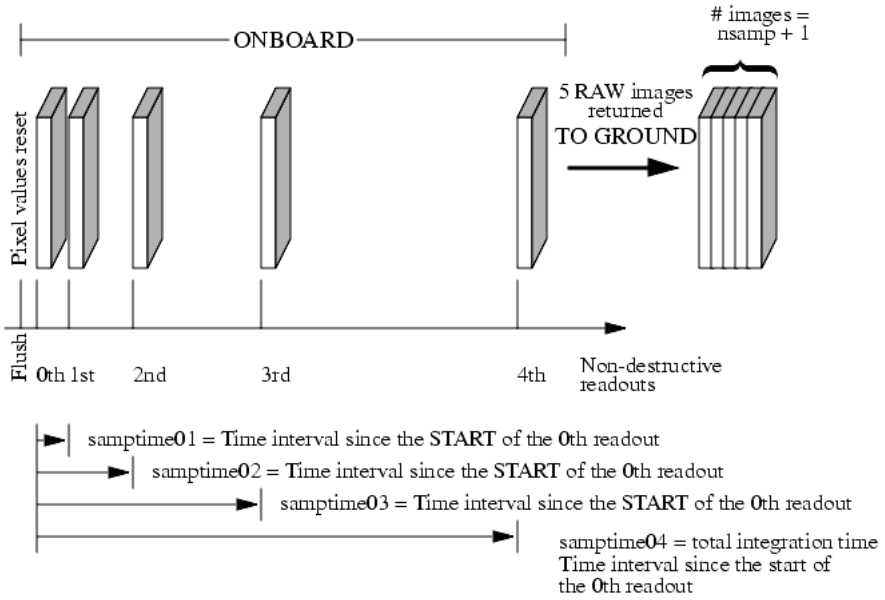

Table 7.10: Table 7.9 Timing of the IR readout modes (1024x1024 Sample Times (sec)

Readout No.	RAPID	SPARS10	SPARS25	SPARS50	SPARS100	SPARS200
0	0.00	0.00	0.00	0.00	0.00	0.00
1	2.93	2.93	2.93	2.93	2.93	2.93
2	5.86	12.93	27.9 3	52.93	102.93	202.93
3	8.79	22.93	52.93	102.93	202.93	402.93
4	11.72	32.93	77.93	152.93	302.93	602.93
5	14.66	42.93	102.93	202.93	402.93	802.93
6	17.59	52.93	127.93	252.93	502.93	1002.93
7	20.52	62.93	152.93	302.93	602.93	1202.93
8	23.45	72.93	177.93	352.93	702.93	1402.93
9	26.39	82.93	202.93	402.93	802.93	1602.93
10	29.32	92.94	227.93	452.93	902.93	1802.93
11	32.25	102.94	252.93	502.93	1002.93	2002.93
12	35.18	112.94	277.93	552.93	1102.93	2202.93
13	38.11	122.94	302.93	602.93	1202.93	2402.93
14	41.05	132.94	327.93	652.93	1302.93	2602.93
15	43.98	142.94	352.93	702.93	1402.93	2802.93

Table 7.11: Table 7.9 Timing of the IR readout modes (1024x1024 Sample Times (sec)

Readout No.	STEP25	STEP50	STEP100	STEP100	STEP200	STEP400
0	0.00	0.00	0.00	0.00	0.00	0.00
1	2.93	2.93	2.93	2.93	2.93	2.93
2	5.86	5.86	5.86	52.93	5.86	5.86
3	8.79	8.79	8.79	102.93	8.79	8.79
4	11.72	11.72	11.72	152.93	11.72	11.72
5	24.22	24.22	24.22	202.93	24.22	24.22
6	49.23	49.23	49.23	252.93	49.23	49.23
7	74.23	99.23	99.23	302.93	99.23	99.23
8	99.23	149.23	99.23	352.93	199.23	199.23
9	124.23	199.23	299.23	402.93	399.23	399.23
10	149.23	249.23	399.23	452.93	599.23	799.23
11	174.23	299.23	499.23	502.93	799.23	1199.23
12	199.23	349.23	599.23	552.93	999.23	1599.23
13	224.23	399.23	699.23	602.93	1199.23	1999.23
14	249.23	449.23	799.23	652.93	1399.23	2399.23
15	274.23	499.23	899.23	702.93	1599.23	2799.23

Table 7.12: Table 7.9 Timing of the IR readout modes (1024x1024 Sample Times (sec)

Readout No.	MIF600	MIF900	MIF1200	MIF1500
0	0.00	0.00	0.00	0.00
1	2.93	2.93	2.93	2.93
2	5.86	5.86	5.86	5.86
3	8.79	8.79	8.79	8.79
4	11.72	11.72	11.72	11.72
5	14.66	14.66	14.66	14.66
6	17.59	17.59	17.59	17.59
7	159.53	234.53	309.53	384.53
8	301.46	451.46	601.46	751.46
9	443.40	668.40	893.40	1118.40
10	585.34	885.34	1185.34	1485.34
11	588.27	888.27	1188.27	1488.27
12	591.20	891.20	1191.20	1491.20
13	594.13	894.13	1194.13	1494.13
14	597.07	897.07	1197.07	1497.06
15	600.00	900.00	1200.00	1500.00

7.6.4 Subarray Timing Sequences

As described in Section xx, it is possible to read out four different sizes of subarrays of the detector, in order to reduce data volume and overhead times. For the subarrays, only the RAPID and SPARS10 sequences will be calibrated by STScI; all of the other MULTIACCUM sequences can be used in principle, but additional calibration observations would have to be made by the observer.

The timings of the sequences are different when subarrays are used. These timings are given in Table 7.10

Table 7.13: TABLE 7.10 a) Readout time for the RAPID sequence in subarray mode

Readout	64x64 Sample Times (sec)	128x128 Sample Times (sec)	256x256 Sample Times (sec)	512x512 Sample Times (sec)
0	0.000000	0.000000	0.000000	0.000000
1	0.060774	0.112705	0.277815	0.853027
2	0.121548	0.225410	0.555630	1.706054
3	0.182322	0.338115	0.833445	2.559081
4	0.243096	0.450820	1.111260	3.412108
5	0.303870	0.563525	1.389075	4.265135
6	0.364644	0.676230	1.666890	5.118162
7	0.425418	0.788935	1.944705	5.971189
8	0.486192	0.901640	2.222520	6.824216
9	0.546966	1.014345	2.500335	7.677243
10	0.607740	1.127050	2.778150	8.530270
11	0.668514	1.239755	3.055965	9.383297
12	0.729288	1.352460	3.333780	10.236324
13	0.790062	1.465165	3.611595	11.089351
14	0.850836	1.577870	3.889410	11.942378
15	0.911610	1.690575	4.167225	12.795405

TABLE 7.10 b) Readout time for the SPARS10 sequence in subarray mode

Readout64x64 Sample Times (sec)	128x128 Sample Times (sec)	256x256 Sample Times (sec)	512x512 Sample Times (sec)	
0	0.00	0.00	0.00	0.00
1	0.060774	0.112705	0.277815	0.853027
2	7.190220	7.294082	7.624302	8.774726
3	14.319666	14.475459	14.970789	16.696425
4	21.449112	21.656836	22.317276	24.618124
5	28.578558	28.838213	29.663763	32.539823
6	35.708004	36.019590	37.010250	40.461522
7	42.837450	43.200967	44.356737	48.383221
8	49.966896	50.382344	51.703224	56.304920
9	57.096342	57.563721	59.049711	64.226619

Readout64x64 Sample Times (sec)	128x128 Sample Times (sec)	256x256 Sample Times (sec)	512x512 Sample Times (sec)	
10	64.225788	64.745098	66.396198	72.148318
11	71.355234	71.926475	73.742685	80.070017
12	78.484680	79.107852	81.089172	87.991716
13	85.614126	86.289229	88.435659	95.913415
14	92.743572	93.470606	95.782146	103.835114
15	99.873018	100.651983	103.128633	111.756813

7.7 IR Sensitivity

7.7.1 Limiting Magnitudes

Table 7.11 presents the predicted limiting-magnitude performance of the WFC3 IR channel and compares it with that of the NIC3 camera. The calculations are based on a 3×3 pixel extraction box on a point source. The limiting ABMAG at a S/N of 10 was calculated for a 1-hour and a 10-hour exposure. The throughput curves for the WFC3 filters listed in column 2 were used; for NIC3, the most similar wide-band filter was used, and its name is given in column 3. The FPA 129 IR detector was assumed for the WFC3/IR calculations.

An online exposure-time calculator (ETC) is available. See Section xx.

Table 7.14: Anticipated limiting-magnitude performance of WFC3 compared with that of NIC3. The table provides limiting ABMAGs at a S/N of 10 for the indicated WFC3 filters and for NIC3 with its most similar filters.

Band	WFC3 Filter	NIC3 Filter	WFC3 limiiting mag in 1 hr	NIC3 limiting mag in 1 hr	WFC3 limiting mag in 10 hr	NIC3 limiting mag in 10 hr
J	F110W	F110W	27.4	26.6	28.7	27.9
H	F160W	F160W	26.7	26.3	28.0	27.6

7.8 Other Considerations for IR Imaging

7.8.1 Gain and Full-well Saturation

Like the UVIS channel, the IR channel uses 16-bit Analog to Digital Converters (ADCs), providing a digital output signal in the range between 0 and 65,535 data numbers (DNs). The default gain setting for the IR channel is 2.5 electrons/DN.

The default gain is compatible with the full-well saturation level of the IR channel, which is about 100,000 electrons (~40,000 DN at the default gain), and with the detector readout noise, of order 25 electrons per correlated double sampling.

7.8.2 Cosmic Rays and Hot Pixels

Cosmic rays affect the image quality. On-orbit measurement of the distribution of cosmic rays on NICMOS shows 1.2 to 1.6 events/second/Camera for 5 events. With a typical hit generating a 5 event in ~2 pixels, this corresponds to 2 to 3 pixels/second/Camera. The physical size of a WFC3 pixels is much smaller than a NICMOS pixel (18micron vs. 40micron size), so the passage of a cosmic ray will presumably affect more pixels. Neglecting crosstalk contamination of nearby pixels and assuming the same thickness of the photosensitive material, the number of affected pixels scales with the linear pixel size. Thus, the 2 to 3 pixel/second of NICMOS correspond to 4-6 pixel/second of WFC3. Taking into account the 3.4 times larger physical area of the WFC3 IR detector (3.39 cm^2 vs. 1.04 cm^2 for NICMOS), we estimate 14-20 pixels affected by cosmic rays per second. For a 2000 second integration, about 3-4% of the pixels will show cosmic ray events, against the 10% of NICMOS. Contamination of nearby pixels will increase the number of affected pixels, whereas the absence of detector substrate may have a beneficial influence. Pending on orbit measures, it seems safe to predict that the level of cosmic ray contamination should not be worse than NICMOS.

As in NICMOS, the use of MULTIACCUM mode makes it possible to filter out cosmic rays since it provides a series of intermediate non-destructive reads. The

intermediate reads are used by the WFC3 data pipeline to identify cosmic ray hits, similarly to what is normally done with the CRSPLITs in CCD observations.

Passages though the South Atlantic Anomaly cause the highest number of cosmic ray hits. The NICMOS operations have been adjusted to minimize the effect of the SAA on instrument performance, and we plan to adopt similar strategies (e.g. continuous flushing the IR detector during the passage) for WFC3-IR.

7.8.3 On-orbit Degradation

As described in Section 6.x, the CCDs in the UVIS channel are subject to gradual degradation in space due to cosmic-ray hits.

Unlike the CCDs minimal cosmic-ray damage to the IR detectors is anticipated. During ground testing using a particle accelerator, the WFC3/IR arrays have been subjected to radiation doses much higher than expected in their entire orbital lifetime, without sustaining any long-term damage or measurable degradation in QE.

7.8.4 Image Persistence

The IR detector is likely to exhibit some image persistence, particularly following observations of targets that saturate to a level of more than 10 to 100 times full well. The specific behavior will depend upon the detector chosen for flight. Measurements on a non-flight device (FPA121) have shown that saturating an extended source results in a dark current initially ~4 σ above nominal, which decays back to nominal levels in ~11-12 minutes.

7.8.5 The IR Background

In space, the dominant sources of background radiation are zodiacal light and earthshine at shorter IR wavelengths, and the telescope thermal emission at longer wavelengths. For HST, the sum of these two background components has a minimum at about 1600 nm (roughly lying in the H band).

The surface brightness of zodiacal light is strongly dependent on the ecliptic latitude and longitude, and reaches a minimum approximately 20 [CHECK] degrees above the anti-Sun direction. Q: I still don't know what is meant by 20 deg above the antisun direction.

Table 7.11 gives low, high and average values of the zodiacal background as seen by HST (for details see Stiavelli 2001, WFC3 ISR 2002-02).

Table 7.15: Table 7.11: Zodiacal backgrounds in flux units and in counts]

Location	erg cm^{-2} s^{-1} $Å^{-1}$ $arcsec^{-2}$		photons (HST area)$^{-1}$ s^{-1} $Å^{-1}$ arcsec-2	
	1.2micron	1.6micron	1.2micron	1.6micron
Minimum	4.90×10^{-19}	2.20×10^{-19}	0.013	0.008
Typical	7.35×10^{-19}	3.31×10^{-19}	0.020	0.012
Average	8.32×10^{-19}	3.86×10^{-19}	0.023	0.014
Maximum	2.15×10^{-18}	9.64×10^{-19}	0.059	0.035

For pointings very close to the bright Earth limb, the zodiacal background may be exceeded by earthshine. The brightness of the earthshine falls very rapidly with increasing angle from the Earth's limb, and for most observations only a few minutes at the beginning and end of the target visibility period will be significantly affected. The major exception to this behavior is a target in the continuous viewing zone (CVZ). Such targets will always be rather close to the Earth's limb, and so will always see an elevated background, even at shorter wavelengths where zodiacal emission ordinarily dominates.

For targets faint enough that the background level is expected to be much brighter than the target, the observer has two options: (1) specify a non-standard Bright Earth Avoidance (BEA) angle, which increases the angle from the Earth's limb from 20 to 25 degrees, or (2) specify the LOW-SKY option, which restricts observations to targets more than 40 degrees away from the Earth's limb and restricts scheduling to times when the zodiacal background is no greater than 30% above the minimum achievable level. The second option decreases the available observing (visibility) time during each orbit and implies scheduling constraints. Both of the options above are available but not supported modes, meaning that the observer must request them through a Contact Scientist during the preparation of the Phase II proposal.

Figure 7.9 illustrates the zodiacal and earthshine background seen by WFC3-IR.

At wavelengths longer than 1600 nm, the background is dominated by the thermal emission of the HST Optical Telescope Assembly (OTA), primarily arising from the telescope's primary and secondary mirrors. The cold stop at the exit pupil of the IR channel effectively masks out telescope spider supports and the central hole of the primary mirror, thus reducing the background level. The WFC3 optics themselves also contributes to the thermal background. The emission of each optical element seen by the detector can be modeled by a blackbody curve at the temperature of that element, modulated by its emissivity. A good approximation (e.g., neglecting scattering, thermal decoupling of dust grains, etc.) is to assume the emissivity equal to one minus the reflectivity or transmissivity of the coating. Thus, by applying in cascade the Kirchhoff law, and taking into account that the total thermal flux results from different paths each one with its own solid angle, it is possible to model the thermal background seen by each pixel.

The thermal background, in fact, depends on the filter on a more subtle way. Whereas within the filter bandpass the background is dominated by the flux reaching the detector, outside the bandpass is the filter itself which contributes with its own background across the entire range of the detector quantum efficiency. For blue and narrow band filters, this contribution is practically a constant, whereas for broad-band red filters it may significantly change and actually may nearly disappear. In Figure 7.9 we have plotted two curves for the background levels: the lower curve is the out-of-band background produced by the filter, the upper curve is the in-band background due to the telescope. The thermal background is thus given by the lower curve except across the filter bandpass, where it jumps to the upper curve (assuming perfect transmission).

Q: I believe the 2 previous paragraphs could be shortened. Massimo replies: This is model. A simple reference to the WFC3 ISR describing the model may suffice. Otherwise it is pretty interesting and new (not in NICMOS, e.g.).

Figure 7.11: Figure 7.9: background flux seen by WFC3-IR. The zodiacal and earthshine contributions are average values (check with TOM). The thermal background is detailed in Section 7.8. The curves do not take into account the filter transmission and the detector quantum efficiency.

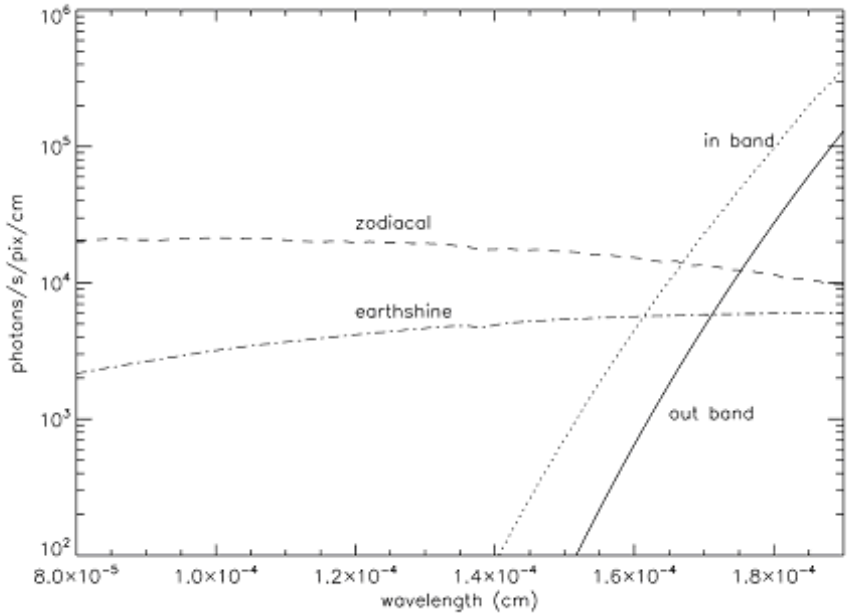

Figure 7.12 shows that the thermal background increases exponentially, since at the temperatures ~250-300K of the optical elements the planckian curve is in the Wien regime. A small increase of long wavelength passband would therefore have a major impact in terms of background. For this reason the WFC3-IR channel has been designed with a cutoff at ~1.7micron.

Table 7.16: Table 7.12: Predicted background levels in e/s/pix for all WFC3-IR filters in units of e/s/pixel.

Filter	thermal	zodiacal	earthshine
F098M	0.036	0.161	0.158
F105W	0.036	0.29	0.278
F110W	0.036	0.503	0.466
F125W	0.036	0.31	0.278
F126N	0.036	0.015	0.013
F127M	0.036	0.072	0.064
F128N	0.036	0.016	0.014
F130N	0.036	0.016	0.014
F132N	0.036	0.016	0.014
F139M	0.036	0.064	0.055
F140W	0.024	0.396	0.341
F153M	0.043	0.066	0.054
F160W	0.103	0.269	0.223
F164N	0.05	0.019	0.015
F167N	0.056	0.019	0.015

7.9 IR Observing Strategies

7.9.1 Dither Strategies

Dithering is used to improve image quality and resolution. By acquiring multiple images of a target at slightly different positions on the detector, one can compensate for detector artifacts (blemishes, hot pixels, and plate-scale irregularities), remove cosmic-ray events, and improve the effective resolution. When improved resolution is the goal, dithering is usually accomplished with sub-pixel offsets; this is especially important for WFC3/IR, because the PSF is undersampled by a factor of 2 at 1600 nm (see Section X). Integral-pixel steps are more convenient when dithering is aimed at removing detector artifacts.

Larger dithers are used for mosaicking, used to cover a region of sky larger than the detector field of view. (Large dithers can also be used for “chopping,” e.g., as used by NICMOS for background sampling; however, no chopping has been implemented for WFC3/IR.) Mosaicking maneuvers are usually much larger than dithering, but mosaicking and dithering are often combined, i.e., using large mosaic shifts to

increase the sky coverage, accompanied by a number of small dithers to increase resolution and remove artifacts.

In WFC3 all these maneuvers are accomplished by moving the telescope (whereas in NICMOS it is possible to move the Field Offset Mirror). Dithers using the same guide stars must be contained within a ~130 arcsec diameter.

Q: could the next 3 paragraphs be replaced with a simple reference to the Phase II Instructions? Massimo answers: YES.

Previous HST imaging instruments have included dithering options in their operations design. Following this strategy, a general-purpose pattern syntax has also been developed for WFC3 to make dither, chop, and mosaic patterns easy to specify. (Q: but you just said that there is no chopping for WFC3) Patterns are specified via a set of parameters: pattern shape, number of points, spacing between adjacent points, pattern orientation, coordinate frame, and whether the target should be placed at the first pattern point or centered relative to the pattern. The coordinate-frame option indicates whether the pattern is being done in the POS TARG frame (using coordinates defined in the POS TARG system for the given instrument) or in the celestial frame (using offsets of the FOV from the original target position on the sky). For dithering, the POS TARG frame is normally used. All images from the pattern are combined in the data-reduction pipeline as an "association."

For each SI, a set of predefined patterns with most of the parameters filled in are provided to observers. The observer defines the set of exposures to be executed at each pattern point. The observer also has the option to bypass the pattern syntax and perform dithering "by hand" using the POS TARG special requirement. This provides more control over the process, but it also means more work. If this option is selected, exposures will not be associated during data reduction and more manual effort will be required in that stage as well.

Details of the predefined WFC3 dither patterns are available in the Phase 2 Proposal Instructions for WFC3, available at http://www.stsci.edu/instruments/wfc3/WOWG/ under the "Ground System Requirements from Integrated Schedule" link. The pattern shapes provided include lines, squares (boxes), and spiral patterns at various orientations.

Above is a wrong link. Where do you really want this to go?

7.9.2 Exposure Strategies

Given the variety of requirements of the scientific programs that will be executed with WFC3/IR, it is impossible to establish a general observing strategy. In this section we will therefore guide the reader through the main constraints that should be taken into account when designing an observation, and provide a few examples.

Let us first summarize the constraints. To attain the ultimate sensitivity one has:

1. to integrate long enough to enter into the background-limited regime (beating down the readout noise).
2. to dither enough so that bad pixels and cosmic-ray impacts can be removed, while maintaining a homogeneous S/N ratio across the field. Q: aren't cosmic rays removed during the multiaccum sequence, rather than by dithering? Massimo answers: only those identified. But, we don't actually say much anywhere in this chapter about the details of CR removal.
3. to split the MULTIACCIUM ramps with as many reads as possible for readout noise suppression.

These constraints put contradictory requirements on the ideal observing strategy. It is clear that, given a certain amount of total observing time, the requirement of long integrations for background limited performance is incompatible with a large number of dithering positions. Also, to split ramps for readout noise suppression decreases the observing efficiency, with a negative impact on the signal to noise ratio. Since the background seen by each pixel depends on the filter (Section 7.x), the optimal compromise needs to be found on a case-by-case basis.

In this regard, it is useful to consider Table 7.13, which summarizes the total background seen by a pixel, including sky, telescope, and nominal dark current, and the time needed to reach 400 e/pixel of accumulated signal, corresponding to 20 e/pixel of background noise. This last value, higher than the expected readout noise of ~15 electrons after 16 reads, is used here to set the threshold for background-limited performance. The passage from readout-limited performance to background-limited performance can be regarded as the optimal exposure time for that given filter, in the sense that it allows for the largest number of dithered images without loss of S/N ratio (for a given total exposure time, i.e., neglecting overheads). For faint sources, the optimal integration time strongly depends on the background (zodiacal, thermal, and dark current) in each filter, ranging from just 360 s for the F110W filter to 2400 s for some of the narrow-band filters.

Table 7.13. Background (e/pix/s) seen by the WFC3-IR detector. The columns show, from left to right: a) filter name; b) thermal background; c) zodiacal background; d) earthshine background; e) dark current; f) total backaground; g) integration time needed to reach background limited performance, set at an equivalent readout noise of 20electrons.

Table 7.17:

filter	thermal	zodiacal	earthshine	DC	Tota	IOpt. IT (s)
F098M	0.036	0.161	0.158	0.1	0.455	879
F105W	0.036	0.29	0.278	0.1	0.704	568
F110W	0.036	0.503	0.466	0.1	1.105	362
F125W	0.036	0.31	0.278	0.1	0.724	552
F126N	0.036	0.015	0.013	0.1	0.164	2439
F127M	0.036	0.072	0.064	0.1	0.27	21471
F128N	0.036	0.016	0.014	0.1	0.166	2410
F130N	0.036	0.016	0.014	0.1	0.166	2410
F132N	0.036	0.016	0.014	0.1	0.166	2410
F139M	0.036	0.064	0.055	0.1	0.255	1569
F140W	0.024	0.396	0.341	0.1	0.861	465
F153M	0.043	0.066	0.054	0.1	0.263	1521
F160W	0.103	0.269	0.223	0.1	0.695	576
F164N	0.05	0.019	0.015	0.1	0.184	2174
F167N	0.056	0.019	0.015	0.1	0.19	2105

The optimal integration time shown in Table 7.13 can be compared with the total integration time of the sampling sequences, reported in Table 7.14 for the full array. Table 7.15 synthesizes the results, showing for each filter which ramp of the different types (SPARS, STEP, MIF) most closely matches the optimal integration times. These ramps may be considered as the recommended readout pattern for a given integration time.

Table 7.18: Table 7.14. Total duration of the WFC3-IR sequences for full array mode.

Sequence Name	total time (s)
RAPID	44
SPARS10	110
SPARS25	330
SPARS50	680
SPARS100	1380
SPARS200	2780
STEP25	256
STEP50	480
STEP100	880
STEP200	1580
STEP400	2780
MIF600	580
MIF900	880
MIF1200	1180
MIF1500	1480

The final selection of the ramp to be used must take into account the science goals. SPARS ramps, with their uniform sampling, maintain the detector in the most steady thermal condition, provide the most robust rejection of cosmic-ray events, and can be trimmed by removing a few of the final reads to fine-tune the integration time with little degradation of the achieved readout noise. They may therefore be regarded as the standard sampling mode. STEP ramps are preferable for a high-dynamic-range scene, e.g., for photometry of a stellar clusters. MIF ramps have the multiple reads clustered at the extremes of the integration time. These ramps provide for the ultimate reduction of the readout noise through multiple sampling, and are therefore ideal for faint targets. On the other hand, they cannot be effectively trimmed to adjust the integration time and provide marginal capability of recovering cosmic-ray events, since the linear fit to the accumulated signal before and after a cosmic-ray impact must rely on single measures taken in the middle of the exposure. MIFS ramps are therefore well suited for programs with multiple exposures and several dithered pointings, like deep surveys of extragalactic fields.

Table 7.19: Table 7.15. Optimal exposure time for each WFC3-IR filter and sequences that most closely match it with 16 read.

filter	Opt. IT (s)	SPARS	STEP	MIF
F110W	362	SPARS25	STEP25	MIF600
F140W	465	SPARS25	STEP50	MIF600
F125W	552	SPARS50	STEP50	MIF600
F105W	568	SPARS50	STEP50	MIF600
F160W	576	SPARS50	STEP50	MIF600
F098M	879	SPARS50	STEP100	MIF900
F127M	1471	SPARS100	STEP200	MIF1500
F153M	1521	SPARS100	STEP200	MIF1500
F139M	1569	SPARS100	STEP200	MIF1500
F167N	2105	SPARS200	STEP200	MIF1500
F164N	2174	SPARS200	STEP200	MIF1500
F128N	2410	SPARS200	STEP400	MIF1500
F130N	2410	SPARS200	STEP400	MIF1500
F132N	2410	SPARS200	STEP400	MIF1500
F126N	2439	SPARS200	STEP400	MIF1500

CHAPTER 8:

Slitless Spectroscopy with WFC3

In this chapter . . .

8.1 Overview

WFC3 provides the capability of slitless spectroscopy in both of its channels. The UVIS channel has a single grism and the IR channel two grisms, which enable low-resolution slitless spectroscopy over the entire field of view of the respective detectors.

In the UVIS channel, the G280 grism allows spectroscopy over a useful wavelength range of 2000-4000 Å, at a dispersion of about 14 Å per pixel in first order. Above 4000 Å the sensitivity is lower, and there may be overlap from second-order light from above 2000 Å.

The two grisms for the IR channel cover the wavelength ranges 800-1100 nm (G102), and 1100 nm to the detector sensitivity cutoff at 1700 nm (G141). The dispersions are 2.2 and 4.1 nm per pixel, respectively. Table 8.1 summarizes the capabilities of the three WFC3 grisms in first-order mode. The two-pixel resolving power is listed for each grism at a wavelength near the center of its range of coverage. The dispersion differs slightly between the two chips of the UVIS channel, and the mean value is listed. The tilt of the dispersion direction relative to the detector X axis is also listed.

Table 8.1: Optical Parameters of WFC3 Dispersers

Grism	Channel	Wavelength range (A)	Resolving Power*	Dispersion (A/pixel)	Tilt (deg)**
G280	UVIS	2000-4000	104 @ 3000 A	14	-3
G102	IR	8000-11500	230 @ 10000 A	22	9
G141	IR	11000-17000	170 @ 14000 A	41	9

* Resolving power is defined as the wavelength divided by the 2-pixel resolution of the spectra.
** Tilt of dispersion direction with respect to the positive X-axis of the data frame.

8.2 Slitless Spectroscopy with the UVIS G280 Grism

The G280 grism is a WF/PC1 spare. Figure 8.1 shows a spectrum of a continuum lamp taken during ground testing of WFC3. The circled spot shows the location of a direct image of the source obtained with a separate (undispersed) F300W filter exposure, but superposed on the grism image for illustrative purposes only. The prominent star-like feature near the center of the picture is the zeroth-order grism image, and the +1st and -1st orders extend towards the left and right of the zeroth order, respectively. The +1st order is defined to be the order with the higher throughput (due to the grating blaze), even though it lies to lower X pixels than the position of the zeroth order.

There are several features of this grism which differ, for example, from the G800L grism on ACS. There is an offset of about 170 pixels in the Y direction between the direct image and the spectra, the zeroth order is relatively bright due to a lower grating efficiency, and there is curvature of the spectra at the blue ends of the first orders (nearest the zeroth order). The curvature of the spectra can be fitted well by a fourth-order polynomial, and the amplitude of the trace distortion is about four pixels in the detector Y direction.

The dispersion has been measured during ground calibration and is well fitted by a linear function with values of 14.1 and 15.7 Å per pixel in the +1st and -1st orders, respectively. The dispersion per pixel in the higher orders is higher by the approximate ratio of the orders; for example, in +3rd order it is 4.8 Å per pixel. These values were determined for UVIS Chip 1, and slight differences can be expected for Chip 2. Figure 8.2 plots the flux in orders -4 to +4 relative to the total flux in all orders, as a function of wavelength. Figure 8.3 shows the absolute throughput for the +1st order, including the OTA, instrument, and CCD detector. Thus the +1st order is more sensitive than the zeroth order at wavelengths less 3200 Å, but at 5000 Å the zeroth order has about three times more flux than the sum of all the other orders. On very deep exposures, orders out to -8 and +8 have been detected. The distortion of the spectral traces and the dispersion solution for at least the first few positive and negative orders will be calibrated to allow determination of absolute wavelengths to better than one pixel. The

G280 grism will also be calibrated in sensitivity, allowing the determination of absolute fluxes to better than about 10% accuracy.

First-order spectra longward of 4000 Å are likely to be overlapped by second-order light longward of 2000 Å, for sufficiently hot sources.

Operationally, a grism exposure should always be accompanied by a direct image taken at the same guide-star pointing. This direct image enables the zero-point of the wavelength scale, and the size of the dispersed target, to be determined; the latter enables the size of the software extraction slit to be tuned to the object size. For slitless spectra, since the object takes the place of the slit in a conventional spectrograph, the spectral resolution is dependent on the object size, being lower for larger objects. The "natural" choice of a direct-imaging filter to provide the reference image for a grism exposure is F300X, since its response matches most closely the +1st-order grism response. However for fainter objects, or those with an unknown spectrum, the broader F200LP filter may be preferable.

For sufficiently bright objects, the multiple spectral orders may extend across the full field of view of the camera. This will lead to overlapping of fainter spectra in the vicinity of the bright-object spectrum. Therefore, a careful determination of the optimum telescope roll angle is required if one wants to obtain non-overlapped spectra of faint objects in the vicinity of much brighter objects.

8.3 Slitless Spectroscopy with the IR G102 and G141 Grisms

At this writing, new IR grisms have been manufactured and installed, in order to correct a focus problem that was encountered with the first set of flight-candidate IR grisms. Although the rulings of the new grisms are identical to those of the old ones, no actual tests of these new grisms have as yet been conducted. The following discussion thus reflects the expected performance of the IR grisms, pending further laboratory and on-orbit verification.

8.3.1 IR G102

The G102 grating provides first-order spectra over the wavelength range from the detector short-wavelength cut-off at about 800 nm up to 1300 nm. [Q: the detector cutoff is no longer at 0.8 micron.] The dispersion is high enough that only the positive and negative first-order spectra, as well as the zeroth-order image, are visible on the detector when the target is centered in the field of view.

Figure 8.4 shows the disposition of the zeroth-order image and +1st-order spectrum (which has much higher sensitivity than the -1st order due to the grating blaze) for the old G102 grism. The circled point shows the location of the object (superposed from an F105W undispersed exposure). The trace of the first-order spectra is well described by a first-order polynomial. The tilt of the spectrum of 9

degrees with respect to the detector X axis is expected to be reduced with the installation of the new IR grism. The sensitivity in the zeroth order is much lower than for the +1st order, and is shown in Figure 8.5 as a function of wavelength. The absolute throughput as a function of wavelength in +1st order is shown in Figure 8.6.

Suitable filters for the accompanying direct images for source selection and wavelength zero-point determination are F098M or F105W.

8.3.2 IR G141

For the lower-dispersion G141 grism, the zeroth-, first-, second-, and third-order spectra all lie within the field of view when the target is centered. Figure 8.7 shows the appearance of the spectra on the detector, with the superposed direct image circled, for the old G141 grism. The measured spectral range is from 980 nm to the detector's long-wavelength cutoff at 1700 nm. Over most of the spectral range more than 80% of the throughput is in the +1st-order spectrum. The dispersion in +1st order varies over the field by about ±4% for the superseded flight grism; this variation will be calibrated from ground and in-orbit data to allow absolute wavelength calibration to better than one pixel. The relative throughput of the various orders is shown in Figure 8.8; the first order is the most efficient. The absolute throughput of the G141 +1st-order spectrum, including all optical elements and detector is shown in Figure 8.9.

The usual filter recommended for the accompanying direct image is F140W, although F160W could be used for extremely red sources.

8.4 Sensitivities and Exposure-Time Estimation

Table 8.2 lists current estimates of the detection limits for slitless spectroscopy with the UVIS and IR modes. The numbers in the table are the V magnitudes of sources for which a 1-hour exposure will yield a 5-sigma detection of the spectrum. V magnitudes are given for three different assumed source spectral types.

QUESTION: define more carefully what 5-sigma detection means. Is it a S/N of 5 for a 2-pixel resolution element, or per single pixel, or what? Does it assume the spectrum is one pixel high (perpendicular to the dispersion)?

Table 8.2: V band detection limits for the WFC3 grism modes for 1 hour exposure and 5-sigma detection

Mode	Spectral Type			Wavelength (A)
	O5 V	A0 V (Vega)	G2 V	
UVIS/G 280	nn	nn	nn	2500
IR/G102	mm	mm	mm	10500
IR/G141	rr	rr	rr	15500

[Values TBD]

For more accurate estimations of exposure times, observers should use the WFC3 Exposure Time Calculator (ETC). The ETC supports all three spectroscopic modes. It should be noted that the current pre-launch version employs estimated dispersion solutions and sensitivities based on component throughputs provided by the manufacturers or from integrated ground tests only. The data in Table 8.2 were derived from these measurements. [Q: is this description of the ETC correct?]

For more detailed simulations of WFC3 spectra, an image-spectral simulator, will also be available. This tool will allow synthetic target fields to be constructed and dispersed images from spectrum templates to be formed.

For more detailed simulations of WFC3 slitless data, a simulator will also be available which can generate 2-dimensional images (dispersed as well as direct) of synthetic target fields. The simulator package will be available three months prior to the proposal deadline and available via a web interface (reduced functionality) and as a stand-alone IRAF package (full functionality).

8.5 Extraction and Calibration of Spectra

Since there is no slit in the WFC3 grism mode, the PSF of the target determines the spectral resolution. In the case of non-stellar sources it is the extension of the target in the direction of dispersion that limits the spectral resolution. Based on the extent of the direct image, the size of the software extraction slit can be set.

The dispersion of the grisms will be well characterized, but in order to set the wavelength zero-point, it is necessary to know the position of the target in the direct image. The zeroth order will generally be too weak in a dispersed image to allow the wavelength zero point to be set reliably. Given the typical spacecraft jitter, wavelength zero-points to +/-1 pixel should be routinely achievable using a direct image taken just before or after the grism image.

An extraction software package, called aXe, is available to extract, wavelength calibrate, flat field, and flux calibrate WFC3 grism spectra. Full details can be found

at: http://www.stecf.org/instruments/ACSgrism/axe/ The package is also available in STSDAS.

Q: In Fig 8.2 and similar plots, it is not very clear what is plotted. What does flux/flux(total) mean?

Figure 8.1:

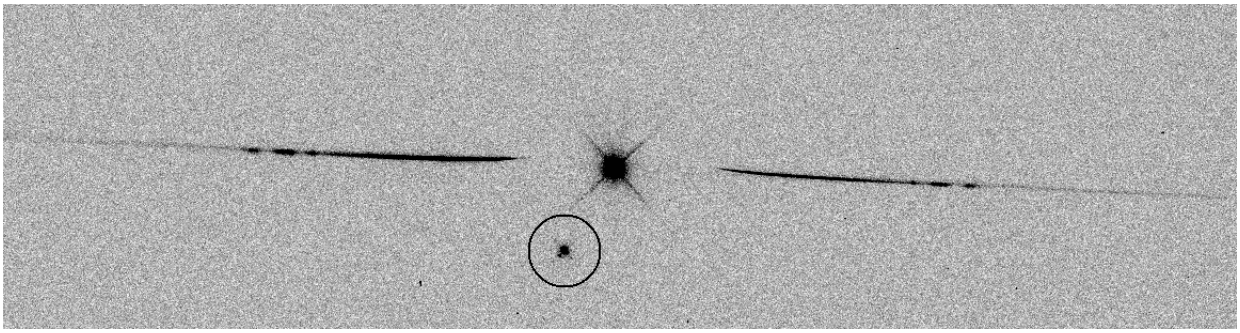

1. G280_F300.gif The appearance of the G280 spectral orders on the detector. The circled source is the position of the direct image formed by summing an F300W image with the grism image. The stronger first order is to the left and the zeroth order is in the center.

Figure 8.2:

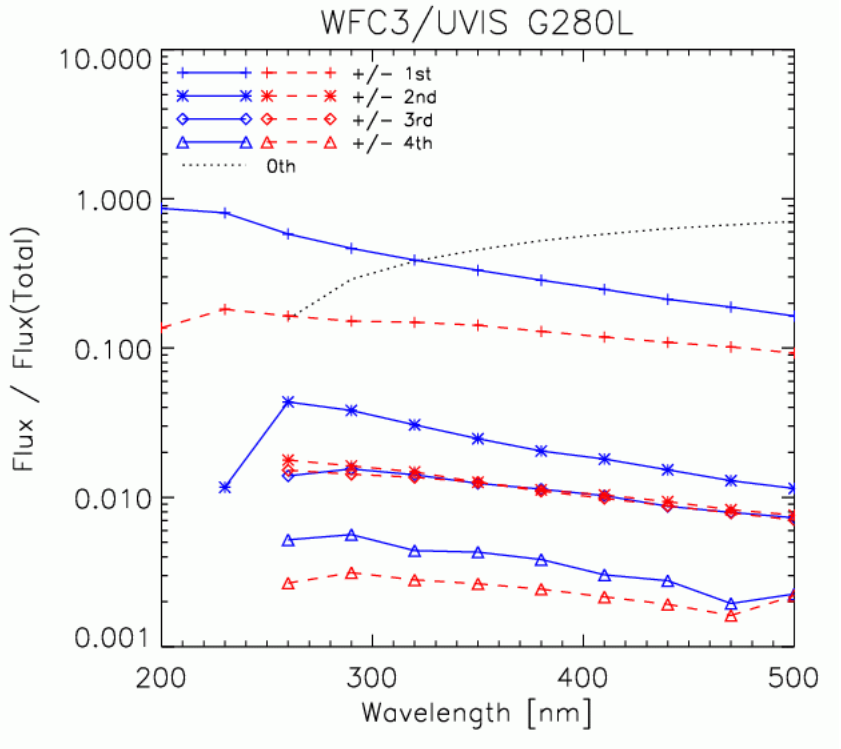

2. ofluxG280.gif The relative flux measured in the different orders for the G280 grism as a function of wavelength. Positive and negative orders are shown with solid blue and dashed red lines, respectively,

Figure 8.3: Susan, please replace this figure with wfc3_UV_G280.gif

3. wfc3_UV_G280.gif The absolute throughput of the G280L grism +1st order, as a function of wavelength, is shown.

Figure 8.4:

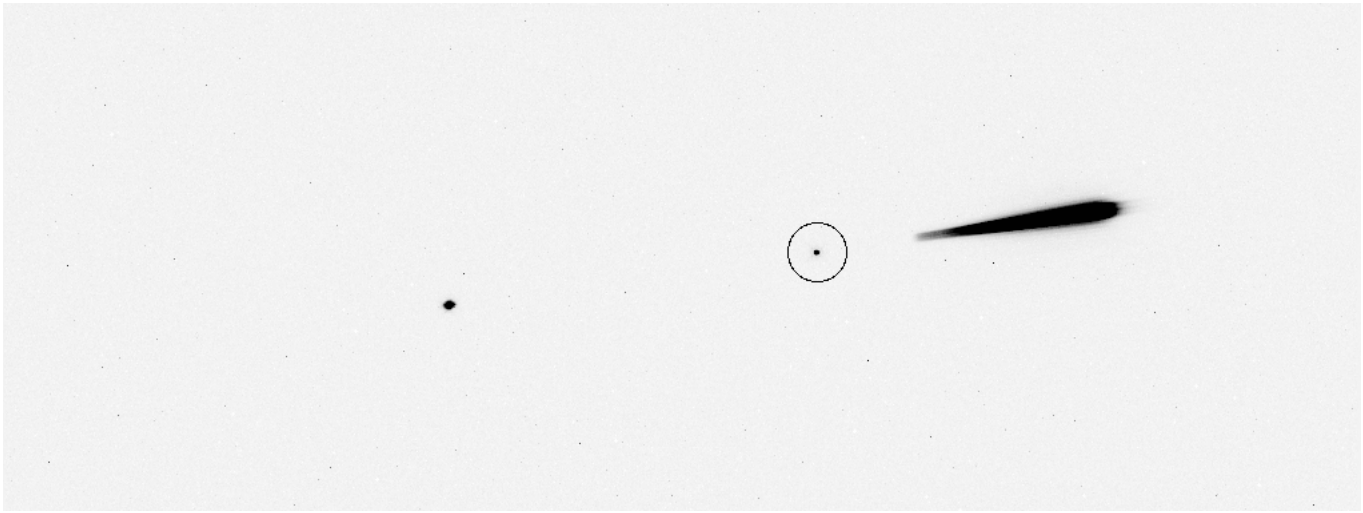

4. G102_sum.gif A G102 grism image is shown superposed with an F105W direct image (circled) to illustrate the relative positioning. The slight dispersion of the zeroth order, to the left, is

visible.

Figure 8.5:

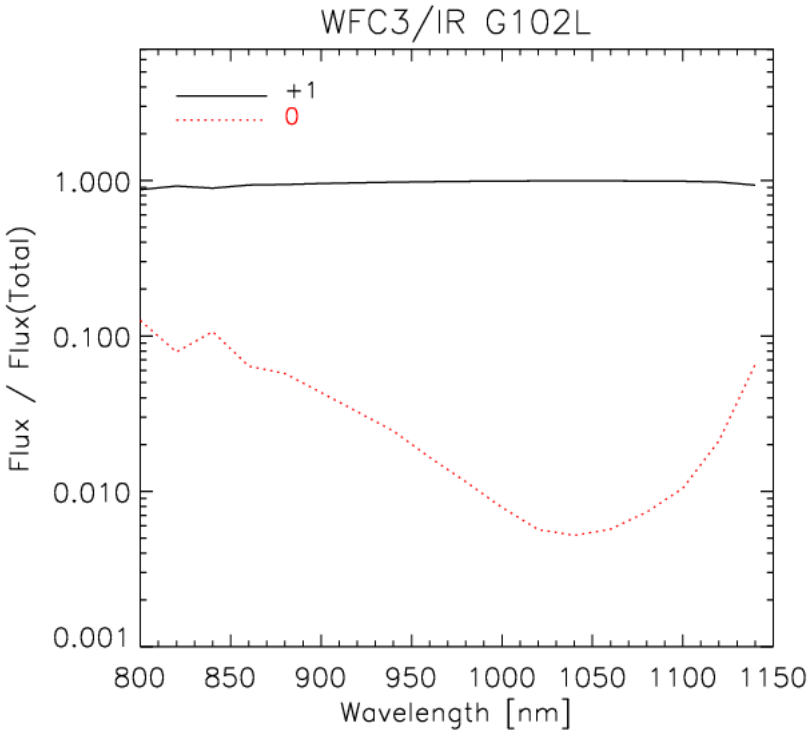

5. ofluxG102.gif The relative throughput of the zeroth and +1st orders for grism G102 are shown as a function of wavelength.

Figure 8.6:

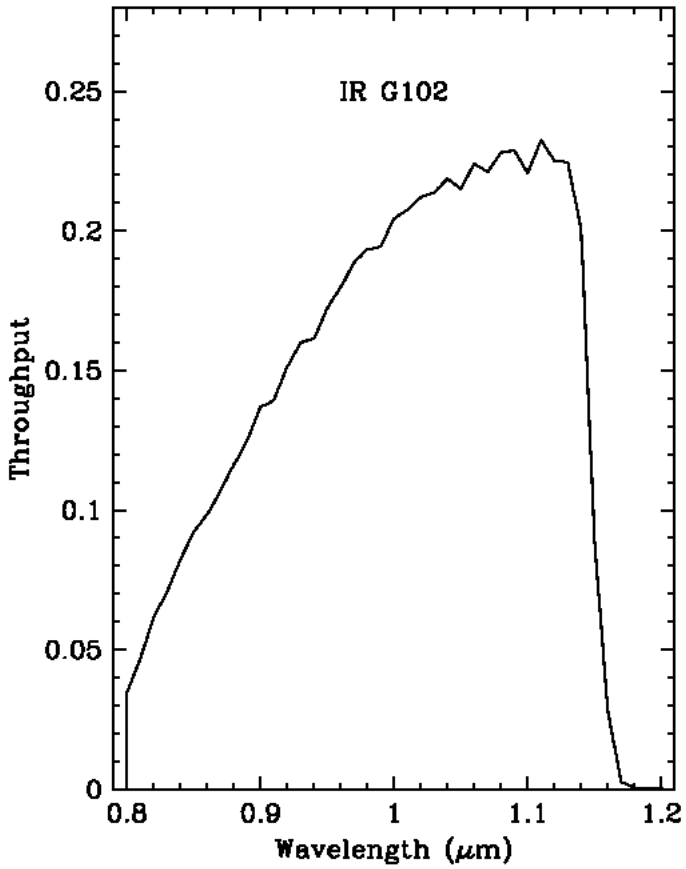

6. G102_thru.gif The absolute throughput of the G102 +1st order spectrum as a function of wavelength is shown.

Figure 8.7:

7. g141_sum_better_col.gif A G141 grism image superposed with an F139M direct image (circled) is shown. The +2nd order can be seen to the far right and the -1st order; the zeroth order is near the center of the figure.

Figure 8.8:

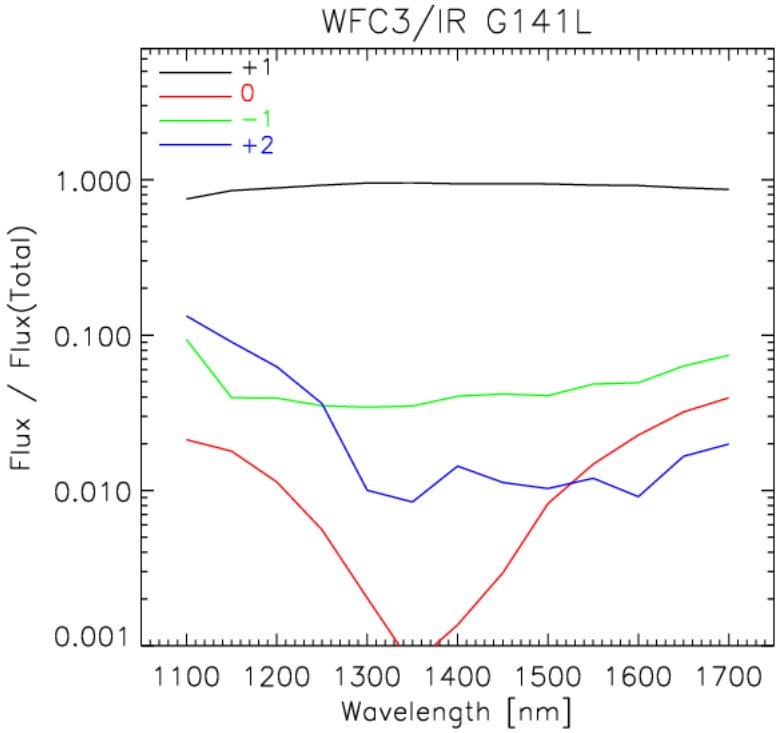

8. ofluxG141.gif The relative throughput of the zeroth, +1st order (the strongest), the -1st and +2nd orders for grism G141 are shown as a function of wavelength

Figure 8.9:

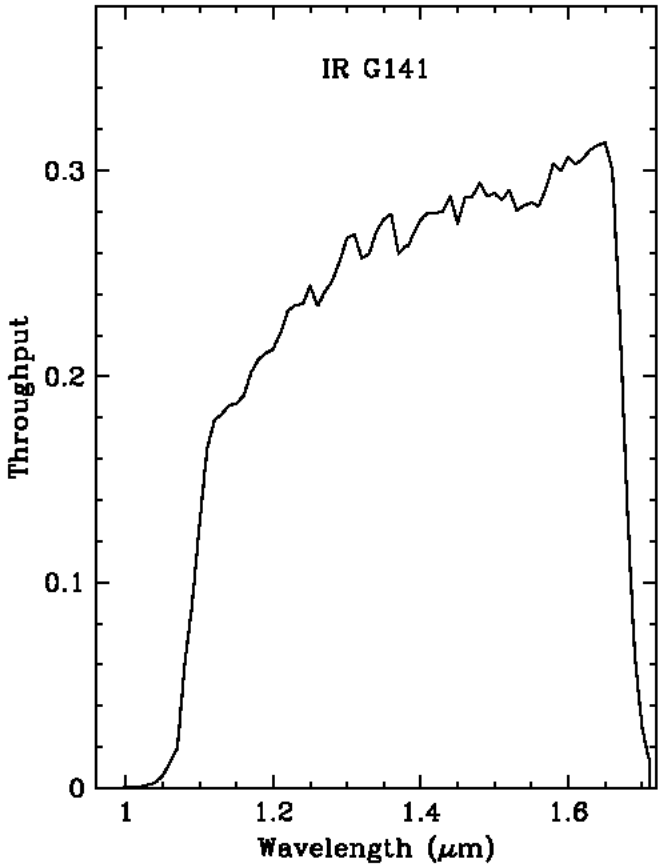

9. G141_thru.gif The absolute throughput of the G141 +1st order spectrum is shown as a function of wavelength.

CHAPTER 9:

WFC3 Exposure-Time Estimation

In this chapter . . .

9.1 Overview

Chapter 4 of this Handbook describes the procedures for designing a Phase I WFC3 observing proposal. Two of the steps involved in this process are estimating the exposure times needed to achieve your scientific goals, and then combining these individual exposures with their associated overheads to derive the number of spacecraft orbits that you will request in your Phase I proposal.

This chapter gives guidance on estimating exposure times. The following chapter, Chapter 10, then describes how to include the various overheads so as to determine the total number of spacecraft orbits needed for your program.

You should also refer to the *Phase I Call for Proposals,* which includes information on policies and practices with respect to orbit-time requests. The *HST Primer* provides specific advice on orbit determination. Below, we provide a summary of the WFC3 sensitivities and give several examples that illustrate how to calculate your exposure times for Phase I Proposals.

9.2 The WFC3 Exposure-Time Calculator (ETC)

In most cases, you will find it convenient to use the online WFC3 Exposure-Time Calculator (ETC) to make estimates of the required exposure times for your project. The ETC is available at the WFC3 home page:

http://www.stsci.edu/hst/wfc3

The ETC calculates count rates for given source and background parameters. Once these are entered, the ETC then outputs signal-to-noise (S/N) ratios achieved for a given exposure time, or the exposure times required to achieve a given S/N ratio. The ETC supports both direct-imaging and spectroscopic (grism) observations. A variety of extraction apertures may be assumed, both circular and square, allowing the user to select either a radius in arcseconds or a size in pixels. It is possible to input a calibrated spectral-energy distribution of your source directly to the ETC. The ETC also outputs peak per-pixel count rates and total count rates to aid in feasibility assessment. Warnings will appear if the source will saturate the detector, which would not only compromise CCD and IR observations, but might even affect subsequent exposures with the IR channel (see Appendix D for further information). The ETC has extensive online help for its execution and interpretation of results.

It is also possible to use ***synphot*** in STSDAS to calculate count rates and the wavelength distribution of detected counts.

The remaining sections of this chapter give detailed information on the sensitivities of the UVIS and IR channels when combined with spectral element, and the use of this information in the determination of count rates, for those who wish to understand the subject in depth.

9.3 Sensitivity Data

In this section, formulae appropriate for WFC3's imaging and spectroscopic modes are provided, from which one can calculate the expected count rates and the S/N ratio achieved in a given exposure time, based on the spectral energy distribution of a source. The formulae are given in terms of sensitivities, but we also provide transformation equations between throughput (QT) and sensitivity (S) for imaging and spectroscopic modes.

Throughputs are presented in graphical form as a function of wavelength for each of the imaging filters and grisms in Appendix A. Given the source characteristics and the sensitivity of the WFC3 configuration, calculating the expected count rate over a given number of pixels is straightforward. The additional information required is the encircled energy fraction (ε_f) in the peak pixel, the plate scale, and (for the spectroscpic modes) the dispersions of the grisms.

The sensitivity information is summarized in table 9.1 and Table 9.2. In these two tables, and in the following discussion, the filter transmission functions are denoted $T(\lambda)$, and the overall system response function (apart from the filter transmission) is denoted $Q(\lambda)$. The terms "counts" and "count rates" always refer to the number of detected *electrons* (which is converted to data numbers, or DN, according to the gain factors for the detectors, as discussed in sections xx and yy; the gain is always 1.5

e^-/DN for the UVIS channel and 2.5 e^-/DN for the IR channel). At present, the tables are based on measured detector sensitivities for the flight-candidate detectors UVIS-1 and FPA 129, and will be updated later when the final flight detectors are chosen.

In Table 9.1 and Table 9.2, the following quantities are listed:

1. The filter or grism designation.
2. The "pivot wavelength" for that filter or grism, λp. Pivot wavelength is a source-independent measure of the characteristic wavelength of a bandpass, defined such that it is the same if the input spectrum is given in units of F_λ or F_ν (see A. Tokunaga & W. Vacca 2006, PASP, 117, 421):

$$\lambda_p = \sqrt{\frac{\int Q(\lambda)T(\lambda)\lambda d\lambda}{\int Q(\lambda)T(\lambda)d\lambda/\lambda}}$$

3. The integral $\int Q_\lambda T_\lambda \, d\lambda/\lambda$, used to determine the count rate when given the astronomical magnitude of the source.
4. The ABmag zero point, defined as the AB magnitude of a source with a flat F_ν that yields 1 count s^{-1} with the specified configuration.
5. The sensitivity integral, $\int S_\lambda \, d\lambda$, defined (see section 9.4) as the count rate that would be detected from a flat F_λ source with a flux of 1 erg cm^{-2} s^{-1} $Å^{-1}$.
6. The encircled energy, defined as the fraction of PSF flux enclosed in the default photometry aperture (5×5 pixels for the UVIS and 3×3 pixels for the IR).
7. The fraction of the total PSF flux in the central pixel for a centered stellar source, useful for determining the peak count rate to check for saturation (see also Appendix D).
8. The sky background count rate (electrons s^{-1}), which is the count rate that would be measured with average zodiacal background and average earthshine. For the IR channel, this quantity also includes the thermal background from *HST* and the instrument. It does not include the contribution from the detectors themselves (i.e., dark current and read noise).

The next two sections describe how to calculate two quantities:

- The count rate in counts s^{-1}, C, from your source over some selected area on the detector containing $N_{\rm pix}$ pixels.
- The peak count rate in counts s^{-1} pixel $^{-1}$, P_{cr}, from your source, which is useful for avoiding saturated exposures.

We consider the cases of point sources and diffuse sources separately in each of the following imaging and spectroscopy sections.

Table 9.1: Sensitivity Data for WFC3 UVIS Channel

Spectral Element	Pivot λ (Å)	$\int Q_\lambda T_\lambda \, d\lambda/\lambda$	ABMAG zero point	$\int S_\lambda \, d\lambda$	Encircled energy	Energy in central pixel	Background (Sky) Rate
F200LP	5159.3	0.2978	27.17	1.81E+19	0.76	0.18	0.1079
F218W	2239.3	0.0037	22.41	4.22E+16	0.72	0.14	0.0004
F225W	2383.4	0.0111	23.60	1.43E+17	0.73	0.14	0.0043
F275W	2716.7	0.0132	23.79	2.22E+17	0.75	0.15	0.0024
F280N	2844.1	0.0007	20.62	1.31E+16	0.76	0.16	0.0000
F300X	2848.1	0.0279	24.60	5.15E+17	0.76	0.16	0.0088
F336W	3357.4	0.0243	24.45	6.24E+17	0.78	0.17	0.0015
F343N	3435.1	0.0123	23.71	3.31E+17	0.78	0.17	0.0009
F350LP	5915.5	0.2203	26.84	1.76E+19	0.77	0.19	0.0961
F373N	3729.8	0.0021	21.80	6.69E+16	0.78	0.18	0.0002
F390M	3896.3	0.0102	23.51	3.53E+17	0.79	0.18	0.0015
F390W	3927.7	0.0498	25.23	1.75E+18	0.79	0.18	0.0084
F395N	3954.1	0.0042	22.54	1.50E+17	0.79	0.19	0.0007
F410M	4107.8	0.0100	23.48	3.84E+17	0.79	0.19	0.0024
F438W	4324.7	0.0307	24.70	1.31E+18	0.79	0.19	0.0085
F467M	4681.3	0.0108	23.57	5.40E+17	0.79	0.19	0.0039
F469N	4687.4	0.0019	21.68	9.48E+16	0.79	0.19	0.0007
F475W	4777.1	0.0683	25.57	3.55E+18	0.79	0.19	0.0241
F475X	4953.9	0.1061	26.05	5.93E+18	0.79	0.19	0.0392
F487N	4870.6	0.0028	22.09	1.49E+17	0.79	0.20	0.0010
F502N	5008.9	0.0030	22.18	1.72E+17	0.79	0.20	0.0012
F547M	5449.9	0.0290	24.64	1.96E+18	0.79	0.20	0.0134
F555W	5317.4	0.0761	25.69	4.90E+18	0.79	0.20	0.0335
F600LP	7506.6	0.0826	25.78	1.06E+19	0.73	0.17	0.0518
F606W	5879.7	0.0992	25.98	7.81E+18	0.78	0.19	0.0503
F621M	6209.8	0.0258	24.52	2.27E+18	0.77	0.19	0.0145
F625W	6224.2	0.0597	25.42	5.26E+18	0.77	0.19	0.0331
F631N	6303.1	0.0021	21.79	1.89E+17	0.77	0.19	0.0012
F645N	6451.7	0.0028	22.11	2.68E+17	0.77	0.19	0.0016

Spectral Element	Pivot λ (Å)	$\int Q_\lambda T_\lambda d\lambda/\lambda$	ABMAG zero point	$\int S_\lambda d\lambda$	Encircled energy	Energy in central pixel	Background (Sky) Rate
F656N	6561.0	0.0006	20.37	5.58E+16	0.76	0.19	0.0003
F657N	6564.9	0.0041	22.53	4.06E+17	0.76	0.19	0.0024
F658N	6583.9	0.0009	20.93	9.37E+16	0.76	0.19	0.0005
F665N	6654.1	0.0044	22.59	4.42E+17	0.76	0.19	0.0026
F673N	6764.1	0.0038	22.44	3.96E+17	0.76	0.19	0.0023
F680N	6876.2	0.0120	23.68	1.29E+18	0.75	0.19	0.0073
F689M	6876.5	0.0219	24.34	2.36E+18	0.75	0.19	0.0133
F763M	7612.3	0.0177	24.11	2.33E+18	0.73	0.17	0.0114
F775W	7659.7	0.0283	24.62	3.79E+18	0.72	0.17	0.0183
F814W	8069.8	0.0419	25.04	6.22E+18	0.71	0.16	0.0275
F845M	8443.3	0.0131	23.78	2.13E+18	0.69	0.16	0.0088
F850LP	9164.2	0.0130	23.77	2.49E+18	0.67	0.14	0.0089
F953N	9530.6	0.0006	20.51	1.33E+17	0.65	0.14	0.0004
FQ232N	2464.7	0.0003	19.69	4.19E+15	0.73	0.14	0.0000
FQ243N	2495.8	0.0004	20.07	6.08E+15	0.74	0.14	0.0000
FQ378N	3791.4	0.0046	22.64	1.51E+17	0.79	0.18	0.0005
FQ387N	3873.2	0.0014	21.32	4.63E+16	0.79	0.18	0.0002
FQ422M	4218.0	0.0044	22.60	1.79E+17	0.79	0.19	0.0011
FQ436N	4366.5	0.0017	21.54	7.24E+16	0.79	0.19	0.0005
FQ437N	4370.4	0.0012	21.19	5.24E+16	0.79	0.19	0.0003
FQ492N	4932.1	0.0052	22.77	2.86E+17	0.79	0.20	0.0020
FQ508N	5089.8	0.0059	22.91	3.48E+17	0.79	0.20	0.0024
FQ575N	5756.7	0.0007	20.59	5.24E+16	0.78	0.20	0.0004
FQ619N	6197.5	0.0023	21.91	2.04E+17	0.77	0.19	0.0013
FQ634N	6347.4	0.0023	21.90	2.12E+17	0.77	0.19	0.0013
FQ672N	6715.4	0.0006	20.46	6.35E+16	0.76	0.19	0.0004
FQ674N	6729.7	0.0004	20.07	4.43E+16	0.76	0.19	0.0003
FQ727N	7274.1	0.0016	21.52	1.98E+17	0.74	0.18	0.0010
FQ750N	7500.5	0.0016	21.46	1.99E+17	0.73	0.17	0.0010
FQ889N	8889.6	0.0011	21.06	1.92E+17	0.67	0.15	0.0007

Spectral Element	Pivot λ (Å)	$\int Q_\lambda T_\lambda d\lambda/\lambda$	ABMAG zero point	$\int S_\lambda d\lambda$	Encircled energy	Energy in central pixel	Background (Sky) Rate
FQ906N	9055.4	0.0010	20.93	1.78E+17	0.67	0.15	0.0006
FQ924N	9245.3	0.0008	20.72	1.52E+17	0.66	0.14	0.0005
FQ937N	9370.5	0.0007	20.59	1.39E+17	0.66	0.14	0.0005
G280	5159.3	0.2978	25.82	1.95e+18	0.76	0.16	0.1079

Table 9.2: Sensitivity Data for WFC3 IR Channel

Spectral Element	Pivot λ (Å)	$\int Q_\lambda T_\lambda d\lambda/\lambda$	ABMAG zero point	$\int S_\lambda d\lambda$	Encircled energy	Energy in central pixel	Background (sky + thermal) Rate
F098M	9880.3	0.0402	25.00	8.94E+18	0.79	0.36	0.3554
F105W	10581.6	0.0715	25.62	1.82E+19	0.78	0.35	0.6036
F110W	11589.6	0.1218	26.20	3.73E+19	0.76	0.33	1.0053
F125W	12492.6	0.0738	25.66	2.62E+19	0.74	0.32	0.6243
F126N	12585.2	0.0035	22.34	1.26E+18	0.74	0.32	0.0641
F127M	12738.8	0.0171	24.07	6.32E+18	0.73	0.32	0.1727
F128N	12832.3	0.0038	22.43	1.42E+18	0.73	0.31	0.0661
F130N	13004.0	0.0038	22.44	1.47E+18	0.73	0.31	0.0668
F132N	13186.8	0.0037	22.41	1.47E+18	0.72	0.31	0.0657
F139M	13835.4	0.0149	23.92	6.51E+18	0.71	0.30	0.1553
F140W	13963.5	0.0935	25.91	4.15E+19	0.71	0.30	0.7605
F153M	15323.4	0.0155	23.96	8.28E+18	0.67	0.28	0.1631
F160W	15440.6	0.0641	25.50	3.48E+19	0.67	0.28	0.5946
F164N	16412.9	0.0047	22.66	2.86E+18	0.64	0.26	0.0846
F167N	16646.0	0.0045	22.63	2.87E+18	0.64	0.26	0.0894
G102	10036.6	0.0588	25.41	1.35E+19	0.78	0.36	0.6391
G141	13989.1	0.1106	26.10	4.93E+19	0.71	0.30	1.1710

9.4 Count Rates (Imaging)

9.4.1 Point Source

For a point source, the count rate, C, can be expressed as the following integral over the bandpass of the filter:

$$C = A\int F_\lambda \frac{\lambda}{hc} Q_\lambda T_\lambda \varepsilon_f d\lambda = \int F_\lambda S_\lambda \varepsilon_f d\lambda$$

where:

- A is the area of an unobstructed 2.4-m telescope (i.e., 45,239 cm^2)
- F_λ is the flux from the astronomical source in erg cm^{-2} s^{-1} $Å^{-1}$.
- The factor λ/hc (where h is Planck's constant and c is the speed of light) converts ergs to photons.
- $Q_\lambda T_\lambda$ is the system fractional throughput, i.e. the probability of detecting a count per incident photon, including losses due to obstructions of the full 2.4-m OTA aperture. It is specified this way to separate out the instrument sensitivity Q_λ and the filter transmission T_λ.
- ε_f is the fraction of the point-source energy encircled within N_{pix} pixels.
- S_λ is the total imaging point-source sensitivity in units of counts s^{-1} $Å^{-1}$ per incident erg cm^{-2} s^{-1} $Å^{-1}$.

The peak counts s^{-1} $pixel^{-1}$ from the point source, C_{peak}, is given by the following integral over the bandpass:

$$C_{peak} = \int F_\lambda S_\lambda \varepsilon_f(1) d\lambda$$

where:

- F_λ, and S_λ are as above.
- $\varepsilon_f(1)$ is the fraction of energy contained within the peak pixel.

If the flux from the source can be approximated by a flat continuum (F_λ = constant) and ε_f is roughly constant over the bandpass, then:

$$C = F_\lambda \varepsilon_f \int S_\lambda d\lambda$$

We can now define an equivalent bandpass of the filter, B_λ, such that:

$$\int S_\lambda d\lambda = S_{peak} B_\lambda$$

where:

- S_{peak} is the peak sensitivity.
- B_λ is the effective bandpass of the filter.

The count rate from the source can now be written as:

$$C = F_\lambda \varepsilon_f S_{peak} B_\lambda$$

In Table 9.1 and Table 9.2 above, we give the value of $\int S_\lambda d\lambda$ for each of the filters. Alternatively, we can write the count-rate equation in terms of *V* magnitudes:

$$C = 2.5 \times 10^{11} \varepsilon_f (\int QT d\lambda / \lambda) \times 10^{-0.4(V + AB_\nu)}$$

where *V* is the visual magnitude of the source, the quantity under the integral is the mean sensitivity of the detector+filter combination (also tabulated in Tables 9.1 and 9.2), and AB_ν is the filter-dependent correction for the deviation of the source spectrum from a constant F_ν spectrum. This latter quantity is tabulated for some representative astronomical spectra in Appendix A.

9.4.2 Diffuse Sources

For a diffuse source, the count rate, *C*, which is now per pixel, due to the astronomical source can be expressed as:

$$C = \int I_\lambda S_\lambda m_x m_y d\lambda$$

where:

- I_λ is the surface brightness of the astronomical source, in erg cm^{-2} s^{-1} Å^{-1} arcsec^{-2}.
- S_λ is as above.
- m_x and m_y are the plate scales in arcsec pixel^{-1} along orthogonal axes.

9.4.3 Emission-Line Sources

For a source where the flux is dominated by a single emission line, the count rate can be calculated from the equation

$$C = 2.23 \times 10^{12} \cdot (QT)_\lambda \cdot F(\lambda) \cdot \lambda$$

where *C* is the observed count rate in counts s^{-1}, (*QT*) is the system throughput at the wavelength of the emission line, $F(\lambda)$ is the emission-line flux in units of erg cm^{-2} s^{-1}, and λ is the wavelength of the emission line in angstroms. $(QT)_\lambda$ can be determined by inspection of the plots in Appendix A. See Section 9.6.4 for an example of count-rate estimation for an emission-line source.

9.5 Count Rates (Slitless Spectroscopy)

We now turn to estimation of count rates for slitless spectroscopy using the WFC3 grisms. In this case we are dealing with a dispersed image of the source.

For a point source with a continuous spectrum, the count rate, C, is calculated per pixel in the dispersion direction, and is integrated over a fixed extraction height N_{spix} in the spatial direction perpendicular to the dispersion. The count rate is:

$$C = F_\lambda S_\lambda^{'} \varepsilon_{Nspix}^{'} = F_\lambda A \frac{\lambda}{hc} T_\lambda \varepsilon_{Nspix}^{'} d$$

where:

- S_λ is the total point source sensitivity in units of counts s^{-1} per incident erg cm^{-2} s^{-1} $Å^{-1}$; and $S_\lambda^{'} = S_\lambda \cdot d$.
- d is the spectral dispersion in Å $pixel^{-1}$.
- $\varepsilon_{Nspix}^{'}$ is the fraction of the point-source energy within N_{spix} in the spatial direction.
- the other quantities are as defined in the previous section.

For a source with an unresolved emission line with a flux of F_λ in units of erg cm^{-2} s^{-1}, the total count rate recorded over the N_{spix} extraction height is:

$$C = F_\lambda S_\lambda^{'} / d$$

These counts will be distributed over pixels in the dispersion direction according to the instrumental line-spread function.

In contrast to the case of imaging sensitivity S_λ, the spectroscopic point source sensitivity calibration ($S_\lambda^{'} \times \varepsilon_{Nspix}^{'}$) for a default extraction height of N_{spix} will be measured directly from observations of stellar flux standards after installation of WFC3 into *HST*. Therefore, the accuracy in laboratory determinations of T_λ for the WFC3 grisms will not be crucial to the final accuracy of their sensitivity calibrations, but at the current time the throughputs for these grisms are still somewhat uncertain.

The peak counts s^{-1} $pixel^{-1}$ from the point source is given by:

$$P_{cr} = \varepsilon_f^{'}(1) F_\lambda S_\lambda^{'}$$

where:

- $\varepsilon_f^{'}(1)$ is the fraction of energy contained within the peak pixel.
- the other quantities are as above.

9.6 Estimating Exposure Times

9.6.1 S/N Reached in a Given Exposure Time

To derive the exposure time to achieve a given S/N ratio, or to derive the S/N ratio achieved in a given exposure time, there are four principal ingredients: [Tom, um, there are 5 bullets....]

- Expected counts *C* from your source over some area.
- The area (in pixels) over which those counts are received (N_{pix}).
- Sky background (B_{sky}) in counts s^{-1} $pixel^{-1}$.
- The detector background, or dark, (B_{det}) in counts s^{-1} $pixel^{-1}$ and the read-noise (*R)* in counts.
- Section 9.7 provides the information for determining the sky-plus-detector background.

The S/N ratio achieved in exposure time *t* seconds, is given by:

$$S/N = \frac{Ct}{\sqrt{Ct + N_{pix}(B_{sky} + B_{det})t + N_{pix}N_{read}R^2}}$$

where:

- C = the signal from the astronomical source in counts s^{-1} . (Note that the actual output image uses DN, which will be equal to Ct/G, where G is the gain.)
- N_{pix} = the total number of detector pixels integrated over to achieve C.
- B_{sky} = the sky background in counts s^{-1} $pixel^{-1}$.
- B_{det} = the detector dark current in counts s^{-1} $pixel^{-1}$.
- R = the read noise in electrons; 3 e^- for the UVIS channel and 14 e^- for the IR channel (this is the effective read noise achieved by fitting the ramp of IR readouts).
- N_{read} = the number of detector readouts.

The above equation assumes the optimistic (but often realistic) condition that the background zero-point level under the object that is subtracted is sufficiently well known that it does not significantly contribute to the error budget; in crowded fields this may not be true.

9.6.2 Exposure Time to Reach a Given S/N

Observers normally take sufficiently long integrations that the read noise is not important. This condition is met when:

$$Ct + N_{pix}(B_{sky} + B_{det})t > 2N_{pix}N_{read}R^2$$

In the regime where read noise is unimportant, the integration time to reach a given signal-to-noise ratio Σ is:

$$t = \frac{\Sigma^2[C + N_{pix}(B_{sky} + B_{det})]}{C^2}$$

If the source count rate is much higher than that of the sky plus detector backgrounds, then this expression reduces further to:

$$t = \frac{\Sigma^2}{C}$$

i.e., the usual result for Poisson statistics of $\Sigma = \sqrt{totalcounts}$.

More generally, the required integration time to reach a given S/N ratio is:

$$t = \frac{\Sigma^2[C + N_{pix}(B_{sky} + B_{det})] + \sqrt{\Sigma^4[C + N_{pix}(B_{sky} + B_{det})]^2 + 4\Sigma^2C^2[N_{pix}N_{read}R^2]}}{2C^2}$$

9.6.3 Exposure Time Estimates for Red Targets in F850LP

At long wavelengths, ACS CCD observations are affected by a red halo due to light scattered off the CCD substrate. An increasing fraction of the light as a function of wavelength is scattered from the center of the PSF into the wings. This problem affects particularly the very broad z-band F850LP filter, for which the encircled energy depends on the underlying spectral energy distribution the most. At the current time, it is thought that this problem has been fixed for WFC3, and so this should not be a concern for those planning WFC3 observations.

9.7 Sky Background

As noted in the previous section, the backgrounds from the sky and from the detector must be taken into account when calculating expected S/N ratios or exposure times.

Detector backgrounds (as well as read-out noise) for the CCDs and IR detector are discussed in Chapter 5. This section deals with the sky backgrounds that can affect WFC3 observations.

The most important sources of sky background are:

- Earthshine (ES).
- Zodiacal light (ZL).
- Geocoronal emission (GC).

The background in counts s^{-1} $pixel^{-1}$ for imaging observations can be computed as:

$$B_{sky} = \int I_\lambda S_\lambda m_x m_y d\lambda$$

where:

- I_λ is the surface brightness of the sky background, in erg cm^{-2} s^{-1} $Å^{-1}$ $arcsec^{-2}$.
- S_λ is the point-source sensitivity for the imaging mode.
- m_x and m_y are the plate scales in arcsec $pixel^{-1}$ along orthogonal axes.

In the case of slitless spectroscopy, the image of the sky through a disperser is not uniform, because some wavelengths fall off the detector for regions of sky near the edge of the field of view (FOV). The regions of lower sky background will be strips at the long- and short-wavelength edges of the FOV; a UVIS grism spectrum is roughly 270 pixels long, while an IR grism spectrum is roughly 170 pixels long. The maximum width of the strips from where the signal starts to decline to the edge, where the signal is down by roughly a factor of 2, will be about half the total length of a spectrum of a point source, i.e., roughly 135 pixels (UVIS) or 85 pixels (IR), in the case of a sky background with a continuum of wavelengths. These small strips of lower sky background are ignored in the following formulae. [Tom: the following few sentences seem to have come from the ACS manual! Is the wording still true??] Furthermore in the SBC and the WFC, since the spectra do not lie along the direction of the anamorphic distortion, the plate scales of m_x and m_y above must be replaced by the plate scales m_s and m_λ in the orthogonal spatial and dispersion directions, respectively. Interior to the strips, a point on the detector sees a region of sky over the full wavelength coverage of the disperser. Thus, for **spectroscopic observations**:

$$B^{\lambda}_{sky} = \int I_\lambda S'_\lambda m_s m_\lambda d\lambda$$

For a **monochromatic** sky emission line at $\lambda = L$ like [O II] 2471, which will dominate the background through the UVIS/G280 grism:]

$$B^{L}_{sky} = I_L S'_\lambda m_s m_\lambda / d$$

where

- I_L is the monochromatic intensity of a line at wavelength L in erg cm^{-2} s^{-1} arcsec^{-2}.

The total sky background is:

$$B_{sky} = B^{\lambda}_{sky} + B^{L}_{sky}$$

Figure 9.1 and Table 9.5 show "high" sky background intensity as a function of wavelength, identifying the separate components which contribute to the background. The "shadow" and "average" values of the earthshine contribution in the WFC3 Exposure Time Calculator correspond, respectively, to 0% and 50% of the "high" values in Figure 9.1 and Table 9.5. For the zodiacal sky background, the values in Figure 9.1 and Table 9.5 correspond to the high value of *V*-band surface brightness of 22.1 mag arcsec^{-2} from Table 9.3, while the "low" and "average" zodiacal light is scaled to *V* surface brightnesses of 23.3 and 22.7 mag arcsec^{-2}, respectively.

Figure 9.1: Sky background intensity as a function of wavelength.

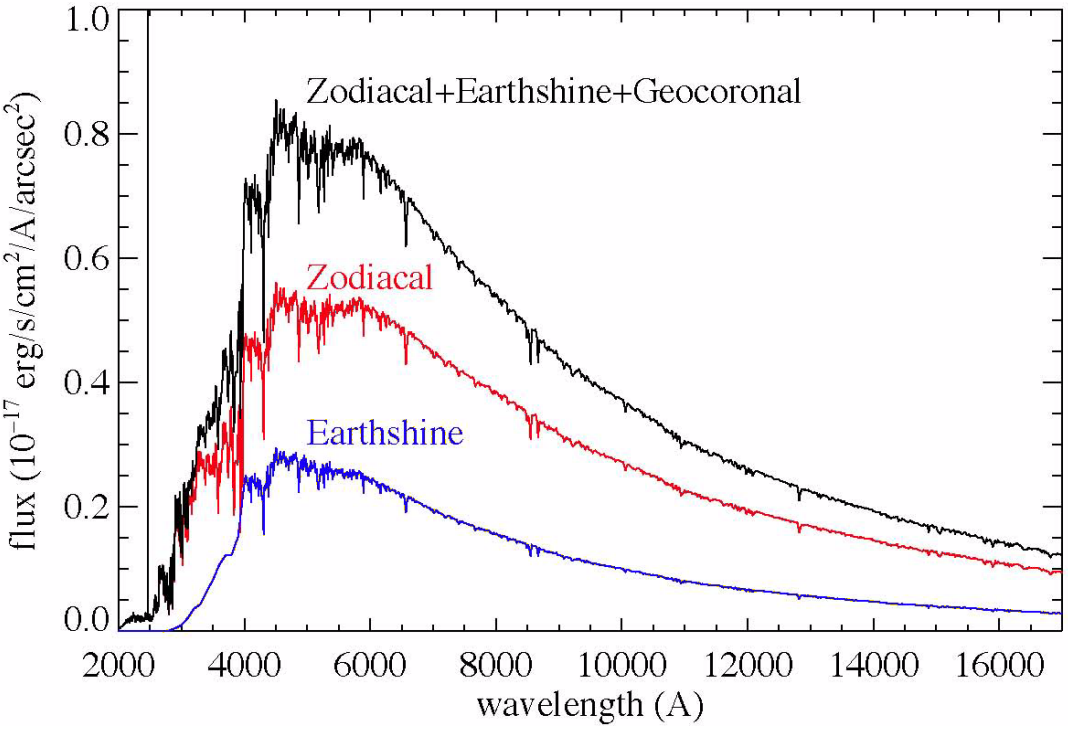

Fig 9.1: The total sky spectrum (black) for the "high-background" case adopted in the WFC3 Exposure Time Calculator, along with the individual contributions from zodiacal light (red) and earthshine (blue). These data correspond to a *V*-band surface brightness of 22.1 mag arcsec^{-2}. The only significant geocoronal emission line in the WFC3 spectral range is [O II] 2471 Å, shown as a black line; it has a flux of 1.5×10^{-15} erg cm^{-2} s^{-1} arcsec^{-2}, extending beyond the upper limit of the plot.

9.7.1 Background Variations and LOW-SKY

In the ultraviolet, the background contains a bright airglow line, which varies in intensity from day to night and as a function of *HST* orbital position. The airglow line may be the dominant sky contributions in the UV both for imaging and spectroscopic observations. Away from the airglow line, at wavelengths shortward of ~3000 Å, the background is dominated by zodiacal light, where the small area of sky that corresponds to a pixel of the high-resolution *HST* instrumentation usually produces a signal that is much lower than the intrinsic detector background. The contribution of zodiacal light does not vary dramatically with time, but does vary by about a factor of about three throughout most of the sky as a function of distance from the Sun and ecliptic. Table 9.3 gives the variation of the zodiacal background as a function of ecliptic latitude and longitude relative to the Sun. For a target near ecliptic coordinates (50,0) or (–50,0), the zodiacal light is relatively bright at 20.9 mag arcsec^{-2}, i.e., about 9 times the faintest value of 23.3 mag arcsec^{-2}. Thus if you are considering deep imaging applications, you must carefully consider expected sky values.

On the other hand, earthshine varies strongly depending on the angle between the target and the bright Earth limb. The variation of the Earthshine as a function of limb angle from the sunlit Earth is shown in Figure 9.2. The figure also shows the contribution of the moon, which is typically much smaller than the zodiacal contribution, for which the upper and lower limits are shown. For reference, the limb angle is approximately 24° when the *HST* is aligned toward its orbit pole (i.e., the center of the CVZ). The Earthshine contribution shown in Figure 9.1 and Table 9.5 corresponds to this position.

Figure 9.2: Background contributions in V magnitude per arcsecond^2 due to the zodiacal light, Moon, and sunlit Earth, as a function of angle between the target and the limb of the Earth or Moon.

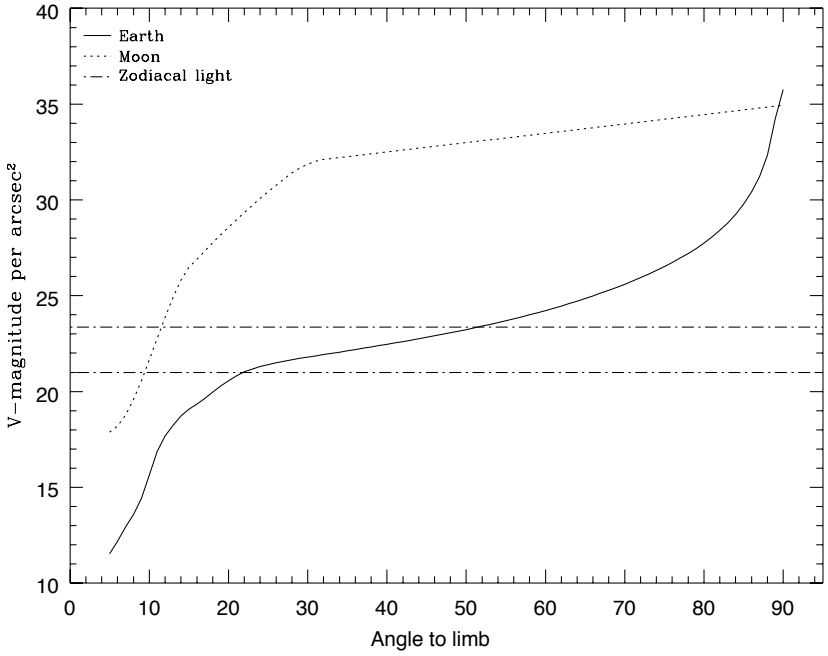

The two zodiacal light lines show the extremes of possible values.

For observations taken longward of 3500 Å, earthshine dominates the background at small (< 22°) limb angles. In fact, the background increases exponentially for limb angles < 22°. The background near the bright limb can also vary by a factor of ~2 on timescales as short as two minutes, which suggests that the background from earthshine also depends upon the reflectivity of the terrain over which *HST* passes during the course of an exposure.

Table 9.3: Approximate zodiacal sky background as a function of ecliptic latitude and ecliptic longitude (in *V* mag per square arcsec).

Ecliptic longitude (degrees)	Ecliptic latitude (degrees)			
	0	30	60	90
180	22.1	22.7	23.2	23.3
145	22.4	22.9	23.3	23.3
110	22.3	22.9	23.3	23.3
50	20.9	22.2	22.9	23.3

Observations of the faintest objects may need the special requirement `LOW-SKY` in the Phase II observing program. `LOW-SKY` observations are scheduled during the part of the year when the zodiacal background light is no more than 30% greater than the minimum possible zodiacal light for the given sky position. `LOW-SKY` in the Phase II scheduling also invokes the restriction that exposures will be taken only at angles greater than 40° from the bright Earth limb to minimize Earthshine and the UV airglow lines. The `LOW-SKY` special requirement limits the times at which targets within 60° of the ecliptic plane will schedule, and limits visibility to about 48 minutes per orbit. The use of `LOW-SKY` must be requested and justified in the Phase I proposal.

The ETC provides the user with the flexibility to adjust separately both the zodiacal (low, average, high) and earthshine (shadow, average, high) sky background components in order to determine if planning for use of `LOW-SKY` is advisable for a given program. However, the absolute sky levels that can be specified in the ETC may not be achievable for a given target; e.g., as shown in Table 9.3, the zodiacal background minimum for an ecliptic target is $m_v = 22.4$ [Tom: the table shows a min of 22.1] which is still brighter than both the low and average options with the ETC. By contrast, a target near the ecliptic pole would always have a zodiacal = low background in the ETC. The user is cautioned to carefully consider sky levels as the backgrounds obtained in *HST* observations can cover significant ranges.

9.7.2 Geocoronal Emission and SHADOW

Background due to geocoronal emission originates mainly from hydrogen and oxygen atoms in the exosphere of the Earth. In the far-UV spectral region, the strongest geocoronal emission lines are Lyman–α at 1216 Å, O I at 1304 Å, and O I] at 1356 Å, but WFC3 is of course not sensitive at these wavelengths. The only significant geocoronal emission line to which WFC3 is sensitive is [O II] 2471 Å. In sunlight this line can be as bright as $\sim 1.5 \times 10^{-15}$ erg cm^{-2} s^{-1} arcsec^{-2}, while in Earth shadow it is much fainter, typically $\sim 7.5 \times 10^{-18}$ erg cm^{-2} s^{-1} arcsec^{-2}.

To minimize geocoronal emission the special requirement `SHADOW` can be requested. Exposures using this special requirement are limited to roughly 25 minutes

per orbit, exclusive of the guide-star acquisition (or reacquisition), and can be scheduled only during a small percentage of the year. `SHADOW` reduces the contribution from the geocoronal emission lines by roughly a factor of ten while the continuum Earthshine is set to zero. `SHADOW` requirements must be included and justified in your Phase I proposal (see the *Call for Proposals*).

9.8 Extinction Correction

[Tom: I feel that this section can probably be omitted. A professional astronomer ought to know about interstellar extinction! Also, the references seem rather old, and don't mention, for example, Cardelli et al's standard paper.]

Extinction can dramatically reduce the counts expected from your source, particularly in the ultraviolet.Figure 9.3 shows the average A_v /$E(B–V)$ values for our galaxy, taken from (Seaton, *MNRAS*, **187**, 73P, 1979). Large variations about the average are observed (Witt, Bohlin, Stecher, *ApJ*, **279**, 698, 1984).

Extinction curves have a strong metallicity dependence, particularly in the UV wavelengths. Sample extinction curves can be seen in Koornneef and Code, *ApJ*, **247**, 860 1981 (LMC); Bouchet et al., *A&A*, **149**, 330 1985 (SMC); and Calzetti, Kinney and Storchi-Bergmann, *ApJ*, **429**, 582, 1994, and references therein. At lower metallicities, the 2200 Å bump which is so prominent in the galactic extinction curve disappears; and $A_v/E(B–V)$ may increase monotonically at UV wavelengths.

Figure 9.3: Extinction versus wavelength.

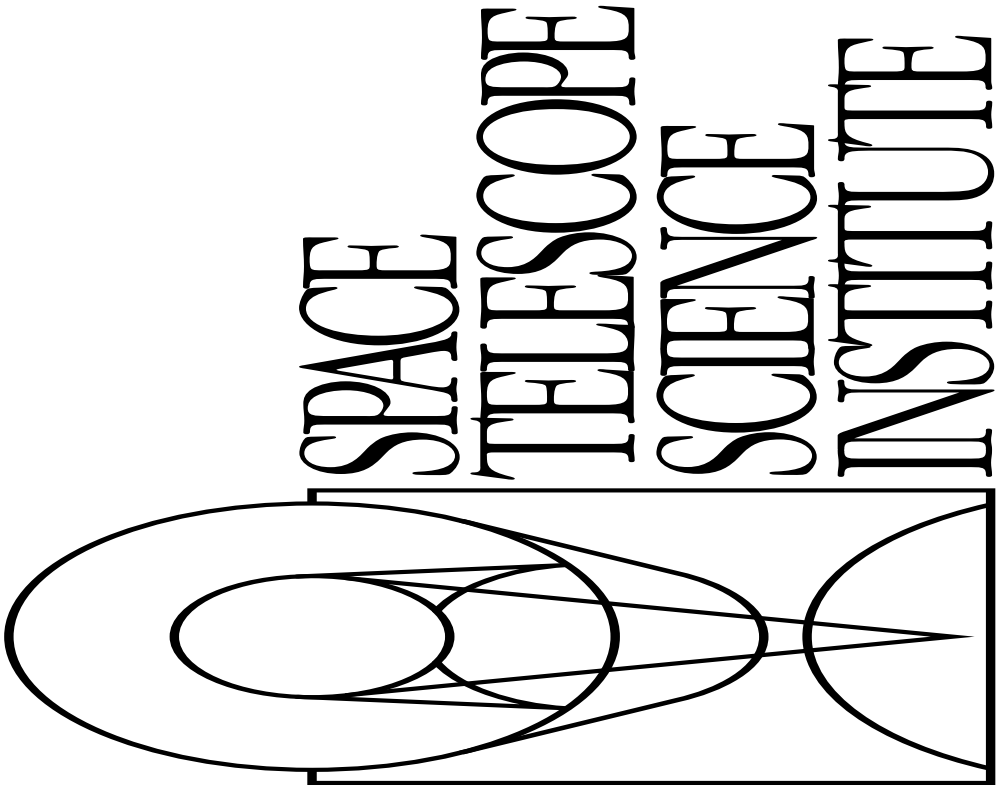

9.9 Exposure-Time Examples

[Tom, there are only 2 examples in thie section, and no grism examples. Is it possible to provide several more examples?]

In the following you will find a set of examples for the two different channels and for different types of sources. The examples were chosen in order to present typical objects for the two channels and also to present interesting cases as they may arise with the use of WFC3.

9.9.1 Example 1: UVIS Imaging of a Faint Point Source

What is the exposure time needed to obtain a signal-to-noise of 10 for a point source of spectral type F0 V, normalized to $V = 27.5$, when using the UVIS F555W filter? Assume a photometry box size of 5x5 pixels, and average sky values.

The WFC Exposure Time Calculator (ETC) gives a total exposure time of 5114 seconds to obtain this S/N in a single exposure. Since such an exposure would be riddled with cosmic rays and essentially useless, it is necessary to specify how many exposures to split the observation into. WFC3/UVIS observations generally should be

split if the exposure time is longer than about 5 minutes, but for multi-orbit observations, splitting into two exposures per orbit is generally sufficient.

For a typical object visibility of 53 minutes, after applying the requisite overheads, there is time for two exposures of approximately 1200 seconds per orbit. The required exposure time can thus be reached in 4 exposures, but re-running the ETC using `CR-SPLIT=4` raises the required exposure time to 5679 seconds (because of the extra noise introduced by the three extra readouts). To achieve the required exposure time would require `CR-SPLIT=5`, or three orbits; iterating the ETC one more time shows a total exposure time of 5847 seconds with this number of reads.

NOTE: References below to Table 10.1, etc., will eventually be updated to refer to tables in Appendix A.

Using the pencil-and-paper method, Table 9.1 gives the integral $\int QTd\lambda/\lambda$ as 0.0761. An F0 V star has an effective temperature of 7,240 K; looking in Table 10.1, the AB_v correction term for an effective temperature of 7,500 K is 0.03. According to Table 9.1, a 5x5 pixel square aperture encloses about 79% of the light from a star. The count rate can then be calculated from the equation

$$C = 2.5 \times 10^{11} \varepsilon_f \left(\int QT d\lambda/\lambda\right) \times 10^{-0.4(V + AB_v)}$$

or $2.5\text{x}10^{11}*0.0761*0.79*10^{-0.4(27.5+0.03)} = 0.146$ counts s^{-1}, which agrees with the ETC-returned value of 0.142. The exposure time can then be found by using the equation

$$t = \frac{\Sigma^2[C + N_{pix}(B_{sky} + B_{det})] + \sqrt{\Sigma^4[C + N_{pix}(B_{sky} + B_{det})]^2 + 4\Sigma^2 C^2 [N_{pix} N_{read} R^2]}}{2C^2}$$

to give $t = 5870$ seconds, which is close to the ETC-derived value of 5847 seconds. We have inserted the background rates of $B_{sky} = 0.0335$ (Table 9.1), $B_{det} = 0.0005$ (Chapter 5), a read noise of 3 e^- per read (Chapter 5), and 5 reads.

9.9.2 Example 2: IR Imaging of a Faint Extended Source

What is the exposure time needed to obtain a signal-to-noise of 10 for an an elliptical galaxy that subtends an area of 1 square arcsec with an integrated V magnitude of 26.7, when using the IR F140W filter? Assume a photometry box size of 8 x 8 pixels, and average sky values.

The WFC Exposure Time Calculator (ETC) gives a total exposure time of 1747 seconds to obtain this S/N in a single exposure. Although the non-destructive multi-accum sequences on the IR channel can mitigate cosmic rays in a single read sequence, users are encouraged to dither their observations so that there are least 2 read sequences per field, to mitigate hot pixels and resample the point spread function. Re-running the calculation again with 2 exposures gives an exposure time of 1913 seconds. If we assume (as in Example 1) that we can fit two 1200-second exposures in

an orbit, this program fits within a single orbit. Two SPARS100 sequences, with 13 samples (1203 seconds) per sequence should work well for this program.

Using the pencil-and-paper method, Table 9.1 gives the integral $\int QTd\lambda/\lambda$ as 0.0935. We will assume that the elliptical galaxy resembles an old (10 Gyr) burst of star formation; looking in Table 10.2, the AB_v correction term is −1.41. We will assume that the 8x8 pixel box encloses all of the light for this object. The count rate can then be calculated from the equation

$$C = 2.5 \times 10^{11} \varepsilon_f (\int QT d\lambda/\lambda) \times 10^{-0.4(V + AB_v)}$$

or $2.5x10^{11}*0.0935*1.0*10^{-0.4(26.7-1.41)} = 1.79$ counts s^{-1}, which is close to the ETC-returned value of 1.89. The exposure time can then be found by using the equation

$$t = \frac{\Sigma^2[C + N_{pix}(B_{sky} + B_{det})] + \sqrt{\Sigma^4[C + N_{pix}(B_{sky} + B_{det})]^2 + 4\Sigma^2 C^2 [N_{pix} N_{read} R^2]}}{2C^2}$$

to give $t = 2140$ seconds, which is close to the ETC-derived value of 1930 seconds. We have inserted the background rates of $B_{sky} = 0.7605$ (Table 9.1), $B_{det} = 0.1$ (Chapter 5), an effective read noise of 14 e^- per read (Chapter 5, assuming we are fitting the multiaccum sequence), and 2 reads.

9.10 Tabular Sky Backgrounds

In Table 9.4 we present the "high" sky-background numbers, which are plotted in Figure 9.1. See the text and the caption of Figure 9.1 for more details. These high sky values are defined as the earthshine at 38° from the limb and the high zodiacal light of $V = 22.1$ mag arcsec^{-2} .

High sky backgrounds.

Wavelength	Earthshine	Zodiacal light	Total background
Å	erg cm^{-2} s^{-1} Å^{-1} arcsec^{-2}	erg cm^{-2} s^{-1} Å^{-1} arcsec^{-2}	erg cm^{-2} s^{-1} Å^{-1} arcsec^{-2}
2000	7.69e-22	7.94e-20	8.02e-20
2500	1.53e-21	3.83e-19	3.84e-19
3000	1.43e-19	1.63e-18	1.77e-18
3500	8.33e-19	2.72e-18	3.55e-18
4000	1.66e-18	3.12e-18	4.78e-18
4500	2.59e-18	4.97e-18	7.57e-18

Wavelength	Earthshine	Zodiacal light	Total background
Å	erg cm^{-2} s^{-1} $Å^{-1}$ $arcsec^{-2}$	erg cm^{-2} s^{-1} $Å^{-1}$ $arcsec^{-2}$	erg cm^{-2} s^{-1} $Å^{-1}$ $arcsec^{-2}$
5000	2.63e-18	5.07e-18	7.70e-18
5500	2.55e-18	5.17e-18	7.72e-18
6000	2.42e-18	5.14e-18	7.56e-18
7000	1.95e-18	4.48e-18	6.42e-18
8000	1.56e-18	3.82e-18	5.38e-18
9000	1.23e-18	3.18e-18	4.40e-18
10000	9.97e-19	2.70e-18	3.70e-18
11000	8.02e-19	2.26e-18	3.06e-18
12000	6.65e-19	1.94e-18	2.61e-18
13000	5.58e-19	1.68e-18	2.24e-18
14000	4.70e-19	1.46e-18	1.93e-18
15000	3.97e-19	1.26e-18	1.66e-18
16000	3.35e-19	1.09e-18	1.43e-18
17000	2.79e-19	9.27e-19	1.21e-18

CHAPTER 10:

Overheads and Orbit Time Determinations

In this chapter . . .

10.1 Overview

This chapter provides information for Phase I proposers who plan to use WFC3 for some or all of their planned HST observations. Because your Phase I proposal must state a specific integer number of HST orbits that are requested for your program, it is important that this number be as accurate as possible.

After you establish a set of scientific exposures, as well as any additional calibration exposures required for your program, you are ready to determine the total number of orbits to request in your Phase I proposal. The time requested should include not only the total exposure time, but also the additional time for the observatory and instrument operations needed to support those exposures. Those operations will usually include acquiring (and possibly re-acquiring) guide stars, configuring WFC3 in preparation for an exposure, transferring data, and possibly repositioning the target in the focal plane between exposures.

It will often be necessary or desirable to achieve the total exposure time through a sequence of shorter exposures. For example, an exposure totalling several hours will be interrupted by target occultations. Moreover, UVIS exposures will almost always be obtained as a sequence of shorter exposures, in order to remove cosmic-ray hits. For your Phase I proposal, you should plan the sequences of exposures and overhead

activities for each of the requested orbits. An overview of observation planning is given in Chapter 4.

Generally, you will need to compile the overheads for your individual exposures, having packed an integer number of exposures and their supporting activities into individual orbits. Some activities may be executed while the target is occulted by the Earth, allowing more efficient utilization of an orbit. Finally, you will tally the exposure times and resulting overhead times required during visibility of the target in order to determine the total number of orbits needed. This may be an iterative process as you refine your exposures to better use the targets' orbit visibility (for non-CVZ targets).

The Phase I Call for Proposals includes instructions on observatory policies and practices regarding orbit time requests; see

http://www.stsci.edu/hst/hst/proposing/documents/cp/cp_cover.html.

The HST Primer provides additional specific advice on how to determine the number of required orbits for your scientific program; see

http://www.stsci.edu/hst/proposing/documents/cp/primer_cover_.html.

In the following sections, we provide a summary of the WFC3-specific overheads and give several examples that illustrate how to calculate your orbit request for a Phase I proposal.

The overheads presented below are approximate. These overhead times are to be used, in conjunction with the exposure times you determine and the instructions in the HST Primer, in order to estimate the total number of orbits for your Phase I proposal. If your HST proposal is accepted, you will then develop and submit a Phase II proposal to support the actual scheduling of your approved observations. At that time you will use the APT scheduling software (which employs more precise values for the various overheads) to craft exposure sequences that match orbital target visibility intervals and your allocation of orbits. Therefore, requesting sufficient time in your Phase I proposal for overhead operations is important; additional time to cover unplanned overhead will not be granted later.

10.2 Observatory Overheads

This section discusses the overheads involved in preparing the telescope for observations of a target. The next section describes the additional instrument-specific overheads involved in obtaining and storing the actual individual WFC3 exposures.

At the beginning of a sequence of WFC3 exposures, the telescope must acquire guide stars. The time required for this initial guide-star acquisition is 6 minutes. If the observations extend into the following orbit(s) following Earth occultation, you must also include the overhead for guide-star re-acquisition (another 5 minutes at the beginning of each new orbit). The only exception to this re-acquisition overhead occurs when you are observing a target in the Continuous Viewing Zone (CVZ; see the

Phase I Proposal Instructions), in which case guide-star re-acquisitions are unnecessary.

Following guide-star acquisition (or re-acquisition) and the first exposure during the orbit, it is likely that you will want to make a series of small telescope motions for the purpose of obtaining dithered observations. Each commanded movement of the telescope requires an amount of time ranging from 20 to 60 seconds, depending on the size of the motion. Furthermore, each time the telescope is moved more than 2 arcmin (e.g., for the purpose of constructing a mosaicked image), an additional guide-star acquisition will be necessary, requiring another 6 minutes.

When using WFC3's UVIS quad filters, it will often be necessary to repoint the telescope to place the target in the desired quadrant. This repositioning will require 1 minute.

Table 10.1 summarizes the observatory-level overheads involved in WFC3 observing.

Table 10.1: Observatory Overhead Times

Action	Overhead Time
Guide-star acquisition	6 minutes (first orbit)
Guide-star re-acquisitions	5 minutes at beginning of each new orbit for non-CVZ observing
	0 minutes for CVZ observing
New guide-star acquisition following dither of >2 arcmin	6 minutes
Spacecraft maneuvers	1 minute for offsets between 10 and 90 arcseconds
	0.5 minute for offsets between 1 and 10 arcseconds
	0.3 minute for offsets less than 1 arcsecond
	1 minute to offset to different UVIS quad filter

10.3 Instrument Overheads

10.3.1 Exposure Overheads

The instrument-specific overhead times for WFC3 exposures are dominated by the time to move the filter wheels, to read out the detector, and especially to transfer and store the data. Although in a Phase II proposal the overheads computed with APT may prove to be smaller than the values given in this section, it is nevertheless important to plan your Phase I proposal using the conservative values given here in order to ensure the award of time adequate to attain your scientific goals.

Several kinds of overhead activities are associated with each exposure, and the specific activities depend on whether the exposure is a new one, or part of a series of

identical ones. Identical exposures are defined as second and subsequent exposures on the same target, with the same filter.

For UVIS ACCUM exposures (i.e., CCD exposures), identical exposures are generated if the observer does any of the following: (1) specifies a CR-SPLIT number greater than 1; (2) does not specify the CR-SPLIT Optional Parameter, in which case it defaults to CR-SPLIT=2 for all exposures regardless of exposure time; (3) specifies the Special Requirement PATTERN (in order to dither, or to mosaic, a set of images); or (4) specifies a Number of Iterations greater than 1.

For IR MULTIACCUM exposures, CR-splitting is not used, and only items (3) and (4) in the preceding list apply. Furthermore, unless otherwise specified, a full 16-read (i.e., 15-sample, specified with NSAMP=15) sequence will be obtained for each IR MULTIACCUM exposure. The full set of samples (i.e., images) is considered to be one exposure.

At the end of each UVIS or IR exposure, images are read into WFC3's internal buffer memory, where they are stored until they are transferred to HST's solid-state data recorder. The time to read out a UVIS image from the CCD detector is 100 seconds. The time to read an IR image from the HgCdTe detector is 3 seconds, leading to a total of 48 seconds of readout time for a full 16-read exposure. These times are included in the overhead times for the first and subsequent exposures presented in Table 10.2 below.

The WFC3 internal buffer memory holds 64 MB of data, which is the equivalent of two full UVIS CCD exposures, or two 16-read IR exposures. Thus, after obtaining two full UVIS exposures, or two IR exposures, the internal buffer memory must be dumped to the telescope's solid-state recorder (SSR) before the next exposure can be taken. It is also possible to dump the buffer after each exposure, which can be advantageous. A buffer dump of one CCD or IR exposure takes 349 seconds (5.8 minutes), and cannot occur while WFC3 is being commanded. Of this time, 339 seconds (for one UVIS image) or 346 seconds (for one 16-read IR exposure) are spent dumping the image.

In regard to planning observations, there are three cases of interest. (1) The buffer dump can be done during the next exposure if its exposure time is longer than the dump time of 339 seconds (UVIS) or 346 seconds (IR). This is called a "parallel" buffer dump. (2) If the next exposure is not longer, then the buffer dump must occur first, and thus will create an extra 5.8 minutes of overhead. This is called a "serial" buffer dump. (3) If an exposure ends just before target occultation, the buffer can be dumped to the SSR during occultation, and no overhead time is required.

This means that a repeating sequence of one short UVIS exposure and one long UVIS exposure will incur no overhead if the short exposure is taken first and the long exposure is more than 339 seconds. Similarly, a repeating sequence of two 15-sample MULTIACCUM IR exposures will incur no overhead if the second exposure is longer than 346 seconds.

If the next exposure time is longer than 339 seconds (for UVIS) or 346 seconds (for IR), the buffer dump will occur during that exposure, and no overhead is imposed. However, if the next exposure time is shorter than 339 seconds (UVIS) or 346 seconds (IR), then the dump must occur before the next exposure can start.

A sequence of many short exposures will fill the WFC3 buffer before the target is occulted, requiring serial buffer dumps while the target is visible. Similarly, this will be required in all cases for CVZ targets. In these cases, the time needed to dump each exposure from WFC3's buffer (5.8 minutes) is an overhead that must be included in the orbit time budget. This overhead can severely constrain the number of short exposures that can be obtained in an orbit. However, subarrays can be used to lower the data volume for some applications and reduce the overhead time for buffer dumps (see the next section)

Both the UVIS and IR channels may be used during a single orbit, although not simultaneously. The time required to reconfigure between the two channels is 1 minute. If the buffer is not empty when switching channels, then time must also be taken to dump it before the exposure can begin with the other channel. Because the centers of the fields of view of the UVIS and IR channels are the same, acquisition of new guide stars is not required when changing channels to observe the same target.

The overhead for each exposure includes an allowance for the time required to position the filter or grism; however, selecting a UVIS quad filter requires an additional 1 minute of overhead to re-position the telescope, as indicated in Table 10.1.

Table 10.2 summarizes all of the instrument overheads described in this subsection.

Table 10.2: WFC3 Instrument Overhead Times

Action	Overhead Time (minutes)
Reconfiguration between UVIS & IR channels during a single orbit	1.0
UVIS ACCUM Mode	
Single exposure or first exposure in a set of identical exposures (e.g., the first sub-exposure of a CR-SPLIT set)	2.6
Subsequent exposures in set of identical exposures within an orbit (e.g., subsequent exposures in a CR-SPLIT set), per exposure	2.0
Buffer dump if exposure is not last one in an orbit, or if next exposure is less than 339 seconds	5.8
IR MULTIACCUM Mode	

Action	Overhead Time (minutes)
Each exposure	1.0
Buffer dump if 16-read exposure is not last one in an orbit, or if next exposure is less than 346 seconds	5.8

10.3.2 Reducing Overheads with Subarrays and Binning

If your science program is such that a field of view smaller than the full detector size is adequate and you require many short exposures, then one way to reduce the frequency of buffer dumps, and hence their associated overheads, is to use a WFC3 subarray. Subarrays are described for the UVIS channel in Section 6.x, and for the IR channel in Section 7.s. When subarrays are used, only a small region of the detector is read out and stored in WFC3's buffer. The reduced data volume permits a larger number of exposures to be stored in the buffer before it becomes necessary to transfer them to the telescope's solid-state recorder. Use of subarrays reduces the amount of time spent dumping the buffer, and also reduces detector readout time.

The subarrays supported by STScI (and recommended for your use) are specified for the UVIS and IR channels by apertures with "SUB" in their names. See Sections 6.x and 7.x for further details.

The areas (A_{SA}) of the UVIS subarrays are 1/2, 1/4, or 1/64 of the area (A_{FF}) of a full-frame image. The areas of the IR subarrays are 1/4, 1/16, 1/64, or 1/256 of the area of a full-frame image. The number of subarray exposures that may be stored in the buffer is $n = 2\ (A_{FF}/A_{SA})$. For example, eight 1/4-area exposures may be stored in the buffer, which would allow eight 4-minute exposures to be taken and stored before having to dump the buffer. If the exposures were full-frame, the buffer would have to be dumped after each pair of observations, thus leading very low observing efficiency.

You may also define a UVIS subarray of arbitrary size and location, on an "available-but-unsupported" basis. However, in that case, matching bias frames will not be provided automatically by STScI and you therefore must specify them yourself. Those bias frames will typically be scheduled during the following occultation of a non-CVZ target (i.e., they do not add to the overheads during the visibility time), but the overhead must be added for CVZ targets. Dark frames and flat fields will be extracted from STScI's full-frame calibration images.

Data volume and overhead time can also be reduced for UVIS images by using on-chip binning of adjacent pixels, as described in Chapter xx. By using 2×2 pixel binning, the data volume is reduced by a factor of 4. For 3×3 pixel binning it is reduced by a factor of 9. IR readouts cannot be binned, but data volume may be reduced by taking less than the default 15 samples during an exposure.

10.4 Orbit Use Examples

The easiest way to learn to estimate total orbit time requests is to work through a few examples. Below we provide five different examples:

1. A simple UVIS CR-SPLIT image using one filter.
2. A set of short UVIS exposures that require large overheads associated with buffer dumps.
3. A one-orbit IR observation using two different filters.
4. A two-orbit UVIS observation using dithering.
5. A one orbit IR grism spectroscopic observation.

These examples represent fairly typical usage scenarios of WFC3.

10.4.1 Example 1: UVIS, 1 orbit, 1 filter

Consider a target to be imaged with UVIS in a given filter in one orbit. Let us suppose that, by using the Exposure Time Calculator (ETC) (see Chapter 9), we find that we need a total exposure time of 2400 seconds (40 minutes) to reach the desired S/N. Given that we desire the observation to be split into two exposures for cosmic-ray removal (using the default CR-SPLIT=2), we map the overheads and the science exposure times onto the orbit as follows:

Table 10.3: Orbit Calculation for Example 1

Action	Time (minutes)	Explanation
Guide-star acquisition	6.0	Needed at start of observation of new target
UVIS overhead for first sub-exposure	2.6	Includes filter change, camera set-up, and readout
First science sub-exposure	20.0	
UVIS overhead for second sub-exposure	2.0	Includes readout
Second science sub-exposure	20.0	Total exposure time is 40 min
Total time used	50.6	

Thus, with a total time of nearly 51 minutes, this set of observations would fit into most typical HST orbits. The exposure time could, if needed, be adjusted so as to fill the actual target visibility interval (which depends on several factors, including the date and target location in the sky, as described in the HST Primer). The time needed to dump the buffer following the second sub-exposure incurs no overhead in this example, because it can be performed during target occultation.

It should be noted that this simple sequence of two fairly long, non-dithered exposures would produce an image with a gap between the two CCD chips, and that cosmic-ray removal might not be optimal.

10.4.2 Example 2: UVIS, 1 orbit, short exposures

This example illustrates the impact of short exposures on the useful time in the orbit. Suppose we intend to use one orbit to observe a target with UVIS in two filters The observation consists of two sequences, each one with two identical CR-SPLIT exposures, for a total of four individual sub-exposures. Suppose that the ETC shows that the exposure time must be 540 seconds for each of the filters, so each of the CR-SPLIT sub-exposures must be at least 270 seconds long. For the target declination, we find that the visibility time is 55 minutes. The time budget for the orbit is as follows:

Table 10.4: Orbit Calculation for Example 2

Action	Time (minutes)	Explanation
Guide-star acquisition	6.0	Needed at start of observation of new target
UVIS overheads for first sub-exposures in both series	2 × 2.6 = 5.2	Includes filter change, camera set-up, and readouts

Action	Time (minutes)	Explanation
UVIS overheads for subsequent sub-exposures in both series	2 × 2.0 = 4.0	Includes readouts
Buffer dumps after 2nd and 4th sub-exposures	2 × 5.8 = 11.6	First dump needed because next exposure is too short to accommodate dump (270 sec < 339 sec). Second dump completes observation.
Science exposures	4 × 4.5 = 18.0	
Total time used	44.8	

Compared with Example 1, we see that although with the adopted minimum exposure times we can squeeze these observations into one orbit, the efficiency is very low due to the large overheads associated with buffer dumps. We have achieved only 18 minutes of exposure time within 45 minutes of target visibility, whereas in Example 1 we obtained 40 minutes of exposure time within 50.6 minutes of visibility.

However, if we were to increase each exposure time in Example 2 from 9 minutes to 12 minutes, then each CR-SPLIT sub-exposure becomes 360 seconds, which is greater than the buffer dump time. Thus the time usage would become more efficient, freeing nearly 12 minutes of the visibility time for additional exposures.

Alternatively, if compatible with the scientific goals, a subarray could have been used to read out only a fraction of the detector area, allowing more frames to be stored in the buffer before requiring a dump. In this example, using UVIS 2k×4k subarrays for 4 short (<339 seconds) exposures would save about 4 minutes of readout time and could save 12 minutes of dump time.

10.4.3 Example 3: IR, 1 orbit, 2 filters

The third example demonstrates the orbit calculation for a simple IR observation. We want to obtain images of a target in two filters, F110W and F160W. Suppose that the ETC has shown that the exposure times adequate for our scientific goals are 10 minutes in F110W and 20 minutes in F160W. These times can be achieved with the up-the-ramp MULTIACCUM sequences SPARS50 (11.7 min) and SPARS100 (23.4 min), respectively. From the orbit visibility table (see the HST Primer), suppose that we find that at the target declination the target visibility time is 52 minutes. The orbit calculation goes like this:

Table 10.5: Orbit Calculation for Example 3

Action	Time (minutes)	Explanation
Guide-star acquisition	6.0	Needed at start of observation of new target
IR overheads for 2 exposures	2 × 1.0 = 2.0	Includes filter changes, camera set-ups, and readouts

Action	Time (minutes)	Explanation
Science exposure in F110W	11.7	
Science exposure in F160W	23.4	
Total time used	43.1	

The total time used in the orbit shows that our target can indeed be imaged in the selected filters within one orbit. Furthermore, the first exposure can be dumped from the buffer during the second exposure. The ~9 minutes of unused time could be used for an additional exposure, during which the second exposure would be dumped.

10.4.4 Example 4: UVIS, dithering, 2 orbits, 1 filter

This example illustrates the orbit calculation for a UVIS observation with a WFC3 UVIS box dithering pattern, which implements imaging at four pointings. The goal of the observation is to obtain a dithered image of a field in such a way that would allow us to bridge the ~2 arcsec inter-chip gap between the UVIS CCDs in the combined image. As indicated in Table 10.1, for a 2-arcsec offset maneuver, the three dithers will take 0.5 minutes each. Suppose we have determined that the exposure time necessary to reach the desired S/N ratio is 80 minutes, and that the visibility time at our target declination is 58 minutes. Furthermore, we will use the cosmic-ray removal provided by the dither data-reduction package, and therefore set CR-SPLIT=1. As a result, the orbit calculation will involve a sequence of four exposures of 20-minutes duration (i.e., one exposure at each of the four dither pointings). These observations will be distributed across two HST orbits, as shown in the following table:

Table 10.6: Orbit Calculation for Example 4.

Action	Time (minutes)	Explanation
	Orbit 1	
Guide-star acquisition	6.0	Needed at start of observation of new target
UVIS overhead for first exposure	2.6	Includes filter change, camera set-up, and readout
UVIS overhead for second exposure	2.0	Includes readout
Spacecraft maneuver	0.5	To offset from first to second dither pointing
Two science exposures	2 × 20 = 40.0	Exposures at the first two pointings in the dither pattern
Total time used in orbit 1	51.1	
	Orbit 2	
Guide-star re-acquisition	5.0	Needed at start of new orbit to observe same target
UVIS overheads for 3rd and 4th exposures	2 × 2.0 = 4.0	Includes readouts
Spacecraft manaeuvers	2 × 0.5 = 1.0	To offset to the 3rd and 4th dither pointings
Two science exposures	2 × 20 = 40.0	Exposures at the final two pointings in the dither pattern
Total time used in orbit 2	50.0	

No overhead is incurred to dump the exposures, because they are all longer than 339 seconds. Thus the desired exposures can be accomplished within the two orbits, and in fact there are ~7-8 minutes of unused visibility time per orbit that could be used to increase the exposure times.

10.4.5 Example 5: IR, 1 orbit, grism

This example illustrates the orbit calculation for an IR G102 grism spectroscopic observation. We assume we will use the up-the-ramp MULTIACCUM sequence SPARS200 with NSAMP=13, requiring 40 minutes to expose. We will also obtain undispersed images to calibrate target positions and wavelengths, using SPARS10 (2.4-minute) exposures before and after the grism exposure. The overhead calculations are presented in Table 10.7.

Table 10.7: Orbit Calculation for Example 5.

Action	Time (minutes)	Explanation
Guide-star acquisition	6.0	Needed at start of observation of new target
IR overheads for 3 exposures	3 × 1.0 = 3.0	Includes filter changes, camera set-ups, and readouts
Science exposure (undispersed)	2 × 2.4 = 4.8	SPARS10, NSAMP=15
Science exposure (grism)	40.0	SPARS200, NSAMP=13
Total time used	53.8	

The buffer dumps incur no overhead because the first undispersed exposure can be dumped during the long grism exposures, and the last two can be dumped during the subsequent target occultation. Thus, assuming that at least 53.8 minutes of target visibility are available at the target's declination, this set of observations can be obtained in one orbit.

APPENDIX A:

Filter Throughputs

In this appendix . . .

In this Chapter, we provide imaging reference material, in support of the information presented in Chapter 9.

A.1 Introduction

This chapter provides reference material to help you select your filter and detector configuration, and determine your observing plan (e.g., total required exposure time, and number of exposures). This chapter is, for the most part, organized by *filter* and *detector*. For each imaging mode the following are provided:

- Plots of integrated system throughput as a function of wavelength.
- Plots of the time needed to achieve a desired signal-to-noise ratio vs. magnitude for all filters for a point source and a one arcseconds^2 extended source.
- Tables of color corrections AB_ν to go from Johnson V magnitude to AB magnitude for stellar spectra (as a function of effective temperature) and composite populations (as a function of age). The stellar spectra come from the Lejeune (1997, A&AS, 125, 229) grid, and assume a surface gravity of 5 and solar metallicity. The composite populations come from the "instantaneous burst" and "continuous star formation" models of Bruzual & Charlot (1993, ApJ, 405, 539), updated in 1995, assuming a Salpeter IMF spanning 0.1 to 125 solar masses.

A.2 Using the Information in this Chapter

A.2.1 Sensitivity Units and Conversions

This chapter contains plots of throughputs for each imaging mode. "Determining Count Rates from Sensitivities" in Section 9.2 explains how to use these throughputs to calculate expected count rates from your source.

The first figure for each imaging mode gives the integrated system throughput. This is the combination of the efficiencies of the detector and of the optical elements in the light path. The throughputs in this handbook are based on ground test data. The throughput is defined as the number of detected counts/second/cm^2 of telescope area relative to the incident flux in photons/cm^2/second. For the both channels (UVIS and IR), “counts” is the number of electrons detected. In both channels the detected counts obey Poisson statistics. At short wavelengths in the UVIS channel, a single incoming photon has a finite chance of producing two electrons in the CCD; the plots shown in this chapter have been corrected for this "quantum yield" effect. The throughput includes all obscuration effects in the optical train (e.g., due to the HST secondary).

To recalculate the throughput with the most recent detector QE tables in ***synphot***, you can create total-system-throughput tables (instrument plus OTA) using the ***synphot calcband*** task. ***calcband*** takes any valid obsmode command string as input and produces an STSDAS table with two columns of data called “wavelength” and “throughput” as its output. For example, to evaluate the throughput for the F475W

filter and the UVIS detector, chip 1, you would use the command ***calcband wfc3,uvis1,f475w sdssg_thpt.*** The resulting throughput table is stored in ***sdssg_thpt***.

A.2.2 Signal-to-Noise

For each imaging mode, plots are provided to estimate the signal-to-noise ratio (S/N) for a representative source. The first figure shows S/N for point sources. The second figure shows S/N for uniform extended sources of area 1 arcseconds^2.

The different line styles in the S/N figures delineate regions where different sources of noise dominate. If the total noise from backgrounds (read noise, sky, thermal, dark) is larger than the noise from the source, the observation is considered to be background-dominated, and the line style reflects which of these background is largest. Note that for the WFC3 detectors, the dark current can never be the largest source of noise when a source is background-dominated, because the read noise is always larger than the dark count noise when exposures are 1000 sec or less. The point- and extended-source S/N figures assume average sky levels. These plots also indicate where an observation will saturate the full well of the detector.

For point sources, an aperture size of 5 x 5 pixels has been used for the UVIS channel, while an aperture size of 3 x 3 pixels has been used for the IR channel. For extended sources, a 1 arcseconds^2 aperture was used. The read noise has been computed assuming a number of readouts `NREAD`= integer (t / 1000 seconds), where t is the exposure time, with a minimum `NREAD=2`.

In situations requiring more detailed calculations (non-stellar spectra, extended sources, other sky background levels, unknown target V magnitude, etc.), the WFC3 Exposure-Time Calculator should be used.

Follow these steps to use the signal-to-noise plots:

1. Determine the AB magnitude of your source at the wavelength of interest. There are several ways to do this.
   - Examine Table 10.1, 10.2, or 10.3 and find AB_ν for the desired spectral type and filter. Sum the V magnitude of the target and AB_ν derived from the table.
   - Alternatively, compute ABMAG (=V+ABν) from the source flux, using the relation $ABMAG = -2.5\log f_\nu - 48.60$, or $ABMAG = -2.5\log f_\lambda - 5\log\lambda - 2.406$.
2. Find the appropriate plot for the filter in question, and locate $V+AB_\nu$ on the horizontal axis. Then read off the signal-to-noise ratio for the desired exposure time, or vice-versa.

Note that the plots show the S/N as a function of source magnitude for exposure times as short as 0.1 seconds, although the minimum exposure time for the UVIS channel is 0.5 seconds.

WFC/F435W

Description

Johnson B filter.

Figure 10.5: Integrated system throughput for WFC/F435W.

Figure 10.6: Point source S/N vs. V+ABν for the WFC/F435W filter. Top curves are for low sky; bottom curves are for average sky.

Figure 10.7: Extended source S/N vs. V+ABν for the WFC/F435W filter. Top curves are for low sky and bottom curves are for average sky for a 1 arcsec^2 area.

WFC/F475W

Description

Sloan Digital Sky Survey g filter.

Figure 10.8: Integrated system throughput for WFC/F475W.

Figure 10.9: Point source S/N vs. V+ABν for the WFC/F475W filter. Top curves are for low sky; bottom curves are for average sky.

Figure 10.10: Extended source S/N vs. V+ABν for the WFC/F475W filter. Top curves are for low sky and bottom curves are for average sky for

a 1 arcsec^2 area.

WFC/F502N

Description

OIII filter.

Figure 10.11: Integrated system throughput for WFC/F502N.

Figure 10.12: Point source S/N vs. V+ABν for the WFC/F502N filter. Top curves are for low sky; bottom curves are for average sky.

Figure 10.13: Extended source S/N vs. V+ABν for the WFC/F502N filter. Top curves are for low sky and bottom curves are for average sky for a 1 arcsec^2 area.

WFC/F550M

Description

Narrow V filter.

Figure 10.14: Integrated system throughput for WFC/F550M.

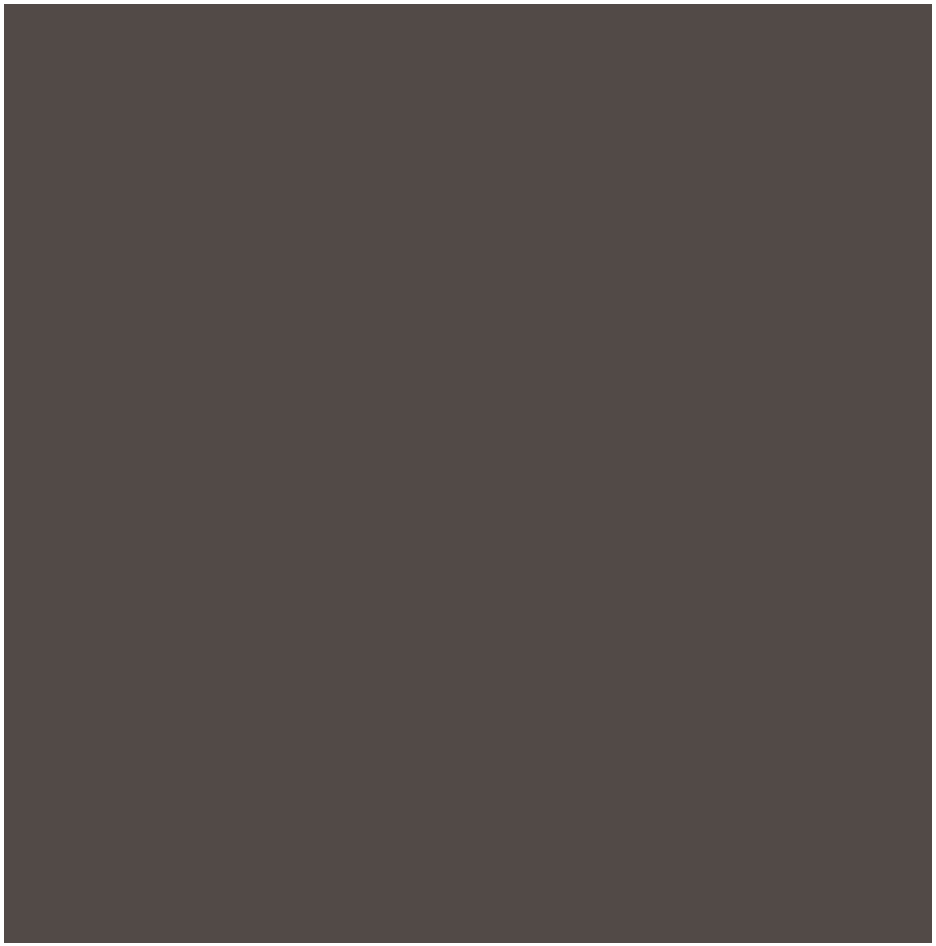

Figure 10.15: Point source S/N vs. V+ABν for the WFC/F550M filter. Top curves are for low sky; bottom curves are for average sky.

Figure 10.16: Extended source S/N vs. V+ABν for the WFC/F550M filter. Top curves are for low sky and bottom curves are for average sky for

a 1 arcsec^2 area.

WFC/F555W

Description

Johnson V filter.

Figure 10.17: Integrated system throughput for WFC/F555W.

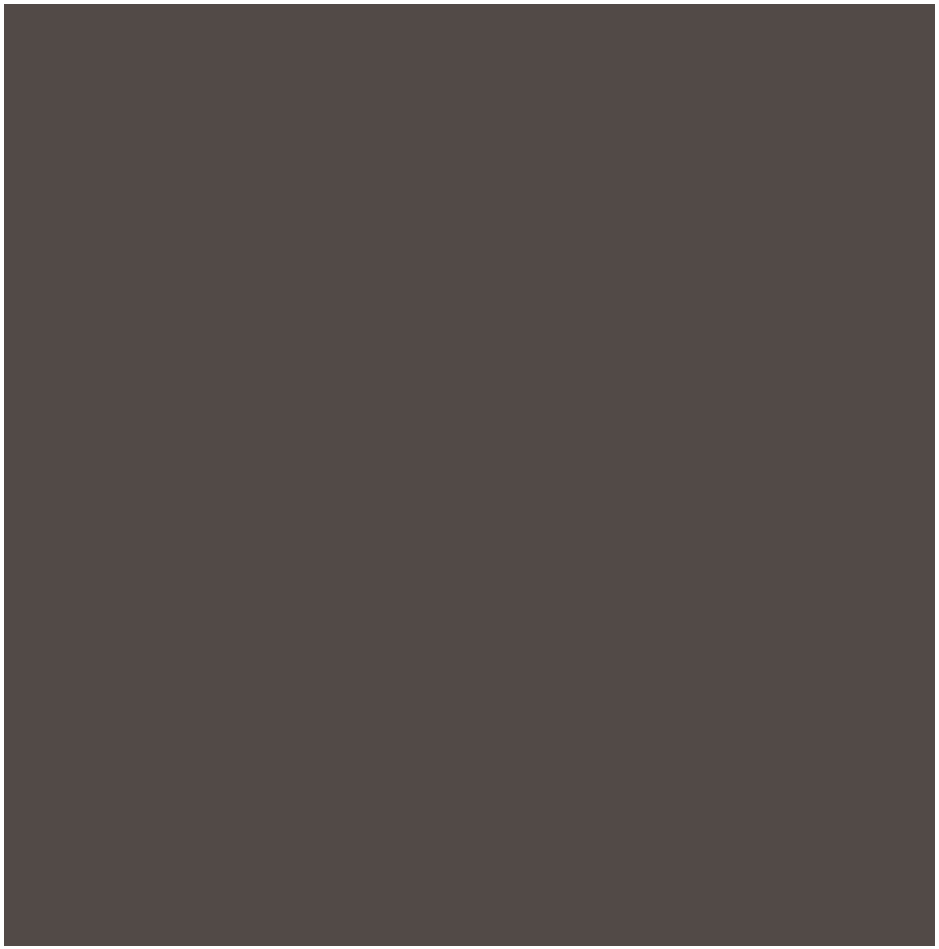

Figure 10.18: Point source S/N vs. V+AB$_\nu$ for the WFC/F555W filter. Top curves are for low sky; bottom curves are for average sky.

Figure 10.19: Extended source S/N vs. V+AB$_\nu$ for the WFC/F555W filter. Top curves are for low sky and bottom curves are for average sky for

a 1 arcsec^2 area.

WFC/F606W

Description

Broad V filter.

Figure 10.20: Integrated system throughput for WFC/F606W.

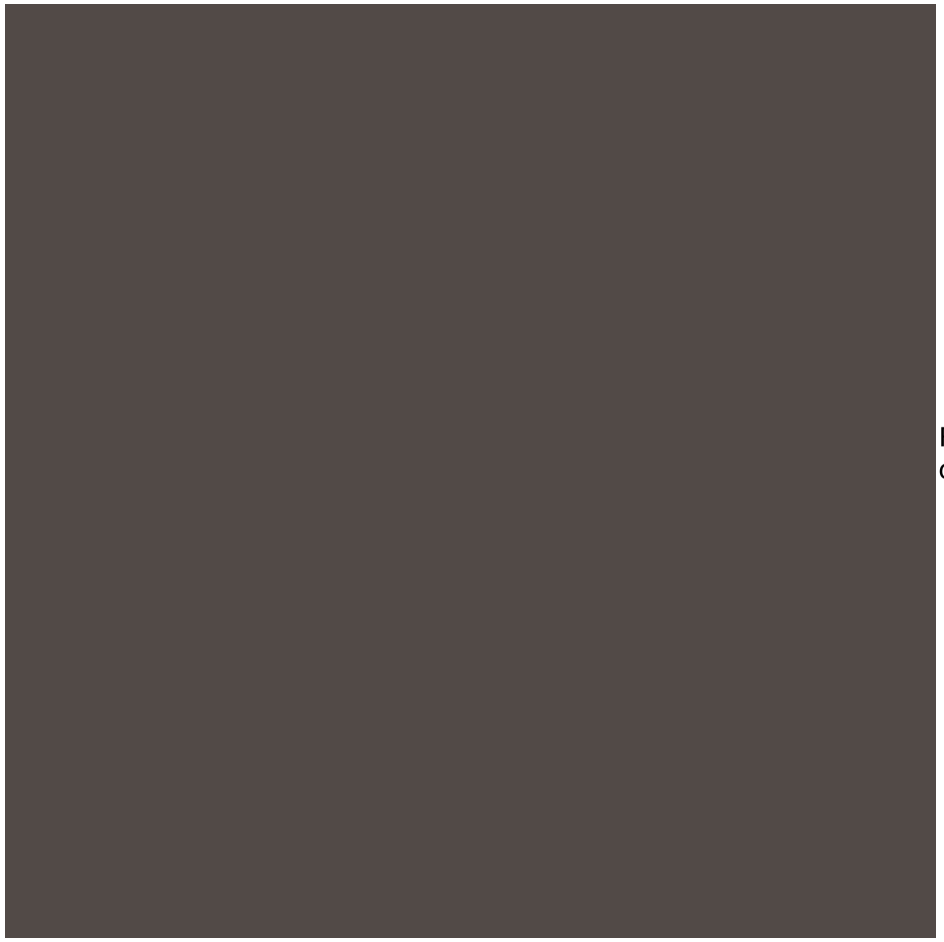

Figure 10.21: Point source S/N vs. V+AB$_\nu$ for the WFC/F606W filter. Top curves are for low sky; bottom curves are for average sky.

Figure 10.22: Extended source S/N vs. V+AB$_\nu$ for the WFC/F606W. Top curves are for low sky and bottom curves are for average sky for a

1arcsec^2 area.

WFC/F625W

Description

Sloan Digital Sky Survey r filter.

Figure 10.23: Integrated system throughput for WFC/F625W.

Figure 10.24: Point source S/N vs. V+AB$_\nu$ for the WFC/F625W filter. Top curves are for low sky; bottom curves are for average sky.

Figure 10.25: Extended source S/N vs. V+ABν for the WFC/F625W filter. Top curves are for low sky and bottom curves are for average sky for a 1 arcsec^2 area.

WFC/F658N

Description

Hα filter.

Figure 10.26: Integrated system throughput for WFC/F658N.

Figure 10.27: Point source S/N vs. V+ABν for the WFC/F658N filter. Top curves are for low sky; bottom curves are for average sky.

Figure 10.28: Extended source S/N vs. V+ABν for the WFC/F658N filter. Top curves are for low sky and bottom curves are for average sky for 1 arcsec^2 area.

WFC/F660N

Description

NII filter.

Figure 10.29: Integrated system throughput for WFC/F660N.

Figure 10.30: Point source S/N vs. V+ABν for the WFC/F660N filter. Top curves are for low sky; bottom curves are for average sky.

Figure 10.31: Extended source S/N vs. V+ABν for the WFC/F660N filter. Top curves are for low sky and bottom curves are for average sky for a 1 arcsec^2 area.

WFC/F775W

Description

Sloan Digital Sky Survey i filter

Figure 10.32: Integrated system throughput for WFC/F775W.

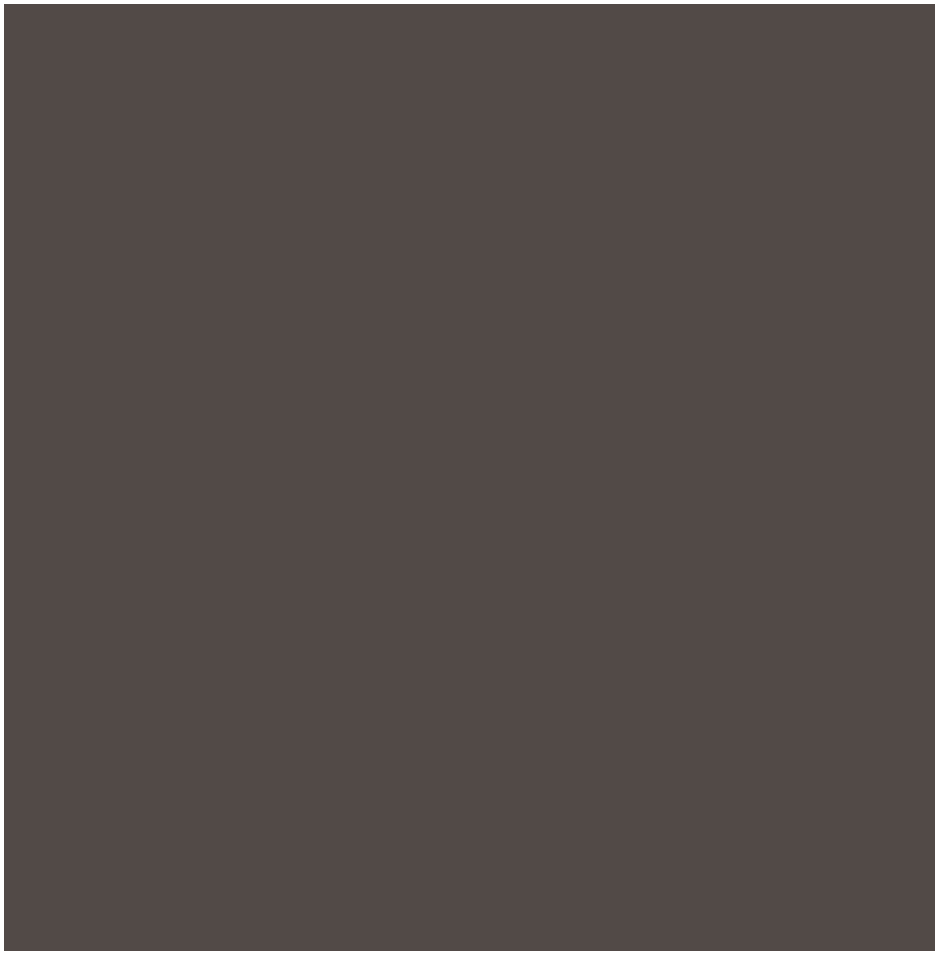

Figure 10.33: Point source S/N vs. V+AB$_\nu$ for the WFC/F775W filter. Top curves are for low sky; bottom curves are for average sky.

Figure 10.34: Extended source S/N vs. V+ABν for the WFC/F775W filter. Top curves are for low sky and bottom curves are for average sky for a 1 arcsec^2 area.

WFC/F814W

Description

Broad I filter.

Figure 10.35: Integrated system throughput for WFC/F814W.

Figure 10.36: Point source S/N vs. V+AB$_\nu$ for the WFC/F814W filter. Top curves are for low sky; bottom curves are for average sky.

Figure 10.37: Extended source S/N vs. V+ABν for the WFC/F814W filter. Top curves are for low sky and bottom curves are for average sky for a 1 arcsec^2 area.

WFC/F850LP

Description

Sloan Digital Sky Survey z filter.

Figure 10.38: Integrated system throughput for WFC/F850LP.

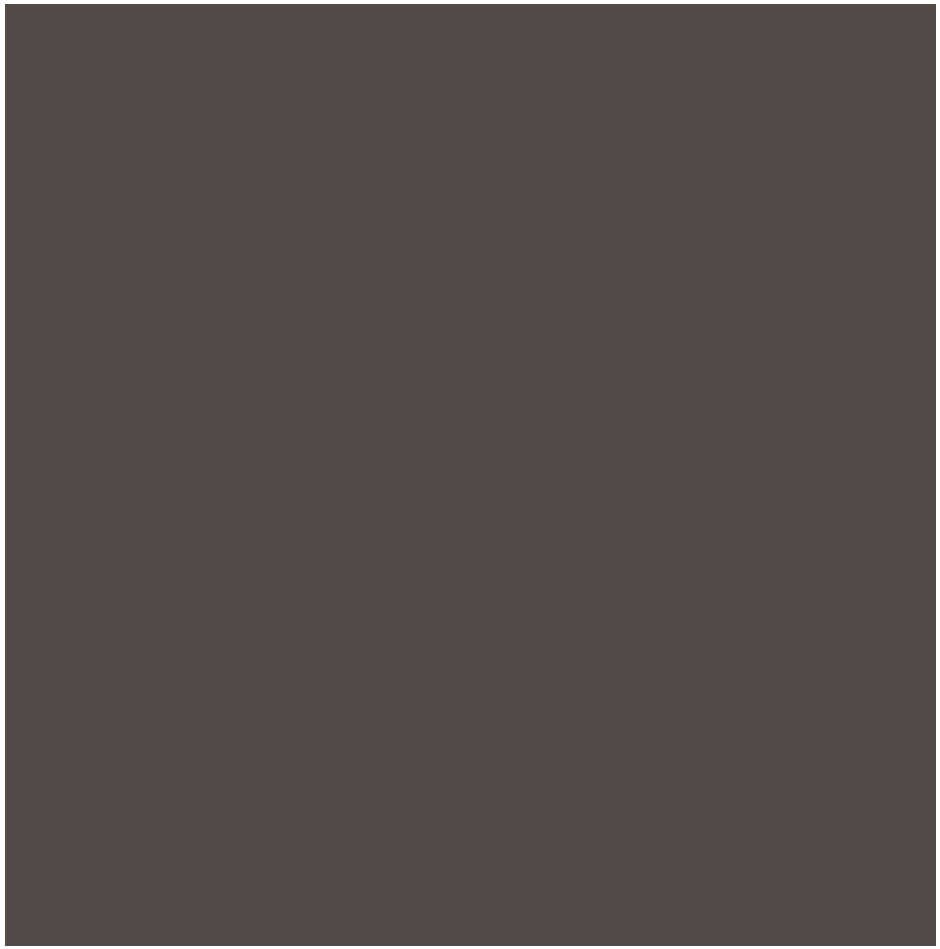

Figure 10.39: Point source S/N vs. V+AB$_\nu$ for the WFC/F850LP filter. Top curves are for low sky; bottom curves are for average sky.

Figure 10.40: Extended source S/N vs. V+ABν for the WFC/F850LP filter. Top curves are for low sky and bottom curves are for average sky for a 1arcsec^2 area.

WFC/G800L

Description

Grism.

Figure 10.41: Integrated system throughput for WFC/G800L.

Figure 10.42: Point source S/N vs. V+AB$_\nu$ for the WFC/G800L filter. Top curves are for low sky; bottom curves are for average sky.

Figure 10.43: Extended source S/N vs. V+ABν for the WFC/G800L filter. Top curves are for low sky and bottom curves are for average sky for a 1arcsec^2 area.

WFC/CLEAR

Description

Clear filter.

Figure 10.44: Integrated system throughput for WFC/Clear.

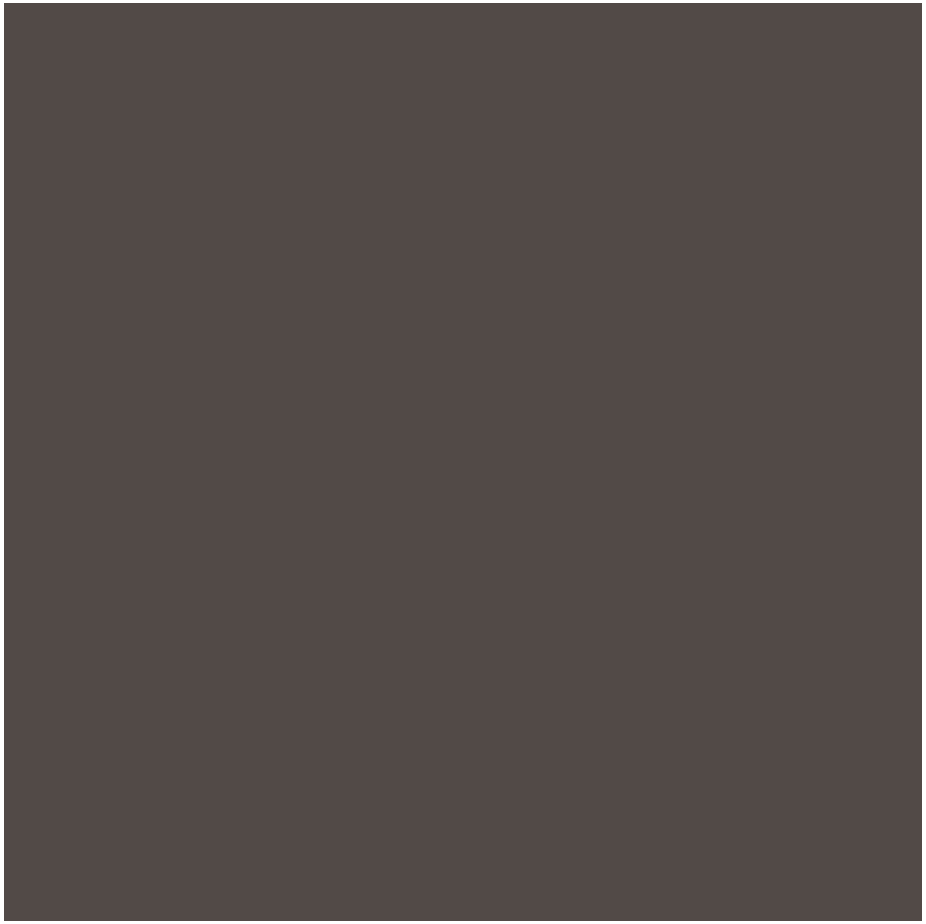

Figure 10.45: Point source S/N vs. V+AB$_\nu$ for the WFC/Clear filter. Top curves are for low sky; bottom curves are for average sky.

Figure 10.46: Extended source S/N vs. V+ABν for the WFC/Clear filter. Top curves are for low sky and bottom curves are for average sky for a 1 arcsec^2 area.

HRC/F220W

Description

Near-UV filter.

Figure 10.47: Integrated system throughput for HRC/F220W.

Figure 10.48: Point source S/N vs. V+AB$_\nu$ for the HRC/F220W filter. Top curves are for low sky; bottom curves are for average sky.

Figure 10.49: Extended source S/N vs. V+ABν for the HRC/F220W filter. Top curves are for low sky and bottom curves are for average sky for a 1 arcsec^2 area.

HRC/F250W

Description

Near-UV filter.

Figure 10.50: Integrated system throughput for HRC/F250W.

Figure 10.51: Point Source S/N vs. V+AB$_\nu$ for the HRC/F250W filter. Top curves are for low sky; bottom curves are for average sky.

Figure 10.52: Extended Source S/N vs. V+AB$_\nu$ for the HRC/F250W filter. Top curves are for low sky and bottom curves are for average sky for a 1 arcsec^2 area.

HRC/F330W

Description

HRC u filter.

Figure 10.53: Integrated system throughput for HRC/F330W.

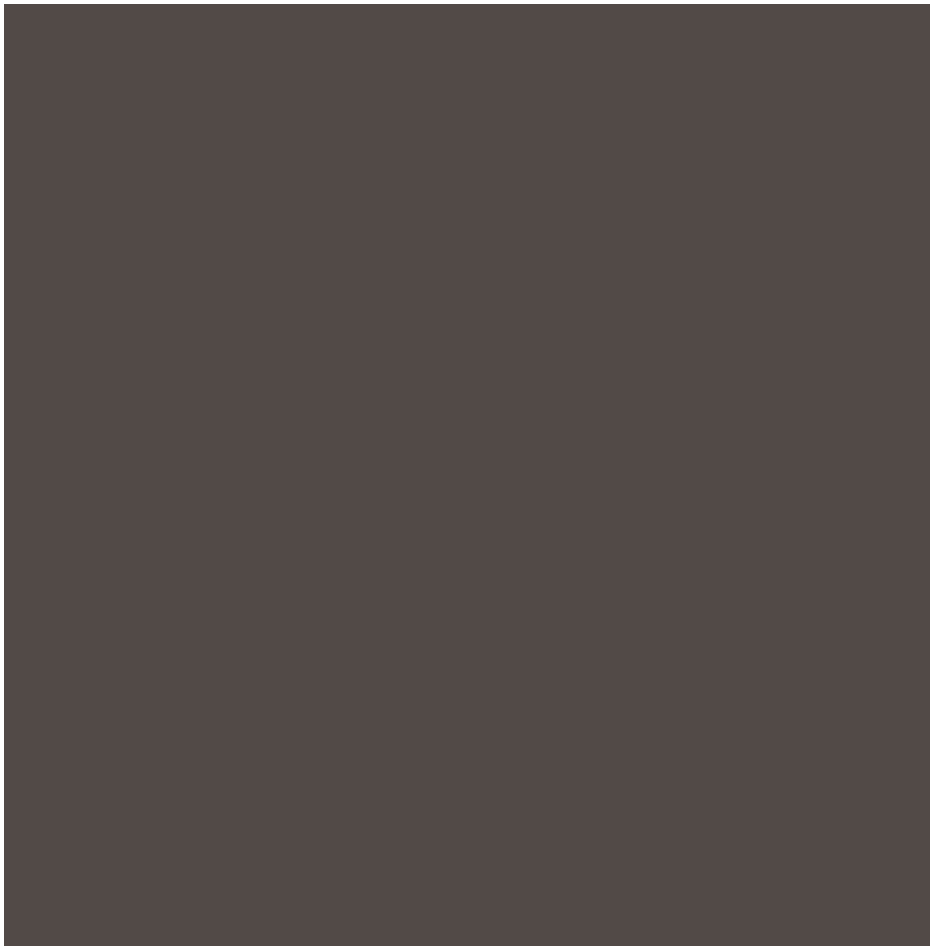

Figure 10.54: Point source S/N vs. V+ABν for the HRC/F330W filter. Top curves are for low sky; bottom curves are for average sky.

Figure 10.55: Extended source S/N vs. V+ABν for the HRC/F330W filter. Top curves are for low sky and bottom curves are for average sky for a 1 arcsec^2 area.

HRC/F344N

Description

NeV filter.

Figure 10.56: Integrated system throughput for HRC/F344N.

Figure 10.57: Point source S/N vs. V+AB$_\nu$ for the HRC/F344N filter. Top curves are for low sky; bottom curves are for average sky.

Figure 10.58: Extended source S/N vs. V+AB$_\nu$ for the HRC/F344N filter. Top curves are for low sky and bottom curves are for average sky for a 1 arcsec^2 area.

HRC/F435W

Description

Johnson B filter.

Figure 10.59: Integrated system throughput for HRC/F435W.

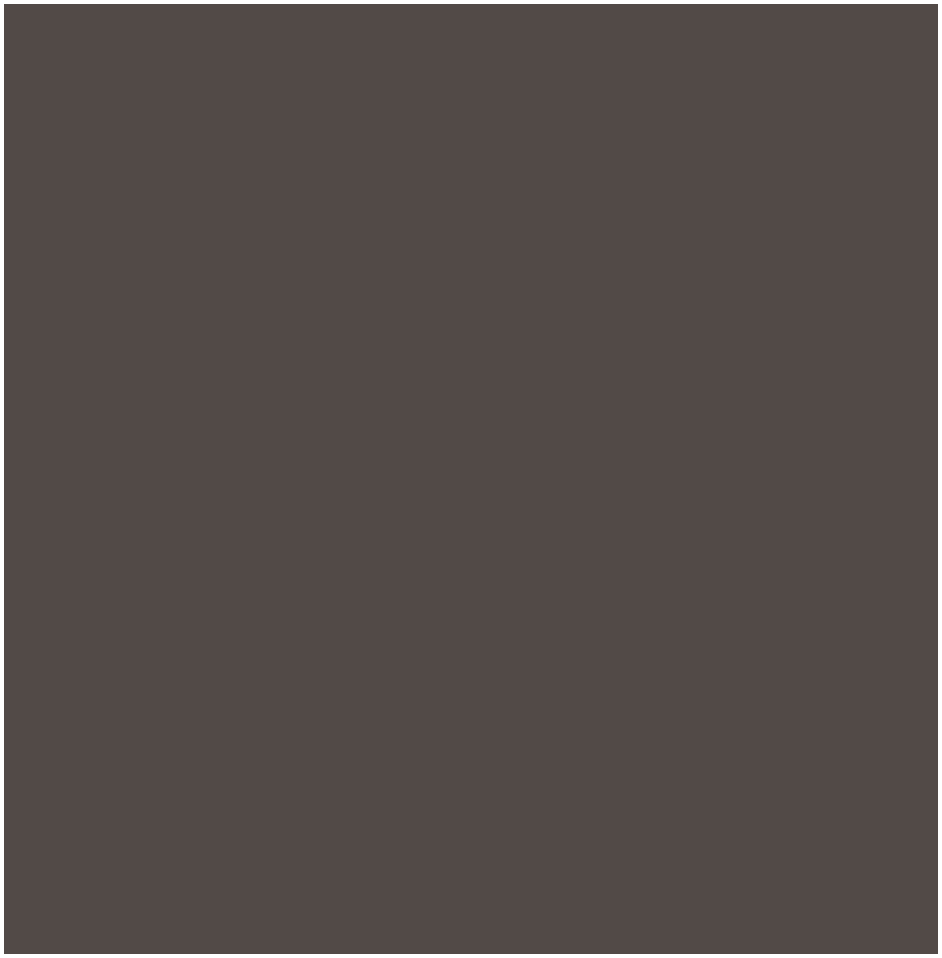

Figure 10.60: Point source S/N vs. V+ABν for the HRC/F435W filter. Top curves are for low sky; bottom curves are for average sky.

Figure 10.61: Extended source S/N vs. V+ABν for the HRC/F435W filter. Top curves are for low sky and bottom curves are for average sky for a 1 arcsec^2 area.

HRC/F475W

Description

Sloan Digital Sky Survey g filter.

Figure 10.62: Integrated system throughput for HRC/F475W.

Figure 10.63: Point source S/N vs. V+AB$_\nu$ for the HRC/F475W filter. Top curves are for low sky; bottom curves are for average sky.

Figure 10.64: Extended source S/N vs. V+ABν for the HRC/F475W filter. Top curves are for low sky and bottom curves are for average sky for a 1 arcsec^2 area.

HRC/F502N

Description

OIII filter.

Figure 10.65: Integrated system throughput for HRC/F502N.

Figure 10.66: Point source S/N vs. V+ABν for the HRC/F502N filter. Top curves are for low sky; bottom curves are for average sky.

Figure 10.67: Extended source S/N vs. V+AB$_\nu$ for the HRC/F502N filter. Top curves are for low sky and bottom curves are for average sky for a 1 arcsec^2 area.

HRC/F550M

Description

Narrow V filter.

Figure 10.68: Integrated system throughput for HRC/F550M.

Figure 10.69: Point source S/N vs. V+ABν for the HRC/F550M filter. Top curves are for low sky; bottom curves are for average sky.

Figure 10.70: Extended source S/N vs. V+ABν for the HRC/F550M filter. Top curves are for low sky and bottom curves are for average sky for a 1 arcsec^2 area.

HRC/F555W

Description

Johnson V filter.

Figure 10.71: Integrated system throughput for HRC/F555W.

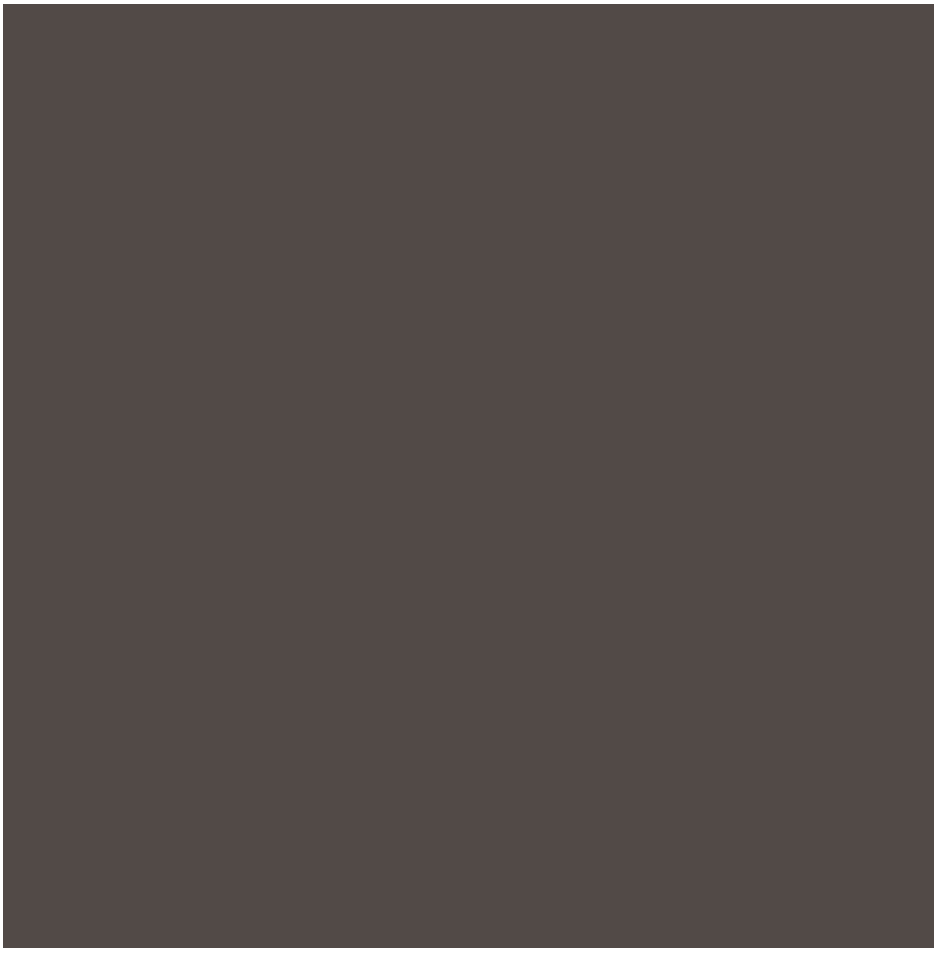

Figure 10.72: Point source S/N vs. V+ABν for the HRC/F555W filter. Top curves are for low sky; bottom curves are for average sky.

Figure 10.73: Extended source S/N vs. V+ABν for the HRC/F555W filter. Top curves are for low sky and bottom curves are for average sky for a 1 arcsec^2 area.

HRC/F606W

Description

Broad V filter.

Figure 10.74: Integrated system throughput for HRC/F606W.

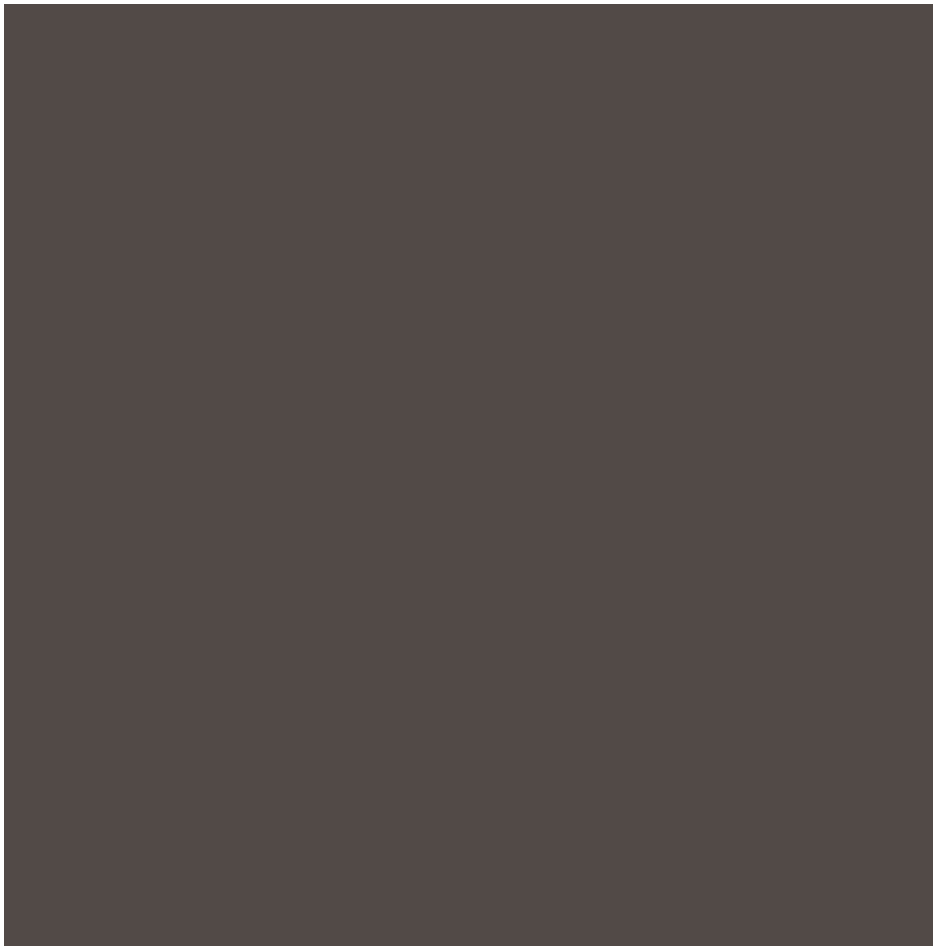

Figure 10.75: Point source S/N vs. V+ABν for the HRC/F606W filter. Top curves are for low sky; bottom curves are for average sky.

Figure 10.76: Extended source S/N vs. V+ABν for the HRC/F606W filter. Top curves are for low sky and bottom curves are for average sky for a 1 arcsec^2 area.

HRC/F625W

Description

Sloan Digital Sky Survey r filter.

Figure 10.77: Integrated system throughput for HRC/F625W.

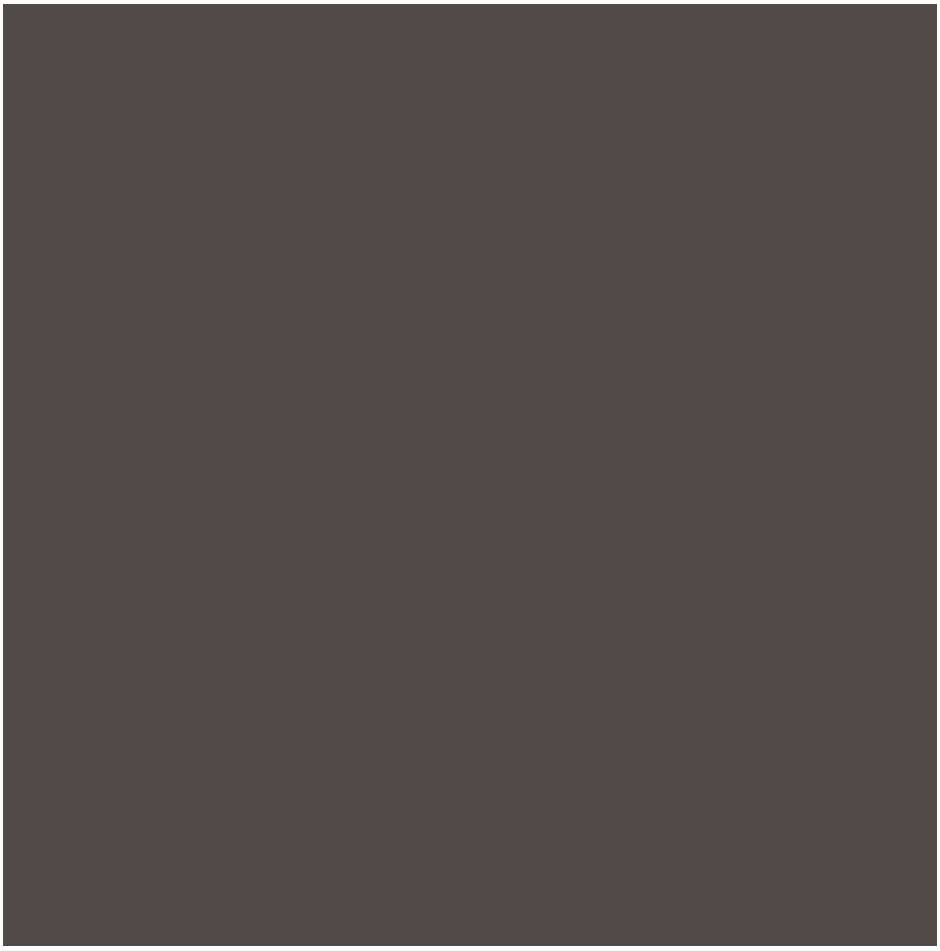

Figure 10.78: Point source S/N vs. V+ABν for the HRC/F625W filter. Top curves are for low sky; bottom curves are for average sky.

Figure 10.79: Extended source S/N vs. V+ABν for the HRC/F625W filter. Top curves are for low sky and bottom curves are for average sky for a 1 arcsec^2 area.

HRC/F658N

Description

Hα filter.

Figure 10.80: Integrated system throughput for HRC/F658N.

Figure 10.81: Point source S/N vs. V+ABν for the HRC/F658N filter. Top curves are for low sky; bottom curves are for average sky.

Figure 10.82: Extended source S/N vs. V+ABν for the HRC/F658N filter. Top curves are for low sky and bottom curves are for average sky for a 1 arcsec^2 area.

HRC/F660N

Description

NII filter.

Figure 10.83: Integrated system throughput for HRC/F660N.

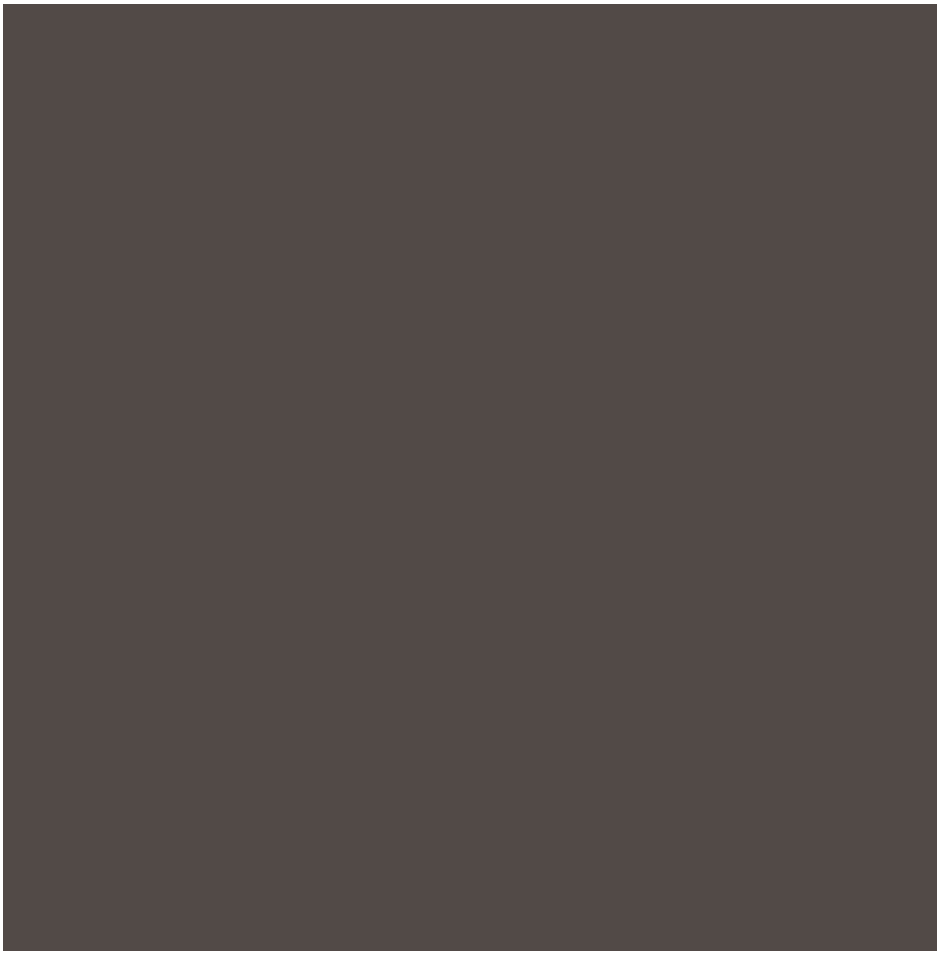

Figure 10.84: Point source S/N vs. V+ABν for the HRC/F660N filter. Top curves are for low sky; bottom curves are for average sky.

Figure 10.85: Extended source S/N vs. V+ABν for the HRC/F660N filter. Top curves are for low sky and bottom curves are for average sky for a 1 arcsec^2 area.

HRC/F775W

Description

Sloan Digital Sky Survey i filter.

Figure 10.86: Integrated system throughput for HRC/F775W.

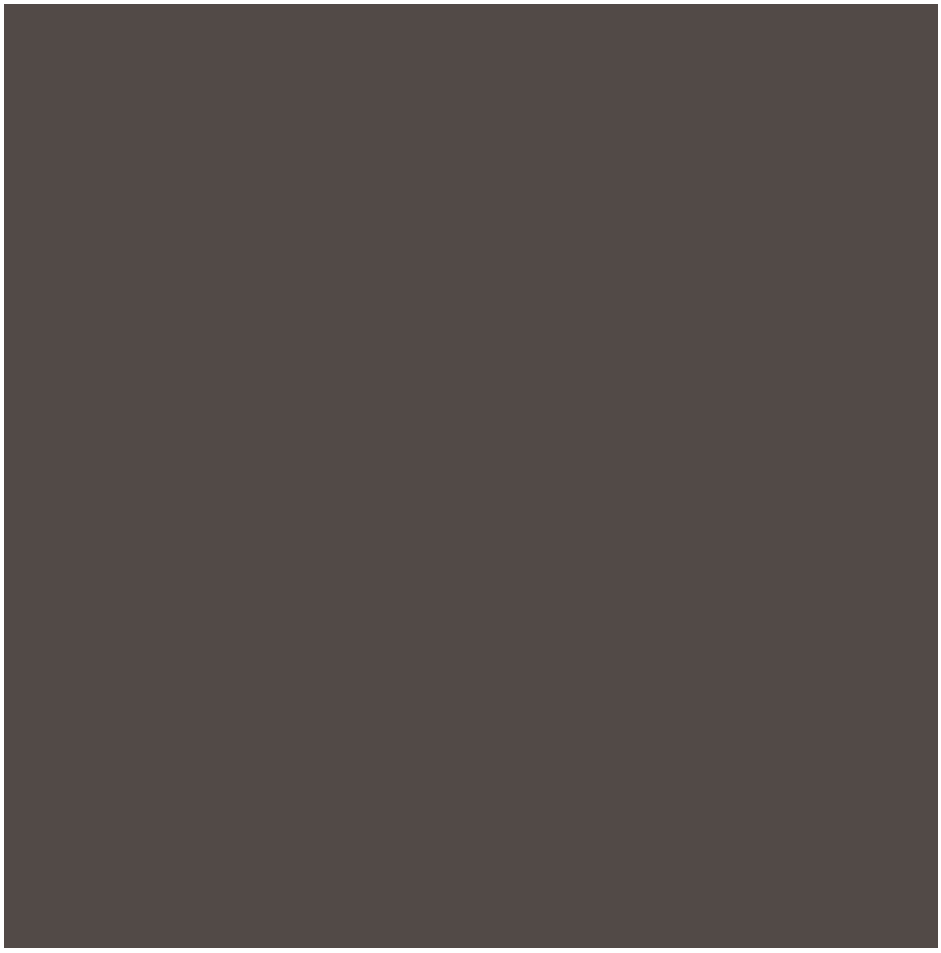

Figure 10.87: Point source S/N vs. V+ABν for the HRC/F775W filter. Top curves are for low sky; bottom curves are for average sky.

Figure 10.88: Extended source S/N vs. V+ABν for the HRC/F775W filter. Top curves are for low sky and bottom curves are for average sky for a 1 arcsec^2 area.

HRC/F814W

Description

Broad I filter.

Figure 10.89: Integrated system throughput for HRC/F814W.

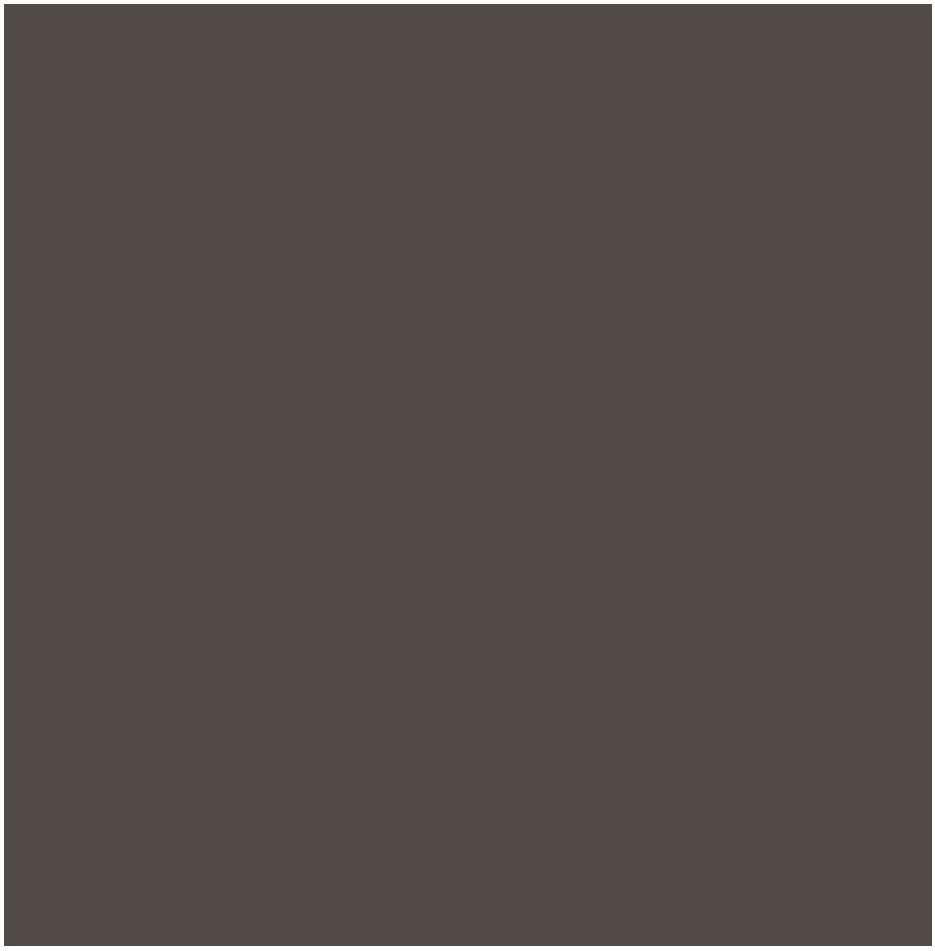

Figure 10.90: Point source S/N vs. V+ABν for the HRC/F814W filter. Top curves are for low sky; bottom curves are for average sky.

Figure 10.91: Extended source S/N vs. V+ABν for the HRC/F814W filter. Top curves are for low sky and bottom curves are for average sky for a 1 arcsec^2 area.

HRC/F850LP

Description

Sloan Digital Sky Survey z filter.

Figure 10.92: Integrated system throughput for HRC/F850LP.

Figure 10.93: Point source S/N vs. V+ABν for the HRC/F850LP filter. Top curves are for low sky; bottom curves are for average sky.

Figure 10.94: Extended source S/N vs. V+ABν for the HRC/F850LP filter. Top curves are for low sky and bottom curves are for average sky for a 1 arcsec^2 area.

HRC/F892N

Description

Methane filter.

Figure 10.95: Integrated system throughput for HRC/F892N.

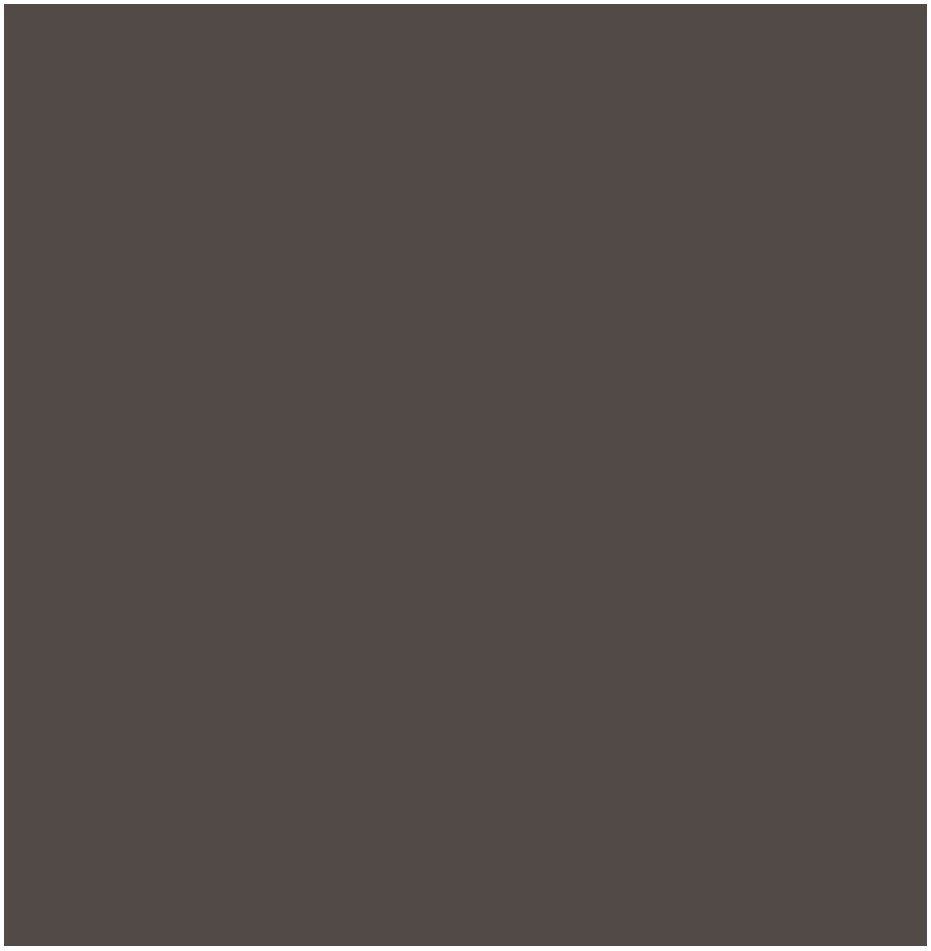

Figure 10.96: Point source S/N vs. V+ABν for the HRC/F892N filter. Top curves are for low sky; bottom curves are for average sky.

Figure 10.97: Extended source S/N vs. V+ABν for the HRC/F892N filter. Top curves are for low sky and bottom curves are for average sky for a 1 arcsec^2 area.

HRC/G800L

Description

Grism.

Figure 10.98: Integrated system throughput for HRC/G800L.

Figure 10.99: Point source S/N vs. V+ABν for the HRC/G800L filter. Top curves are for low sky; bottom curves are for average sky.

Figure 10.100: Extended source S/N vs. V+ABν for the HRC/G800L filter. Top curves are for low sky and bottom curves are for average sky for a 1 arcsec^2 area.

HRC/PR200L

Description

HRC Prism.

Figure 10.101: Integrated system throughput for HRC/PR200L.

Figure 10.102: Point source S/N vs. V+ABν for the HRC/PR200L filter. Top curves are for low sky; bottom curves are for average sky.

Figure 10.103: Extended source S/N vs. V+ABν for the HRC/PR200L filter. Top curves are for low sky and bottom curves are for average sky for a 1 arcsec^2 area.

HRC/CLEAR

Description

HRC Clear Filter.

Figure 10.104: Integrated system throughput for HRC/Clear

Figure 10.105: Point source S/N vs. V+ABν for the HRC/Clear filter. Top curves are for low sky; bottom curves are for average sky.

Figure 10.106: Extended source S/N vs. V+ABν for the HRC/Clear filter. Top curves are for low sky and bottom curves are for average sky for a 1 arcsec^2 area.

SBC/F115LP

Description

MgF_2 filter.

Figure 10.107: Integrated system throughput for SBC/F115LP.

Figure 10.108: Point source S/N vs. V+ABν for the SBC/F115LP filter.Top curves are for low sky; bottom curves are for average sky.

Figure 10.109: Extended source S/N vs. V+ABν for the SBC/F115LP filter. Top curves are for low sky and bottom curves are for average sky for a 1 arcsec^2 area.

SBC/F122M

Description

Lyman α filter.

Figure 10.110: Integrated system throughput for SBC/F122M.

Figure 10.111: Point source S/N vs. V+ABν for the SBC/F122M filter.Top curves are for low sky; bottom curves are for average sky.

Figure 10.112: Extended source S/N vs. V+ABν for the SBC/F122M filter. Top curves are for low sky and bottom curves are for average sky for a 1 arcsec^2 area.

SBC/F125LP

Description

CaF_2 filter.

Figure 10.113: Integrated system throughput for SBC/F125LP.

Figure 10.114: Point source S/N vs. V+ABν for the SBC/F125LP filter. Top curves are for low sky; bottom curves are for average sky.

Figure 10.115: Extended source S/N vs. V+ABν for the SBC/F125LP filter. Top curves are for low sky and bottom curves are for average sky for a 1 arcsec^2 area.

SBC/F140LP

Description

BaF_2 filter.

Figure 10.116: Integrated system throughput for SBC/F140LP.

Figure 10.117: Point source S/N vs. V+ABν for the SBC/F140LP filter. Top curves are for low sky; bottom curves are for average sky.

Figure 10.118: Extended source S/N vs. V+ABν for the SBC/F140LP filter. Top curves are for low sky and bottom curves are for average sky for a 1 arcsec^2 area.

SBC/F150LP

Description

Crystal Quartz filter.

Figure 10.119: Integrated system throughput for SBC/F165LP.

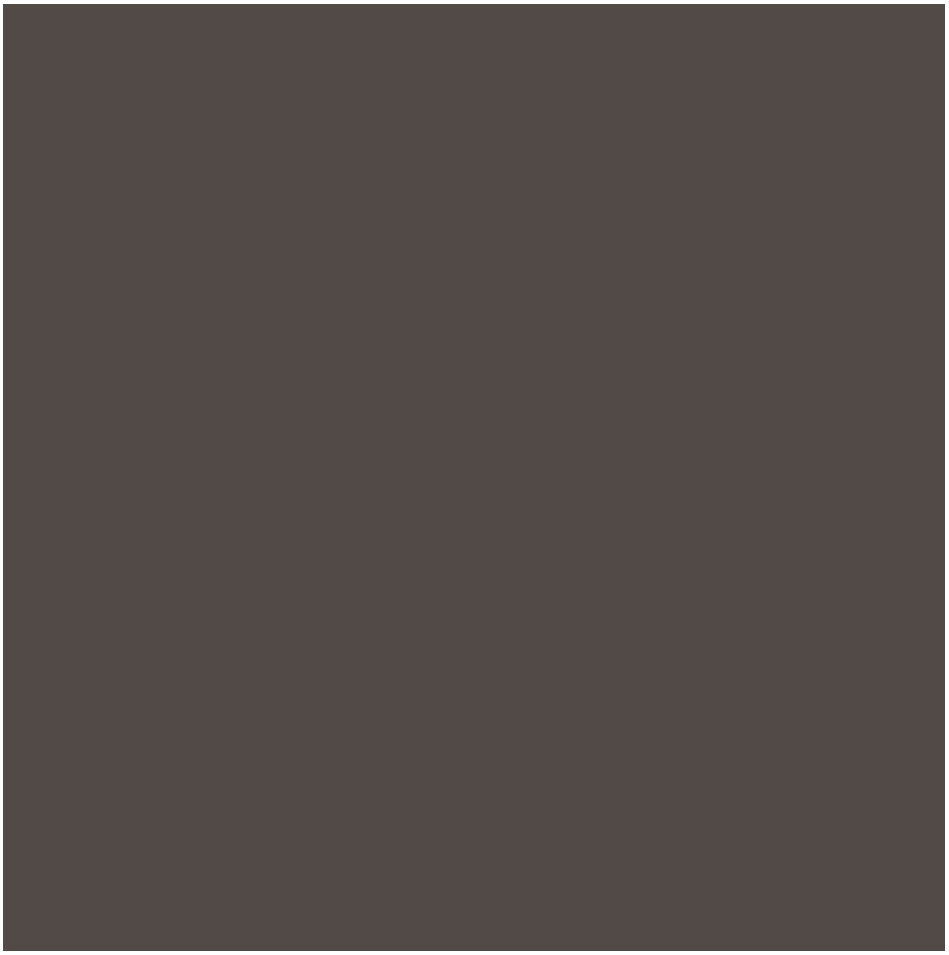

Figure 10.120: Point source S/N vs. V+ABν for the SBC/F150LP filter. Top curves are for low sky; bottom curves are for average sky.

Figure 10.121: Extended source S/N vs. V+ABν for the SBC/F150LP filter. Top curves are for low sky and bottom curves are for average sky for a 1 arcsec^2 area.

SBC/F165LP

Description

Dynasil filter.

Figure 10.122: Integrated system throughput for SBC/F165LP.

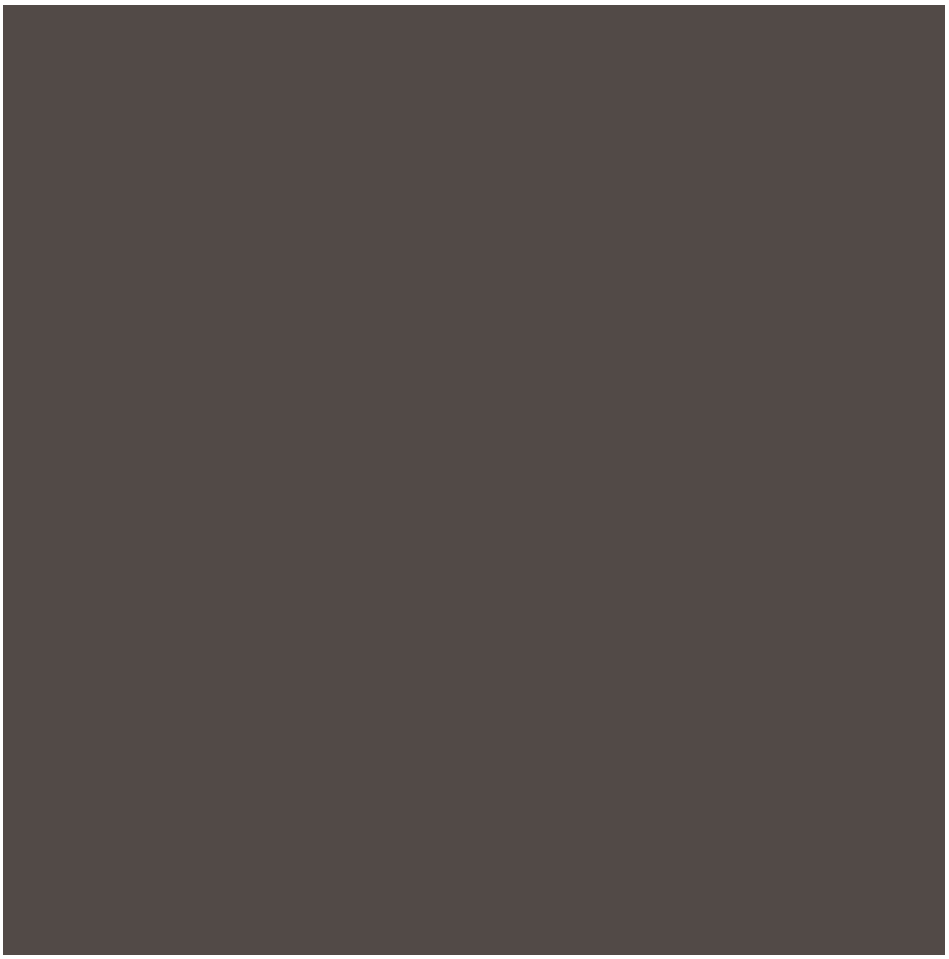

Figure 10.123: Point source S/N vs. V+ABν for the SBC/F165LP filter.Top curves are for low sky; bottom curves are for average sky.

Figure 10.124: Extended source S/N vs. V+ABν for the SBC/F165LP filter. Top curves are for low sky and bottom curves are for average sky for a 1 arcsec^2 area.

SBC/PR110L

Description

LiF_2 Prism.

Figure 10.125: Integrated system throughput for SBC/PR110LP.

Figure 10.126: Point source S/N vs. V+ABν for the SBC/PR110LP filter. Top curves are for low sky; bottom curves are for average sky.

Figure 10.127: Extended source S/N vs. V+ABν for the SBC/PR110LP filter. Top curves are for low sky and bottom curves are for average sky for a 1 arcsec^2 area.

SBC/PR130L

Description

CaF_2 Prism.

Figure 10.128: Integrated system throughput for SBC/PR130LP.

Figure 10.129: Point source S/N vs. V+ABν for the SBC/PR130LP filter. Top curves are for low sky; bottom curves are for average sky.

Figure 10.130: Extended source S/N vs. V+ABν for the SBC/PR130LP filter. Top curves are for low sky and bottom curves are for average sky for a 1 arcsec^2 area.

Table 10.6: Color corrections AB_ν to go from Johnson V magnitude to AB magnitude for WFC3 as a function of stellar effective temperature.

	T_{eff}							
Mode	**2500K**	**5000K**	**7500K**	**10000K**	**15000K**	**20000K**	**30000K**	**50000K**
UVIS/F200LP	-2.22	0.45	0.48	0.40	0.08	-0.12	-0.40	-0.57
UVIS/F218W	7.21	7.82	2.95	1.51	0.09	-0.53	-1.22	-1.55
UVIS/F225W	6.07	7.22	2.84	1.51	0.12	-0.49	-1.15	-1.46

Table 10.6: Color corrections AB_V to go from Johnson V magnitude to AB magnitude for WFC3 as a function of stellar effective temperature.

	T_{eff}							
Mode	**2500K**	**5000K**	**7500K**	**10000K**	**15000K**	**20000K**	**30000K**	**50000K**
UVIS/F275W	7.30	5.30	2.27	1.35	0.10	-0.42	-0.96	-1.24
UVIS/F280N	3.29	4.49	2.50	1.44	0.13	-0.40	-0.90	-1.17
UVIS/F300X	5.96	4.05	1.98	1.26	0.10	-0.39	-0.91	-1.19
UVIS/F336W	4.98	2.71	1.31	1.00	0.10	-0.26	-0.64	-0.86
UVIS/F343N	4.74	2.62	1.24	0.97	0.11	-0.24	-0.60	-0.82
UVIS/F350LP	-2.64	0.07	0.18	0.18	0.09	0.04	-0.02	-0.07
UVIS/F373N	7.03	2.53	1.10	0.94	0.21	-0.09	-0.43	-0.65
UVIS/F390M	4.25	2.08	0.67	0.25	-0.20	-0.33	-0.48	-0.60
UVIS/F390W	3.80	1.63	0.59	0.26	-0.14	-0.29	-0.47	-0.60
UVIS/F395N	3.91	1.92	0.67	0.15	-0.27	-0.37	-0.49	-0.58
UVIS/F410M	2.96	1.16	0.29	-0.10	-0.32	-0.39	-0.46	-0.52
UVIS/F438W	2.28	0.86	0.18	-0.12	-0.28	-0.33	-0.39	-0.43
UVIS/F467M	1.74	0.34	0.02	-0.15	-0.22	-0.24	-0.26	-0.27
UVIS/F469N	1.64	0.33	0.03	-0.14	-0.21	-0.24	-0.26	-0.26
UVIS/F475W	1.23	0.44	0.09	-0.07	-0.17	-0.20	-0.24	-0.26
UVIS/F475X	0.61	0.35	0.12	-0.01	-0.12	-0.15	-0.19	-0.23
UVIS/F487N	1.47	0.29	0.20	0.28	0.06	-0.02	-0.11	-0.17
UVIS/F502N	2.32	0.32	0.02	-0.07	-0.11	-0.12	-0.14	-0.15
UVIS/FQ508N	1.07	0.32	0.01	-0.06	-0.08	-0.10	-0.11	-0.12
UVIS/F547M	0.08	0.03	0.02	0.01	0.01	0.01	0.01	0.02
UVIS/F555W	0.15	0.09	0.03	-0.01	-0.03	-0.04	-0.05	-0.06
UVIS/F600LP	-3.71	-0.42	0.09	0.34	0.47	0.52	0.57	0.60
UVIS/F606W	-0.83	-0.11	0.04	0.10	0.12	0.12	0.13	0.13
UVIS/F621M	-1.23	-0.26	0.03	0.16	0.22	0.25	0.27	0.28
UVIS/F625W	-1.17	-0.25	0.04	0.16	0.22	0.24	0.26	0.27
UVIS/F631N	-0.33	-0.28	0.03	0.17	0.24	0.27	0.30	0.31
UVIS/F645N	-2.20	-0.29	0.04	0.20	0.28	0.31	0.35	0.35
UVIS/F656N	-1.99	-0.26	0.36	0.63	0.56	0.54	0.52	0.45
UVIS/F657N	-2.31	-0.31	0.14	0.37	0.39	0.41	0.42	0.41

Table 10.6: Color corrections AB_V to go from Johnson V magnitude to AB magnitude for WFC3 as a function of stellar effective temperature.

	T_{eff}							
Mode	**2500K**	**5000K**	**7500K**	**10000K**	**15000K**	**20000K**	**30000K**	**50000K**
UVIS/F658N	-2.04	-0.31	0.18	0.42	0.42	0.43	0.44	0.41
UVIS/F665N	-1.30	-0.35	0.06	0.26	0.34	0.38	0.42	0.42
UVIS/F673N	-0.69	-0.37	0.04	0.24	0.35	0.39	0.44	0.45
UVIS/F680N	-1.61	-0.38	0.05	0.26	0.38	0.42	0.47	0.48
UVIS/F689M	-1.69	-0.37	0.06	0.28	0.39	0.43	0.47	0.48
UVIS/F763M	-3.09	-0.45	0.09	0.37	0.53	0.59	0.65	0.69
UVIS/F775W	-3.60	-0.45	0.09	0.38	0.54	0.59	0.65	0.70
UVIS/F814W	-4.14	-0.48	0.12	0.43	0.60	0.67	0.74	0.79
UVIS/F845M	-4.56	-0.51	0.16	0.51	0.70	0.77	0.84	0.91
UVIS/F850LP	-5.03	-0.56	0.21	0.56	0.79	0.89	0.98	1.06
UVIS/F953N	-5.52	-0.59	0.27	0.68	0.91	1.00	1.10	1.16
UVIS/FQ232N	2.15	4.54	2.68	1.53	0.20	-0.43	-1.12	-1.46
UVIS/FQ243N	2.84	5.10	2.76	1.52	0.18	-0.44	-1.11	-1.40
UVIS/FQ378N	4.90	2.32	0.86	0.61	0.01	-0.20	-0.44	-0.62
UVIS/FQ387N	6.34	2.42	0.61	0.25	-0.21	-0.34	-0.49	-0.61
UVIS/FQ422M	5.05	1.17	0.18	-0.22	-0.36	-0.41	-0.46	-0.48
UVIS/FQ436N	2.64	0.84	0.23	0.08	-0.16	-0.24	-0.31	-0.39
UVIS/FQ437N	2.59	0.83	0.18	0.00	-0.21	-0.28	-0.34	-0.40
UVIS/FQ492N	0.91	0.27	0.04	-0.02	-0.10	-0.13	-0.16	-0.17
UVIS/FQ575N	-0.58	-0.18	0.01	0.07	0.10	0.11	0.13	0.13
UVIS/FQ619N	0.72	-0.25	0.03	0.15	0.22	0.24	0.27	0.27
UVIS/FQ634N	-0.96	-0.28	0.03	0.18	0.26	0.29	0.32	0.32
UVIS/FQ672N	-0.77	-0.35	0.04	0.23	0.34	0.38	0.42	0.44
UVIS/FQ674N	-0.39	-0.37	0.04	0.24	0.35	0.39	0.43	0.44
UVIS/FQ727N	-2.81	-0.41	0.07	0.32	0.46	0.52	0.57	0.60
UVIS/FQ750N	-3.06	-0.44	0.08	0.36	0.51	0.57	0.63	0.66
UVIS/FQ889N	-4.98	-0.55	0.20	0.57	0.78	0.86	0.95	1.01
UVIS/FQ906N	-5.15	-0.56	0.21	0.57	0.79	0.88	0.98	1.05
UVIS/FQ924N	-4.89	-0.57	0.26	0.66	0.87	0.95	1.04	1.10

Table 10.6: Color corrections AB_ν to go from Johnson V magnitude to AB magnitude for WFC3 as a function of stellar effective temperature.

	T_{eff}							
Mode	**2500K**	**5000K**	**7500K**	**10000K**	**15000K**	**20000K**	**30000K**	**50000K**
UVIS/FQ937N	-5.19	-0.58	0.19	0.48	0.77	0.89	1.01	1.11
IR/F098M	-5.40	-0.60	0.25	0.60	0.88	1.00	1.12	1.21
IR/F105W	-5.68	-0.62	0.31	0.69	0.98	1.11	1.24	1.34
IR/F110W	-5.77	-0.64	0.39	0.80	1.12	1.25	1.39	1.49
IR/F125W	-5.91	-0.67	0.48	0.94	1.28	1.43	1.58	1.69
IR/F126N	-5.99	-0.67	0.49	0.96	1.31	1.46	1.61	1.72
IR/F127M	-6.04	-0.67	0.52	1.01	1.35	1.49	1.65	1.75
IR/F128N	-6.08	-0.67	0.59	1.11	1.41	1.55	1.69	1.78
IR/F130N	-6.13	-0.68	0.53	1.02	1.37	1.52	1.68	1.79
IR/F132N	-6.04	-0.67	0.54	1.03	1.39	1.55	1.71	1.82
IR/F139M	-5.64	-0.69	0.60	1.11	1.49	1.64	1.81	1.92
IR/F140W	-5.89	-0.69	0.61	1.12	1.49	1.64	1.80	1.92
IR/F153M	-6.03	-0.71	0.73	1.29	1.69	1.85	2.02	2.14
IR/F160W	-6.05	-0.70	0.74	1.30	1.69	1.85	2.02	2.15
IR/F164N	-6.39	-0.70	0.84	1.42	1.82	1.99	2.16	2.28
IR/F167N	-6.32	-0.69	0.84	1.41	1.83	2.00	2.18	2.31

Table 10.7: Color corrections AB_ν to go from Johnson V magnitude to AB magnitude for WFC3 as a function of age in an instantaneous burst population.

	Age				
Mode	**10 Gyr**	**1 Gyr**	**100 Myr**	**10 Myr**	**1 Myr**
UVIS/F200LP	0.27	0.38	0.24	0.00	-0.41
UVIS/F218W	6.05	3.87	1.06	0.15	-1.23
UVIS/F225W	5.78	3.74	1.02	0.16	-1.15
UVIS/F275W	4.73	3.13	0.92	0.19	-0.98
UVIS/F280N	4.21	2.98	0.88	0.21	-0.93

Table 10.7: Color corrections AB_V to go from Johnson V magnitude to AB magnitude for WFC3 as a function of age in an instantaneous burst population.

	Age				
Mode	**10 Gyr**	**1 Gyr**	**100 Myr**	**10 Myr**	**1 Myr**
UVIS/F300X	3.87	2.75	0.88	0.20	-0.93
UVIS/F336W	2.68	1.97	0.76	0.27	-0.68
UVIS/F343N	2.55	1.89	0.75	0.28	-0.64
UVIS/F350LP	-0.12	0.03	0.05	-0.07	-0.04
UVIS/F373N	2.28	1.57	0.66	0.34	-0.50
UVIS/F390M	2.03	1.12	0.21	0.13	-0.51
UVIS/F390W	1.63	1.00	0.26	0.15	-0.50
UVIS/F395N	1.89	1.04	0.14	0.10	-0.50
UVIS/F410M	1.23	0.64	0.01	0.02	-0.48
UVIS/F438W	0.90	0.48	0.00	0.02	-0.40
UVIS/F467M	0.44	0.22	-0.03	-0.01	-0.27
UVIS/F469N	0.47	0.23	-0.02	-0.01	-0.26
UVIS/F475W	0.48	0.27	0.01	0.04	-0.24
UVIS/F475X	0.37	0.23	0.03	0.03	-0.20
UVIS/F487N	0.36	0.27	0.12	0.10	-0.15
UVIS/F502N	0.33	0.17	0.01	0.08	-0.13
UVIS/FQ508N	0.31	0.16	0.03	0.12	-0.10
UVIS/F547M	0.04	0.03	0.02	0.03	0.02
UVIS/F555W	0.10	0.07	0.01	0.01	-0.06
UVIS/F600LP	-0.74	-0.39	-0.05	-0.28	0.54
UVIS/F606W	-0.17	-0.08	0.01	-0.05	0.12
UVIS/F621M	-0.32	-0.18	-0.00	-0.10	0.25
UVIS/F625W	-0.33	-0.17	-0.00	-0.10	0.24
UVIS/F631N	-0.33	-0.19	0.00	-0.10	0.28
UVIS/F645N	-0.42	-0.23	-0.02	-0.15	0.32
UVIS/F656N	-0.45	-0.18	0.06	-0.16	0.36
UVIS/F657N	-0.47	-0.23	-0.00	-0.18	0.36
UVIS/F658N	-0.47	-0.22	-0.00	-0.19	0.36
UVIS/F665N	-0.48	-0.26	-0.03	-0.19	0.38

Table 10.7: Color corrections AB_V to go from Johnson V magnitude to AB magnitude for WFC3 as a function of age in an instantaneous burst population.

	Age				
Mode	**10 Gyr**	**1 Gyr**	**100 Myr**	**10 Myr**	**1 Myr**
UVIS/F673N	-0.49	-0.29	-0.03	-0.15	0.41
UVIS/F680N	-0.54	-0.31	-0.03	-0.17	0.44
UVIS/F689M	-0.53	-0.29	-0.02	-0.19	0.44
UVIS/F763M	-0.77	-0.40	-0.05	-0.32	0.63
UVIS/F775W	-0.78	-0.41	-0.05	-0.32	0.63
UVIS/F814W	-0.89	-0.48	-0.07	-0.36	0.71
UVIS/F845M	-1.00	-0.54	-0.10	-0.42	0.81
UVIS/F850LP	-1.18	-0.65	-0.13	-0.47	0.95
UVIS/F953N	-1.26	-0.71	-0.12	-0.50	1.06
UVIS/FQ232N	4.21	3.31	1.02	0.16	-1.14
UVIS/FQ243N	4.65	3.53	0.97	0.14	-1.11
UVIS/FQ378N	2.24	1.37	0.42	0.22	-0.52
UVIS/FQ387N	2.27	1.16	0.22	0.14	-0.52
UVIS/FQ422M	1.16	0.55	-0.03	0.01	-0.45
UVIS/FQ436N	0.87	0.49	0.04	0.05	-0.37
UVIS/FQ437N	0.86	0.46	-0.00	0.02	-0.38
UVIS/FQ492N	0.31	0.17	0.01	0.05	-0.16
UVIS/FQ575N	-0.18	-0.08	-0.00	-0.07	0.12
UVIS/FQ619N	-0.28	-0.16	0.01	-0.06	0.25
UVIS/FQ634N	-0.37	-0.21	-0.01	-0.12	0.29
UVIS/FQ672N	-0.47	-0.27	-0.03	-0.17	0.40
UVIS/FQ674N	-0.47	-0.27	-0.03	-0.16	0.40
UVIS/FQ727N	-0.64	-0.34	-0.02	-0.26	0.55
UVIS/FQ750N	-0.81	-0.43	-0.07	-0.33	0.60
UVIS/FQ889N	-1.11	-0.61	-0.14	-0.46	0.90
UVIS/FQ906N	-1.22	-0.68	-0.16	-0.49	0.93
UVIS/FQ924N	-1.21	-0.65	-0.12	-0.48	0.99
UVIS/FQ937N	-1.16	-0.65	-0.12	-0.47	0.99
IR/F098M	-1.35	-0.75	-0.15	-0.52	1.09

Table 10.7: Color corrections AB_ν to go from Johnson V magnitude to AB magnitude for WFC3 as a function of age in an instantaneous burst population.

	Age				
Mode	**10 Gyr**	**1 Gyr**	**100 Myr**	**10 Myr**	**1 Myr**
IR/F105W	-1.39	-0.74	-0.14	-0.55	1.22
IR/F110W	-1.38	-0.70	-0.11	-0.57	1.37
IR/F125W	-1.39	-0.67	-0.09	-0.61	1.56
IR/F126N	-1.37	-0.65	-0.07	-0.62	1.59
IR/F127M	-1.38	-0.65	-0.07	-0.63	1.62
IR/F128N	-1.39	-0.64	-0.07	-0.63	1.63
IR/F130N	-1.40	-0.65	-0.07	-0.63	1.65
IR/F132N	-1.40	-0.64	-0.07	-0.62	1.68
IR/F139M	-1.37	-0.62	-0.05	-0.60	1.77
IR/F140W	-1.41	-0.65	-0.07	-0.64	1.77
IR/F153M	-1.49	-0.69	-0.08	-0.70	1.97
IR/F160W	-1.49	-0.69	-0.08	-0.71	1.97
IR/F164N	-1.58	-0.75	-0.12	-0.79	2.09
IR/F167N	-1.58	-0.74	-0.11	-0.78	2.12

Table 10.8: Color corrections AB_ν to go from Johnson V magnitude to AB magnitude for WFC3 as a function of age in a population with constant star formation.

	Age				
Mode	**10 Gyr**	**1 Gyr**	**100 Myr**	**10 Myr**	**1 Myr**
UVIS/F200LP	0.24	0.19	0.02	-0.13	-0.41
UVIS/F218W	1.39	0.78	0.07	-0.48	-1.23
UVIS/F225W	1.39	0.79	0.09	-0.45	-1.15
UVIS/F275W	1.35	0.78	0.12	-0.37	-0.98
UVIS/F280N	1.33	0.77	0.13	-0.34	-0.92
UVIS/F300X	1.30	0.75	0.13	-0.34	-0.93
UVIS/F336W	1.15	0.71	0.19	-0.21	-0.67
UVIS/F343N	1.13	0.71	0.20	-0.19	-0.63

Table 10.8: Color corrections AB_V to go from Johnson V magnitude to AB magnitude for WFC3 as a function of age in a population with constant star formation.

	Age				
Mode	**10 Gyr**	**1 Gyr**	**100 Myr**	**10 Myr**	**1 Myr**
UVIS/F350LP	-0.02	0.02	-0.02	-0.01	-0.04
UVIS/F373N	1.03	0.65	0.23	-0.12	-0.50
UVIS/F390M	0.67	0.28	-0.00	-0.26	-0.51
UVIS/F390W	0.64	0.30	0.02	-0.23	-0.50
UVIS/F395N	0.61	0.21	-0.04	-0.27	-0.50
UVIS/F410M	0.37	0.06	-0.12	-0.31	-0.48
UVIS/F438W	0.29	0.05	-0.09	-0.26	-0.40
UVIS/F467M	0.14	-0.01	-0.08	-0.18	-0.27
UVIS/F469N	0.15	-0.00	-0.08	-0.18	-0.26
UVIS/F475W	0.18	0.04	-0.04	-0.15	-0.24
UVIS/F475X	0.16	0.05	-0.03	-0.12	-0.20
UVIS/F487N	0.21	0.14	0.05	-0.05	-0.15
UVIS/F502N	0.13	0.04	0.00	-0.07	-0.13
UVIS/FQ508N	0.14	0.06	0.04	-0.03	-0.10
UVIS/F547M	0.03	0.03	0.02	0.02	0.02
UVIS/F555W	0.05	0.02	-0.01	-0.03	-0.06
UVIS/F600LP	-0.37	-0.14	-0.06	0.21	0.54
UVIS/F606W	-0.06	-0.01	0.01	0.06	0.12
UVIS/F621M	-0.14	-0.03	0.00	0.12	0.25
UVIS/F625W	-0.14	-0.03	0.00	0.12	0.24
UVIS/F631N	-0.15	-0.03	0.01	0.13	0.28
UVIS/F645N	-0.20	-0.06	-0.01	0.14	0.32
UVIS/F656N	-0.17	0.01	0.02	0.18	0.36
UVIS/F657N	-0.20	-0.04	-0.02	0.15	0.36
UVIS/F658N	-0.20	-0.04	-0.02	0.15	0.36
UVIS/F665N	-0.23	-0.07	-0.03	0.16	0.38
UVIS/F673N	-0.24	-0.07	0.00	0.19	0.41
UVIS/F680N	-0.26	-0.08	-0.00	0.20	0.44

Table 10.8: Color corrections AB_V to go from Johnson V magnitude to AB magnitude for WFC3 as a function of age in a population with constant star formation.

	Age				
Mode	**10 Gyr**	**1 Gyr**	**100 Myr**	**10 Myr**	**1 Myr**
UVIS/F689M	-0.25	-0.07	-0.01	0.19	0.44
UVIS/F763M	-0.39	-0.14	-0.07	0.24	0.63
UVIS/F775W	-0.39	-0.14	-0.07	0.24	0.63
UVIS/F814W	-0.47	-0.19	-0.09	0.26	0.71
UVIS/F845M	-0.54	-0.23	-0.12	0.27	0.81
UVIS/F850LP	-0.66	-0.31	-0.15	0.29	0.95
UVIS/F953N	-0.72	-0.34	-0.15	0.31	1.06
UVIS/FQ232N	1.36	0.78	0.10	-0.44	-1.14
UVIS/FQ243N	1.36	0.77	0.08	-0.44	-1.11
UVIS/FQ378N	0.85	0.45	0.10	-0.21	-0.51
UVIS/FQ387N	0.70	0.28	-0.00	-0.26	-0.52
UVIS/FQ422M	0.32	0.02	-0.13	-0.30	-0.45
UVIS/FQ436N	0.31	0.08	-0.07	-0.23	-0.37
UVIS/FQ437N	0.28	0.05	-0.09	-0.25	-0.38
UVIS/FQ492N	0.12	0.03	-0.02	-0.10	-0.16
UVIS/FQ575N	-0.07	-0.02	-0.01	0.06	0.12
UVIS/FQ619N	-0.12	-0.02	0.03	0.13	0.25
UVIS/FQ634N	-0.17	-0.04	-0.00	0.13	0.29
UVIS/FQ672N	-0.22	-0.06	-0.01	0.17	0.40
UVIS/FQ674N	-0.23	-0.06	-0.00	0.18	0.40
UVIS/FQ727N	-0.31	-0.09	-0.04	0.22	0.55
UVIS/FQ750N	-0.42	-0.17	-0.08	0.22	0.60
UVIS/FQ889N	-0.62	-0.28	-0.15	0.27	0.90
UVIS/FQ906N	-0.69	-0.34	-0.17	0.27	0.93
UVIS/FQ924N	-0.67	-0.31	-0.15	0.31	0.99
UVIS/FQ937N	-0.65	-0.31	-0.14	0.30	0.99
IR/F098M	-0.77	-0.38	-0.17	0.32	1.09
IR/F105W	-0.78	-0.37	-0.18	0.35	1.22

Table 10.8: Color corrections AB_V to go from Johnson V magnitude to AB magnitude for WFC3 as a function of age in a population with constant star formation.

	Age				
Mode	**10 Gyr**	**1 Gyr**	**100 Myr**	**10 Myr**	**1 Myr**
IR/F110W	-0.76	-0.34	-0.17	0.39	1.36
IR/F125W	-0.74	-0.30	-0.17	0.43	1.56
IR/F126N	-0.73	-0.29	-0.18	0.44	1.59
IR/F127M	-0.73	-0.29	-0.18	0.44	1.61
IR/F128N	-0.74	-0.29	-0.18	0.44	1.63
IR/F130N	-0.74	-0.30	-0.18	0.45	1.65
IR/F132N	-0.74	-0.29	-0.17	0.46	1.68
IR/F139M	-0.71	-0.25	-0.14	0.49	1.77
IR/F140W	-0.75	-0.29	-0.18	0.46	1.77
IR/F153M	-0.81	-0.32	-0.21	0.46	1.96
IR/F160W	-0.81	-0.32	-0.21	0.46	1.97
IR/F164N	-0.89	-0.39	-0.28	0.42	2.09
IR/F167N	-0.88	-0.38	-0.27	0.43	2.12

APPENDIX B:

Geometric Distortion

In this appendix . . .

B.1 Overview

WFC3 images will exhibit significant geometric distortions, similar to that seen in ACS images. The required folding, with powered optics, of the light paths in both channels to fit within the optical-bench envelope results in substantial tilts of the focal surfaces with respect to the chief rays. The WFC3 UVIS detector is tilted at ~21 degrees about one of its diagonals, producing a rhomboidal elongation of ~7%. The IR detector has a ~24 degree tilt about its *X* axis, creating a rectangular elongation of ~10%.

If these were the only distortions they would not present much difficulty: their impacts on photometry, mosaicking, or dithering could be computed simply. More problematic, however, is the variation of plate scale across each detector. For the WFC3 UVIS and IR channels this variation in plate scale amounts to a change of 3.5% and 2%, respectively, over the full field. Hence the area on the sky covered by a WFC3 UVIS pixel varies by about 7% from corner to corner, and about 8% for the IR channel. Allowance for this change in plate scale must be made in photometric reductions of WFC3 data.

Dithering and mosaicking are complicated by the fact that an integer pixel shift near the center of the detector will translate into a non-integer displacement for pixels near the edges. Even this is not a fundamental difficulty, but will imply some computational complexity in registering and correcting images. All of these considerations make it necessary to obtain accurate measurements of the distortions. The orientations of the WFC3 detector edges for both detectors are at approximately 45 degrees with respect to the V2 and V3 coordinate axes of the telescope. Figure XX

[Q: I assume Fig XX means the schematic view of the apertures, to be given in one of the introductory sections of the Handbook--HEB] [Q: need to refer to a diagram showing V2,V3.] shows the WFC3 apertures in the telescope's V2,V3 reference frame. For a telescope roll angle of zero this would correspond to an on-sky view with the V3 axis aligned with north and the V2 axis with east.

The information presented here is derived from the optical model of the instrument, and thus must be regarded as preliminary. After installation of WFC3 into HST this information will be revised on the basis of astrometry in rich stellar fields, as has been done previously for the ACS. For the ACS, the residuals in the distortion corrections in the data pipeline are now at the 0.01 pixel level.

B.2 UVIS Channel

Figure B.1 illustrates the shape of the UVIS channel field of view as projected onto the sky. As noted above, its rhomboidal shape is due primarily to the diagonal tilt of the CCD focal plane with respect to the chief ray (see the schematic mechanical drawing of the instrument in Figure 2.1). The angle between the X and Y axes is ~86.1 degrees. The field diagonals are tilted slightly from the V2 and V3 axes.

The UVIS distortion is illustrated in Figure B.1, a vector-displacement diagram that shows the contribution of the non-linear part of a quadratic fit to the data. The vectors represent the displacements, and have been scaled up by a factor of 10 for display. In the diagrams in the Appendix, the square points indicate the actual location and the other end of the line shows where the image would be located without non-linear distortion.

The corner displacements are about 30 pixels, corresponding to 1.3 arcsec. The principal effect is the diagonal variation of scale. At the center of chip UVIS1, the scale in the X direction is 0.0396 arcsec/pixel, and 0.0393 arcsec/pixel in the Y direction. For UVIS2 these scales are 0.0400 arcsec/pixel, and 0.0398 arcsec/pixel, respectively. Between the corner of the UVIS image nearest to the V1 axis and the diagonally opposite corner, the overall scale increases by 3.5%. UVIS1 forms a slightly distorted rectangle 162×81 arcsec in size, while UVIS2 subtends 164×81 arcsec.

Figure B.1: Non-linear component of the WFC3 UVIS channel distortion.

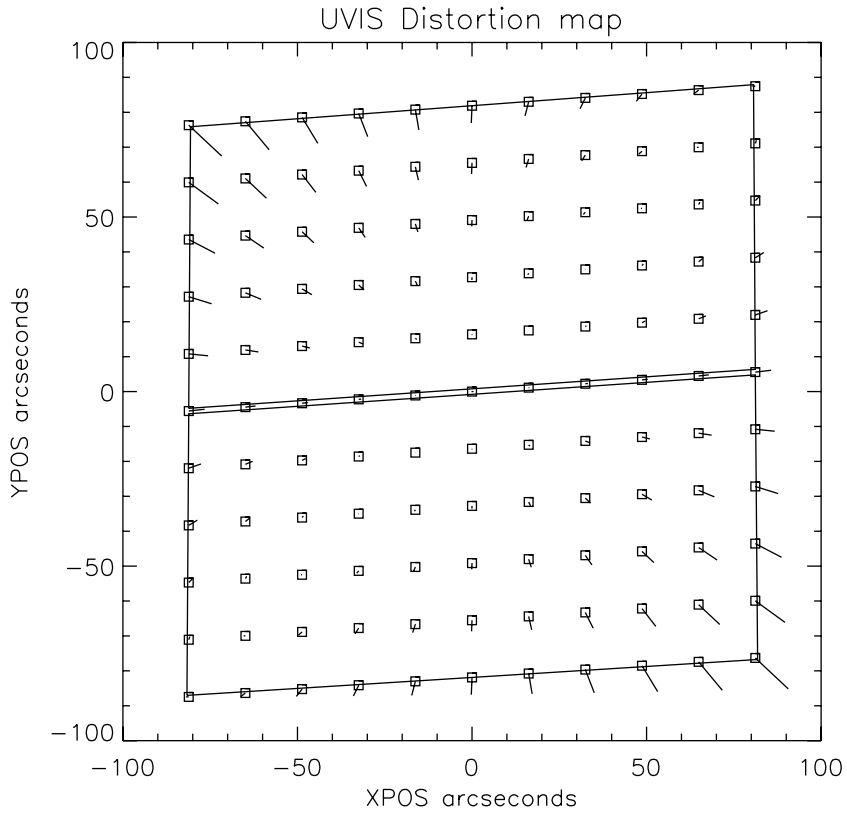

There is an approximately 1.5 arcsec gap between the two chips. The resulting variation of the projected pixel area on the sky requires corrections to photometry of point sources using geometrically corrected images. A contour plot of relative pixel size across the UVIS image, normalized to the central pixel, is shown in Figure B.2. The range of pixel area is from 0.965 to 1.035 times the central value.

Figure B.2: Variation of the UVIS channel effective pixel area with position in detector coordinates.

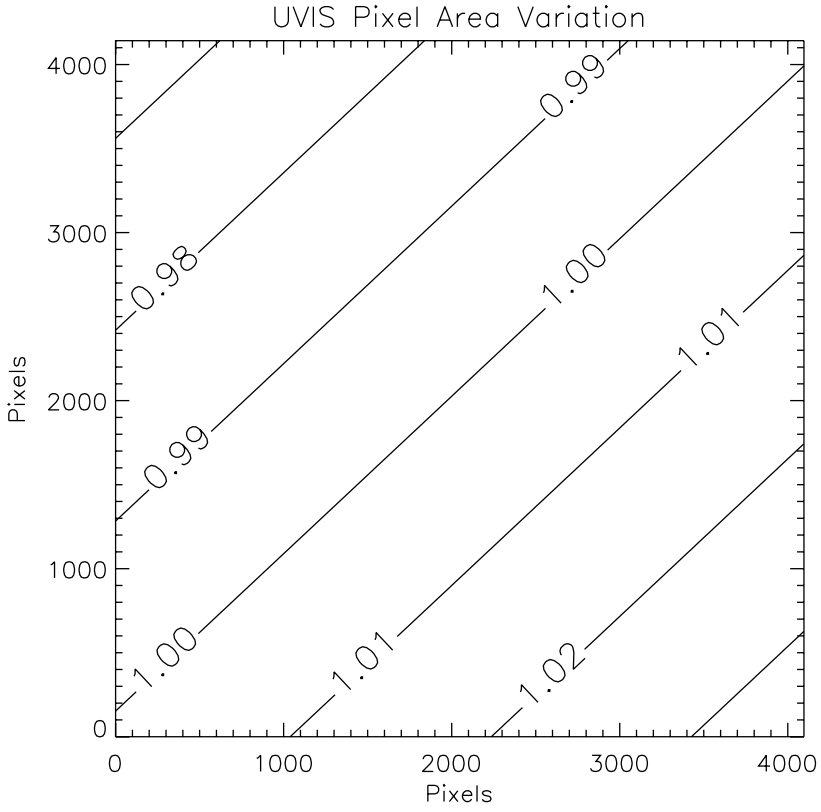

B.3 IR Channel

The IR channel field of view is nominally concentric with the UVIS field, but subtends a somewhat smaller area on the sky, 136×123 arcsec. The detector tilt is about the X (USER1) axis, so the projected aperture shape is nearly an elongated rectangle, with the angle between the X and Y axes on the sky nearly 90 degrees, as shown by the outline in Figure B.3. At field center, the X and Y scales are 0.135 and 0.121 arcsec/pixel respectively. A vector plot of the deviation from linearity is given in Figure B.3, in which the deviations have been magnified by a factor of 10 for illustrative purposes. The largest deviation is 10 pixels, corresponding to about 1.4 arcsec.

Figure B.3: Non-linear component of the WFC3 IR channel distortion..

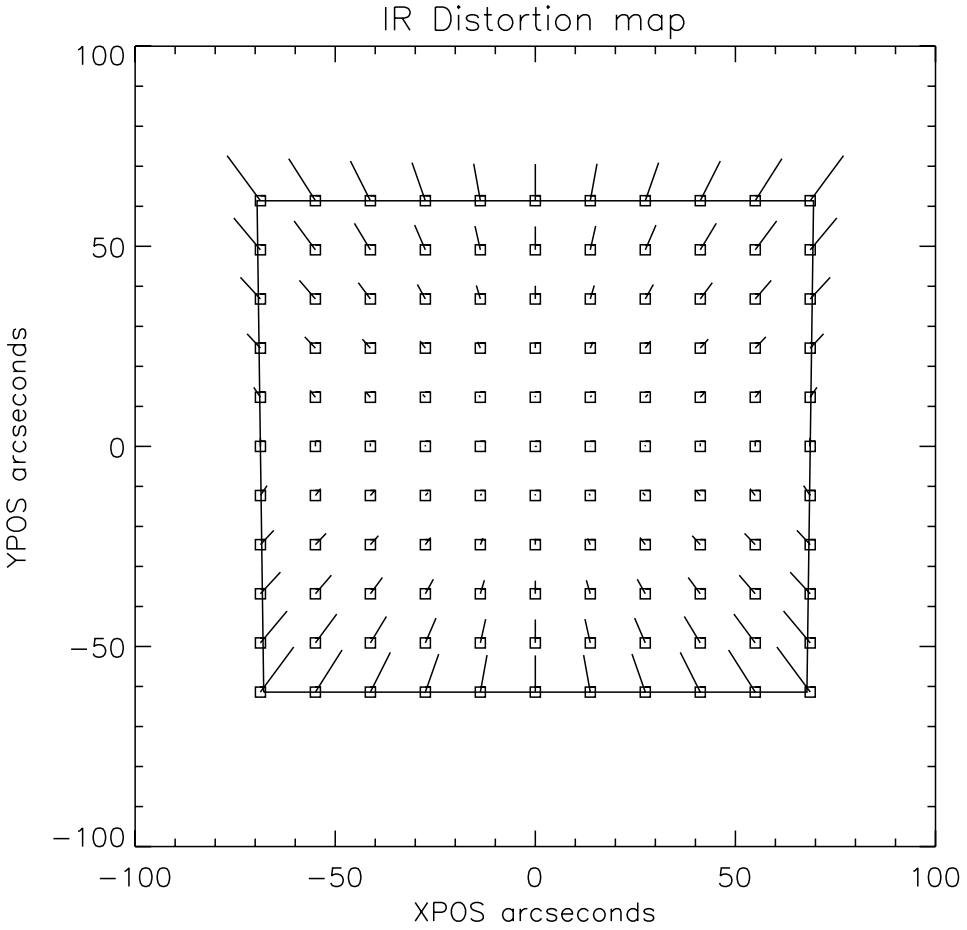

The variation of pixel area across the IR channel to be used for correction of point-source photometry from distortion-corrected images is shown in Figure B.4. The maximum deviation from the central value is 4.1%.

Figure B.4: Variation of the IR channel effective pixel area with position in detector coordinates.

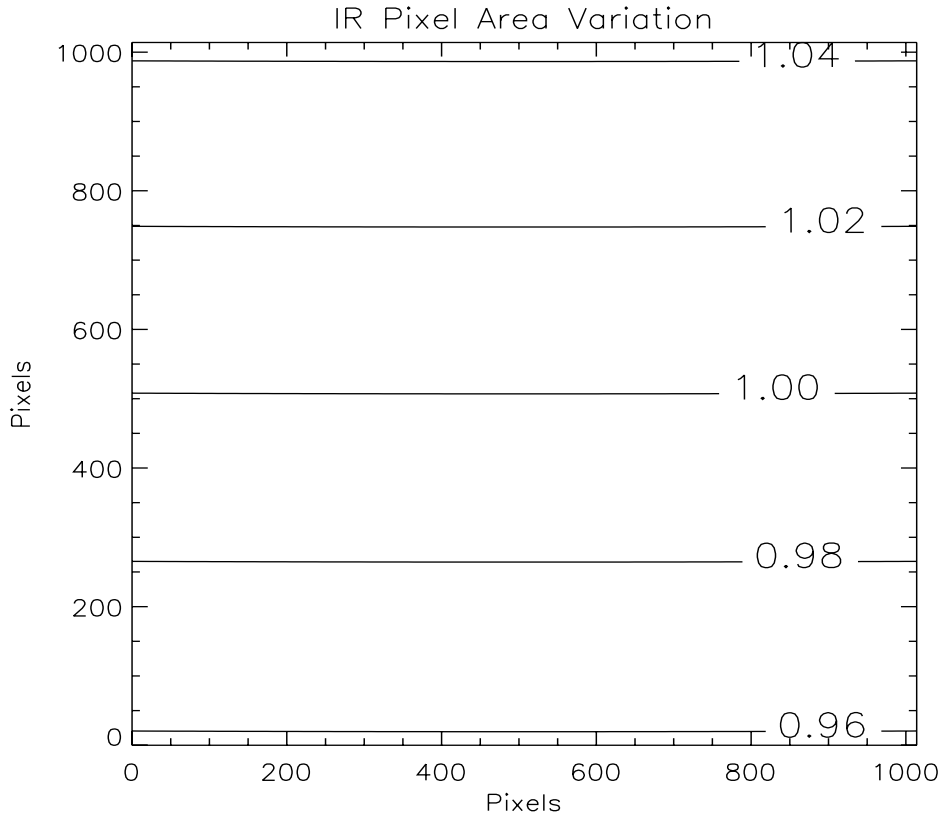

B.4 Summary

Images produced by both WFC3 channels will be affected by considerable geometric distortion, dominated by a linear anamorphism induced by tilt of the image surface to chief ray. This is compounded by non-linear terms that produce changes across the field of view in both plate scale and area subtended by the pixels.

All values presented here are based on optical modeling of the instrument, and corroborated with measurements using a telescope simulator in ground thermal-vacuum tests. We expect that on-orbit measurements of the distortion scale factors will deviate by less than 1% from those presented here.

APPENDIX C:

Dithering and Mosaicking

In this appendix . . .

C.1 Why Mosaicking and Dithering are Needed

It is frequently desirable to shift the telescope pointing between successive exposures. The sizes of these offsets can be very different, depending on the purpose of changing the pointing.

It is useful to distinguish between "*mosaicking*" and "*dithering*." Mosaicking is done with the aim of increasing the area of sky covered by a particular set of exposures, usually with the goal of providing a seamless joining of contiguous frames. The angular offsets used when mosaicking are generally large, comparable to the size of the field of view.

Dithering generally involves much smaller telescope offsets, often just a few pixels in size. It is done for a variety of reasons, including:

- removal of hot pixels and other detector blemishes
- improving sampling of the PSF
- improving photometric accuracy by averaging over flat-fielding errors
- bridging over the gap between the chips in the UVIS channel.

C.2 WFC3 Patterns

A number of different types of patterns are available to support dithered and mosaicked WFC3 observations. Use of these patterns has the advantage that it allows exposures to be associated automatically during ***calwfc3*** pipeline processing. However, the following restrictions apply: only pattern exposures obtained within a single visit, and those patterns where the cumulative offset is smaller than the ~100 arcsecond guide-star limitation, can be associated.

The current set of available patterns is summarized in Table C.1. The parameters of these patterns (e.g., the sizes of the offsets and their directions) can be adjusted by the observer. These patterns have not been finalized at the time of writing, but they will be described in detail on a WFC3 Dither Web page linked on the main WFC3 page:

http://www.stsci.edu/hst/wfc3

As described in Appendix B, the plate scales for both WFC3 channels vary significantly over the field of view, such that an integer-pixel dither near the center of the field will not be an integer-pixel dither in the corners. For this reason, dither patterns attempt to strike a balance between being large enough to reject detector artifacts, but being as compact as possible to maintain the integrity of the pattern over the entire field of view. Larger displacements will have varying sub-pixel properties across the image.

Table 10.9: Dithering and Mosaicking Patterns

Pattern Name	Description
WFC3 UVIS Patterns	
WFC3-UVIS-DITHER-LINE	Provides linear offsets useful for better UVIS PSF sampling
WFC3-UVIS-DITHER-BOX	A UVIS sub-pixel dither box, with minimum sub-pixel steps placed to miss diffraction spikes.
WFC3-UVIS-MOS-DITH-LINE	A combination mosaic primary pattern with a 2-point dither at each primary position.
WFC3-UVIS-MOS-BOX-LRG	A 4-point box that results in the largest areal coverage with the UVIS detector.
WFC3-UVIS-MOS-BOX-GAP	A pattern that combines large areal coverage while sampling the UVIS inter-chip gap.
WFC3-UVIS-MOS-BOX-IR	A pattern useful for covering the same field of view with both channels.
WFC3-UVIS-MOSAIC-LINE	A pattern useful for WFC3 UVIS observations with ACS WFC in parallel.
WFC3 IR Patterns	
WFC3-IR-DITHER-LINE	Provides linear offsets useful for better IR PSF sampling.
WFC3-IR-DITHER-BOX-MIN	An IR sub-pixel dither box, with minimum sub-pixel steps placed to miss diffraction spikes.
WFC3-IR-DITHER-BOX-GAP	Covers the UVIS inter-chip gap when imaging one field with both channels.

Table 10.9: Dithering and Mosaicking Patterns

Pattern Name	Description
WFC3-IR-DITHER-BOX-MED	Dithers over steps larger than the IR detector defects, for higher photometric accuracy.
WFC3-IR-DITHER-BOX-UVIS	Dithers the IR detector to cover the same area as the UVIS detector.
WFC3-IR-MOSAIC-BOX	A pattern to increase the size of the IR channel field of view.

In addition to the plate-scale variation associated with the significant WFC3 geometric distortion, there can also be a temporal variation of overall image alignment. Some CR-SPLIT images taken during ACS SMOV testing, in which the two components were separated by the scheduling system across orbital occultations (about a one-hour gap), showed registration differences of about 0.5 pixels corner-to-corner. Thus, to combine multiple images to create oversampled images at the resolution WFC3 is capable of providing, the user may need to allow for the general problem of combining distorted, misregistered images. A variety of tools are being made available within STSDAS and **pyraf** to assist with these tasks, including ***pydrizzle*** and ***multidrizzle***. The issues for WFC3 are similar to those for ACS, so users should see the ACS Drizzle Web page and the *ACS Data Handbook* for more discussion at this time. Analogous resources are being developed for WFC3.

Additional information on dithering, and processing drizzled data using ***multidrizzle*** can be obtained from the *Dither Handbook*

APPENDIX D:

Bright-Object Constraints and Image Persistence

In this appendix . . .

D.1 UVIS Channel

The UVIS channel's CCDs have no known bright-object constraints. It is not anticipated that overexposures on very bright targets will have any adverse health and safety issues, nor should they affect subsequent exposures.

D.2 IR Channel

The IR channel likewise has no bright-object constraints that are imposed due to instrument safety concerns. However, observers should bear in mind that there is a potential for image-persistence effects that could compromise observations made immediately following an exposure on a very bright target. Such observations could potentially contain an "afterglow" image at the location of the overexposed object, which would gradually fade away over an interval of several hours.

The WFC IR channel will be at least as sensitive as NICMOS, but have a field of view seven times larger than NICMOS Camera 3. This combination of high sensitivity and large field size means that WFC3/IR images will often contain saturated stellar images. These can impact subsequent observations if the WFC3/IR detector exhibits

significant persistence. At the time of writing, it is not yet known how much persistence there will be with the IR detector selected for flight, and we are still developing procedures for dealing with potential severe overexposures that might affect subsequent observations from a different program.

If you are planning a sequence of IR observations that may contain severely overexposed images, you may wish to estimate the degree of overexposure. An IR observer might expect that the Two Micron All Sky Survey (2MASS) would be the appropriate catalog for examining the frequency of WFC3/IR saturations, but in fact the 2MASS catalog is generally not deep enough for this purpose. Although the depth of the survey varies across the sky, the faint limit is typically near 15th mag in *J*, *H*, and *Ks* (the formal Level 1 requirements on limiting magnitudes of the 2MASS catalog are $J = 15.8$, $H = 15.1$, and $Ks = 14.3$). Stars near this faint limit will saturate the WFC3/IR detector in a relatively short time (of order 100 s in some of the wide IR bandpasses). The STScI Guide Star Catalog (GSC), currently at version 2.3, generally goes much fainter (down to 22nd mag in *V*), but the extrapolation from the optical into the infrared depends on the accuracy of the spectral type implied by the optical colors and the assumed extinction (which will be a large source of systematic errors along sightlines of high extinction).

Thus, neither the 2MASS nor the GSC catalog is particularly well suited to predicting the number of saturated stars in WFC3 IR images. However, if persistence proves to be a problem for the WFC3 IR channel, it will likely only arise when the detector is oversaturated by a factor of 100 or more; in this case, the 2MASS catalog should be sufficiently deep for screening observations against extreme saturations.

As described in Chapter 9, the WFC3 ETC can be used to estimate the count rate in the central pixel for a given astronomical source. However, as a rough guideline, below we present tables of the count rates for two cases: a "hot star" with $T_{eff} = 50{,}000$ K, [Fe/H] = −2, and $\log g = 5$; and a "cool star" with $T_{eff} = 2{,}500$ K, [Fe/H] = 0, and $\log g = 3$.

Tables D.1, D.2, D.3, and D.4 give the results for the cases where one normalizes to 2MASS *J*, *H*, and *Ks* magnitudes, and to Johnson *V,* respectively. In each case a magnitude of 15 in the respective bandpass is assumed. The count rates are given in electrons/s for the central pixel of a star centered in a WFC3 IR pixel. To interpret these numbers, one should note that saturation occurs at a total pixel signal of ~75,000 electrons (see Chapter xx). These tables give the most reliable results when normalizaing to a ground-based bandpass that overlaps with the WFC3 bandpass, regardless of the assumed spectral energy distribution. However, when normalizing to Johnson *V,* one must know the underlying spectral energy distribution to high accuracy in order to predict the count rate in the WFC3 IR bandpasses.

The calculations in the four tables were done using the sensitivity function of the FPA 129 flight-candidate detector, and the results will be slightly different for the final flight detector choice.

The Bright Object Tool (BOT) in the Astronomer's Proposal Tool (APT) can provide a list of saturated objects for a potential WFC3/IR observation, given a Phase II proposal. Because the 2MASS survey is sufficiently deep for objects that would severely oversaturate the detector (by more than a factor of 100), the BOT uses

2MASS data where they are available, and the GSC2 where no 2MASS data are available.

Table 10.10: Count Rates(e/s) for Source with *J* = 15

WFC3 IR filter	cool star	hot star
F098M	1132.4	2418.3
F105W	2238.5	3732.1
F110W	3857.1	5351.8
F125W	2434.2	2562.4
F126N	127.0	116.2
F127M	645.3	551.2
F128N	146.4	119.4
F130N	150.1	117.3
F132N	129.7	109.7
F139M	333.9	391.1
F140W	2832.6	2476.5
F153M	503.1	311.0
F160W	2126.6	1274.9
F164N	214.5	77.3
F167N	193.7	72.4

Table 10.11: Count Rates (e/s) for Source with *H* = 15

WFC3 IR filter	cool star	hot star
F098M	573.7	2745.9
F105W	1134.0	4237.7
F110W	1953.9	6076.8
F125W	1233.1	2909.5
F126N	64.4	132.0
F127M	326.9	625.9
F128N	74.2	135.5
F130N	76.0	133.2

Table 10.11: Count Rates (e/s) for Source with H = 15

WFC3 IR filter	cool star	hot star
F132N	65.7	124.6
F139M	169.1	444.1
F140W	1435.0	2812.0
F153M	254.8	353.1
F160W	1077.3	1447.6
F164N	108.7	87.8
F167N	98.1	82.2

Table 10.12: Count Rates (e/s) for Source with Ks = 15

WFC3 IR filter	cool star	hot star
F098M	418.6	2938.5
F105W	827.4	4534.8
F110W	1425.7	6502.8
F125W	899.7	3113.5
F126N	47.0	141.2
F127M	238.5	669.8
F128N	54.1	145.0
F130N	55.5	142.6
F132N	47.9	133.3
F139M	123.4	475.2
F140W	1047.0	3009.2
F153M	185.9	377.9
F160W	786.1	1549.1
F164N	79.3	93.9
F167N	71.6	88.0

Table 10.13: Count Rates (e/s) for Source with $V = 15$

WFC3 IR filter	cool star	hot star
F098M	312074.4	1199.3
F105W	616880.2	1850.9
F110W	1062930.2	2654.1
F125W	670814.9	1270.8
F126N	35010.0	57.6
F127M	177833.0	273.4
F128N	40339.9	59.2
F130N	41358.1	58.2
F132N	35732.5	54.4
F139M	92004.4	194.0
F140W	780603.4	1228.2
F153M	138635.2	154.2
F160W	586053.8	632.3
F164N	59120.0	38.3
F167N	53382.1	35.9

APPENDIX E:

WFC3 Calibration Plan

In this appendix . . .

E.1 Calibration Plan

Waiting for Godot... ah... MacKenty.

Glossary

The following terms and acronyms are used in this Handbook.

ADC: Analog to digital

ABMAG: $-2.5 \log (F_\nu) - 48.60$ where F_ν is the flux from the source in erg cm^{-2} sec^{-1} Hz^{-1}

AB$_\nu$: Correction to ABMAG to account for the fact that the source spectrum is not constant in F_ν ($ABMAG=V+AB_\nu$)

ACS: Advanced Camera for Surveys

APT: Astronomer's Proposal Tool

aXe: Spectroscopic Data Extraction Software

BOP: Bright Object Protection

calacs: ACS calibration pipeline software

CCD: Charge Coupled Device. Solid-state, light detecting device

CMD: Color Magnitude Diagram

CP: Call for Proposals

CR: Cosmic ray

CR-SPLIT: Division of a CCD exposure into shorter exposures to be used for cosmic ray rejection

CTE: Charge transfer efficiency

CVZ: Continuous viewing zone

DN: Data number

ETC: Exposure Time Calculator. ETCs are Web-based tools which can be accessed through the ACS Web pages.

ERO: Early release observations

FGS: Fine Guidance Sensors

FOS: Faint Object Spectrograph

FOV: Field of view

FTP: File Transfer Protocol. Basic tool used to retrieve files from a remote system. Ask your system manager for information about using FTP.

FUV: Far ultraviolet (~912 to 2000 Å)

FWHM: Full width at half maximum

GALEX: Galaxy Evolution Explorer

GHRS: Goddard High-Resolution Spectrograph

GO: General Observer

GSC: Guide Star Catalog

GSCII: Guide Star Catalog II

GTO: Guaranteed Time Observer

Help Desk: Facility for getting help on HST related topics via email. help@stsci.edu.

HRC: High Resolution Channel

HST: Hubble Space Telescope

IDT: Investigation Definition Team

IR: Infrared

IRAF: Image Reduction and Analysis System. The environment in which STSDAS operates.

ISR: Instrument Science Report

IUE: International Ultraviolet Explorer Satellite

K: Degree Kelvin

L-flats: Low Frequency Variations Flats

LMC: Large Magellanic Cloud

MAMA: Multi-Anode Microchannel Array

MCP: Microchannel Plate

MPP: Multi Pinned Phased, a CCD mode that reduces dark current rate

NICMOS: Near-Infrared Camera and Multi-Object Spectrograph

NUV: Near ultraviolet (~2000 to 4000 Å)

OTA: Optical Telescope Assembly

PASP: Publications of the Astronomical Society of the Pacific

PC: Program Coordinator

Phase I proposal: A proposal for observing time on HST

Phase II program: An approved HST program; includes precise detail of how program is to be executed

PI: Principal investigator

P-flats: pixel-to-pixel high-frequency flats

PRF: Pixel Response Function

PSF: Point-spread function.

PyRAF: version of IRAF implemented in the Python language

QE: Quantum Efficiency

QEH: Quantum Efficiency Hysteresis

Quadrant: Section of detector that is read-out by an amplifier. For WFC, there are 4 amplifiers, two for each detector, so each amplifier reads one 2048 x 2048 pixel quadrant.

RA: Right Ascension

RAS: HST simulator used in ground tests to accurately simulate the full field OTA illumination, and is used to calibrate HST instruments. Also know as RAS/HOMS, the Refractive Aberrated Simulator/Hubble Opto-Mechanical Simulator.

reference file: data file containing ACS parameters or calibration information which is used by the calibration pipeline

rms: Root mean square

RQE: Responsive Quantum Efficiency

SAA: South Atlantic anomaly

SBC: Solar-Blind Channel

SDSS: Sloan Digital Sky Survey

SITe: Scientific Image Technologies; company that designed the ACS CCDs

SLIM: Slitless Spectroscopy Simulator

SMOV: Servicing Mission Observatory Verification

S/N: signal-to-noise ratio

SNAPSHOT: Short exposures taken during unused blocks of telescope time.

ST-ECF: Space Telescope European Coordinating Facility

STAN: Space Telescope Analysis Newsletter

STIS: Space Telescope Imaging Spectrograph

STScI: Space Telescope Science Institute

STSDAS: Space Telescope Science Data Analysis System. The complete suite of IRAF data analysis and calibration routines used to process HST data.

synphot: STSDAS synthetic photometry (IRAF) software package

TAC: Telescope Allocation Committee

TECs: Thermal Electric Coolers

Tiny Tim: PSF simulation software developed by John Krist & Richard Hook

URL: Uniform resource locator. Address for WWW.

UV: Ultraviolet

VTT: a tool in APT that displays HST instrument apertures superimposed on FITS format sky images.

WFC: Wide-Field Channel

WFPC2: Wide Field Planetary Camera-2. Replacement for WF/PC installed during first servicing mission of December 1993.

WWW: World Wide Web. Hypertext-oriented method for finding and retrieving information over the Internet.

Index